Multiscale assessment of hydrological responses of Nature-Based Solutions to improve urban resilience

Yangzi Qiu

To cite this version:

Yangzi Qiu. Multiscale assessment of hydrological responses of Nature-Based Solutions to improve urban resilience. Other. École des Ponts ParisTech, 2021. English. NNT : 2021ENPC0007 . tel-03404617

HAL Id: tel-03404617
https://pastel.hal.science/tel-03404617v1

Submitted on 26 Oct 2021

Thèse présentée pour obtenir le grade de

Docteur de l' École des Ponts ParisTech

Spécialité: Sciences et Techniques de l'Environnement

par

Yangzi QIU

ECOLE DOCTORALE : SCIENCES, INGÉNIERIE ET ENVIRONNEMENT

Évaluation multi-échelle des réponses hydrologiques des Solutions Fondées sur la Nature pour améliorer la résilience urbaine

Multiscale assessment of hydrological responses of Nature-Based Solutions to improve urban resilience

Thèse soutenue le 16 avril 2021 devant le jury composé de :

Čedo Maksimovic	*Président*
Klaus Fraedrich	*Rapporteur*
Ana Maria Tarquis	*Rapporteur*
Jiannan Wu	*Examinateur*
Bruno Tisserand	*Examinateur*
Ioulia Tchiguirinskaia	*Co-directrice de thèse*
Daniel Schertzer	*Directeur de thèse*

Acknowledgement

I would like to express my sincere gratitude to my supervisors Daniel and Ioulia for their guidance. I'm really grateful to have the last three years dedicated to my research with my supervisor's help. Thank you for giving me this great opportunity to allow me to grow as a researcher. Thank you for always encouraging me to try innovative paths in my research work.

I would also like to show my gratitude to my thesis committee: Professor Ana Maria Tarquis, Professor Klaus Fraedrich, Professor Čedo Maksimovic, Professor Jiannan Wu and Mr. Bruno Tisserand. I appreciated very much for your time review this dissertation and to provide valuable contributions. Your suggestions and comments are helpful to improve this work.

My sincere appreciation to my HM&Co friends for their support and the pleasant moments over these three years. Thanks to Pierre-Antoine and Igor for involvement and assistance for this work. Thanks to Auguste, who has always answered my frequent queries. Thanks to Abdellah for his help on Multi-Hydro model. Thank you Catherine and Albertine for being here for administrative support. Thanks to Alejandra, Angel, Aderson, Arun, Chloé, Filip, Guillaume, Hai, Ilektra, Jisun, Julien, Jerry, Lin hui, Lucas, Mario, Rosa, Tim, Wiam, Xin, Yannis, I will miss you, guys.

Many thanks to the ENPC colleagues. I would like to mention in particular Ms. Christelle Berol, Ms. Chantal Dekeyser for all your support and assistance.

Some special words of gratitude go to my family, my parents. Thanks for always being my side, encouraging and motivating me. I can’t forget to thank all my friends who supported me.

Finally, I would like to acknowledge the financial support of the China Scholarship Council, La foundation des Ponts, and the Chair “Hydrology for Resilient Cities” (endowed by VEOLIA) and express gratitude to colleagues from SIAVB and Veolia.

Abstract

Over the past few decades, the urban hydrologic cycle has been greatly altered by the built environment, resulting in rapid runoff and an increased risk of waterlogging. Nature-based solutions (NBS), which apply green infrastructures, have been widely considered as sustainable approaches for urban stormwater management. However, as the urban environment is heterogeneous, the hydrological responses of NBS are still unclear. Therefore, the main objective of this thesis is to evaluate the performance of nature-based solutions using a fully distributed hydrological model Multi-Hydro to better manage stormwater in urban watersheds.

The field analysed in the case study is a 5.2 km^2 semi-urban catchment belonging to the Guyancourt city, which is located in the South-West suburb of Paris. Three types of rainfall data are used as rainfall inputs for different purposes. These rainfall data were obtained from: (i) polarimetric X-band radar of École des Ponts ParisTech (ENPC); (ii) the Météo-France polarimetric C-band radar of Trappes; and (iii) the uniform rainfall by spatially averaging the X-band radar data at each time step. Three types of NBS are studied: permeable pavement, rain garden and green roof. Based on the properties of these NBS and catchment conditions, several groups of NBS scenarios characterised with different spatial distributions were created and investigated by using the fully-distributed and physical-based hydrological model Multi-Hydro with a spatial resolution of 10 m.

Since the hydrological responses of NBS sensitively depend on: (i) the spatial variability in rainfall; (ii) the spatial distributions of NBS; and (iii) their intersection effects, which implies that the overall performances of NBS scenarios simulated with uniform rainfall or lumped/semi-distributed model may not be entirely convincing. Thus, the first goal of this thesis is to investigate the uncertainty of hydrological responses in various NBS scenarios resulting from the spatial variability in rainfall and the heterogeneous distribution of NBS at the urban catchment scale. The results show that the uncertainty on peak flow of NBS scenarios was largely influenced by the spatial variability in rainfall, and the intersection effects produce a somewhat significant impact on the peak flow of green roof scenarios and the total runoff volume of combined scenarios.

To further investigate the impacts of small scale rainfall variability on the hydrological responses of NBS scenarios, six different rainfall products from C-band radar and X-band radar are used as the rainfall inputs. The result indicates that the hydrological performances of NBS scenarios simulated with X-band radar data are more stable than that of the C-band radar data in terms of the studied rainfall events.

To characterise the hydrological performance of NBS scenarios over a wide range of scales, the theoretical framework of Universal Multifractals (UM) was applied. In particular, the maximum probable singularity has been shown to be the scale independent indicator to effectively infer the critical extremes of overland flow, to optimize the intervention, increasing the city's resilience for stormwater management at multiple scales.

Finally, the scale-independent cost-effectiveness indicator based on the UM framework has been developed and validated in comparison to the scale-independent one. It appears to be much more adapted to the multi-scale developments and, hence, more effective in supporting the future process of urban planning and decision-making.

Keywords

Nature-based solutions; X-band radar data; C-band radar data; Hydrological modelling; Universal Multifractal; Spatial variability; Stormwater management.

Résumé

Au cours des dernières décennies, le cycle hydrologique urbain a été fortement modifié par l'environnement bâti, ce qui entraînant un ruissellement rapide et une augmentation du risque d'inondation. Les Solutions fondées sur la Nature (SFN), qui utilisent des infrastructures vertes, sont de plus en plus considérées comme des approches durables pour la gestion des eaux pluviales urbaines. Cependant, en raison de l'environnement urbain est hétérogène, les réponses hydrologiques du SFN ne sont toujours pas claires. Pour cette raison, l'objectif principal de cette thèse est d'évaluer les performances des Solutions fondées sur la Nature à l'aide du modèle hydrologique entièrement distribuée pour mieux gérer les eaux pluviales dans les bassins versants urbains.

Le site analysé dans le cas d'étude est un bassin versant périurbain avec de surface environ 5,2 km^2 appartenant à la ville de Guyancourt, située dans la banlieue Sud-Ouest de Paris. Trois types de données précipitations sont utilisés comme entrées précipitations à des fins différentes. Ces données précipitations ont été obtenues à partir : (i) du radar polarimétrique en bande-X de l'École des Ponts ParisTech (ENPC) ; (ii) le radar polarimétrique en bande-C de Météo-France de Trappes ; et (iii) les précipitations uniformes en calculant la moyenne spatiale des données radar en bande-X à chaque pas de temps. Trois types de SFN sont étudiés : le pavé imperméable, le jardin pluvial et le toit vert. Sur la base les propriétés de ces SFN et les conditions du bassin versant, plusieurs groupes de scénarios SFN caractérisés avec différentes distributions spatiales sont créés et étudiés en utilisant le modèle physique complètement distribué Multi-Hydro avec une résolution spatiale de 10 m.

Étant donné que les réponses hydrologiques des SFN dépendent de façon sensible : (i) de la variabilité spatiale des précipitations ; (ii) les distributions spatiales des SFN ; et (iii) leurs effets d'intersection, ce qui implique que les performances globales des scénarios SFN simulés avec des précipitations uniformes ou un modèle forfaitaire / demi-distribué peuvent ne pas être entièrement convaincantes. Ainsi, le premier objectif de cette thèse est d'étudier l'incertitude des réponses hydrologiques dans divers scénarios SFN résultant de la variabilité spatiale des précipitations et de la distribution hétérogène des SFN à l'échelle du bassin versant urbain. Les résultats montrent que l'incertitude sur le débit de pointe des scénarios SFN a été largement influencée par la variabilité spatiale des précipitations, et les effets d'intersection produisent un impact assez significatif sur le débit de pointe des scénarios de toiture verte et le volume total de ruissellement des scénarios combinés.

Pour étudier plus en détail les impacts de la variabilité des précipitations à petite échelle sur les réponses hydrologiques des scénarios SFN, six produits précipitations différentes du radar en bande-C et du radar en bande-X sont utilisés comme entrées de pluie. Le résultat indique que les performances hydrologiques des scénarios SFN simulés avec des données radar en bande-X sont plus stables que celles des données radar en bande-C pour les événements précipitations étudiées.

Pour caractériser les performances hydrologiques des scénarios SFN sur une large gamme d'échelles, le cadre théorique de Multifractals Universels (UM) a été appliqué. En particulier, la singularité probable maximale s'est avérée être l'indicateur indépendant de l'échelle pour déduire efficacement les extrêmes critiques de l'écoulement de surface, pour optimiser l'intervention, en augmentant la résilience de la ville pour la gestion des eaux pluviales à plusieurs échelles.

Enfin, l'indicateur coût-efficacité indépendante de l'échelle basée sur le cadre de l'UM a été développé et validé par rapport à l'indicateur indépendant de l'échelle. Il semble être beaucoup plus adapté aux développements multi-échelles et, ainsi, plus efficace pour soutenir le futur processus d'urbanisme et de prise de décision.

Mots clés :

Solutions Fondées sur la Nature; Données radar en bande-X; Données radar en bande-C; Modélisation hydrologique; Multifractals Universels; Variabilité spatiale; La gestion des eaux pluviales.

Contents

List of figures

List of tables

Abbreviations

BGS	Blue Green Solutions
BGI	Blue Green Infrastructure
CALAMAR	Calcul de LAMes d’eau à l’Aide du RADAR
CE	Cost-effectiveness
CASQY	Comunauté d’Agglomération de Saint-Quentin-en-Yvelines
DTM	Double Trace Moment
DEM	Digital Elevation Model
DPSRI	Dual Polarisation Surface Rainfall Intensity
ENPC	École des Ponts ParisTech
GIS	Geographic Information System
GR	Green Roof
GHGs	Concentration of Greenhouse Gases
HM&Co	Hydrology Meteorology & Complexity
HRU	Hydrological Response Unit
IDF	Intensity-Duration-Frequency
IGN	French National Institute of Forest and Geographic Information
IPCC	Intergovernmental Panel on Climate Change
KDP	Specific Differential Phase
LCC	Life cycle costs
LID	Low Impact Development
MH	Multi-Hydro
MHDC	Multi-Hydro Drainage Module
MHGC	Multi-Hydro Groundwater Module
MHRC	Multi-Hydro Rainfall Module
MHSC	Multi-Hydro Surface Module

NSE	Nash-Sutcliffe Efficiency
NBS	Nature-based solutions
PA	Porous Asphalt
PC	Porous Concrete
PICP	Permeable Interlocking Concrete Pavers
PD	Percentage difference
PVC	Present values of Cost
PP	Permeable Pavement
PPRI	Plan de Prévention des Risques Inondation
PMRS	Renormalized maximum probable singularity
RI	Renormalized maximum probable singularity indicator
RG	Rain Garden
RMSE	Root-Mean-Square Error
SRI	Surface Rainfall Intensity
SRIMP	Surface Rainfall Intensity Multi-Parameters
SIAVB	Syndicat Intercommunal d’Assainissement de la Vallée de la Bièvre
SWMM	Storm Water Management Model
SD	Standard Deviation
SUSTAIN	System for Urban Stormwater Treatment and Analysis Integration
SV	Salvage Value
SWAT	Soil & Water Assessment Tool
TM	Trace Moment
TREX	Two-Dimensional Runoff Erosion and Export
UM	Universal Multifractal
UHE	Urban hydrological Element
VS2DT	Variably Saturated and 2-Dimensional Transport
WSUD	Water Sensitive Urban Design used in Australia
ZDR	Differential reflectivity

Symbols

A	Total implementation area of NBS	m^2
A_l	Total implementation areas of NBS at scale *l*	
C_1	Mean intermittency	
C_a	Annual operation and maintenance cost	$€/m^2$
C_0	Capital cost	$€/m^2$
c_M	Codimension of measured rainfall	
c_N	Codimension of rain gauge network	
c_R	Codimension of real rainfall	
$c(\gamma)$	Codimension function	
$CE\gamma_{max}(\lambda)$	Scale-dependent cost-effectiveness indicator at resolution λ	
$CE\gamma_s(\lambda)$	Scale-independent cost-effectiveness indicator at resolution λ	
D_F	Fractal dimension	
D_M	Fractal dimension of measured rainfall	
D_N	Fractal dimension of rain gauge network	
D_R	Fractal dimension of real rainfall	
D	Dimension	
D_s	Sample dimension	
D_p	Depth of depression storage	
f	Infiltration rate	m/s
f_p	Infiltration rate at time *t*	m/s
FC	Field capacity	
h	Surface water depth	m
h_p	Depth of permeable layer	m

h_b	Depth of bedding layer	*m*
H	Hurst's exponent	
$H_s(\lambda)$	Maximum probable overland flow at resolution λ	*m*
H	Overland flow	*m*
$H_{max}(t)$	Maximum overland flow at each time step	*m*
$H_{mean}(t)$	Mean overland flow at each time step	*m*
$H_{max,t_n}(\lambda)$	Maximum overland flow at resolution λ	*m*
$H_{mean,t_n}(\lambda)$	Mean overland flow at resolution λ	*m*
$H_r\,(t)$	Level of reservoir at time t	*mm*
i_e	Excess precipitation rate	*L/t*
IS	Initial substrate saturation	
K_{sat}	Saturated hydraulic conductivity	*mm/s*
KDP	Specific differential phase	*deg/km or rad/km*
$K(q)$	Scaling moment function	
l	Pixel size	
L	Outer scale	
L_A	Time span from the year of last maintenance to the end of the year of lifespan	year
M	Measured rainfall	*mm*
N	Rain gauge network	
n	Porosity of green roof substrate	
n_p	Porosity of pavement layer	
n_p	Porosity of beding layer	
LCC	Life cycle costs	*million €*
LCC (λ)	Life cycle costs at resolution λ	*million €*
PD_{Qp}	Percentage difference in peak flow	
PD_{V}	Percentage difference in total runoff volume	

$\boldsymbol{O_i}$	Observation water level	*m*
$\boldsymbol{Q_{out}(t)}$	Runoff generated by green roof at time *t*	*mm*
$\boldsymbol{q}$	Statistical moment	
$\boldsymbol{Q_{P_{base}}}$	Peak flow of baseline scenario	
$\boldsymbol{q_D}$	First-order critical moment	
$\boldsymbol{q_S}$	Second-order critical moment	
$\boldsymbol{Q_{p_{NBS}}}$	Peak flow of NBS scenario	
$\boldsymbol{R}$	Rainfall rate	*mm/h*
$\boldsymbol{S_i}$	Simulated water level	*m*
$\boldsymbol{S_{p\,max}}$	Maximum storage capacity of permeable pavement	*m*
$\boldsymbol{r}$	Discounting rate	
$\boldsymbol{t}$	Each time step	*min*
$\boldsymbol{t_n}$	Last time step	*min*
$\boldsymbol{T}$	Lifespan	*year*
Thick	Substrate thickness	mm
$\boldsymbol{V}$	Volume of precipitation stored in depression storage	
$\boldsymbol{V_{base}}$	Total runoff volume of the baseline scenario	
$\boldsymbol{V_{NBS}}$	Total runoff volume of the NBS scenario	
$\boldsymbol{W}$	Unit discharge from or to a point source	L^2/t
Z	Radar reflectivity factor	mm^6/m^3
ZDR	Differential reflectivity	*dB*
$\boldsymbol{\alpha}$	Multifractality index	
$\boldsymbol{\beta}$	Spectral exponent	
$\boldsymbol{\gamma_s}$	Maximum probable singularity	
$\boldsymbol{\gamma_{max}}$	Maximum singularity	
$\gamma_{max,t_n}(\lambda)$	Maximum singularity at scale λ	
$\boldsymbol{\Delta Q_{\mathrm{p}}}$	Peak flow reduction	
$\boldsymbol{\Delta V}$	Total runoff volume reduction	

Δt	Loop for each time step
ε_λ	Conservative field at scale λ
λ	Scale ratio

Introduction

General Context

The increased risk of flooding from urban storms appears to be closely linked to the following two key factors: rapid urbanisation and climate change (Lovejoy and Schertzer, 2013; Miller and Hutchins, 2017; Cai et al., 2019). According to the estimation of the world urbanisation prospects from United Nation[1], there are 4.1 billion people (55 %) living in urban regions (in 2017), and it is expected to increase to 68 % by 2050. The Intergovernmental Panel on Climate Change (IPCC) indicated that the globally averaged combined land, and ocean surface temperature had warmed by 0.85 °C from 1880 to 2012. This is due to the human activities induce an increase in the concentration of greenhouse gases (GHGs) in the atmosphere (IPCC, 2014). Furthermore, the extreme precipitation events will likely become more intense and more frequent in most continental regions, particularly in the high- and mid-latitude regions (Fraedrich et al., 1999). The increasing frequency of extreme precipitations can substantially worsen the flood risk from surface runoff in many urban areas. Apparently, the adaptation to climate change and the prevention of urban flooding now constitute significant societal challenges (Loukas et al., 2010). Impervious surfaces directly connected to grey infrastructures result in a rapid transfer of rainfall into runoff, which largely increases the risks of flood events, especially in urban watersheds (Fry and Maxwell, 2017; Ercolani et al., 2018). According to the statistics of natural disasters in Europe from 1980 to 2017, floods and storms were the most common disasters, which caused the largest economic damage (around 7 billion Euros[2]), especially in urban areas.

Generally, many cities built the hydraulically efficient drainage systems to cope with the stormwater runoff. However, as mentioned earlier, with the increase of the extreme precipitations, some of the built drainage systems are not able to sustain the extreme rainfall. Expanding and upgrading the capacity of the existing drainage system has been proved costly and unsustainable, which is challenging to realize in highly urbanised cites (Qin et al., 2013).

---

[1] https://population.un.org/wup/, last access: 16 June 2021

[2] https://www.eea.europa.eu/, last access: 16 June 2021

Increasing urban resilience to reduce the risk of urban flood has been emphasised in many countries (Kelman, 2015). Therefore, many Europe research projects were committed to stormwater management with the purpose of increasing the resilience of cities, such as the RainGain[3], Climate KIC Blue Green Dream[4] and SMARTesT[5]. Furthermore, some countries and regions have raised the interests in some sustainable alternations, such as nature-based solutions (NBS), low-impact development (LID), and blue green solutions (BGS), for managing stormwater runoff and mitigating the negative impacts of urbanisation on the urban hydrological cycle (Rozos et al., 2013; Maksimovi et al., 2015; Song et al., 2019;). NBS refer to a sustainable strategy, capable of reducing the influences of human activities on the natural environment, which is especially efficient for stormwater management (European Commission, 2015; Cohen-Shacham et al., 2016). These natural systems use small scale hydrological measures to store, detain, infiltrate, and evaporate stormwater runoff on spots, to help recover the hydrological regime of watersheds back to pre-development conditions (Ahiablame et al., 2012, Ahiablame et al., 2013; Palla and Gnecco, 2015). This often includes bio-retention swale, permeable pavement, green roof, and rain garden, because these infrastructures are able to conserve or recover the natural environment of a region (Newcomer et al., 2014).

Overall, these challenges and the sustainable development strategies highlight the main objective of this PhD research: multi-scale assessment of hydrological responses of nature-based solutions with the help of the fully-distributed hydrological model to improve urban flood resilience.

Main Issues (Scientific Questions)

Space-time variability

As indicated by some researchers (Dietz, 2007; Cohen-Shacham et al., 2016; van den Bosch and Ode Sang, 2017), NBS provides many benefits to urban environments. However, the hydrometeorological conditions are heterogeneous in different watersheds, which makes the NBS highly depends on the site conditions, and this can explain why the range of hydrological performances of NBS is extensive in different researches (Eckart et al., 2017).

The hydrological performances of such NBS have been approached in terms of the reduction

---

[3] http://www.raingain.eu, last access: 16 June 2021
[4] http://www.bgd.org.uk, last access: 16 June 2021
[5] http://floodresilience .eu/, last access: 16 June 2021

of total runoff volume and peak flow at the urban catchment scale (Zahmatkesh et al., 2015; Ahiablame and Shakya, 2016; Bloorchian et al., 2016). Generally, the results of a large number of studies are based on lumped or semi-distributed models (Ahiablame et al., 2013; Liu et al., 2015; Massoudieh et al., 2017; Guo et al., 2019). Indeed, as underlined by Fry and Maxwell, (2017) and Her et al., (2017), fully-distributed models are rarely used (Versini et al., 2016; Hu et al., 2017; Versini et al., 2018). While there is a general consensus that these models should better assess the hydrological performances of NBS implemented at smaller scales, the deployment of the fully distributed models has been stuck for some time by the following three main factors: (i) availability of reliable high-resolution forcing, (ii) complex interactions between the processes, and (iii) reliable parameterization process (e.g. Imhoff et al., 2020). Among all these hydrological models, the semi-distributed Storm Water Management Model (SWMM) remains the one that is most frequently used to investigate the impact of NBS on urban runoff and water quality (Jia et al., 2012; Sun et al., 2014; Palla and Gnecco, 2015; Cipolla et al., 2016; Kwak et al., 2016). Nevertheless, Rossman et al. (2010) demonstrated that SWMM has some limitations in reflecting complicated urban catchments, which in turn presents some difficulties for sustainably replicating show different hydrological responses to a variety of urban land uses. The study of Burszta-Adamiak and Mrowiec (2013) confirmed that SWMM is not really explicit for presenting the hydrological responses of catchments with only the help of the percentage of pervious and impervious land covers. These gaps imply strong limitations to the results obtained with the help of lumped and the semi-distributed models. Thus, to make the modelling results more accurate and credible, there is a strong need to use fully-distributed and physically-based models. Indeed, under the conditions of reliable high resolution forcing and parameterisation of the model (Imhoff et al., 2020), such models can better assess the hydrological performances of NBS in a small scale (Fry and Maxwell, 2017; Versini et al., 2018).

At the same time, due to the long-standing challenge of the availability of reliable and high-resolution spatio-temporal precipitation measurements in urban areas, some studies have been devoted to assessing the performance of NBS under the simplifying assumption of an uniform rainfall (design storm or data from rain gauges), hence the impact of spatial rainfall variability in the heterogeneous urban context was not considered (Holman-Dodds et al., 2003; Gilroy and McCuen, 2009; Qin et al., 2013; Versini et al., 2018; Zhu et al., 2019; Guo et al., 2019). However, the hydrological responses of NBS (model outputs) largely depend on: (i) the highly spatially variable rainfall fields; (ii) the spatial distribution of the NBS; and (iii) their intersection effects. The rainfall and the NBS represent two heterogeneous fields that do not coincide, which implies that the overall performances of NBS scenarios simulated with uniform rainfall or lumped/semi-distributed model may not be entirely convincing. Therefore, such mentioned impacts remain to be investigated, in particular over higher spatial resolutions, by using the space-time rainfall fields together with a fully-distributed model, allowing for heterogeneous NBS scenarios.

Regarding the available rainfall data, weather radar has been widely applied to provide local rainfall measurements (Diss et al., 2009; Tabary et al., 2011; Emmanuel et al., 2012; Wang et al., 2013). Weather radar provides space-time rainfall estimation, even they do not directly measure the rainfall. For the rainfall with high intensity, the technology of dual polarization has been used to enhancement the estimation (Figueras i Ventura et al., 2012). This technology can directly estimate the rainfall intensity based on the phase difference of the reflected (vertical and horizontal) signals. Some studies used hydrological models to compare different radar products and analyse the different hydrological responses of the catchment (Alves de Souza et al., 2018; Paz et al., 2018; Paz et al., 2019).

In this respect, the first goal of this thesis is to investigate the uncertainty of hydrological responses in various NBS scenarios resulting from the spatial variability in rainfall and the heterogeneous distribution of NBS at the urban catchment scale, and thus not those associated to the model structure, hypothesis or parameterization for instance. Furthermore, there is a great interest to assess the hydrological responses of NBS in terms of the rainfall products with different spatial and temporal resolutions. Because the choice of the rainfall input strongly influences the simulated hydrological responses of NBS, and affects the evaluation of the performances of NBS in the catchment and the corresponding future urban planning.

Scales

As the scale issue is a common one in hydrology, for assessing the hydrological performances of NBS in terms of multi-scales for mitigating urban waterlogging, it is essential to investigate the intrinsic complexity of the heterogeneity of overland flow (Adeyemo et al., 2008; Maksimović et al., 2015), especially across the range of scales (Gires et al., 2018). As mentioned earlier, most of the modelling based studies used peak flow reduction and total runoff volume reduction concerning the discharge in the outlet of the sewer system as the evaluation indicators (Sun et al., 2014; Versini et al., 2015; Zahmatkesh et al., 2015; Ahiablame and Shakya, 2016; Bloorchian et al., 2016; Peng et al., 2019), which did not consider the dynamical behaviour of the overland flow. Although some of the studies used Flo-2D model to analyse the overland flow with the help of the 2D hazard map (Hu et al., 2013; Luo et al., 2018; Gao et al., 2019), they only considered at a single scale (i.e., the highest available resolution). Thus, the intrinsic complexity of the heterogeneity of overland flow across range of scales are not considered in those studies.

With this respect, it is significant to propose a scale-independent indicator for evaluating this complexity. The Universal Multifractal (UM) framework (Schertzer and Lovejoy, 1987) is considered as an appropriate technique to investigate this issue, which is a stochastic approach used widely in geophysics to characterise extremely variable fields over a wide range of scales.

Socio-economics

The issues mentioned above are related to the evaluation of hydrological performances (e.g, infiltration, retention, detention) of NBS. However, for future urban planning, the environmental assessment and management coupling with sustainable development is significant (Wu et al., 2018). Therefore, it is essential to consider both hydrological and socio-economic impacts of NBS to support the decision-making process (Liao et al., 2013; Li et al., 2020). At present, few studies considered both of the technical and economic criteria to investigate the cost-effective NBS alternations (Liao et al., 2013; Li et al., 2020). Martin et al. (2007) and Hua et al. (2020) pointed out the multi-criteria analysis approach is significant for future NBS scenarios evaluation due to the importance of each criterion is quite different, and it needs to use the integrated evaluation process to quantify and find an optimal alternation. For instance, Hua et al. (2020) had used the integrated evaluation method to evaluate the performances of different land use scenarios with implantation of varies types of NBS in an urban catchment. However, they used the semi-distributed model and uniform rainfall data (i.e., the design storm), which did not consider the spatial heterogeneity distribution of NBS and small scale rainfall variability. Thus, the predictions of hydrological responses of NBS scenarios are not entirely reliable and affect the design of cost-effective alternations.

As indicated previously, the hydrological performances of NBS scenarios are strongly related to the studied scale. Thus, the heterogeneity of the hydrological performances and the economic costs of NBS scenarios across a range of scales need to be further analysed. It is necessary to propose a scale-independent indicator to design the cost-effective NBS scenarios for improving the urban resilience in multi-scale.

PhD Thesis Objectives

Following the main issues raised in the previous section, the objectives of this PhD thesis intend to contribute to the comprehension of the scientific perception of urban resilience to flooding risk, which can be summarised as follow:

(i) Numerical modelling of hydrological responses of various NBS scenarios at the urban catchment scale by using the fully-distributed and physically-based hydrological model (Multi-Hydro). More precisely, the first goal is to investigate the space variability of hydrological responses of NBS scenarios and the resulting uncertainty. Then, to further study the impacts of the small scale rainfall variability on the hydrological performances of NBS scenarios.

(ii) To characterise the overland flow of various NBS scenarios across a wide range of scales with the help of Universal Multifractal (UM) theoretical framework (Schertzer and Lovejoy, 1987). This approach appears to be an appropriate tool due to its ability to deal with both temporal and spatial variability of different geophysical fields.

(iii) To design the cost-effective NBS scenarios under different rainfall conditions at the catchment scale by integrating the classical hydrological indicators (i.e., peak flow reduction can total runoff volume reduction) and economic indicator (i.e., life cycle costs).

(iv) To propose the scale-independent cost-effectiveness indicator based on the UM framework to adapt to the multi-scale developments and, hence, more effective in supporting the future process of urban planning and decision-making.

Thesis Structure

Based on the mentioned objectives, this thesis was structured from a single scale of numerical modelling, then gradually transiting to the multi-scale assessment of performances of NBS scenarios.

The research background, the concept of NBS, the specific NBS measures (i.e., permeable pavement, rain garden and green roof) that studied in thesis and the modelling approach are presented in Chapter 1. In Chapter 2, the case study of Guyancourt catchment, and all the corresponding materials that used for this thesis are described in detail. More precisely, it includes: (i) the data processing process (e.g. Geographic Information System (GIS) data and rainfall data), selected rainfall events that used for different objectives; (ii) the fully-distributed and physically-based hydrological model Multi-hydro, and the model validation for Guyancourt catchment; and (iii) the NBS scenarios that created for the numerical modelling experiments. Chapter 3 starts with fractal dimension, and then introduces the Universal Multifractal framework, and finally presents the application of UM techniques on the rainfall data. As mentioned previously, one of the objectives of this thesis is numerical investigation of the hydrological performances of various NBS scenarios in mutiscale and this is mainly investigated in Chapter 4. This Chapter includes three modelling experiments: (i) to study the space variability of hydrological responses of NBS scenarios and the resulting uncertainty (Section 4.1); (ii) to investigate the impacts of small scale rainfall variability on the hydrological performances of NBS scenarios with the help of C-band and X-band radar data (Section 4.2); (iii) multifractal characterisation of overland flow of NBS scenarios across a wide range of scales (Section 4.3). Chapter 5 respects to the social economic issue, thus, the main objective of this chapter is to design the cost-effective NBS scenarios. This Chapter has two sections, the Section 5.1 is to design the cost-effective NBS scenarios under different rainfall conditions at the urban catchment scale by integrating the classical technical indicator with the economic indicator. Then, Section 5.2 is to propose a scale-independent cost-effectiveness indicator based on UM framework to design the cost-effective NBS scenarios across a wide range of scales.

Chapter 1

Urban stormwater management

A typical urbanisation process is always accompanied by the expansion of impervious surface areas, for example, roads and buildings (Ercolani et al., 2018). These modifications changed the original urban hydrological cycle, which hampered rainfall infiltration and resulted in the increase of corresponding stormwater runoff peak and volume (Fry and Maxwell, 2017). To cope with the urban waterlogging, the hydraulically efficient drainage systems were designed and implemented in many urbanised cities. However, with climate change, a large number of extreme rainfalls occur more frequently all over the world. Thus, the current designed drainage systems in many cities are not able to support such fast surface runoff. Besides, the approach by improving the capacity of the drainage systems is considered unsustainable and costly in highly urbanised cities (Qin et al., 2013). Such limitations have raised the interest in nature-based solutions, which can increase the urban resilience and decrease the negative impacts of urbanisation on the hydrological cycle (European Commission, 2015; Cohen-Shacham et al., 2016; Faivre et al., 2017; Turconi et al., 2020).

Because of the complexity of small scale rainfall variability and the heterogeneity of the urban environment context, the hydrological responses of NBS in the urbanised or semi-urbanised areas are still not clear, which needs a more comprehensive evaluation of the rainfall-runoff process with the help of hydrological models (Zahmatkesh et al., 2015; Bloorchian et al., 2016; Ahiablame and Shakya, 2016; Hu et al., 2017). At present, most modelling-based studies adopted lumped or semi-distributed models, which showed some difficulties to present the heterogeneity of catchments (Miller and Hutchins, 2017; Gao et al., 2019). This type of model uses lumped parameters which significantly affect the model predictions and may neglect some critical information related to the spatial distributions of precipitation and land use (Bhaduri et al., 2008; Lee et al., 2004; Yao et al., 2016; Bell et al., 2016; Fry and Maxwell, 2017; Bai et al., 2019).

Thus, to obtain more accurate and credible modelling results, there is a strong need to adopt the fully-distributed and physically-based models (Versini et al., 2016; Hu et al., 2017a; Versini et al., 2018). The distributed geographic information can be easily applied in such models, and the corresponding physically-based parameters need few calibrations (Ichiba et al., 2018), which can better evaluate the hydrological performances of NBS with a high resolution. Furthermore, the urban catchment is a very complex system, thus the hydrological performances of NBS significantly depend on the scale of studies. Therefore, there is a strong need to find a scale-independent indicator to assess the performances of NBS in a wide range of scales and a more universal solution for varies watersheds. With this respect, the Universal Multifractal (UM) framework (Schertzer and Lovejoy, 1987; Lovejoy and Schertzer, 1990; Schertzer and Lovejoy, 1997; Tchiguirinskaia et al., 2004; Lovejoy and Schertzer, 2011) can be considered as an effective and innovative approach to achieve the goal of this thesis.

In this chapter, the main objective is to present the general framework of this thesis and the main theories adopted. Therefore, the following sections (Sections 1.1 and 1.2) introduce the risks of urban waterlogging and the corresponding details of the stormwater management strategy: nature-based solutions. Several typical NBS studied in this thesis are described in detail. Then, in Section 1.3, the hydrological modelling approaches are reviewed, and the fully-distributed and physically-based model (Multi-Hydro) is presented in detail (Giangola-Murzyn, 2013; Ichiba et al., 2018). Finally, the Universal Multifractal theory is detailed introduced in Section 1.4, from the concept of fractal and gradually to the universal multifractals.

1.1 Urban flooding risk and resilience

Human activities are one of the reasons which increase the risk of urban flooding/waterlogging. To meet the needs of human survival and development, urban environments have been largely transformed. Furthermore, meteorological extremes (e.g. the increase of severe events) happen more frequently all over the world, which make urban areas more vulnerable subject to the flooding/waterlogging.

In order to define the level of a flood hazard in urban regions, many researchers used the criteria of flood intensities (Meon et al., 2006; Hu et al., 2017; Gao et al., 2019), which was considered as a guide for modelling the urban flooding (Flo-2D manual, 2012). This criterion is quantified with respect to the maximum water depth h (m) and a result of the maximum velocity multiplied by the maximum depth vh (m^2/s). Overall, three levels can be defined as follows:

(i) The h higher than 1.2 m and vh higher than 1.5 m^2/s, indicates a high hazard level. In this level, people inside or outside the building are in danger and facilities are in risk of being destroyed.

(ii) The *h* and *vh* in the medium level are corresponding to 0.6 to 1.2 m and 0.5 to 1.5 m^2/s, respectively. In this level, people outside the structures are in danger, and some vulnerable buildings with low supporting construction materials may be deconstructed or damaged.

(iii) The *h* between 0.1 and 0.6 m and *vh* between 0.1 and 0.5 m^2/s is corresponding to the low level. In this level, the flooding risk is less dangerous for people. The structures of buildings may be affected, but the risk of being destroyed is relatively low.

As indicated in some previous literatures of urban hydrology, the expansion of cities and populations caused that some buildings and infrastructures near the river beds or easily flooding areas were faced with more flooding risks (Wheater et al., 2012; Nardi and Rinaldi, 2015).

In France, the actions for improving the resilience of cities to cope with the flooding can trace back to the 18th century. In that period, resilience to flooding was based on the dynamics of territories at a city scale. For instance, the city of Amiens was flooded many times during the 17th and 18th centuries. However, in 1658 and 1784, two severe flooding events had little impact on the food and textile market of Amiens. This was thanks to the municipalities did many prevention actions and made the corresponding law for it (PITEL, 2011). These examples show that the concept of resilience has shifted from a simple status of consciousness to the construction and integration of risk into social activities.

In the 20th century, a flood risk prevention plan called “Plan de Prevention des Risques Inondation (PPRI)” was proposed in France based on the law No. 87-565 of July 22, 1987. Since February 2, 1995, based on the law No. 95-101, every city faced with flood risk must set up a PPRI, which is obligated.

Figure 1.1 shows an example of the flood risk prevention plan of the Bièvre valley (South-West of Paris, France) with highlighting the city of Guyancourt (one of the sub-catchment of Bièvre catchment, more information about this catchment can be found in Chapter 2). This map indicates the areas exposed to the flooding risk and the red zone represents the areas with high flood risk, where any constructions are not allowed. The blue zone means the areas which are allowed to be developed but with some limitations based on the historical flooding events.

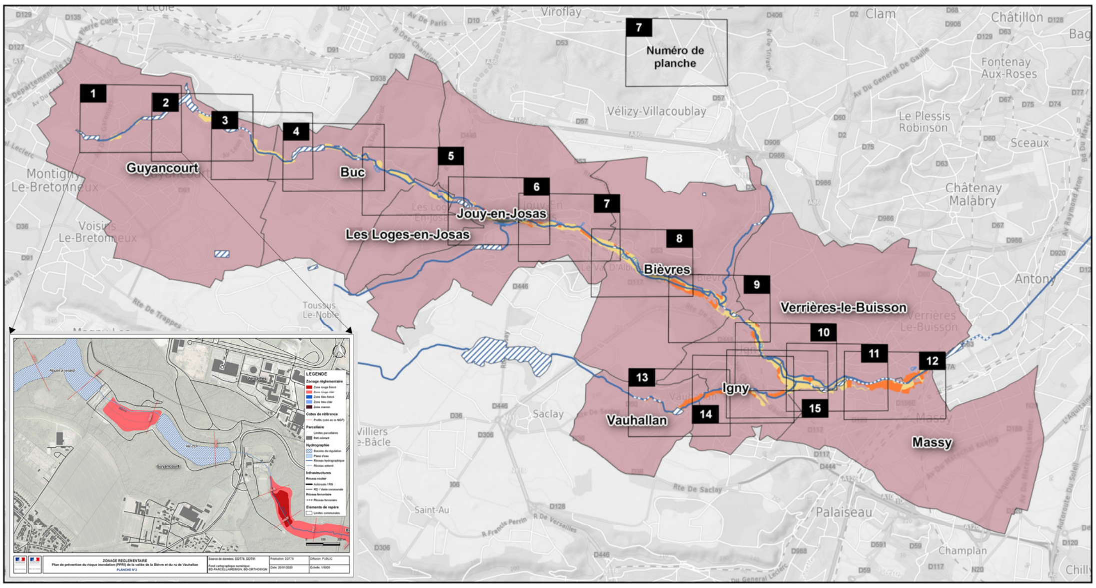

Figure 1.1: The flood risk prevention plan (Plan de Prévention des Risques Inondation) of Bièvre valley, with highlighting the Guyancourt city (obtained from http://www.yvelines.gouv.fr/, last access: 16 June 2021).

Recently, the interest in resilience has been devoted in the area of natural disaster mitigation, especially associated to the flooding risk. Assessment of urban resilience in terms of flooding is usually concerning the cities runoff volume regulation, increasing drainage capacity, spatial planning, etc. Some researchers have defined the urban resilience as the degree of cities that can tolerate some disturbance before reorganizing around a new set of structures and processes (Holling, 1973). Although the concept of "resilience" has been widely mentioned for stormwater management by different researchers in an ecological context (Holling, 1973) or social field (Galderisi, 2005; Balica and Wright, 2010; Cashman, 2011; Vicari et al., 2019), a corresponding definition in mathematics is still rather elusive. To be more specific, analyses of scenarios require the mathematical definition of the units of resilience, which are based on those conceptual definitions (Holling, 1973; Cashman, 2011).

Apparently, the dynamic conceptualization of the resilience system is strongly related to the general definition of the dynamic system (Arrowsmith, 1990). Although the dynamic system approach seems to be fairly general, as indicated by Giangola-Murzyn (2013), it has some limitations. For instance, there are many technical difficulties in going beyond ordinary differential systems: the fundamental differences between time-complex systems (ordinary differential systems) and those which are complex in both space and time (partial differential systems). The key point of the latter is the emergence of the spatial scale and the dependence of associated state variables, as well as the interaction between the spatial and temporal scales (May, 1973; Pimm, 1984). This is particularly important for estimating inverse return times, as they depend on the spatial scale of observation and it is not possible to apply the multiplicative ergodic theorem (Schertzer and Lovejoy, 2004).

Regarding the mentioned limitations, as indicated by Folke et al. (2010), the multi-scale resilience is fundamental for understanding the interplay between persistence and change, adaptability and transformability. Without the dimension of scale, resilience and transformation may appear to be at odds or even in conflict. Therefore, multi-scale resilience needs to be further investigated. Indeed, it is possible to be defined with consideration of the symmetries of scales, because they considerably reduce the space-time complexity by defining independent observable scales from the initial fields which are substantially scale-dependent (see more details in Schertzer et al., 2010).

Furthermore, to be independent of the scale or across scales, the multi-scale resilience needs to be defined with the help of the singularities of the field. Namely, the exponent of the divergence (algebraic) of the field observed in increasingly small scales. For instance, the scale-independent indicator (maximum probable singularity γ_s) was used for quantifying the evolution of multi-scale simulated precipitation under the climate change scenarios over France (Royer et al., 2008), analysing the extremes of rainfall storm over Paris region (Tchiguirinskaia et al., 2011), and assessing the multi-scale resilience in terms of flood resilience system (Giangola-Murzyn, 2013).

This scale-independent indicator is also initially applied in this thesis to quantify the performances of NBS scenarios (see a short description in Section 1.4 and more results and discussions can be found in Chapter 5).

1.2 Urban stormwater management strategies: nature-based solutions

According to the UN 2030 Agenda and following international agreements (in particular Habitat III), the aim of the present work is to greatly enhance urban resilience, for instance, the UN Sustainable Development Goal 11. Apparently, nature-based solutions are more and more considered as the key solution to achieve this goal.

The European Commission defines nature-based solutions as a way to address societal challenges with '*solutions that are inspired and supported by nature, which are cost-effective, simultaneously provide environmental, social and economic benefits and help build resilience. Such solutions bring more, and more diverse, nature and natural features and processes into cities, landscapes and seascapes, through locally adapted, resource-efficient and systemic interventions*' (European Commission, 2015). NBS is the concept used in EU, which builds on and supports similar, widely used concepts. Such as the low-impact development (LID) proposed in the U.S (Ahiablame et al., 2013; Grebel et al., 2013), Blue–Green Infrastructures (BGI), and some more local ones, like sustainable urban drainage system (SUDS) used in the U.K (Rozos et al., 2013; Bozovic et al., 2017), water–sensitive urban design (WSUD), from Australia (Morison and Brown, 2011; Wong 2006), or a "sponge city", proposed recently in China (Chan et al., 2018). Nature-based solutions is beneficial for bringing nature back into cities and degraded ecosystems, improving human health and well-being, and adapting to climate change has been indicated in some researches (Cohen-Shacham et al., 2016; van den Bosch and Ode Sang, 2017). With respect to stormwater management, NBS suggests using a suite of small scale and on-site controlled measures to manage stormwater runoff. According to the report by the European Commission (2015), more than 200 measures with the implementation of NBS are listed. Some researchers also indicated that multiple societal challenges can be addressed simultaneously through nature-based solutions (i.e., decreasing the risk of urban floods, increasing the resilience of cities, combatting the effects of heat islands, and conserving biodiversity (Cohen-Shacham et al., 2016; Raymond et al., 2017).

The purpose of implementing small scale controlled measures is to infiltrate and retain the runoff on site as much as possible, to use the natural system of the site to filter the runoff and to improve the water quality. The application of NBS on site is beneficial for recovering the site to the pre-development hydrological regime. Fletcher et al. (2013) and Eckart et al. (2017) categorised them into two different types: infiltration-based measures and retention-based measures. The infiltration-based NBS can be described as measures which can help restore base flows by replenishing of subsurface flows and groundwater (Fletcher et al., 2013). This type of NBS is largely dependent on the environmental conditions of a site, and the corresponding researches provide results in a wide range (Brattebo and Booth, 2003; Newburn and Alberini, 2016; Kamali et al., 2017; Yuan et al., 2017). The infiltration-based NBS mainly includes permeable pavements, rain gardens, swales, infiltration trenches, basins, bio-retentions, and sand filters. The retention-based NBS can be characterised as measures which retain stormwater to reduce outflow (Fletcher et al., 2013), including ponds, green roofs, wetlands, rain tanks/barrels or storage basin.

The specific measures in terms of infiltration-based and retention-based are introduced in details in the following sub-sections.

1.2.1 Permeable pavement

Permeable pavement is a kind of infiltration-based NBS with high porosity, which can efficiently store surface runoff temporarily and allow that the runoff infiltrates slowly into the subsoil (Scholz and Grabowiecki, 2007). Permeable pavements have different types, such as porous asphalt (PA), porous concrete (PC) and permeable interlocking concrete pavers (PICP). PAs can be laid out on highways, PCs are usually used in parking lots or some areas with light traffic, and PICP is individual units that can be implemented with an interlocking grid pattern, the spaces between every single unit are generally filled with small stones or grass. Due to the aesthetics appeal of PICP, they are commonly used in parks or residential streets.

Overall, a typical cross-section of permeable pavement was shown in Figure 1.2. This typical permeable pavement includes block pavers, plastic grid systems, porous asphalts, and porous concretes. Through permeable pavements, the runoff can be reduced efficiently even during the intensive storm rainfall events (Bean et al., 2007; Winston et al., 2020). Compared to the traditional concrete pavements and traditional asphalt, permeable pavements can infiltrate storm runoff into the subsurface gradually, and promote the treatment of pollutants and recharge. Fassman and Blackbourn (2010) indicated that the application of permeable pavements was beneficial for that the catchment hydrological regime gradually returns to the pre-development condition.

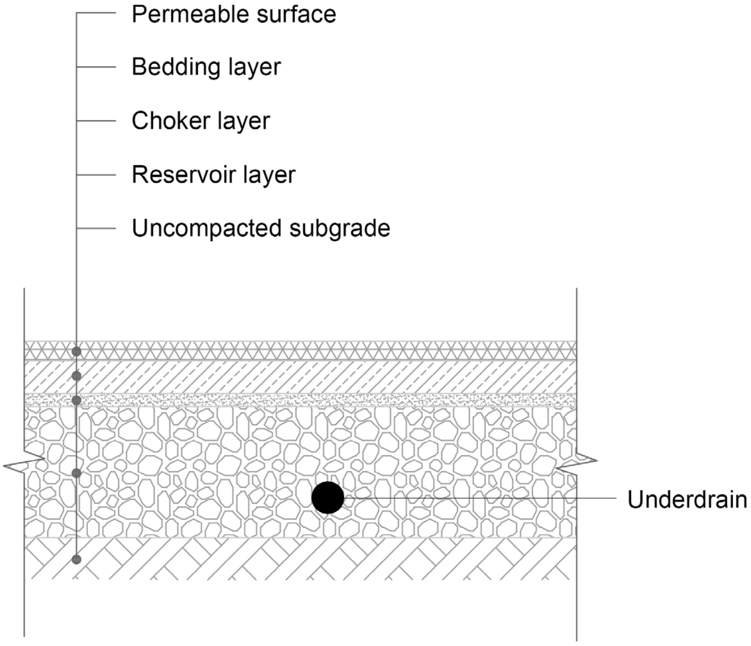

Figure 1.2: A basic section of a permeable pavement.

1.2.2 Rain garden/ Bioretention

Rain garden, or bioretention also belongs to the infiltration-based NBS, which is the artificial low-elevation/depressed greenbelt in the landscape which is used to infiltrate the stormwater runoff from the surrounding impervious surfaces (Davis and Asce, 2008; Singh, 2019; Wisconsin 2014). They are usually implemented around residential and commercial settings. In some cases, they also implemented in some agricultural areas for improving water quality. Typically, rain garden (or bioretention) is planted with shrubs, herbaceous perennials, or grasses, which can tolerate both saturated and dry soil in terms of the soils and climates of the planting area (Dietz, 2007). The benefits of rain garden/bioretention areas include that they can decrease stormwater runoff, increase the recharge of groundwater, and treat pollutant through several ecological processes (Prince George's County, 1993). Several municipalities have created the standards for the design and construction of rain garden/bioretention. WI DNR (2006) proposed the standards with full details on the site criteria, specifications of design, construction guidance, and recommendations for operation and maintenance. As shown in Figure 1.3, a typical section of rain garden consists of soil layers and vegetation layers.

The researches on rain garden/bioretention start from the individual scale (e.g. laboratory prototypes (Davis et al., 2001), filed investigation (Davis et al., 2003; Davis and Asce, 2008), and gradually to watershed scale (Ahiablame et al., 2013). These studies provided some positive results that rain garden/bioretention can efficiently reduce the runoff volume and peak flow (Hunt et al., 2012; Winston et al., 2016), rapid infiltration, recharging groundwater and retained pollutant (e.g. TSS, NO3–N, TP and TN).

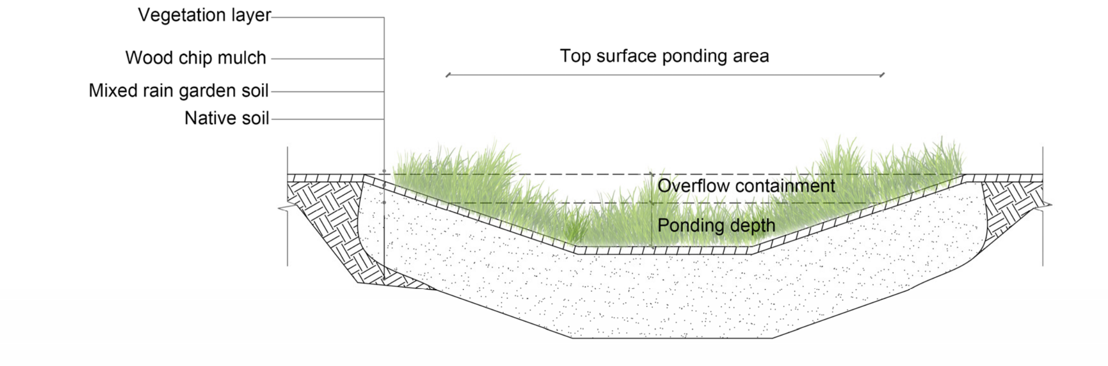

Figure 1.3: A basic section of a rain garden/ bioretention.

1.2.3 Green roof

Different from permeable pavement and rain garden, green roof is considered as a kind of retention-based NBS (USEPA, 2000). The green roof provides an effective approach for replacing an impervious rooftop with a pervious rooftop that partially or completely covered with vegetation. As indicated by many researchers(Vanwoert et al., 2005; Bianchini and Hewage, 2012; Stovin et al., 2012; Berndtsson, 2010; Berretta et al., 2014; Razzaghmanesh and Beecham 2014; Zhang et al., 2019), green roofs provide a range of benefits to the urban areas. For stormwater management, green roofs can effectively reduce peak flow and total runoff volume. As summarised by Dietz (2007), green roofs were able to reduce the peak flow between 60 % and 70 % in a variety of locations, and the average retention capacity is around 63 %. Furthermore, green roofs are beneficial for reducing urban heat island, extending the life-cycle of a building, and energy-saving (Niachou et al., 2001; Takebayashi and Moriyama, 2007; Sailor, 2008).

The green roof can be categorised as several different types, including extensive, semi-intensive, and intensive (Berndtsson, 2010; Bianchini and Hewage, 2012; Hakimdavar et al., 2014). The extensive green roof is the one that most popular for single family residential, which uses a relatively shallow growing medium (≤10 cm) with planting grasses or sedum families. This type of green roof can fit well on roofs with slopes. Regarding the semi-intensive and the intensive green roofs, which are widely applied on commercial buildings where owners prefer to have large vegetated areas that containing a wide range of plants with different sizes and types. These roofs can be planted with grasses, mosses, flowers, shrubs and even trees because of their relatively thick medium (≥ 20 cm). They usually are designed with paths and walkways to provide a variety of ecological and esthetical service.

A typical green roof structure can be found in Figure 1.4, which mainly includes vegetation layer, substrate layer (200 mm to 600 mm), drainage layer, and support substrate.

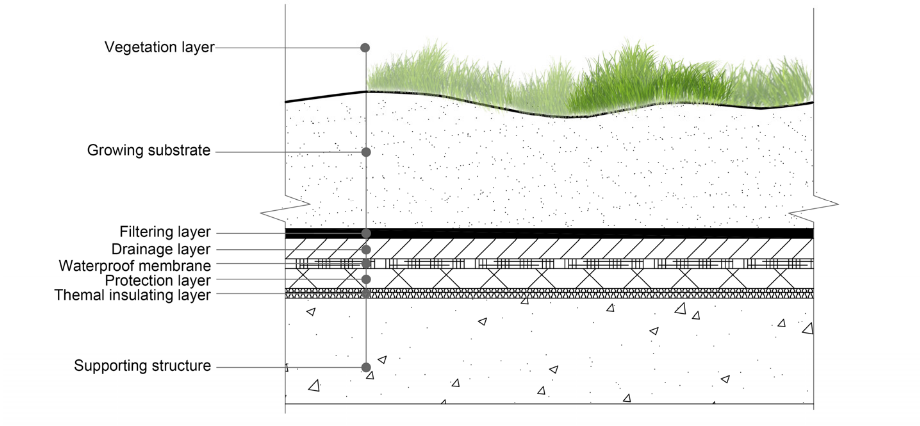

Figure 1.4: A basic section of a green roof.

1.3 Hydrological models

The heterogeneity of the urban environments makes it an extremely complex system. In last few decades, to enhance the understanding on hydrological issues (e.g. flooding disasters, water resource management, and water quality) and predict alternations in the future (e.g. climate change, land use change), hydrological models have been widely applied in urban hydrological science (Salvadore et al., 2015). To be more specific, hydrological models are generally used to simulate the water cycle in an urban catchment scale. Apparently, the development of hydrological models is also strongly related to the advancement of computing capabilities, remote sensing devices. In the meantime, for managing stormwater in an urban catchment scale, numerical modelling seems to be the most appropriate and effective approach (Todini, 2007).

The state of art of hydrological modelling approaches was reviewed by a large number of researches (Blöschl and Sivapalan, 1995; Salvadore et al., 2015; Moradkhani and Sorooshian, 2009; Praskievicz and Chang, 2009; Pechlivanidis et al., 2011; Van der Knijff et al., 2010), including the main components of the water cycle in urban regions. They mainly focused on the different modelling approaches used in urban hydrology field. A brief overview of water cycle components and modelling approaches is given in the following section.

1.3.1 Modelling water cycle in urban regions

The water cycle in urban regions is generally composed of a suite of physical processes which presents the movement of water in urban areas. The modelling process usually starts with precipitation. As precipitation falls, a part of them is intercepted by vegetation covers, and the other parts of them infiltrate into the soil, evaporates back to the atmosphere, enters into the urban drainage system or are stored by depressions. Besides, there is a remaining part which generates surface runoff, called effective precipitation.

The part of precipitation which participates the processes of interception, evapotranspiration, depression storage and infiltration, does not participate in the urban runoff process. Therefore, they are considered as losses, and the surface runoff can be calculated by misusing the rate of all losses with the gross precipitation. However, due to the complexity of the urban catchment, the estimation of the rate of all losses always needs a lot of information (e.g. land use, elevation, soil).

- Precipitation

The spatio-temporal resolution of the precipitation data is always an essential issue for hydrological modelling, because the precipitation (especially the rainfall) is one of the main inputs for hydrological models (Cole and Moore, 2009). Generally, the rainfall inputs have two different formats: uniform or distributed. Most modelling-based studies used uniform rainfall which was obtained from rain gauge networks or the design storm based on the Intensity-Duration-Frequency (IDF) curve (Holman-Dodds et al., 2003; Gilroy and McCuen, 2009; Qin et al., 2013; Versini et al., 2018; Zhu et al., 2019; Guo et al., 2019). With the development of the weather radar network, an increasing number of studies used the distributed radar data with consideration of the small scale rainfall variability (Gires et al., 2015; Paz et al., 2018; Paz et al., 2019).

Apparently, these two types of rainfall data can be taken into account in most of hydrological models. However, the modelling approach decides how the rainfall inputs are dealt with. For semi-distributed models, the rainfall is considered as uniform in sub-catchments (Rossman et al., 2010; Burszta-Adamiak and Mrowiec, 2013). Thus, the small scale rainfall variability is not effectively presented in such type of model. Different from the semi-distributed model, the fully-distributed models can take into account the rainfall data with a high spatial resolution (e.g. radar data).

• Interception

As mentioned, a certain percentage of precipitation is intercepted by ground objects (e.g. vegetation) when they reach the surface of these ground objects (Viessman et al., 1989). The intercept process is particularly significant in vegetated regions, and the interception capacity of the vegetation is significantly dependent on its type, structure and meteorological factors (Geiger et al., 1987).

Horton (1919) proposed a formula for estimating interception loss. This formula is expressed as the sum of the water stored on the vegetation covers at the end of a rainfall storm and the evaporation from wet vegetation covers during a storm. Linsley et al. (1949) supposed that the rainfall did not fully fill into the vegetation storage, and suggested an improved formula based on the Horton's equation. As mentioned by Chow (1964), several formulas were proposed and applied in urban hydrology. However, in highly urbanised regions, the interception is less essential compared to the other water cycle component because of most land use covers are impervious.

• Evapotranspiration

The process of evapotranspiration can be divided into two parts: the evaporation and the plant transpiration. These two parts occur simultaneously, the evaporation process presents the movement of water to the air from the Earth's land and water bodies, and transpiration accounts for the movement of water within the vegetation. In urban hydrology, the Penman equation and Penman-Monteith equation are widely used for estimating the evapotranspiration (Penman, 1948; Viessman et al., 1989). As the increase of the imperviousness in urban areas, the evapotranspiration from vegetation largely reduces. Therefore, the evapotranspiration needs to be simulated with continuous-based models to make it more significant.

• Infiltration

Infiltration is the process that describes water from the ground surfaces into the soils. Infiltration is forced by two main drivers, gravity and capillary action. The soil properties, such as the hydraulic conductivity, capillary action, gravity and moisture content, are the main physical factors which make contributions to the infiltration rate. In urban hydrology, several methods are commonly used to calculate infiltration (e.g. Green-Ampt, Horton, and Holtan).

The Green-Ampt method (Heber Green and Ampt, 1911) is widely used in physically-based models because the empirical equation of Green-Ampt considered many physical variables (e.g. hydraulic conductivity, porosity, and soil suction head). This empirical equation was express as (Li et al., 1976):

$$f = K_h(1 + \frac{H_c(1-S_e)\theta_e}{F}) \tag{1.1}$$

where f represents the infiltration rate (m/s), K_h, H_c, S_e and θ_e is the effective hydraulic conductivity (m/s), the capillary suction (m), effective soil saturation and soil porosity, respectively. F is the cumulative infiltration water depth (m).

Besides, the method of Horton (1933) estimates the infiltration rate based on a conceptual approach, which is widely applied in semi-distributed and lumped models. The Horton equation can be expressed as follows:

$$f_p = f_c + (f_0 - f_c)e^{-kt} \tag{1.2}$$

where f_p represents the infiltration rate at time t, f_0 is the initial infiltration rate, f_c is the constant infiltration rate after the soil has been saturated and k is the decay constant specific to the soil. All these parameters need to be calibrated by using measured data.

- Depression storage

Depression storage accounts for the precipitation stored in small low-elevation points on terrains. The stored precipitation in these points either infiltrates into the soil or evaporates. Depression storage can be found in pervious and impervious land use surface. However, the urban constructions largely remove the natural depressions, which leads to depression storage reduced. Some researchers studied the depression storage with different selected land covers (Tholin and Kiefer, 1960; Viessman, 1996), which pointed out the depression storage ranges from 0.2 mm (impervious pavement) to 15 mm (vegetated areas or bare lands). Linsley (1975) proposed an equation to estimate the volume of water in depression storage, and it can be expressed as follows:

$$V = S_d(1 - e^{-kP_e}) \tag{1.3}$$

where V is the volume of precipitation stored in depression storage, S_d is the maximum depression storage capacity, k is a constant equal to $1/S_d$, and P_e is the rainfall excess.

1.3.2 Urban hydrology modelling approach

The rainfall-runoff modelling and routing modelling are two main components of hydrological models, which estimate the effective precipitation participating in the runoff and the movement of storm runoff in urban water infrastructures. To simulate these two components, a variety of modelling approaches have been developed and applied. Firstly, the hydrological models can be classified based on the algorithms which they employed. Here, three different types of model are briefly described as following:

· Empirical model

Empirical model focuses on the establishment of a direct relationship between the input and the output, which is based on a statistical approach.

· Conceptual model

The conceptual model uses a simplified approach to present the complex hydrological physical process. Because this modelling approach involves some non-physical parameters, it needs to be calibrated carefully.

Generally, this conceptual approach is often applied in semi-distributed models, which subdivide a whole catchment into several ‘sub-regions’ called sub-catchments. These models mainly attempt to represent two functions which can describe the hydrological response of the catchment.

(i) The production function is used to estimate the effective rainfall hyetograph from the gross rainfall by quantifying all urban water losses.

(ii) The routing function applies the hydrograph from the effective rainfall in terms of the meteorological, physical and hydrological characteristics of the catchment. This process is based on either the hypothesis of linear rainfall-runoff relationship or the application of linear cascade reservoirs (i.e., the outputs of each reservoir is regarded as the inputs for the next one).

· Physically-based model

The physically-based model attempts to present the intrinsic mechanisms of the urban water cycle as accurately as possible. The main characteristic of this type of models is that they present physical processes by using all existing physical functions (e.g. the conservation of mass, of energy and of momentum). Theoretically, physically-based models are dependent on measurable physical parameters on site. Thus, these models do not need to be calibrated. However, the spatio-temporal resolution becomes a significant challenge for them.

Fully-distributed /grid-based models are usually physically-based. Namely, the spatial distribution of the main components of an urban catchment (i.e., rainfall, topography, land use, sewer system) is presented with a distributed approach using pixels. The adaptable spatial resolution is based on the quality of the available input data and the objective of the modelling.

Another way to classify the hydrological model is based on the spatial resolution which is used for representing the complexity of the hydrological cycle (i.e., lumped, semi-distributed and fully distributed).

The study by Salvadore et al. (2015) classified five modelling approaches used in urban hydrology. They are: (i) lumped models; (ii) semi-distributed models; (iii) Hydrological Response Unit (HRU) based models; (vi) grid-based spatially distributed models; and (v) Urban hydrological Element (UHE) based.

Concerning the lumped models, it simply considers the entire catchment as a single unit. Thus, all the spatial information is homogeneous in this type of model. For the semi-distributed models and HRU based models, they subdivide the whole catchment into several sub-catchments or HRUs, and the hydrological processes are applied as uniform at these sub-regions. The main difference between these two models is the way to define sub-catchment. Semi-distributed models identify sub-catchments based on the topography or the sewer system. The HRU based models create HRU according to the geo-morphological information (i.e., a combination of soil and land use types) (Rivas-Tabares et al., 2020). More specifically, this type of models represents the heterogeneity of the catchment by defining parcel cells as UHE.

Regarding the fully-distributed (grid-based) models, they take into account the spatial variability of the catchment and the corresponding scale issues.

1.3.3 Modelling of nature-based solutions

As mentioned, many studies analysing the hydrological performances of NBS in urban catchment scale are based on the modelling approach (Brunetti et al., 2017; Ercolani et al., 2018; Hu et al., 2018; Zölch et al., 2017; Wang et al., 2018). Indeed, some models are specifically developed for considering and representing the NBS/LID, such as the GSSHA (Fry and Maxwell, 2018), GIFMod (Massoudieh et al., 2017), SLR conceptual model (Liu et al., 2015), Long-Term Hydrologic Impact Assessment-LID (Ahiablame et al., 2013; Liu et al., 2015), and

SG WATER (Pyke et al., 2011). Nevertheless, most of them are lamped or semi-distributed models. One of the most commonly used model is the semi-distributed Storm Water Management Model (SWMM) (Khader et al., 2009; Qin et al., 2013; Zahmatkesh et al., 2015; Baek et al., 2015; Palla and Gnecco, 2015; Versini et al., 2015; Baek et al., 2015; Ahiablame and Shakya, 2016; Chui et al., 2016; Xing et al., 2016; Bai et al., 2019; Liu and Chui, 2019; Liang et al., 2019; Guo et al., 2019; Zhu et al., 2019), which contains a physically-based LID module (Rossman, 2010). Different kinds of LIDs can be presented in sub-catchment with the corresponding percentage. However, one of the significant caps is that SWMM is not sufficient to specify the surface spatial heterogeneity in the simulation. Furthermore, Gilroy and McCuen (2009) developed a model based on Matlab to simulate the hydrological performances of bioretention and cisterns in terms of spatio-temporal features of rainfall and runoff. Versini et al. (2015) improved the green roof module in SWMM to physically present green roofs based on a linear reservoir. Gülbaz and Kazezyılmaz-Alhan (2017) integrated the Rainfall-Watershed-Bioretention system (HM-RWB) into SWMM to model the responses of bioretentions. Ercolani et al. (2018) developed a distributed model SMART-GREEN to evaluate the impact of green roof scenarios with homogeneous and heterogeneous spatial implementation under various design storms with different duration and return periods. They found that increasing green roof implementation level at the outlet of the drainage network respond non-linearly to the urban system, which is related to the flow convey capacity of the network. Freni et al. (2010) developed a model to compare the hydrological performances of decentralised and centralised LIDs. Brunetti et al. (2017) analysed the hydrological performances of NBS based on HYDRUS-2D, which presents that the model response is strongly affected by the shape parameter and the saturated hydraulic conductivity. Based on the SWAT model, Her et al. (2017) developed computational modules, which indicated that hydrological performances of NBS are sensitive to their configurations, performed areas and rainfall characteristics. In addition, some researchers developed models based on GIS. For instance, Shoemaker et al. (2009) created the SUSTAIN model (System for Urban Stormwater Treatment and Analysis Integration) to simulate the location of varies types of NBS at multiple catchment scales. Jato-Espino et al. (2016) coupled the GIS and hydrological model for characterising LID/NBS measures and their locations.

Some studies evaluated the performances of NBS measures for multiple aspects. Helmi et al. (2019) developed WetSpa-Urban model to investigate the most-optimised scenario. Hua et al. (2020) assessed the NBS performances in terms of mitigating flooding and life-cycle costs under different precipitation scenarios by using MIKE URBAN. Jia et al. (2015) used SUSTAIN model to simulate different NBS at a college campus regarding urban runoff control and pollutant loads, and the Non-dominated Sorting Genetic Algorithm was applied for optimizing scenarios.

Although a series of studies have investigated the hydrological performances of NBS/LID by using different modelling approaches, the sensitivity and uncertainty associated with the spatial variability of both rainfall and NBS are still crucial issues which strongly influence the accuracy of model outputs. Therefore, the hydrological performances of NBS scenarios associated with the small scale variability need to be investigated by using the fully-distributed and physical-based model on a small scale.

Chapter 2

Case study of Guyancourt

In this chapter, the study context, including the description of the studied catchment, the data preparation process, the Multi-Hydro model, and the simulation scenarios are detailed presented. In this thesis, the case study was conducted at the part of Guyancourt city, which is located at the South-West suburbs of Paris (France). The Guyancourt catchment is one of the sub-catchments belonging to the Bièvre catchment. As shown in Figure 2.1, the Guyancourt sub-catchment is highlighted in red, which is situated at the upstream of the Bièvre River. The reasons for why the Guyancourt sub-catchment was selected in this study can be found in Section 2.2.

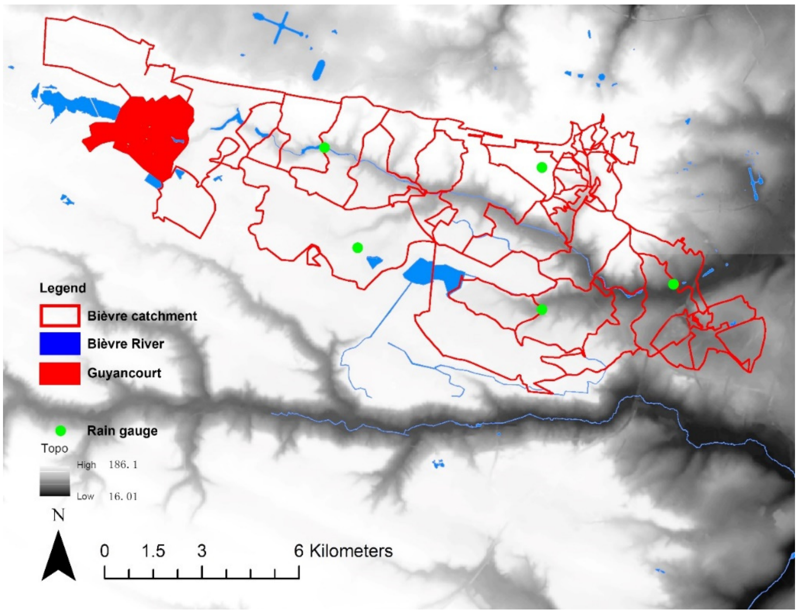

Figure 2.1: The location and the topography of the Bièvre catchment (Guyancourt sub-catchment is highlighted in red cover).

2.1 Bièvre catchment

The source of the Bièvre River lies in the city of Guyancourt (Saint-Quentin-en-Yvelines Community). The Bièvre River is a tributary of the Seine River and has a length around 36 km, which flows through several increasingly urbanised areas (e.g. Jouy-en-Josas, Antony, Fresnes, Gentilly, Massy) and joins the Seine River in Paris. The total area of Bièvre catchment is around 101 km^2. The upstream and downstream of Bièvre catchment are charged by two local authorities, respectively. To be more specific, the upstream is charged by the Comunauté d'Agglomération de Saint-Quentin-en-Yvelines (CASQY) and the downstream is organised by Syndicat Intercommunal d'Assainissement de la Vallée de la Bièvre (SIAVB). Since 1991, a real-time control system of Bièvre River was designed, installed and managed by Veolia (a large French multinational company). The map of the Bièvre catchment is shown in Figure 2.1. The urbanisation level of the catchment increases from upstream to downstream (i.e., from West to East). The topography of the whole Bièvre catchment is quite complex (the lowest altitude is around 16 m, while the highest altitude is about 186.1 m), and the Bièvre River flows in a valley with steep slopes on each side (e.g. the A-A section of the elevation of the Bièvre valley in Figure 2.2).

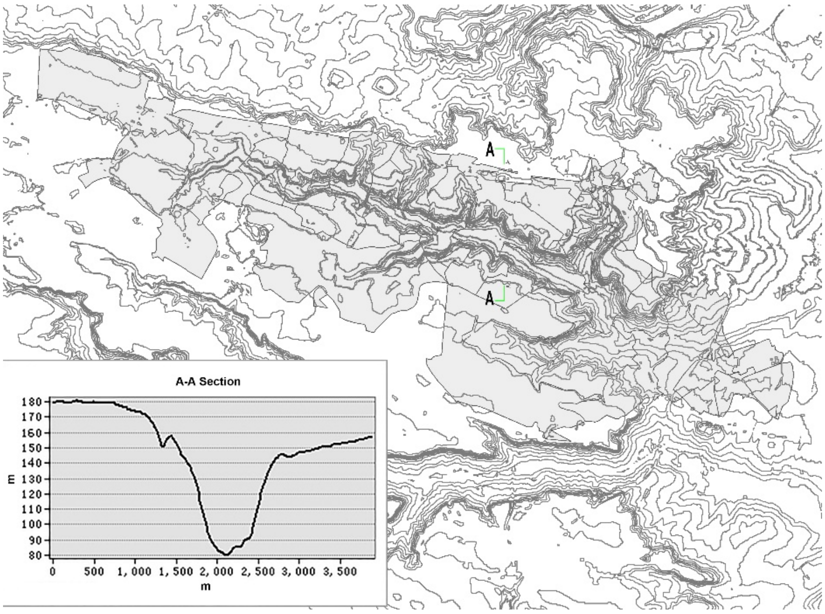

Figure 2.2: The elevation of the A-A section of the Bièvre valley.

Bièvre River is well-known for its drastic contribution to the historical 1910 flood in Paris and still easily generated flash floods during the heavy rainfall events (e.g. two severe floods occurred in 1973 and 1982). For the extreme event of 1982, the recorded precipitation reached 110 mm in three hours over the whole Bièvre catchment, of which 80 mm in only 40 min. In total, this severe rainfall event generated surface runoff around 10×10^6 m^3, and about 2×10^6 m^3 total runoff volume (see Paz, 2018 for more details).

The local authorities started to construct some storage basins to reduce the risk of extreme flood after the mentioned two severe events. Generally, these storage basins are locally regulated in terms of the water levels continuously monitored in downstream. In some extreme cases, the water levels in storage basins and the rainfall data provided by six rain gauges (marked in green point in Figure 2.1) were used for the optimisation of flows and storage capacity of the storage basin at the catchment scale.

2.2 Guyancourt sub-catchment

The case study in this thesis is conducted on a semi-urban catchment, a part of the city of Guyancourt (France), located on the Saclay Plateau in the South-West suburbs of Paris (Figure 2.3). The recent statistical report of Météo-France (2020) indicated that this area is characterised by an oceanic climate with an average annual temperature of 10.7°C and total annual precipitation of 695 mm. In this context, the Guyancourt catchment is an interesting and appropriate case study for several reasons.

Firstly, as mentioned previously, Guyancourt is one of the sub-catchments in the upstream of the Bièvre River. Therefore, the case of Guyancourt has a reference significance for the Paris region.

Secondly, the Guyancourt city is expected to become a part of the "French Silicon Valley", which currently undergoes a rapid urbanisation process over its total area of around 5.2 km^2, with a population of about 30,000 (INSEE, 2020).

However, due to climate change, a clear tendency towards the growing number of somewhat shorter, but much heavier rainfall events, was perceived in this region (Hoang, 2010), causing a large amount of fast surface runoff and higher peak flow rates in recent years. The existing stormwater drainage system is not able to sustain the future modifications of the watershed, and some low-lying areas in the catchment could suffer more easily from waterlogging, even during moderate rainfalls.

As Figure 2.3 displays, some vulnerable areas and buildings subject to a risk of waterlogging were defined in the Guyancourt catchment by using the ModelBuilder of ArcGIS software (a geoprocessing model, for identifying landscape sinks[6]). This geoprocessing model is based on a sequential chain of GIS analysis tools, it firstly finds the landscape sinks on the DEM with the help of ArcGIS hydrology tools[7]. The landscape sinks were firstly identified, on this figure, the blue spots represent the low-lying areas with a total area of 0.6 km^2 that can be easily flooded by stormwater (average rainfall depth of 53 mm). Then, the locations of the landscape sinks can be compared with the locations of existing buildings, and the buildings that are situated inside or adjacent to the landscape sinks are defined as the vulnerable buildings.

Thirdly, the local authority installed a gauge at the storage basin (outlet) to monitor water levels, which provides a measurement point in the Guyancourt catchment.

Overall, the relative complexity of the catchment makes it a typical "case study" for analysing hydrological responses of NBS scenarios, aiming to help the local authorities to find more reasonable and ecological alternatives for the future urban planning.

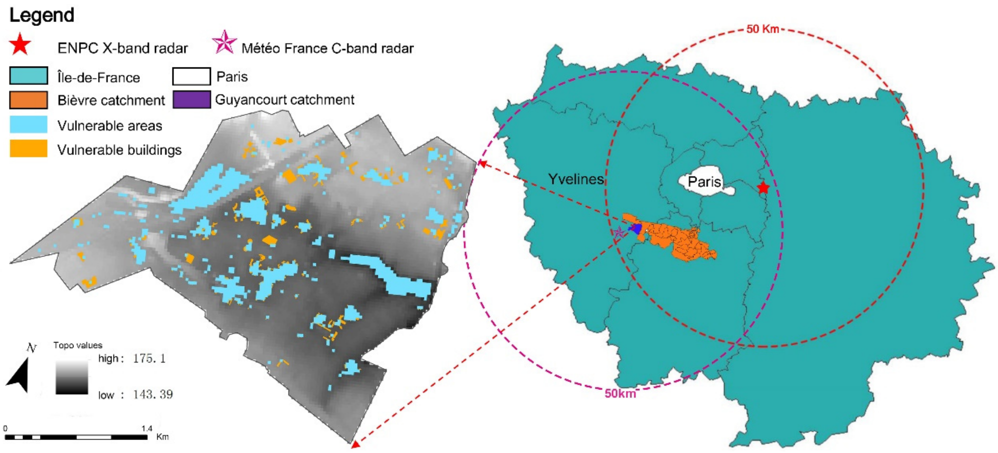

Figure 2.3: The location of the Guyancourt catchment.

2.3 Geographic data and information

The Geographic information data that used in this thesis need to be firstly pre-processed to adapt the numerical modelling in Chapters 4 and 5.

2.3.1 Topography

The available raw Digital Elevation Model (DEM) with a resolution of 25 m was obtained from

---

[6] https://learn.arcgis.com/en/, last access: 16 June 2021

[7] https://desktop.arcgis.com, last access: 16 June 2021

the French National Institute of Forest and Geographic Information (IGN), which presents the whole catchment is relatively flat (see the left side of Figure 2.3). The altitude in the North is slightly higher than that of the South. The highest altitude in the whole catchment reaches 175.1 m (upstream), while the lowest one (143.39 m) corresponds to the location of the storage basin (i.e., the outlet of the catchment: Etang des Roussières).

2.3.2 Land use

Based on the data from IGN, the current land use in this area consists of seven main types, including road, parking, building, gully, forest, grass, and water. In total, these seven land use types cover 9.6 %, 10.6 %, 15.5 %, 1.9 %, 28.8 %, 32.7 %, and 0.9 % of the total area, respectively, as shown in Figure 2.4. Currently, the pervious surface accounts for 62.4 % of the total area, and the corresponding impervious surface is around 37.6 %. The commercial centre and industrial buildings are mainly located in the north of the catchment, and the individual houses surrounded by green spaces concentrate at the southern part. In the east corresponding to the downstream, there exists a large forest around the storage basin.

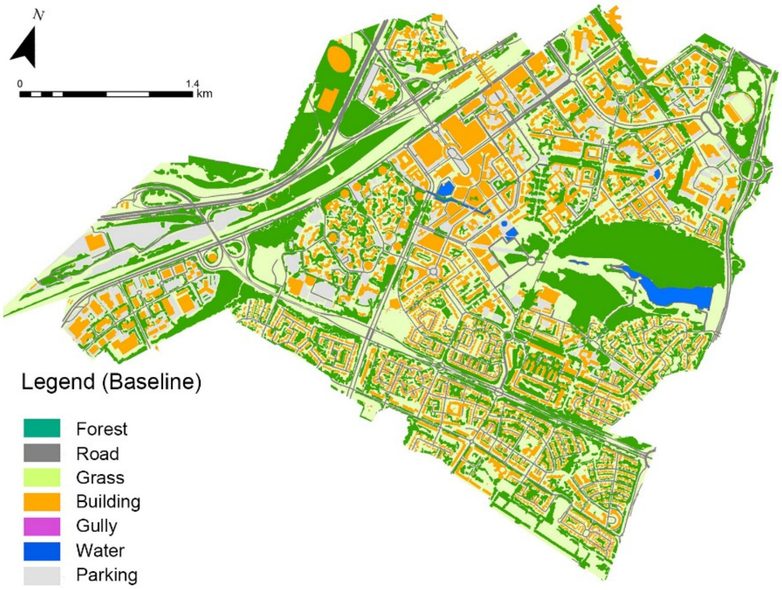

Figure 2.4: The land use distributions of Guyancourt catchment

2.3.3 Drainage system

The local authority, the agglomeration community of Saint-Quentin-en-Yvelines (“La communauté d'agglomération de Saint-Quentin-en-Yveline"), manages the urban drainage system of the catchment and provides some related data (Figure 2.5). The total length of the drainage system is about 76 km and consists of 4,474 nodes and 4,534 conduits. Overall, the drainage system was designed with a capacity characterised by a return period ranging from 2 to 10 years. The rainfall amount corresponding to the mentioned return periods (from 2 to 10 years) depends on the considered duration (usually equal to the concentration time). So this duration value depends on the location of pipes in the catchment and its upstream area. Here are the corresponding values for different durations that can be found on the studied watershed (by using the Montana coefficients): (i) duration 5 minutes: 187 mm/h for T = 10 years and 125 mm/h for T = 2 years; (ii) Duration 30 minutes: 50 mm/h for T = 10 years and 31 mm/h for T = 2 years; (iii) duration 1 hour: 30 mm/h for T = 10 years and 18 mm/h for T = 2 years; (iii) Duration 2 hours: 20mm/h for T = 10 years and 13 mm/h for T = 2 years. Overall, the diameters of conduits range between 0.1 m and 1.6 m, 70 % of them between 0.2 and 0.5 m (marked with a yellow line in Figure 2.5). The conduits with a diameter ranging from 0.9 to 1.6 m (marked with a purple line in Figure 2.5) are the primary conduits, which converge the flow into the storage basin and the outlet.

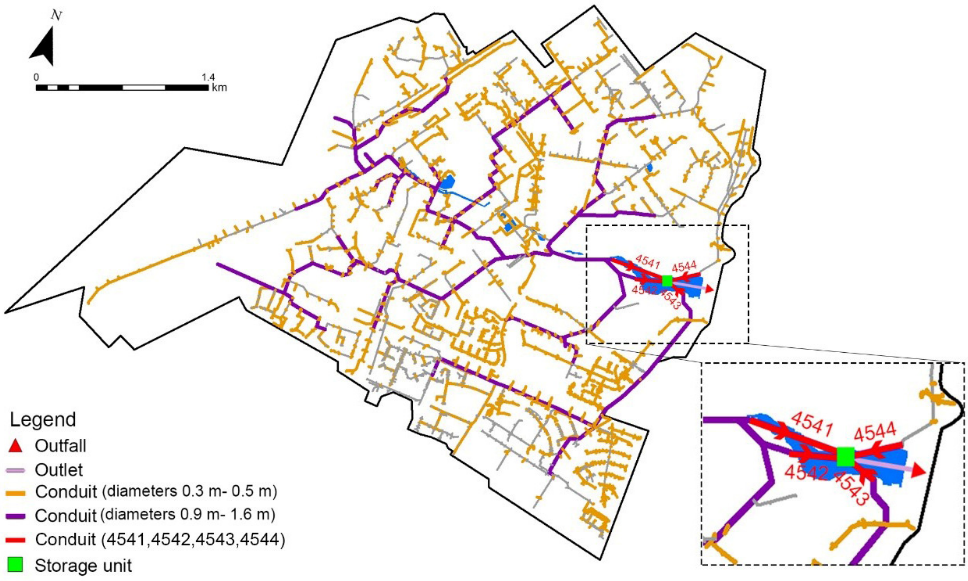

Figure 2.5: The drainage system of Guyancourt catchment (four conduits 4541, 4542, 4543, and 4544 that finally merged into the storage unit are highlighted).

2.4 Precipitation forcing

2.4.1 Data types

The rainfall data used in this thesis was provided from two different sources: the Météo-France (the French national meteorological service) C-band radar of Trappes and the ENPC (École des Ponts ParisTech) dual-polarimetric X-band radar of Champs-sur-Marne. The distances of Guyancourt catchment to the C-band radar and the X-band radar are around 6 km and 45 km, respectively. The spatio-temporal resolution of the C-band radar data is 1 km and 5 min, and the data from X-band radar data has a spatio-temporal resolution of 250 m and 3.41 min.

2.4.2 Data processing

Before presenting the selected rainfall events, it is essential to briefly introduce the radar data processing progress. For C-band radar products, Météo-France uses the standard *Z-R* relation (Marshall and Palmer, 1948) to convert the corrected reflectivity factor Z (mm^6/m^3) to rainfall rate Z (mm/h):

$$Z = aR^b \tag{2.1}$$

where the parameters a and b are fixed equal to 200 and 1.6, respectively (Tabary, 2007). As shown in Figure 2.6, the Météo-France radar network provides the precipitation data (radar mosaic) over around 95 % of the entire territory. This network was initially named ARAMIS (Application Radar à la Météorologie Infra-Synoptique, Parent-du Châtelet, 2003), which contains 32 radars (in 2017). Some of the new radars were installed within the project of PANTHER (Project ARAMIS New Technologies Hydrometeorology Extension and Renewal) after 1995 (Parent-du-Châtelet, 2003). This network was mixed with C-band radar, S-band radar and X-band radar, which are distributed over the whole France territory (including Corsica). These radars have a range of around 100 km for measuring the precipitation amount and a range of about 200 km for detecting them. Several “individual radar” products transmit the data every 5 minutes to the centre of Météo-France located in Toulouse. Then, mosaics are constructed from these products.

Concerning the X-band radar data of ENPC, it was processed with the standard software Rainbow (Selex, 2015). Based on the primary choice of the angle step and pulse width, the highest spatial resolution of the ENPC X-band radar data is 250 m, and the temporal resolution is 3.41 min. Apparently, this spatio-temporal resolution of products needs to be improved with selecting more appropriate scan parameters. In this thesis, three different X-band radar products were applied. They are Dual Polarisation Surface Rainfall Intensity (DPSRI), Surface Rainfall Intensity (SRI) and Surface Rainfall Intensity Multi-Parameters (SRIMP). The DPSRI product was generated with both the horizontal and vertical reflectivity data. The vertical data was obtained with the ZDR (differential reflectivity) and KDP (specific differential phase). Concerning the product of SRI, it was only generated with the horizontal reflectivity data. For the product of SRIMP, it was generated with both the horizontal and vertical reflectivity data, and the *Z-R* parameters of *a* and *b* (Eq. 2.1) were not fixed and changed during the whole rainfall period.

The DPSRI Selex product applied a *Z-R* relation (Eq. 2.1) only for very low intensities (dBZ), and *R-KDP* for high intensities.

$$R = 19.63 \mid K_{DP} \mid^{0.823}, \text{for } Z > 35dBZ \text{ and } K_{DP} > 0.3deg/km \tag{2.2}$$

Paz (2018) compared DPSRI products with different filter and *Z-R* parameters. By comparing with the observation data from six mentioned rain gauges of Bièvre catchment (this work has been done in the thesis of Paz (2018), the DPSRI FIR filtered KDP with *Z-R* parameters a = 150 and b =1.3 is finally used for the hydrological modelling in this thesis for three rainfall events of 2015 (see next sub-section for more details).

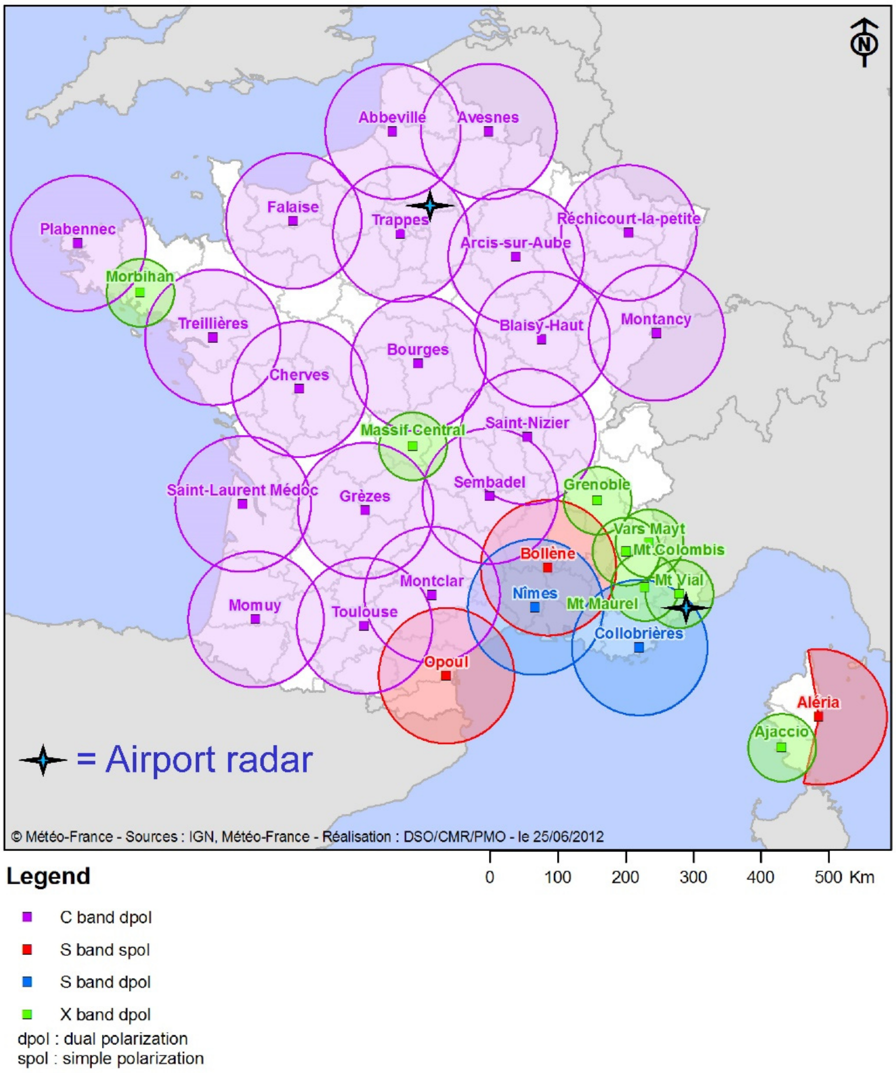

Figure 2.6: The radar network of Météo-France (©Météo-France).

2.4.3 Selected rainfall events

In this thesis, three rainfall events occurred in 2015, and three events of 2018 are selected for different objectives. More precisely, the rainfall events of 2015 are used for the first and third sets of modelling experiments in Chapter 4. The rainfall events of 2018 are only used for the second set of modelling experiments in Chapter 4.

2.4.3.1 Rainfall events of 2015

Firstly, the three rainfall events of 2015 happened in 12-13/Sep/2015, 16/Sep/2015, and 5-6/Oct/2015 are briefly introduced (more details on these events can be found in Paz, 2018). These three events lasted relatively long with high intermittencies, which can be artificially subdivided into several sub-events (see Chapter 4 and Chapter 5 for the studies applying the synthetic subdivided events). The main characteristics (i.e., duration, intensity and total amount) of these events of X-band and C-band radar data are summarised in Table 2.1.

Figure 2.7 presents the temporal evolution of the areal averaged rainfall rate (left) and cumulative rainfall (right) for both C-band and X-band radar data over the whole Guyancourt catchment for the three studied events of 2015. It is found that the data from two different radars have some significant differences in terms of the estimation of the rainfall. It seems that X-band radar is able to detect some rainfall peaks, while these spikes are less evident for the C-band radar data. As summarised in Table 2.1, the areal averaged maximum rainfall intensities (mm/h) of three events for X-band radar data are 20.5, 9 and 36.4 mm/h respectively, and that of the C-band data are corresponding to 12.9, 10.6, 25.1 mm/h. For EV1 and EV3, the areal average maximum rainfall intensity of C-band radar data is much lower than that of the X-band radar data. However, regarding the cumulative rainfall (total depth), the C-band radar data yields a higher estimation than those of the X-band radar data.

Furthermore, Figure 2.8 displays the maps of the rainfall intensity at the largest rainfall peak (per radar pixel) of both C-band (left) and X-band (right) radar data of three studied events. Correspondingly, Figure 2.9 displays the maps of the cumulative rainfall (per radar pixel) for both C-band (left) and X-band (right) radar data. Compared with the rainfall intensity at the largest rainfall peak (per radar pixel) of C-band radar data, X-band radar data is about 40 % higher than that of the C-band radar data. Regarding the maximum total rainfall depth (per radar pixel) of both radar data, X-band radar data is around 30 % lower than that of C-band radar data. These could be related to the data processing of the two types of radar data. For X-band radar data, the estimation of rainfall rate was obtained by the DPSRI product at the height of 1.5 km above the ground. Concerning the C-band radar data, the rainfall rate was estimated in terms of the height with the highest quality indicator over the pixel. According to the same rainfall events analysed by Paz (2018) over the whole Bièvre catchment, compared with the rain gauge data, it seems that the X-band radar data slightly underestimated the rainfall, while C-band radar data relatively overestimated it. However, due to the small scale rainfall variability and the lack of the comparison of rain gauge data with both radar data in Guyancourt catchment, this observation remains non-conclusive.

Event ID	**EV1 (C-BAND)**	**EV1 (X-BAND)**	**EV2 (C-BAND)**	**EV2 (X-BAND)**	**EV3 (C-BAND)**	**EV3 (X-BAND)**
Date	12-13/Sep/2015		16/Sep/2015		05-06/Oct/2015	
Duration (h)	43.1 (04:05-00:00)		8.75 (08:05-16:50)		30.9 (09:10-16:05)	
Total depth (mm) (areal average/pixel min/pixel max)	37.9/35.1/43.4	31.5/27.4/36.9	13.5/12.3/23.1	12/10.43/14.1	30.7/25.7/33.9	20/17.6/25.4
Max intensity (mm/h) over 1 min (areal average/individual pixel)	12.9/24.9	20.5/41.2	10.6/15.9	9/29.1	25.1/30.6	36.4/55.6
SD of rainfall intensity at the largest rainfall peak (mm/h)	N/A	4.31	N/A	6.11	N/A	5.75
SD of total rainfall depth (mm)	N/A	1.21	N/A	0.82	N/A	1.35

Table 2.1: Main characteristics of the three rainfall events of 2015 (X-band radar data and C-band radar data) and standard deviation (SD) of the rainfall intensity at the largest rainfall peak and the total rainfall depth of the three rainfall events of X-band radar data.

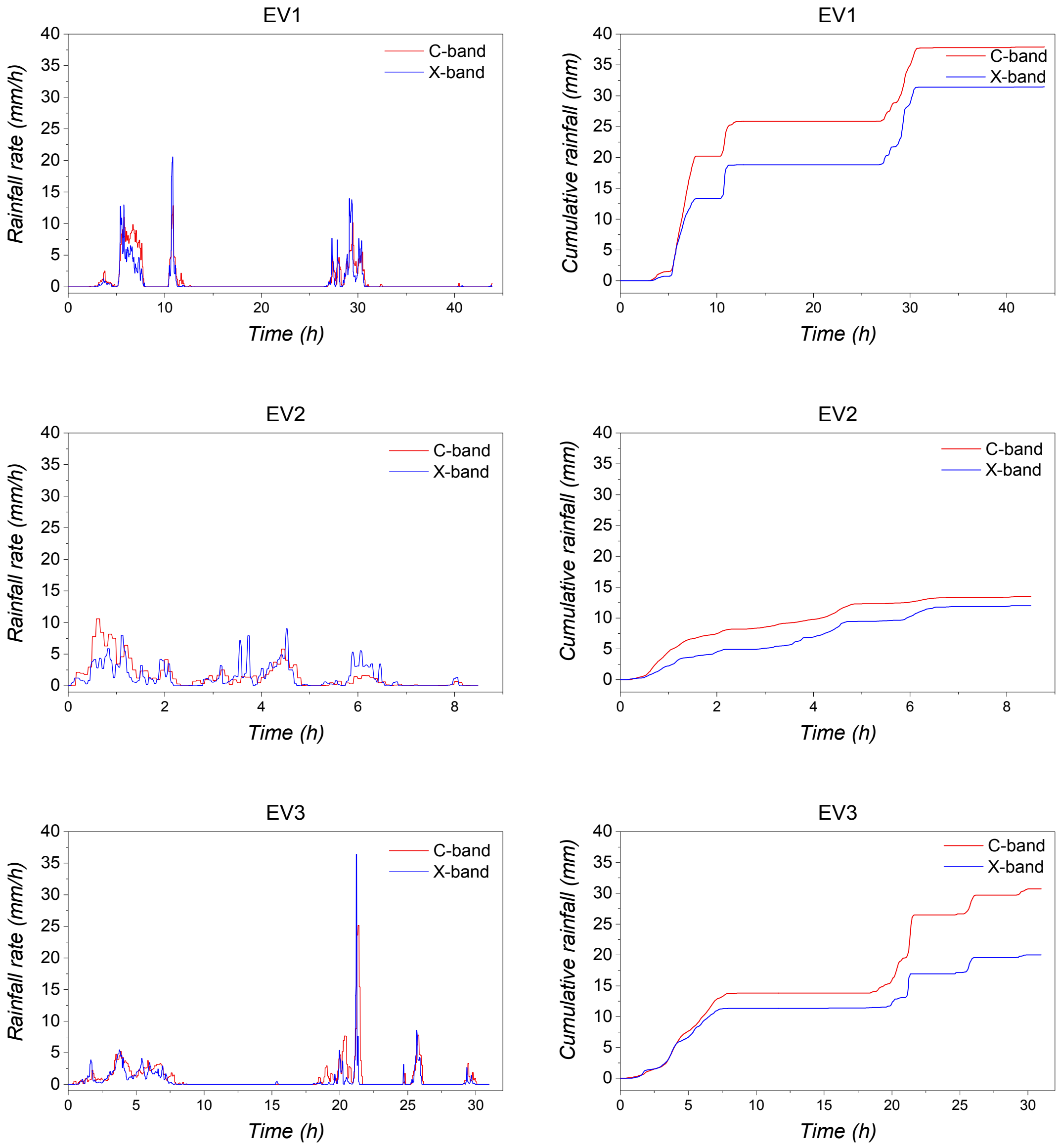

Figure 2.7: Temporal evolution of the areal averaged rainfall rate (left) and cumulative rainfall (right) over the whole Guyancourt catchment for three studied events of 2015.

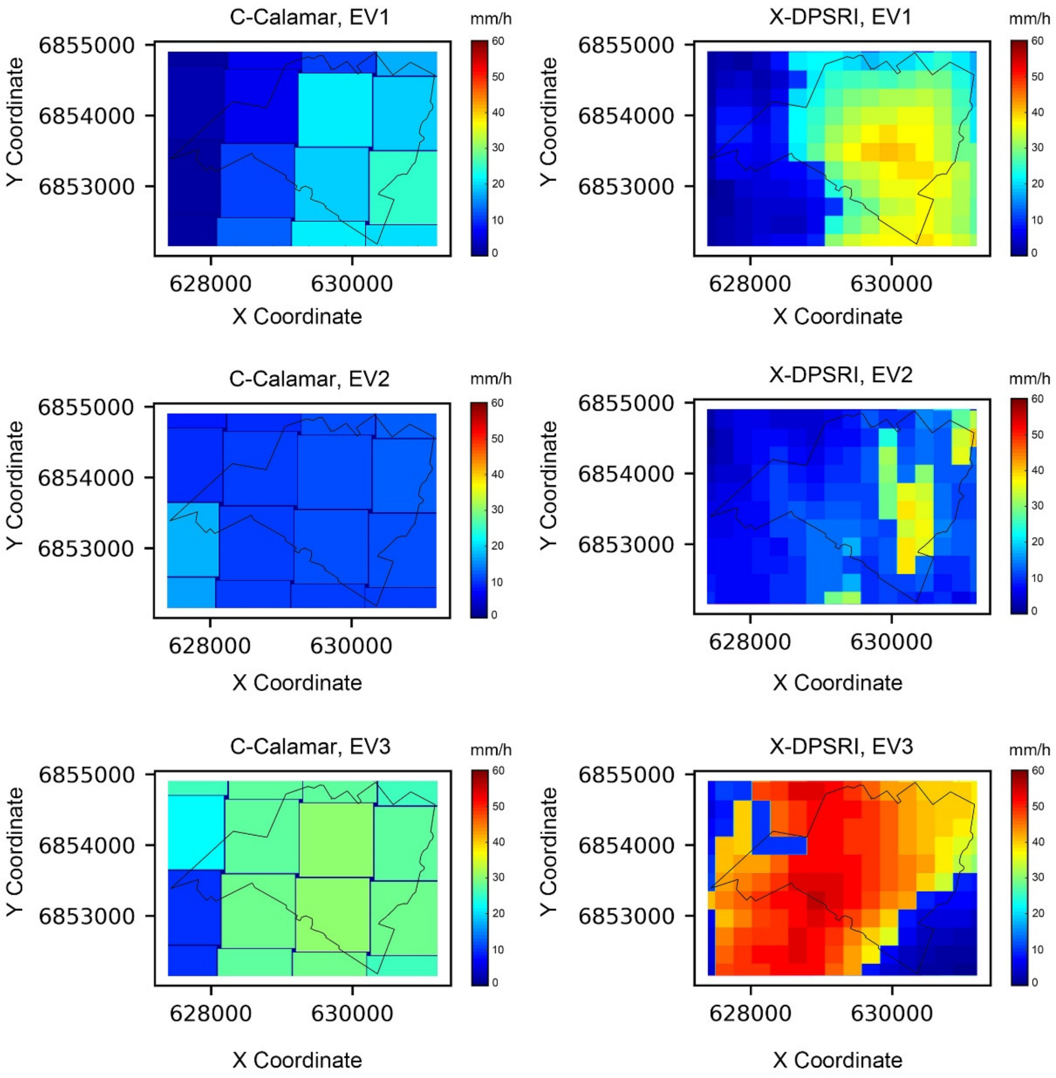

Figure 2.8: Rainfall intensity at the largest rainfall peak (per pixel) of C-band radar data (left) and X-band radar data (right) over the whole Guyancourt catchment for three studied events of 2015.

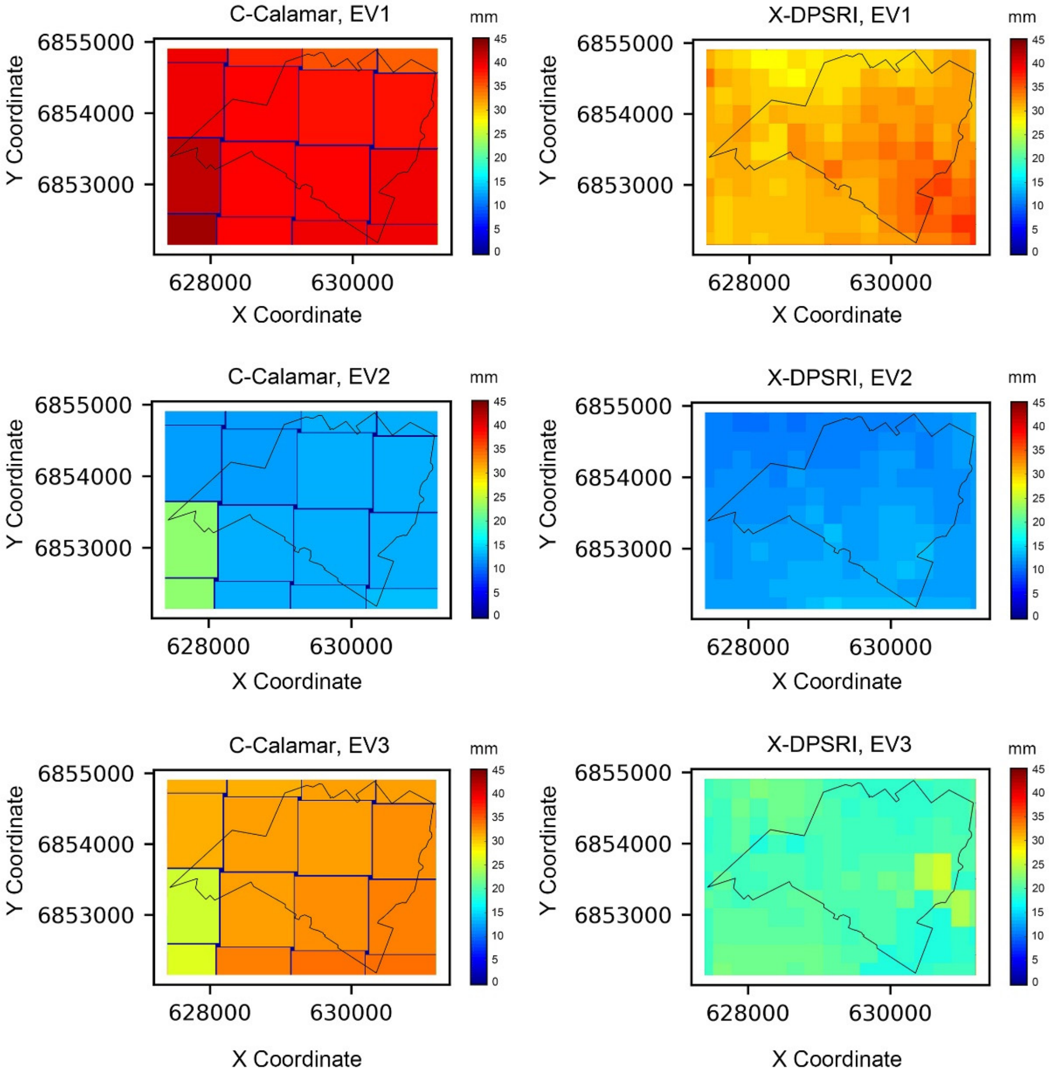

Figure 2.9: Cumulative rainfall (per pixel) of C-band radar data (left) and X-band radar data (right) over the whole Guyancourt catchment for three studied events of 2015.

2.4.3.2 Rainfall events of 2018

Regarding the rainfall events of 2018, three specific rainfall events in 22/May/2018 (EV4), 11-12/June/2018 (EV5), and 28-29/August/2018 (EV6) were selected. More precisely, EV4 occurred in the Northeast of France because of intense thunderstorms, and the storm cells formed in the Paris region. A mount of hails was observed in these storm cells. The cumulated precipitation in 24 h reached 36.5 mm in Vélizy-Villacoublay (located 2 km from the Bièvre catchment), especially 24.9 mm is accumulated in only one hour. EV5 is associated with the precipitation from the Mediterranean. These storms moving very slowly from South to North, which gave a significant amount in 24 hours (i.e., in Paris region, the cumulative rainfall reached 75.4 mm at Orly, 78.2 mm at Paris-Montsouris, and 78.9 mm at Achères and 95 mm at Torcy). Regarding EV6, it was due to the high-pressure cyclone, which formed intense storms that extend from west to east. In Vélizy-Villacoublay, the cumulative precipitation reached 25 mm in 24 hours.

The data from C-band radar retrieved from three different products: CALAMAR, ZPHI, and MeteoGroup. The data from X-band radar mainly retrieved from two products: DPSRI and SRI. An additional X-band radar product SRIMP is only applied in EV6 for analysing the impact of the changes of the parameters (*a* and *b*) of X-band radar product on the hydrological response of the catchment.

In addition, it is necessary to mention that a summary of the main characteristics of the selected rainfall events for both C-band and X-band radar data is presented in Table 2.2. Figure 2.10 displays the temporal evolution of the rainfall rate (left) and the cumulative rainfall (right) averaged over the Guyancourt catchment at each time step for all available products of three rainfall events. Figures 2.11, 2.12, and 2.13 present the cumulative rainfall (per radar pixel) over the Guyancourt catchment for each radar product of three rainfall events. Due to the lack of rain gauge in this catchment, the following observations are only based on the comparisons between each radar product.

Comparing the C-band radar data and the X-band radar data for three rainfall events, it is noticed that the rainfall peaks of C-band radar data and X-band radar data are generally consistent for EV5 and EV6, but the peaks of C-band data appear around 1 hour earlier than that of the X-band data for EV4 (Figure 2.10). In addition, it is worth noting that the peak rainfall intensity of CALAMAR and ZPHI are at least 50 % higher than that of the other products. However, the peak rainfall intensity of MeteoGroup is relatively lower compared to the CALAMAR and ZPHI. For EV6, the areal averaged peak rainfall intensity of CALAMAR reaches 124 mm/h, while that of the MeteoGroup is only 8.47 mm/h. Similarly, for EV5, the areal averaged peak rainfall intensity of ZPHI is 45.66 mm/h, which is 87 % higher than that of the MeteoGroup. Regarding the data from the two products of X-band radar (DPSRI and SRI), the peak intensity is generally 30 % - 50 % higher than that of the MeteoGroup, but around 70 % lower than that of CALAMAR and ZPHI. As mentioned earlier, the SRIMP was only added for the EV6, it is noticed that the rainfall intensity of SRIMP at the first rainfall peak is slightly higher than that of the two other X-band radar products, but at the last rainfall peak, the rainfall intensity of SRIMP is the highest of all available products.

As shown in Figure. 2.10, the cumulative rainfall of CALAMAR and ZPHI are approximately 70 % higher than that of the other rainfall products in three rainfall events, because the rainfall intensity at the largest rainfall peak is very pronounced for CALAMAR and ZPHI. For EV4 and EV5, the cumulative rainfall is highest for ZPHI, which is around 14.2 mm and 59.8 mm, respectively. Correspondingly, the MeteoGroup has the lowest cumulative rainfall in EV4, which is approximately 2.7 mm. The cumulative rainfall of two X-band products (DPSRI and SRI) are very close during the whole rainfall period for three rainfall events. For EV6, the highest cumulative rainfall is computed for CALAMAR (about 23 mm). At 5:00 (local time), around the 6 hours, the rainfall accumulated very fast for CALAMAR, approximately 20 mm in only a few minutes. Indeed, at this moment, the rainfall intensity of CALAMAR was approximately 124 mm/h. At 13:00 (local time), around the 14 hours, the rainfall accumulated fastest for SRIMP, which accumulated around 10 mm in 1 hour. Concerning the cumulative rainfall of per radar pixel of each rainfall product, the data from both radars are relatively variable in space. In general, the maximum cumulative rainfall (per radar pixel) of C-band radar products is higher than that of the X-band radar products for three studied events.

Event ID	**Main characteristics**	**C-CALAMAR**	**C-ZPHI**	**C-MeteoGroup**	**X-DPSRI**	**X-SRI**	**X-SRIMP**
EV4	Duration (h)	11.2 (12:45-24:00)					
	Cumulative rainfall (mm) (pixel max)	18.36	27.32	7.35	9.79	11.99	
	Maximum intensity (mm/h) at the largest rainfall peak (areal average)	18.26	22.03	10.42	7.09	8.22	
	Cumulative rainfall (mm) (areal average)	10.98	14.15	2.65	5.03	4.99	
EV5	Duration (h)	33 (04:41-13:44)					
	Cumulative rainfall (mm) (pixel max)	24.29	156.59	39.79	21.69	21.80	
	Maximum intensity (mm/h) at the largest rainfall peak (areal average)	21.17	45.66	5.59	20.07	13.39	
	Cumulative rainfall (mm) (areal average)	19.08	59.78	20.56	16.37	14.68	
EV6	Duration (h)	19.2 (22:50-17.59)					
	Cumulative rainfall (mm) (pixel max)	28.58	22.53	7.94	14.39	13.04	26.7
	Maximum intensity (mm/h) at the largest rainfall peak (areal average)	124.03	52.13	8.47	18.97	12.91	21.99
	Cumulative rainfall (mm) (areal average)	23.05	15.59	4.57	9.57	6.76	14.99

Table 2.2: The main characteristics of three rainfall events from C-band and X-band radar products of three rainfall events of 2018.

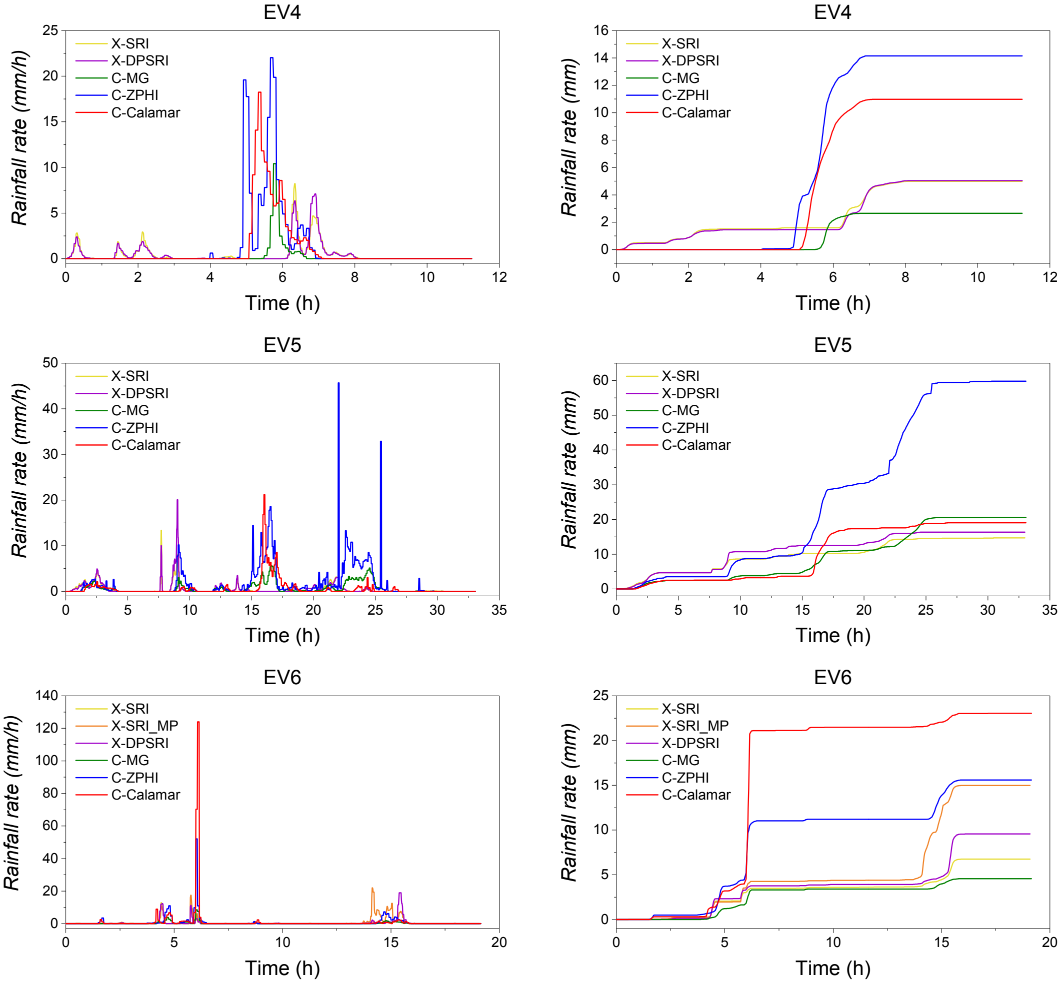

Figure 2.10: Temporal evolution of rainfall rate and cumulative rainfall over the whole Guyancourt catchment for C-band radar data and X-band radar data of three rainfall events: EV4 (Top), EV5 (centre) and EV6 (bottom).

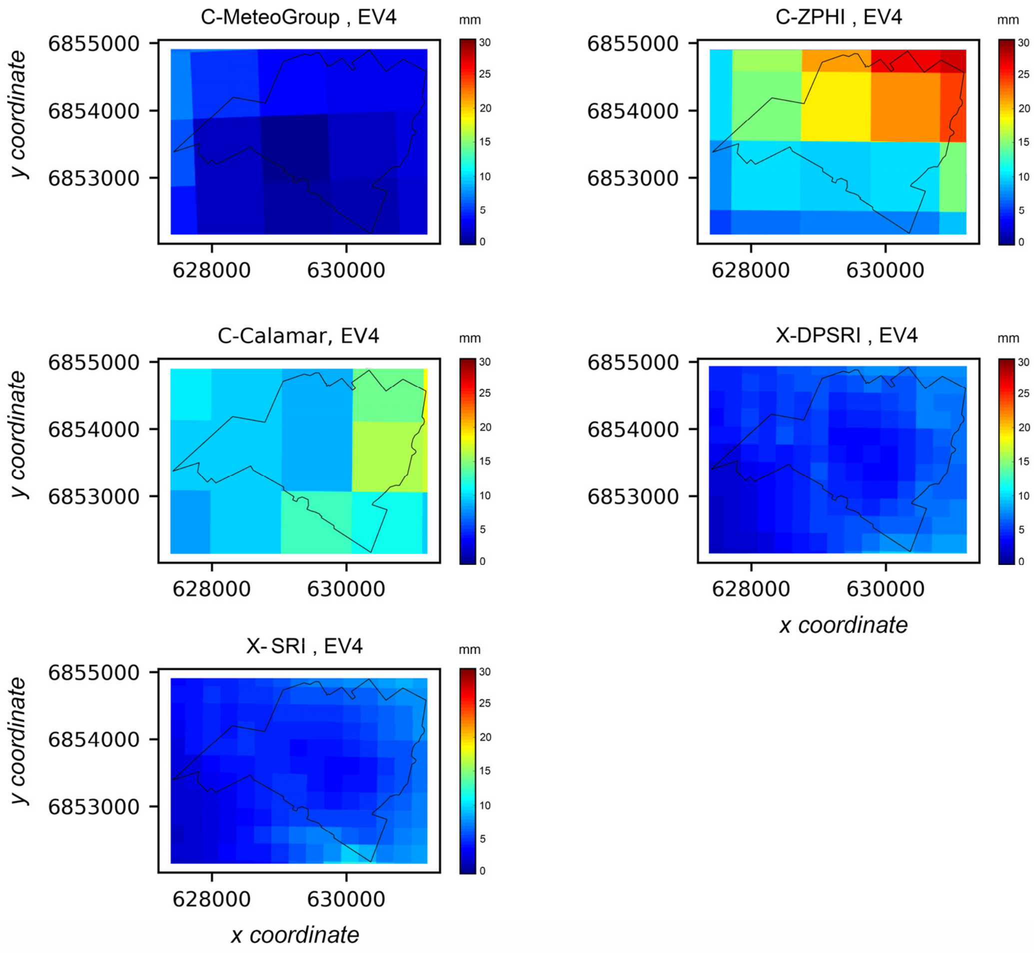

Figure 2.11: Cumulative rainfall (per radar pixels) over the Guyancourt catchment for C-band radar data and X-band radar data of EV4.

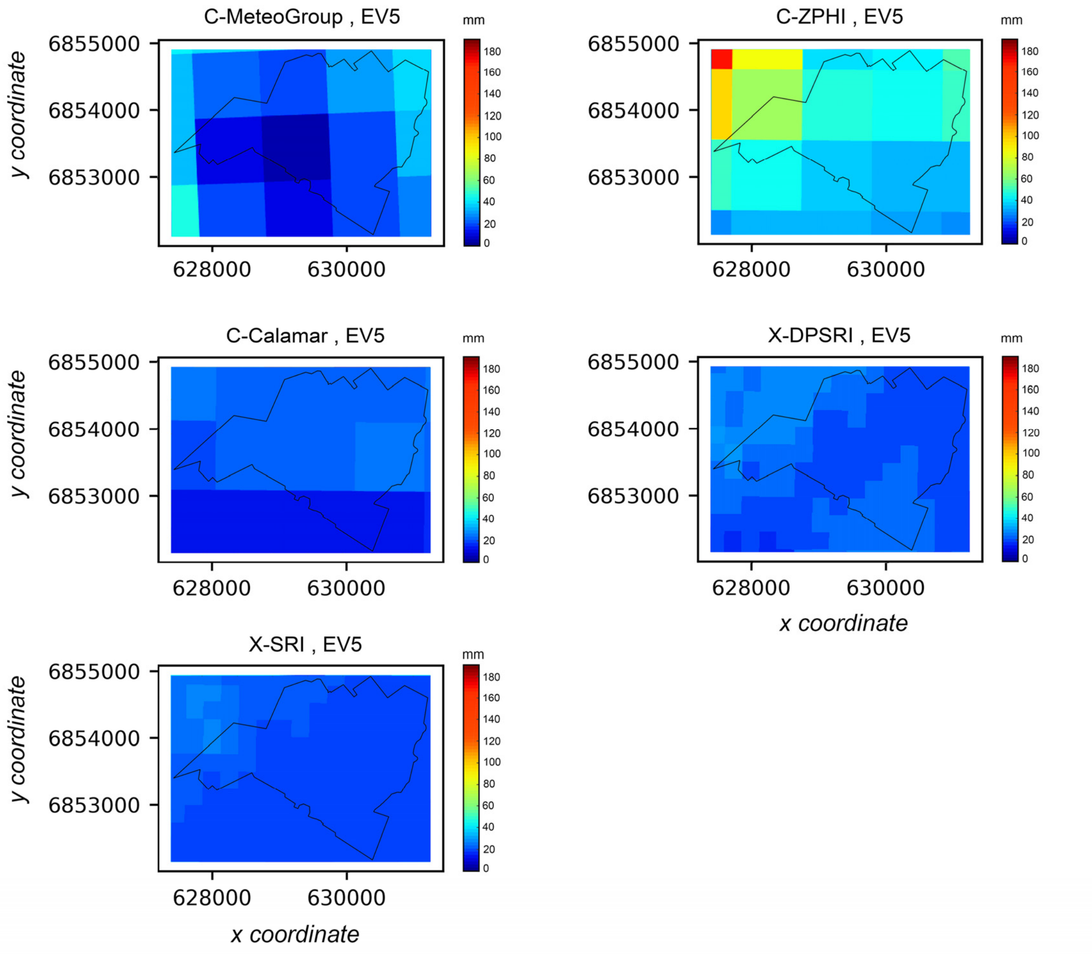

Figure 2.12: Cumulative rainfall by radar pixels over the Guyancourt catchment for C-band radar data and X-band radar data of EV5.

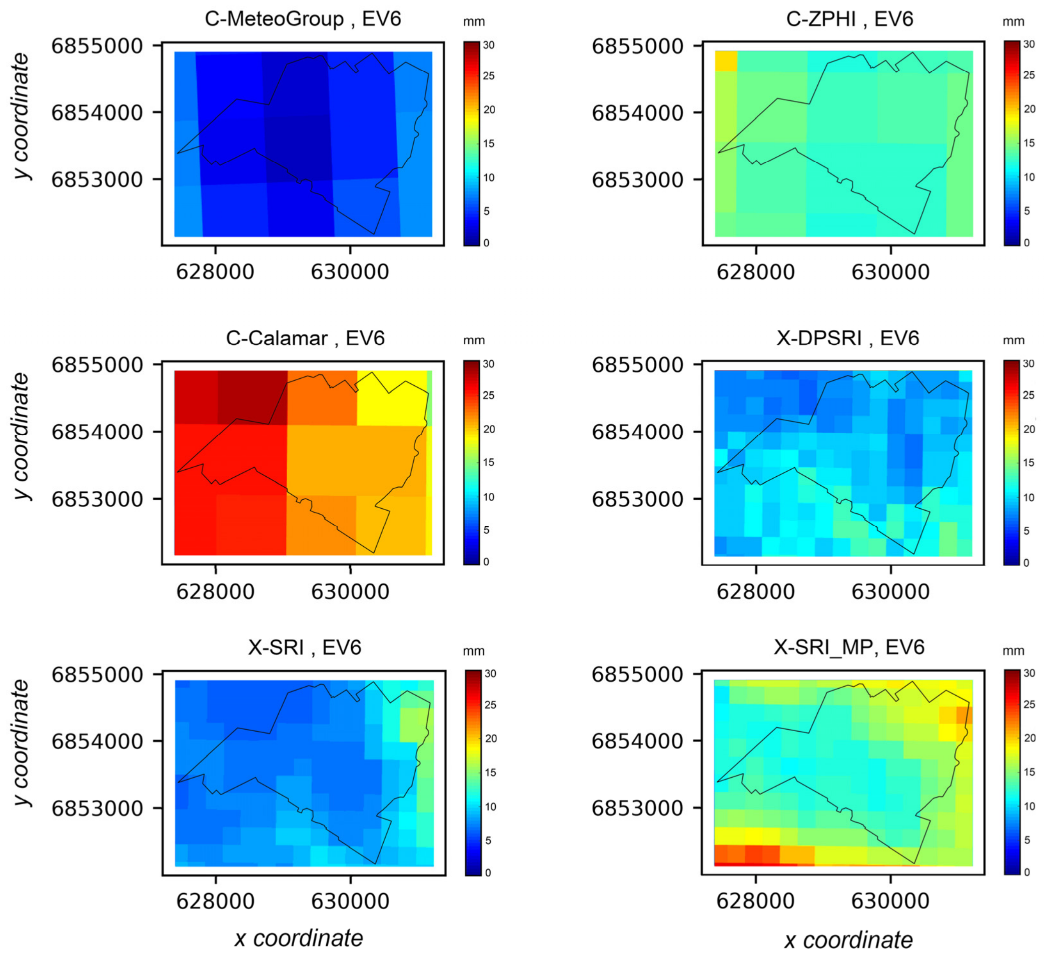

Figure 2.13: Cumulative rainfall by radar pixels over the Guyancourt catchment for C-band radar data and X-band radar data of EV6.

2.4.3.3 Classical metrics

For the statistical analysis of the rainfall events, the classical metrics of Nash-Sutcliffe coefficient (NSE) (Eq. 2.3), correlation coefficient (Eq. 2.4) and Root-Mean-Square Error (RMSE) (Eq. 2.5) are used. These indicators are widely applied for comparing time series.

The Nash-Sutcliffe Efficiency (NSE ≤1) is an indicator generally used to verify the quality of the simulation results of hydrological models (Nash and Sutcliffe, 1970), described as follows:

$$NSE(S_i, O_i) = 1 - \frac{\sum_{i=1}^{n}(O_i - S_i)^2}{\sum_{i=1}^{n}(O_i - \overline{O})^2} \tag{2.3}$$

where S_i refers to the simulated values, O_i refers to the observed values, and $\overline{O}$ represents the average of the observed values. The NSE closer to 1 indicates that the model is more reliable, while *NSE* closer to 0 indicates that the simulation is not better than that of the average observed value $\overline{O}$, which means the simulation performance is rather poor. If NSE is far less than 0, it means that the simulation is even less performing than $\overline{O}$.

In general, the correlation coefficient quantifies the relationship between two mathematical variables. It ranges from -1 to 1: the value of 1 indicates that two variables have a perfect positive linear relationship; the value of -1 means two variables have a total negative linear relationship; for 0, there is no linear correlation.

$$Correlation\ (S_i, O_i) = \frac{\sum_{i=1}^{n}(O_i-\overline{O})\cdot\sum_{i=1}^{n}(S_i-\overline{S})}{\sqrt{\sum_{i=1}^{n}(O_i-\overline{O})^2}\cdot\sqrt{\sum_{i=1}^{n}(S_i-\overline{S})^2}} \tag{2.4}$$

The Root-Mean-Square Error is generally used to present the difference between observed and predicted values. The value approach to 0 indicates the observed values have a good match with the predicted values.

$$RMSE = \sqrt{\frac{1}{n}\cdot\sum_{i=1}^{n}(S_i - O_i)^2} \tag{2.5}$$

In this thesis, the X-band radar product DPSRI with the Z-R relationship of *a* = 150 and *b* = 1.3 was considered as the reference data. Because this product has been presently considered as the "optimal" product for the ENPC X-band radar. Indeed, the estimations of statistical coefficients are very dependent on the choice of reference rainfall data. However, the general conclusions concerning the relative performance of each product remain entirely independent of this choice.

It is essential to point out that the C-band radar data and the X-band radar data that performed in this comparison have different temporal resolutions (3.41 min for all X-band radar data, and 5 min for all C-band radar data). In order to make a comparison, all the rainfall data are firstly transferred to the same temporal resolution of 1 min.

The results of the three classical metrics for six selected rainfall events and different radar products are presented, as shown in Figure 2.14 and summarised in Tables 2.3, 2.4 and 2.5. The values of NSE, correlation and RMSE indicate that the SRI product exhibits a good fit with the reference data (i.e., the NSE values range from 0.73 to 0.9, the correlation ranges from 0.9 to 0.95, and the RMSE ranges from 0.36 to 1.11). However, the NSE values of all C-band radar products are less than 0 (except for EV1), especially for the CALAMAR and ZPHI. In EV4 and EV6, the NSE values of ZPHI and CALAMAR are even around -12.3 and -18.96, respectively. These results indicate that a significant difference is found between the two C-band radar products (i.e., ZPHI and CALAMAR) and the reference product. Similarly, the values of the correlation coefficient of three C-band products are around 0 for EV4, EV5 and EV6. Correspondingly, for three rainfall events of 2018, the values of RMSE are around 2 for MeteoGroup, and larger than 2 for CALAMAR and ZPHI. The maximum value is about 9.5 for EV6 of CALAMAR. Compared with the product of CALAMAR and ZPHI for the rainfall events of 2018, the data of MeteoGroup seems closer to the reference data.

As discussed previously, the data of CALAMAR and ZPHI are less close to the reference data for three rainfall events of 2018. However, it is noticed that the CALAMAR data appears to be close to the reference data for EV1. For instance, in EV1, the NSE value, the correlation coefficient and the *RMSE* of CALAMAR are around 0.65, 0.82, and 1.32, respectively.

Concerning the three classical metrics computed for SRIMP of EV6, it is noticed that this rainfall product is less correlated with the reference data compared with the SRI. The value of NSE, correlation and RMSE is -0.2, 0.5, and 2.31, respectively.

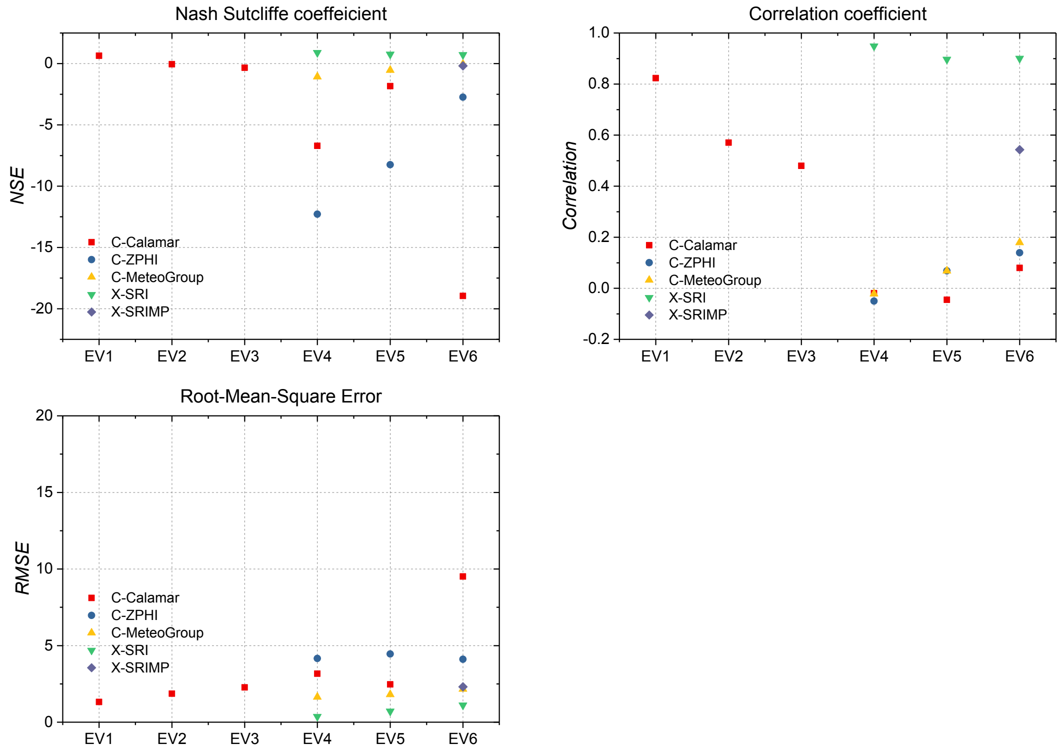

Figure 2.14: Representation of statistical values for the six selected rainfall events and all the rainfall data from C-band radar and X-band radar (the X-band DPSRI is considered as the reference data. The ■, ●, ▲, ▼ and ◆ represents the product of CALAMAR, ZPHI, MeteoGroup, SRI, and SRIMP, respectively).

Rainfall data	EV1	EV2	EV3	EV4	EV5	EV6
C- CALAMAR	0.649	-0.04	-0.34	-6.71	-1.84	-18.96
C-ZPHI	N/A	N/A	N/A	-12.28	-8.26	-2.73
C-MeteoGroup	N/A	N/A	N/A	-1.07	-0.52	-0.04
X-SRI	N/A	N/A	N/A	0.9	0.77	0.73
X-SRIMP	N/A	N/A	N/A	N/A	N/A	-0.18

Table 2.3: The NSE values of the six selected rainfall events and all the rainfall data from C-band radar and X-band radar.

Rainfall data	EV1	EV2	EV3	EV4	EV5	EV6
C- CALAMAR	0.82	0.57	0.48	-0.02	-0.04	0.18
C-ZPHI	N/A	N/A	N/A	-0.05	0.07	0.14
C-MeteoGroup	N/A	N/A	N/A	-0.02	0.04	0.18
X-SRI	N/A	N/A	N/A	0.95	0.9	0.90
X-SRIMP	N/A	N/A	N/A	N/A	N/A	0.54

Table 2.4: The correlation coefficient values of the six selected rainfall events and all the rainfall data from C-band radar and X-band radar.

Rainfall data	EV1	EV2	EV3	EV4	EV5	EV6
C- CALAMAR	1.32	1.86	2.27	3.16	2.47	9.51
C-ZPHI	N/A	N/A	N/A	4.16	4.45	4.11
C-MeteoGroup	N/A	N/A	N/A	1.64	1.81	2.17
X-SRI	N/A	N/A	N/A	0.36	0.71	1.11
X-SRIMP	N/A	N/A	N/A	N/A	N/A	2.31

Table 2.5: The RMSE values of the six selected rainfall events and all the rainfall data from C-band radar and X-band radar.

2.4.4 Synthetic rainfall events

To support different objectives of the thesis, several synthetic rainfall events were created based on the X-band radar data of EV1-EV3. The detailed information of these synthetic rainfall are presented in the following subsections.

2.4.4.1 EV1U – EV3U

In this thesis, as one of the purposes is to investigate the space variability of hydrological responses of NBS scenarios and the resulting uncertainty (i.e., the first set of modelling experiment in Section 4.1). Hence, two kinds of rainfall data were prepared as meteorological inputs for these modelling experiments of Section 4.1: distributed and uniform. The distributed rainfall inputs are based on the EV1-EV3 of the X-band radar data (see Table 2.1 for more details). To establish a link with classical approaches (e.g. Hamidi et al., 2018), the standard deviation (SD) was used to quantify the variability of the rainfall fields. As presented in Table 2.1, the SD of the rainfall intensity at the largest rainfall peak of the three rainfall events (X-band radar data) is 4.31, 6.11, and 5.75 mm/h, respectively. This illustrates that while the strongest rainfall intensity was observed during the EV3, the highest variability of rainfall intensity occurred in the EV2. Figure 2.9 (right) presents the total (cumulative) rainfall depth (per radar pixel) for the three rainfall events. The SD of the total rainfall depth of the three rainfall events is 1.21, 0.82, and 1.35 mm, respectively. This demonstrates that the spatial distributions of cumulative rainfall are much less variable compared to those of the rainfall intensity at the peak, with the highest variability computed for the EV3.

The three spatially uniform rainfall events (EV1U, EV2U and EV3U) were constructed by spatial averaging over the whole catchment of original (distributed) rainfall fields at each time step. Figure 2.7 presents the time evolution of the corresponding rainfall rates and cumulative rainfall depths. Each of these events is sufficiently long to contain several rainfall peaks and dry periods. For EV1U, the highest rainfall intensity reaches 20 mm/h, and the total rainfall accumulates (around 31.5 mm) fast between the first and the third rainfall periods (approximately 24 h). The maximum rainfall intensity of the EV2U and EV3U is 9 mm/h and 36.4 mm/h, and the total rainfall amounts about 12 mm and 20 mm, respectively. Although the largest rainfall peak of the EV3U is 36.4 mm/h, it lasted only for 3 min, just sufficient to contribute about 10 % to the total rainfall depths.

Overall, this initial analysis suggests that in spite of some very similar characteristics, the selected events cover a truly wide spectrum of rainfall space-time variability.

2.4.4.2 EV1S – EV4S

To deepen the understanding of the intersection effects between the spatial variability in rainfall and spatial distribution of NBS, four synthetic rain events (EV1S-EV4S) were created additionally. These rainfall events are used for the modelling experiments in Section 4.1. All these events are based on the uniform rainfall of EV3U, by selecting the 2 hours period with the highest rainfall peak around 35 mm/h (areal averaged), as illustrated on Figure 2.15 (a). However, during the 3 min that lasted at the largest rainfall peak of the EV3U, a new space distribution and/or intensity of the rainfall was imposed for each synthetic rainfall event. As shown in Figure 2.15 (b), the areal averaged maximum rainfall peak is about 37 mm/h for the EV1S, and the corresponding areal averaged cumulative rainfall is about 4.1 mm. During these 3 minutes, the rainfall was re-distributed in a binary manner in space (Figure 2.15 (c)), with the maximum intensity around 55 mm/h only for green roofs (GR) in the GR1 scenario (see Section 2.6 for more descriptions of this NBS scenario), and the other areas are received uniform rainfall around 38 mm/h. For the remaining synthetic rain events, this binary distribution was modified as follows (see Figure 2.15 (d-f)): the same maximum intensity of 55 mm/h only for GRs, and zero rainfall elsewhere (EV2S), the maximum intensity of 17 mm/h only for GRs, and zero rainfall elsewhere (EV3S), and the maximum intensity of 55 mm/h has been replaced by zero rainfall (EV4S), and 38 mm/h rainfall elsewhere.

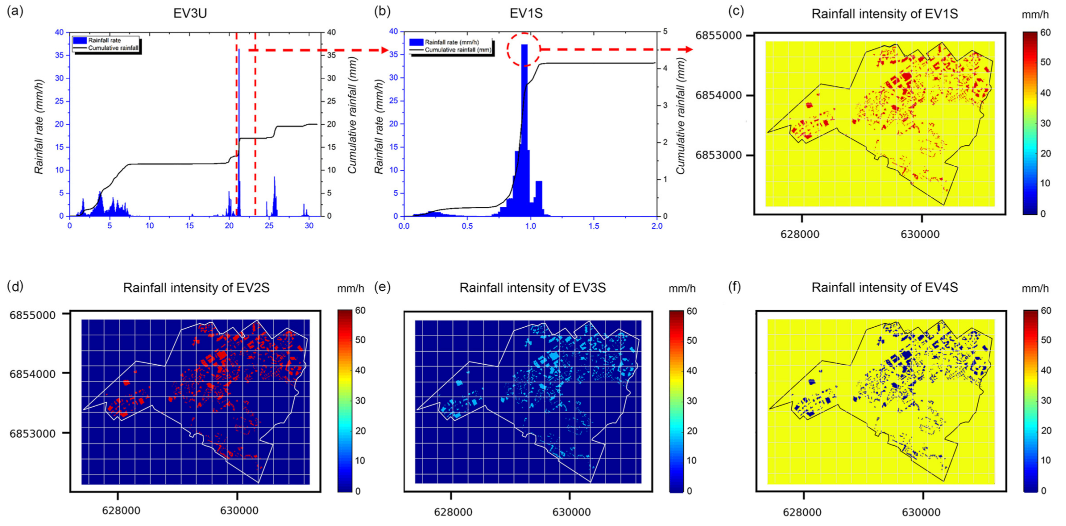

Figure 2.15: Temporal evolution of rainfall rate (mm/h) and cumulative rainfall (mm) of the EV3U over the whole catchment (the period between the red dash lines is the selected period for creating the EV1S); (b) Temporal evolution of rainfall rate (mm/h) and cumulative rainfall (mm) of the EV1S over the whole catchment; (c) The rainfall intensity at the largest rainfall peak (distributed) of EV1S (the red areas are the location of GRs in GR1 scenario, and the rainfall over other areas is uniform); (d) EV2S; (e) EV3S; (e) EV4S.

2.4.4.3 EV5S – EV6S

For investigating the multifractal characterisation of the overland flow of different NBS scenarios, the EV1-EV3 of the X-band radar data were selected as the metrological inputs for the modelling experiments (i.e., the third set of modelling experiments in Section 4.3). For the purpose of obtaining larger values of overland flow to investigate its impacts on the estimation of UM parameters and γ_s, the syntactic rainfall event (EV5S) was artificially created. The rainfall intensity of this rainfall event was enlarged by 10 times based on EV2. The main characteristics of the event EV5S are summarised in Table 2.6. The areal averaged maximum rainfall rate over the whole catchment reaches 116 mm/h, and the corresponding cumulative rainfall is 121 mm (Figure 2.16). Concerning the peak rainfall intensity (per radar pixel) and the maximum cumulative rainfall (per radar pixel) of the event EV5S, they are around 291 mm/h and 141 mm, respectively (Figure 2.17).

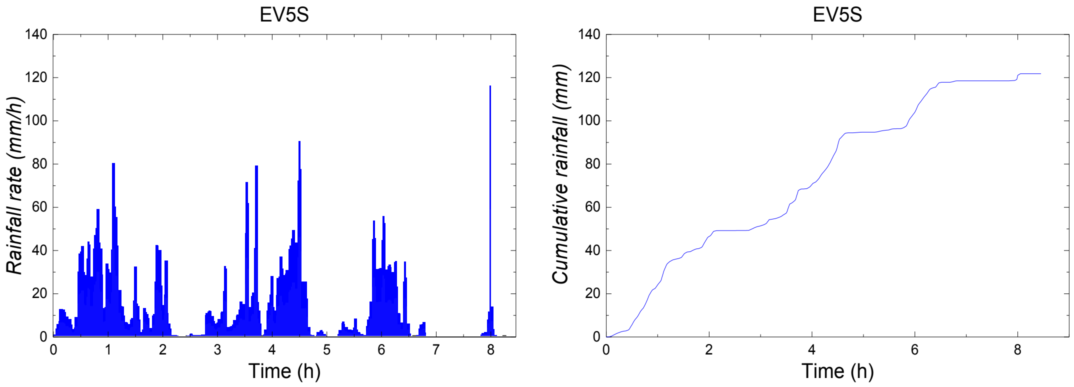

Figure 2.16: Temporal evolution of rainfall rate (left) and cumulative rainfall (right) of the EV5S.

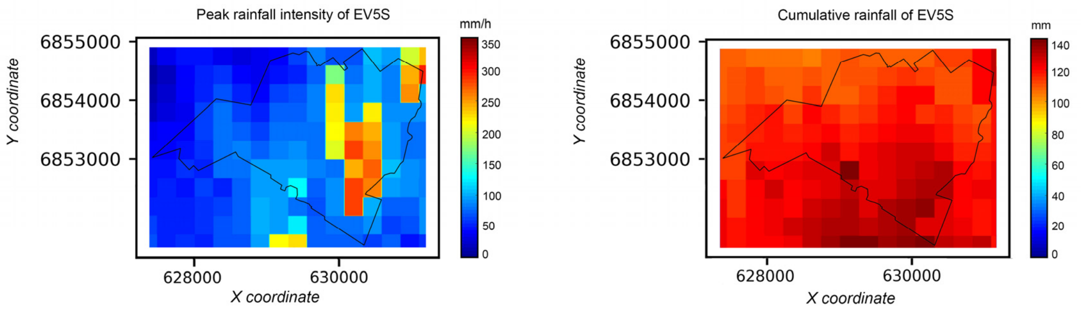

Figure 2.17: Peak rainfall intensity (per radar pixel) (left) and cumulative rainfall (right) over the whole Guyancourt catchment for the EV5S.

To investigate the variation of overland flow under the rainfall with short duration and high intensity and to find its effects on the estimation of UM parameters and γ_s, a two hours subdivided rainfall (EV6S) is characterised with a strong rainfall peak is artificially created based on EV3 (the detailed information can be found in Table 2.6).

As shown in Figure 2.18, the areal averaged maximum rainfall rate and cumulative rainfall of this subdivided rainfall event are around 35 mm/h and 4.1 mm, respectively. Regarding the peak rainfall intensity (per radar pixel) of this subdivided rainfall, which is approximately 55.6 mm/h (Figure 2.19). Correspondingly, the maximum cumulative rainfall (per radar pixel) of this rainfall event is about 8 mm.

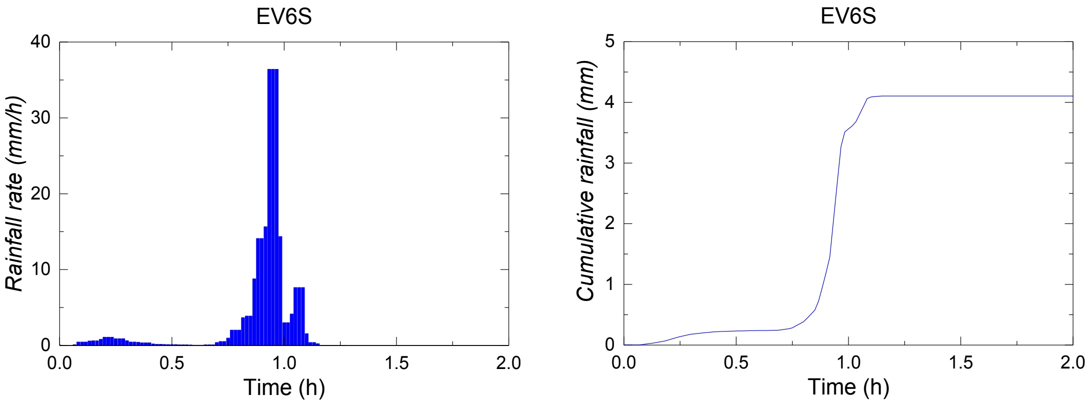

Figure 2.18: Temporal evolution of rainfall rate (left) and cumulative rainfall (right) of the EV6S.

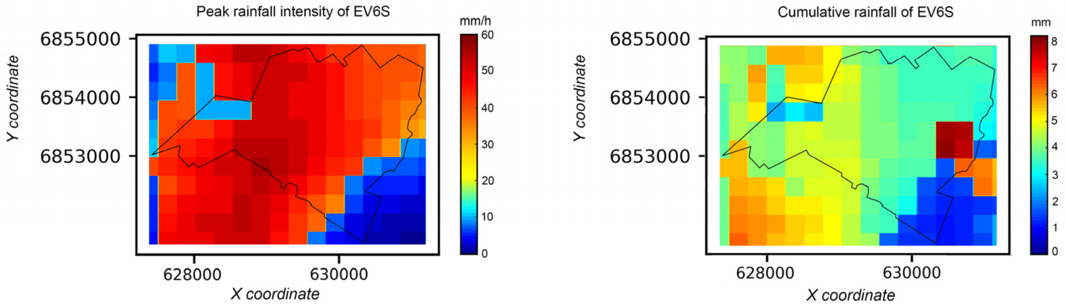

Figure 2.19: Peak rainfall intensity (per radar pixel) (left) and cumulative rainfall (right) over the whole Guyancourt catchment for the EV6S.

Event ID	Date	Duration (h)	Total depth (mm) (areal average/pixel min/pixel max)	Max intensity (mm/h) over 1 min (areal average/individual pixel)
EV5S	16/Sep/2015	8.75 (08:05-16:50)	121/104.3/141	9/29.1
EV6S	06/Oct/2015	2 (04:27-06:27)	4.11/8.01	36.4/55.6

Table 2.6: Main characteristics of the event EV5S and EV6S.

2.4.4.4 EV7S – EV14S

To deepen the knowledge on the hydrological performances of NBS under different rainfall conditions (Section 5.1), the EV1-EV3 were selected and then subdivided into eight short subdivided rainfall events (EV7S – EV14S). The duration of these rainfall events were artificially set with 3 hours to limit the high rainfall intermittency. The main characteristics of these eight rainfall events differ by their total amounts and intensity (see more details in Table 2.7). The rainfall intensity (mm/h) and cumulative rainfall (mm) by averaged in space of the selected rainfall events are shown in Figure 2.20. It is noticed that the two strongest rainfall events are EV8S and EV14S, with the peak rainfall intensity (averaged in space) corresponding to 20.6 mm/h, and 36.4 mm/h, respectively. Regarding the maximum rainfall intensity (per radar pixel) of the two strongest events (Table 2.7), it is 41.2 mm/h and 55.6 mm/h, respectively. This indicates that some locations are characterised with strong rainfall cells. For the other rainfall events, they are relatively weak, with the maximum rainfall intensity (areal averaged) ranging from 2.91 mm/h to 9.03 mm/h. However, regarding the maximum rainfall intensity (per radar pixel) of these events, it ranges from 5.33 mm/h to 29.1 mm/h. Apparently, for these rainfall events, the rainfall intensity of per radar pixel has a large range of spectral. Concerning the total amounts (cumulative rainfall) of each rainfall event, the EV8S is the highest, with the cumulative rainfall by averaged in space and per radar pixel around 5.46 mm and 8.14 mm, respectively (Figure 2.20 and Figure 2.21). Although EV14S has a higher peak rainfall intensity than that of the EV8S, it only lasts for a few minutes, which is not significant for the cumulative rainfall.

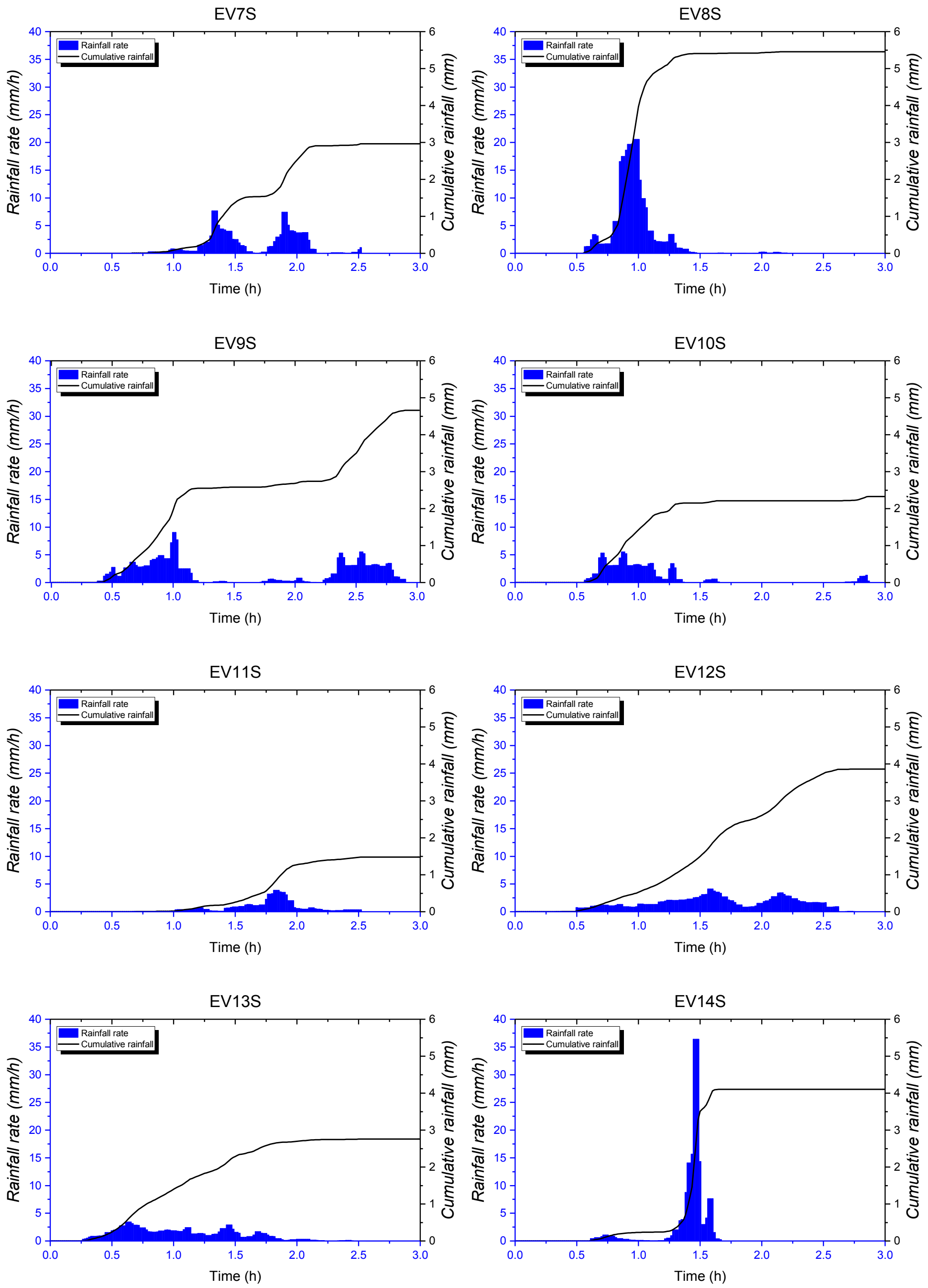

Figure 2.20: The rainfall intensity (mm/h) and cumulative rainfall (mm) by averaged in space over the whole catchment for the eight subdivided rainfall events (EV7S – EV14S).

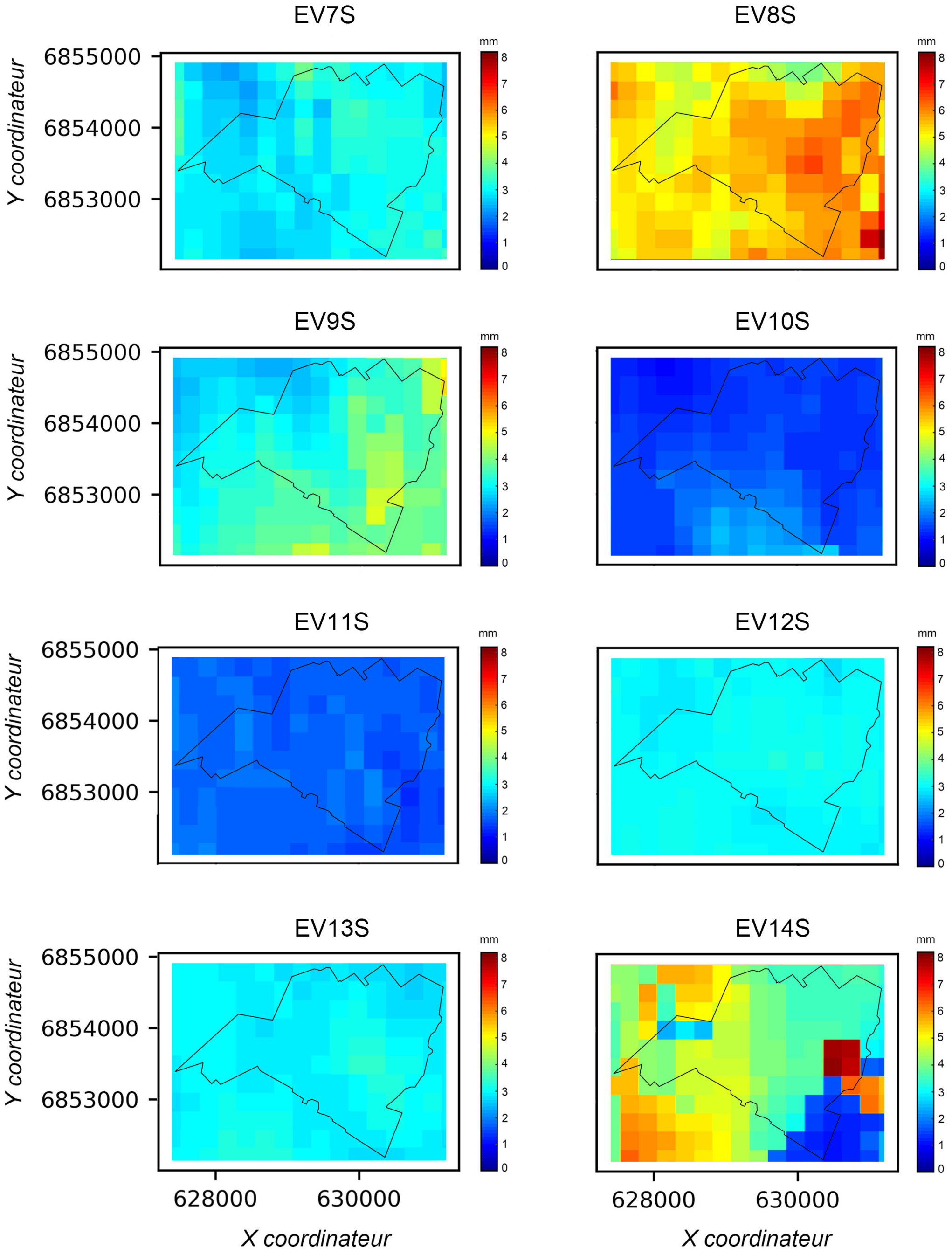

Figure 2.21: The cumulative rainfall (per radar pixel) over the whole catchment of the eight subdivided rainfall events (EV7S – EV14S).

Event ID	Data	Duration (h)	Maximum intensity (mm/h) (areal average/per pixel)	Cumulative rainfall (mm) (areal average/maximum per pixel)
EV7S	13/Sep/2015	3 h	7.68/19.7	2.96/3.89
EV8S	13/Sep/2015		20.6/41.2	5.46/8.14
EV9S	16/Sep/2015		9.03/29.1	4.66/5.35
EV10S	16/Sep/2015		5.55/9.53	2.32/2.58
EV11S	05/Oct/2015		3.87/6.9	1.48/1.77
EV12S	05/Oct/2015		4.11/6.72	3.86/4.05
EV13S	05/Oct/2015		2.91/5.33	2.75/3.43
EV14S	06/Oct/2015		36.4/55.6	4.11/8.01

Table 2.7: The main characteristic of the selected rainfall events.

2.5 Multi-Hydro model

Multi-Hydro model is a fully-distributed and physically-based hydrological model, which was developed by laboratory of Hydrology Meteorology & Complexity (HM&Co)/ENPC (El Tabach et al., 2009; Giangola-Murzyn, 2013; Ichiba, 2016; Ichiba et al., 2018). It has been successfully implemented and validated in several catchments (e.g. Versini et al., 2016; Ichiba et al., 2018; Gires et al., 2017; Gires et al., 2018; Alves de Souza et al., 2018; Versini et al., 2018; Paz et al., 2019). In this thesis, it is used for assessing hydrological responses of the NBS scenarios at the urban catchment scale. Multi-Hydro contains an interactive core among the four open-source modules (rainfall, surface, groundwater and drainage), which represent essential elements of the hydrological cycle in the urban environment, as illustrated in Figure 2.22.

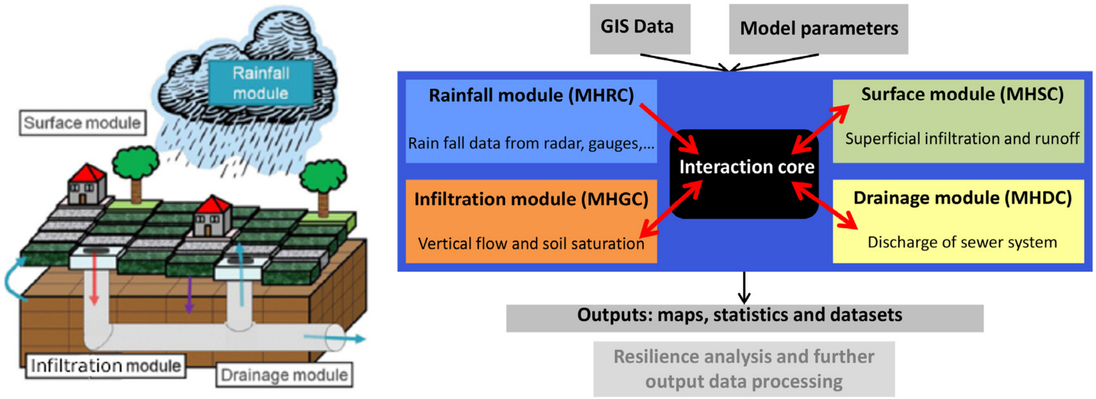

Figure 2.22: The structure of Multi-Hydro model.

The rainfall module (MHRC) can treat different kinds of rainfall data (from radar or rain gauge). The surface module (MHSC) of Multi-Hydro uses the code of Two-Dimensional Runoff Erosion and Export (TREX) model (Velleux et al., 2008). The surface module computes the interception, storage and superficial infiltration occurring at each pixel in terms of the properties of each land use. The superficial infiltration process of the surface module is governed by simplification of Green and Ampt equation. The overland flow occurs when the water depth on the overland plane exceeds the threshold of depression storages. It is governed by equations of conservation of mass (continuity) and conservation of momentum. The diffusive wave approximation of the Saint-Venant equations is used for calculating the overland flow.

The groundwater module (MHGC) is based on the Variably Saturated and 2-Dimensional Transport (VS2DT) model developed by the U.S. Geological Survey, which can be used to simulate variably saturated transient water flow and solute transport in one or two dimensions (Lappala et al., 1987; Healy, 1990). Because of the groundwater recharge and solute transport are not the purpose of this thesis, this module is not applied in this thesis.

The drainage module (MHDC) in Multi-Hydro uses the code of 1D SWMM model proposed by James et al. (2010) to simulate the sewer network. This model represents the flow computed by 1D Saint-Venant equations in conduits and nodes.

The high spatial resolution of Multi-Hydro allows an easy implementation of small scale controlled measures, like the rain garden, green roof, bio-retention swale, permeable pavement, and rainwater tank, by locally modifying the land use parameters to link the size and shape of the corresponding NBS infrastructures with their infiltration and storage capacities.

2.5.1 NBS module

In this thesis, a special module for simulating green roof is applied. This module is based on a linear reservoir structure (Versini et al., 2015, 2016) and is applied in the pixels, defined as a green roof. It assumes that the water content and the hydrological conductivity are constant in the substrate of a green roof.

In detail, a simplified in/out relationship is defined for the fluctuation of the reservoir level:

$$H_r(t+\Delta t) = H_r(t) + R(t) - Q_{out}(t) \tag{2.6}$$

where $H_r(t)$ is the level of reservoir (mm), Δt is the time step for each loop (0.05 h in this study), $R(t)$ refers to the rainfall rate (mm/h), and $Q_{out}(t)$ represents the runoff generated by green roof at time *t* (mm).

The $Q_{out}(t)$ is calculated with following equation:

$$Q_{out}(t) = max\left[\frac{K_{sat}\times\Delta t}{Thick} \times (H_r(t) - FC \times Thick), 0\right] \tag{2.7}$$

where K_{sat} is the saturated hydraulic conductivity (mm/s), $Thick$ is the substrate thickness (mm), FC is the field capacity, adjusted by thickness and porosity.

The initial water level is defined at the first time step of the simulation:

$$H_r(0) = Thick \times n \times IS \tag{2.8}$$

where n is the porosity, IS is the initial substrate saturation.

Besides the green roof, a simple procedure representing both infiltration and storage processes has been carried out for modelling the permeable pavement and rain garden. For each time step, if the rainfall rate is lower than the infiltration rate of permeable pavement/rain garden, the water is stored. If not, then the ponding occurs.

As rain garden is the artificial depression green belt, the depth of depression storage (denoted as D_p m) should be equal to the maximum storage capacity of the rain garden system.

Because the permeable pavement generally consist of the pavement layer and the bedding layer, the maximum storage capacity of a permeable pavement system (denoted as $S_{p\,max}$, in m) without underdrains can be computed with the following equation:

$$S_{p\,max} = h_p n_p + h_b n_b \tag{2.9}$$

where h_p (m) and n_p (dimensionless) is the depth and porosity of the pavement layer, respectively; and h_b (m) and n_b (dimensionless) is the depth and porosity of the bedding layer, respectively.

2.5.2 Data processing for Multi-Hydro

2.5.2.1 Rainfall data generation

In order to adapt the rainfall inputs for Multi-Hydro, the intersection between the pixels of the model (a 10 m spatial resolution used in this study) and the pixels of the radar data (X-band with a 250 m spatial resolution, C-band with a 1 km spatial resolution) was performed by the QGIS interface using the following equations (Paz et al., 2018):

$$R_{i_M,j_M} = \frac{\sum_{i_X,j_X} R_{i_X,j_X} |A_{i_M,j_M} \cap A_{i_X,j_X}|}{|A_M|} \tag{2.10}$$

$$R_{i_M,j_M} = \frac{\sum_{i_C,j_C} R_{i_C,j_C} |A_{i_M,j_M} \cap A_{i_C,j_C}|}{\sum_{i_C,j_C} |A_M|} \tag{2.11}$$

where R_{i_M,j_M} is the rainfall rate computed on the model pixel A_{i_M,j_M} of coordinates (i_M, j_M); R_{i_X,j_X} is the rainfall rate measured by the X-band radar on its pixel A_{i_X,j_X} of coordinates (i_X, j_X); R_{i_C,j_C} is the rainfall rate measured by the C-band radar data on its pixel A_{i_C,j_C} of coordinates (i_C, j_C); $|S|$ denotes the surface of any pixel S, in particular $|A_M|$ is the surface of the model pixel (it does not depend on the coordinates, but only by the model resolution).

Here, the X-band DPSRI data (grid file) is taken as an example to illustrate this process (Figure 2.23). This approach can be applied for the grid files of both X-band radar and C-band radar.

Firstly, for the purpose of computing the intersection area of the radar pixels A_{i_X,j_X} with the model pixel A_{i_M,j_M} ($A_{i_X,j_X} \cap A_{i_M,j_M}$), a new layer with the intersection of the prior two layers was created (Figure 2.24). Then, the attribute table of QGIS was exported to an auxiliary ".csv" file, resulting in a matrix with n rows and n columns (with the order of the corresponding radar data pixel's coordinates i_X, j_X, the corresponding Multi-Hydro coordinates pixels i_M, j_M, and the entity area).

Finally, the auxiliary ".csv" file and Eqs. 2.10 and 2.11 were used to generate a 275×380 column matrix containing the rainfall rates of X-band radar data and C-band radar data, respectively.

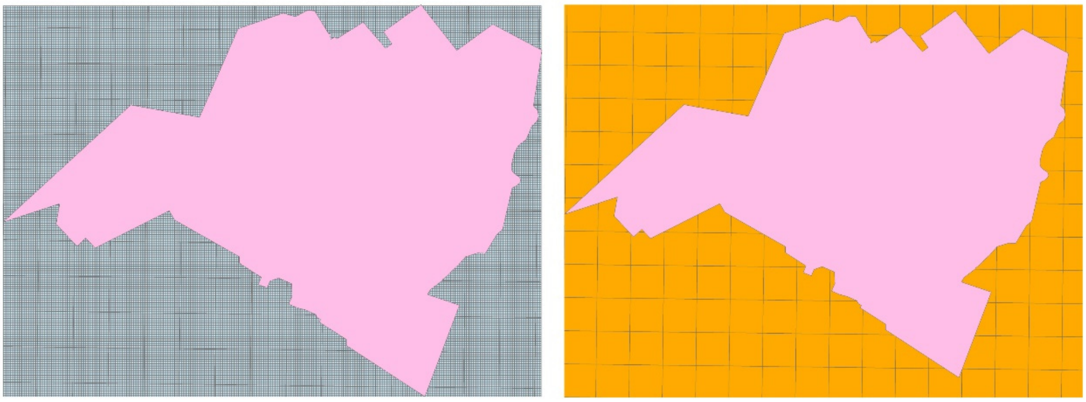

(a) (b)

Figure 2.23: The Guyancourt sub-catchment layer with: the Multi-Hydro grid layer at a 10 m resolution (a), and ENPC X-band radar grid layer at a resolution of 250 m x 250 m (b).

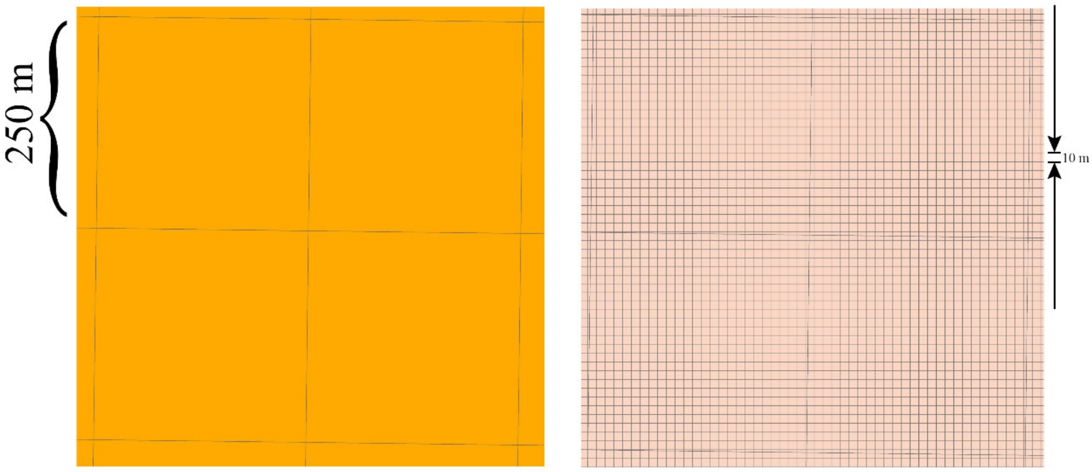

Original radar pixel intersected radar pixel for Multi-Hydro

Figure 2.24: The original layer of X-band radar pixel (left) and the intersected layer of radar pixel for Multi-Hydro (right).

In analogy with Eqs. 2.10 and 2.11, the rainfall input for Multi-Hydro has been also time interpolated from the X-band radar and C-band radar measurements, as follows:

$$R_m(j) = \frac{\sum_i R_r(i)|\Delta_m(j) \cap \Delta_r(i)|}{\delta_m} \tag{2.12}$$

where $R_m(j)$ is the rainfall rate during the j-th time interval $\Delta_m(j)$ of the model, $R_r(i)$ is the rainfall rate during the i-th time interval $\Delta_r(i)$ of the X-band radar/C-band radar. $|\Delta|$ denotes the length of any interval Δ and $\delta_\mathrm{m} = |\Delta_\mathrm{m}|$ is the length of any time interval of the model. Note that while the duration of the time loop to generate the model outputs is 3 min (to keep it comparable with the X-band radar time interval), $\delta_m = 1$ minute for the rain input to Multi-Hydro.

2.5.2.2 GIS data generation: MH-AssimTool

Based on the fully distributed character of Multi-Hydro, users can choose a specific spatial resolution to present the heterogeneity of a catchment, which is a significant advantage of the grid-based model. In this thesis, Multi-Hydro was implemented with a 10 m spatial resolution (the grid system creates square grids with a cell size of 10 m), and a temporal loop of 3 min. The 10 m resolution was adopted because it sufficiently represents the heterogeneity of the catchment and saves the computation time.

The implementation of Multi-Hydro in a new catchment starts with the conversion of the original GIS data (e.g. land use, topography) into the standard rasterised format with the desired resolution by using the MH-AssimTool (Richard et al., 2013), a supplementary GIS-based module for generating the input data for Multi-Hydro. During this process, a unique land use class was assigned to each pixel, specifying its hydrological and physical properties. In order to attribute a unique land use class to each pixel, the following priority order was used in this study: gully, road, parking, house, forest, grass, and water surface. Because the gully is the only land use class able to connect the surface module and the drainage module, it has the highest priority (i.e., if a raster pixel contains gully and the other land use classes, the whole pixel was considered as gully). Generally, this order considers the impervious land use classes have higher priority than the permeable land use classes, which results in an overestimation of impervious land uses (see Ichiba et al., 2017, for an alternative approach). After the rasterization process, the impervious land use occupies 54 % of the Guyancourt catchment (Figure 2.25). In this thesis, all the standard model parameters related to the land use classification were selected from the Multi-Hydro manual (Giangola-Murzyn, 2013). The most important parameters are Manning’s coefficient (no unit), hydraulic conductivity (m/s) and interception (mm), as they are shown in Table 2.8. As already indicated by Ichiba et al. (2018), the Multi-Hydro does not use the traditional calibration of these parameters. If their most common values are always used, the reliable heterogeneity of the watershed for each case study is obtained by a rapid optimization of the spatio-temporal resolution of the model, with possibly refined classes of the land use and their orders.

Besides the land use, the elevation is also assigned to each pixel of the model. For this purpose, the interpolation was used to downscale the raw DEM data from 25 m to 10 m (DEM25-10) to incorporate it with the model resolution. More precisely, each pixel was first subdivided into

25 equal sub-pixels as a proxy of the 5 m resolution, then the elevation data were up-scaled 4 by 4 pixels to produce the 10 m interpolation of the original elevation.

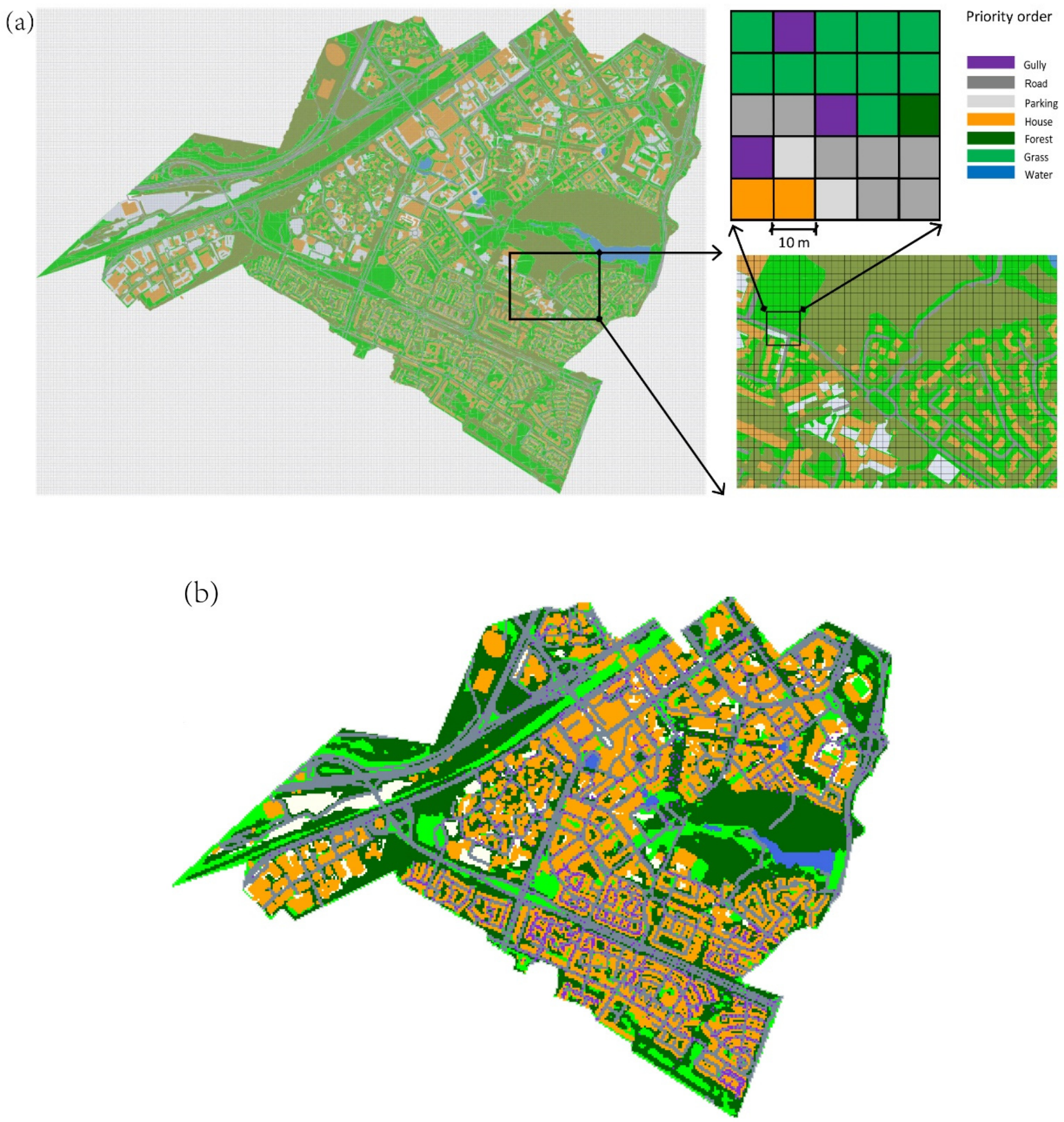

Figure 2.25: (a) Rasterization of the original land use data into 10 m with priority order, and (b) the rasterised land use data.

Land use	**Hydraulic conductivity (m/s)**	**Manning's coefficient (no units)**	**Interception (mm)**
Impervious surfaces (house, road, parking, etc.)	1.0×10^{-10}	0.012	1.9
Grass	1.9×10^{-6}	0.15	3.81
Forest	1.9×10^{-6}	0.8	7.62
Gullies	1.0×10^{-0}	0.9	0
Water	1.0×10^{-0}	0.9	100
Permeable pavement	1.0×10^{-4}	0.014	2.14
Rain garden	1.9×10^{-5}	0.2	7.62
Green roof	3.3×10^{-4}	0.14	3.81

Table 2.8: Hydrological parameters for each land use class.

2.5.3 Multi-Hydro validation for Guyancourt catchment (baseline scenario)

Before the simulation of NBS scenarios, Multi-Hydro was validated with the monitored water levels of the storage basin by applying the baseline scenario under the EV1-EV3 (X-band radar data) of 2015. Furthermore, the simulations were also repeated with the three uniform rainfall events (EV1U – EV3U), respectively. The uniform rainfall is also used to validate the model based on the specific objective of analysing the impact of spatial variability in rainfall and NBS on the hydrological performances of NBS scenarios in Section 4.1.

The model performance was evaluated through two indicators: Nash-Sutcliffe Efficiency (NSE) and percentage difference (*PE*). The NSE has been introduced in Section 2.4.3 (Eq. 2.3). The percentage difference (*PE*) represents the difference between observed values and simulation values, which reflects the reliability of the simulation values.

$$\mathrm{PE}(S_i, O_i) = \frac{\sum_{i=1}^{n}|O_i - S_i|}{\sum_{i=1}^{n} O_i} \times 100\% \tag{2.13}$$

With respect to the observed and simulated water levels in the baseline scenario, the model indeed performs well for the studied area. The NSE coefficients and the PE indicators validated Multi-Hydro's performance (see Table 2.9). For the EV1 – EV3 (Figure 2.26), the NSE values are larger than 0.9, and *PE* values are lower than 5 %. For the uniform rainfall event of EV2U, the model represents the water levels with NSE equal to 0.95, and *PE* equal to 1.96 %: Only a slight overestimation of the water levels is observed between hours 4 to 7. For the uniform rainfall of EV1U and EV3U, the temporal evolutions of simulated water levels slightly underestimate the observed ones, with NSE value around 0.8, as well as *PE* value around 7 %. Regarding the temporal evolutions of simulated water levels under the distributed rainfall of EV1 and EV3, they are consistent with the observed ones. The reason is that the rainfall intensities of the distributed rainfall are generally higher than those of the uniform rainfall at the storage basin location. Namely, in uniform rainfall events, the accumulated water levels in the storage basin are less than that in distributed rainfall events. Overall, the distributed rainfall gives slightly better results, and the simulated water levels using uniform rainfall also match sufficiently well the observed ones to validate the Multi-Hydro implementation in the Guyancourt catchment.

Regarding the validation results, the scalability of Multi-Hydro allowed to define the optimal resolution to finely reproduce the spatial heterogeneity of the watershed. Remember that this resolution is the ratio between the external scale of the watershed and the scale of the grid. The heterogeneity mentioned above propagates from the smallest scale to the largest, impacting the simulation results in any through the hierarchy of spatial scales of the watershed. It should be understood that the selected 10 m grid scale is not the smallest scale possible, but the optimal one to ensure a good balance between, for example, sufficient heterogeneity and the required quantity of the data required, a gain in precision, and involved computing time. Hence, the Multi-Hydro is suitable and sufficiently reliable to investigate the impacts of spatial variability in rainfall and NBS on the hydrological responses under different NBS scenarios.

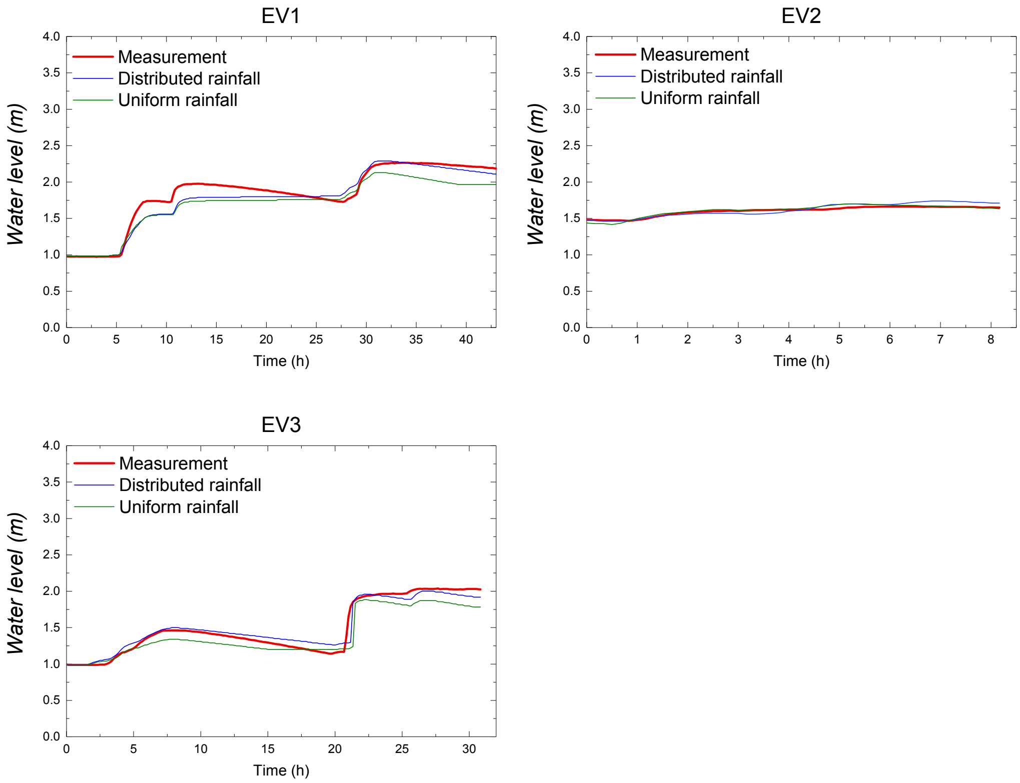

Figure 2.26: Comparison of the observed and simulated water levels (simulated with distributed rainfall and uniform rainfall) of the three rainfall events of 2015.

Event ID	Distributed rainfall		Uniform rainfall	
	NSE	**PE (%)**	**NSE**	**PE (%)**
EV1	0.926	4.6	0.824	7.9
EV2	0.929	2.2	0.948	1.96
EV3	0.954	3.9	0.865	6.9

Table 2.9: NSE coefficients and PE values of baseline scenario under the three distributed rainfall events and three uniform rainfall events.

2.6 Simulation scenarios of NBS and their parameterisation

In order to make a comprehensive assessment of NBS hydrological performances, six sets of NBS scenarios were created with different purposes. For achieving the purpose of the first set of modelling experiments (Section 4.1), the first and second sets of NBS scenarios were created and simulated under both distributed and uniform rainfall (described in Section 2.4.4.1). For designing the cost-effective NBS scenarios, another four sets (the third to sixth) of NBS scenarios were created and simulated under the synthetic rainfall events of EV7S – EV14S (Section 2.4.4.4). The baseline scenario is considered as the current configuration of the Guyancourt catchment, without implementing any NBS (Figure 2.4) and it was used for the model validation in Section 2.5.3.

All details concerning the first and second sets of NBS scenarios, including detailed descriptions of each NBS and the percentage of the space required for its implementation, are presented in Table 2.10, while the maps of the resulting land use are illustrated on Figure 2.27. Because the third – sixth sets of NBS scenarios are used for the cost-effective design, the detailed descriptions for these NBS scenarios are summarised in the separate table (Table 2.11), and the corresponding land use maps are shown in Figure 2.28.

The first set of NBS scenarios includes permeable pavement (PP1), rain garden (RG1), green roof (GR1), and their combined scenario (Combined1). For each scenario, the corresponding NBS are implemented heterogeneously over the catchment, while respecting the local catchment conditions and stormwater management requirements. For instance, with the help of the detailed land use GIS data, all the buildings with flat roofs were initially selected, then these impervious roofs were converted into green roofs for the GR1 scenarios by adapting the land use data. They are applied to assess the impact of spatial variability in rainfall on the hydrological responses of NBS scenarios.

The second set of NBS scenarios (PP2, RG2, GR2, and Combined2) was proposed with a different arrangement to assess the potential effects of a heterogeneous implementation of NBS at the urban catchment scale. Considering now the roofs with certain slopes (≤ 15°), they can be also used to implement green roofs (Stanić et al., 2019). The impervious roofs that satisfied this condition were converted into small and light green roofs and used for the GR2 scenario. While the two scenarios (GR1 and GR2) occupy the same percentage of the whole catchment, their densities are different, simply because of the difference of original densities of the buildings. The designing process for other NBS scenarios follows a somewhat similar logic. Regarding these two sets of NBS scenarios, the ones related to the same type of NBS (e.g. PP1 and PP2) require the same percentage of the space for their implementation over the whole catchment. But, both scenarios significantly differ in terms of spatial distributions of the considered asset. This distribution is characterised by the across-scale indicator, called fractal dimension presented in detail in the next chapter.

The third set of NBS scenario was created for evaluating the hydrological responses of NBS with different implementation levels, which includes scenarios of PP3, PP4, PP5, PP6, RG3, RG4, RG5, RG6, GR3, GR4, GR5, and GR6. These NBS scenarios were created by up-scaling of their implementation level in the whole catchment with the help of quantifying their fractal dimension (more descriptions on these scenarios can be found in Table 2.11).

The fourth set includes four different combined scenarios: PP6+RG6, PP6+GR6, RG6+GR6, and PP6+RG6+GR6. Here, it needs to mention that these combined scenarios are performed with the highest fractal dimension of the single type of NBS over the whole catchment. For instance, the scenario of PP6+RG6+GR6 is the combination of the third set of NBS scenarios of PP6, RG6 and GR6.

The fifth set of NBS scenario was created for assessing the hydrological responses of NBS in a specific spatial location. Here, two specific locations were selected and implemented with NBS: upstream and downstream. Indeed, for the same type of NBS (e.g. PP upstream and PP downstream) has the same percentage of the space over the whole catchment. But, both scenarios significantly differ in terms of spatial distributions, characterised with a different fractal dimension.

The sixth set only contains the GR scenarios, and the aim is to assess the hydrological performances of two different types of GR (extensive and semi-intensive) in terms of different initial substrate conditions. To be more specific, these GR scenarios are simulated with respect to different substrate thickness and initial substrate saturation. The extensive GR is supposed to have the substrate thickness equal to 100 mm, and that of the semi-intensive GR is equal to 200 mm. These two different types of GR are simulated with the initial substrate saturation as 10 %, 25 % and 50 %, respectively. Here, it worth to noting that the extensive GR scenarios and semi-intensive GR scenarios have the same spatial layout and fractal dimension in the catchment in order to avoid the impact of spatial distributions of GRs.

Indeed, as the most considered NBS correspond to more specific land uses, they are characterised with different retention capacities, and the related parameters are based on the literatures (Dussaillant et al., 2004; Kuang et al., 2011; Park et al., 2014). To be more specific, the RGs are characterised with the depression depth of 0.3 m. Thus, the storage capacity of RG is about 300 L/m^2. For the PPs, the thickness of pavements is 0.21 m (i.e., pavement (0.08 m), bedding material (0.03 m) and base material (0.1 m)). The porosities of pavement, bedding material, and base material are 5.4 %, 28.29 % and 22.66 %, respectively. This indicates that the storage capacity of PP is approximately 74 L/m^2 in this study. As mentioned in the Section 2.5.1, the GR is a special NBS which can be simulated by a specific module in Multi-Hydro

(Versini et al., 2016). In total, five parameters need to be signed to the green roofs. These parameters are substrate thinness, porosity, initial moisture condition, field capacity, and hydraulic conductivity. The selected green roof parameters for the GR scenarios used in Chapter 4 and Chapter 5 are different. In detail, for the GR1 and GR2 scenarios used in Chapter 4, the chosen configuration is as following: a substrate with a thinness (*Thick*) of 0.03 m characterised by a porosity of 39.5 %, an initial moisture condition (*IS*) of 10 %, a field capacity of 0.3, and a hydraulic conductivity of 1.2 m/h. For the third – fifth sets of GR scenarios used in Chapter 5, the GRs have *Thick* of 0.05 m, *IS* of 10 %, the porosity of 39.5 %, *FC* of 0.2, and hydraulic conductivity of 1.2 m/s. For the sixth set of GR scenarios (i.e., extensive and semi-intensive), the two types of GRs have the same porosity of 39.5 % and the hydraulic conductivity of 1.2 m/s. The *Thick* and *IS* have been mentioned previously, and the *FC* is 0.39 and 0.79, respectively. These parameters for different GR scenarios are mainly based on the experimental sites of Cerema (Ile-de-France) where several green roof configurations were monitored (see Versini et al., 2016), and the ENPC Green Wave (Champs-sur-Marne) (Stanić et al., 2019). These main properties of the GR are summarised in Table 2.12.

NBS measure	**Scenario**	**Proportion of implementation in whole catchment / selected area (after rasterization)**	**D_F of NBS in small scale/ large scale (after rasterization)**	**Description of scenario**
Permeable pavement (PP)	PP1	8.0 %/13.8 %	1.14/1.92	Permeable pavements were implemented on the non-driveways (width equal and less than 2.5 m) and some parking lots.
	PP2	8.0 %/10.1 %	1.21/1.79	Permeable pavements were implemented on secondary driveways (width between 2.5 m to 5 m).
Rain garden (RG)	RG1	8.2 %/6 %	0.93/1.77	The low elevation greenbelts around houses were implemented by rain gardens, which can collect and store up the surface runoff from surrounding impermeable areas before infiltration on site. When rain garden saturated, the redundant surface runoff will drain into the drainage system.
	RG2	8.2 %/7 %	1.04/1.78	The low elevation greenbelts around public buildings and parking lots.
Green roof (GR)	GR1	8.6 %/13.5 %	1.18/1.87	Small and light green roofs consisting of a soil layer and a storage layer are implemented on all flat roofs.
	GR2	8.6 %/6 %	1.05/1.75	Impervious roofs with slightly slope (≤ 15°) were converted to small and light green roofs (Stanić et al., 2019).

NBS measure	**Scenario**	**Proportion of implementation in whole catchment / selected area (after rasterization)**	**D_F of NBS in small scale/ large scale (after rasterization)**	**Description of scenario**
NBS combination	Combined1	24.8 %/38.5 %	1.59/1.95	A combination of PP1, RG1, GR1
	Combined2	24.8 %/30.4 %	1.45/1.98	A combination of PP2, RG2, GR2

Table 2.10: The details of simulation: the first and second sets of NBS scenarios.

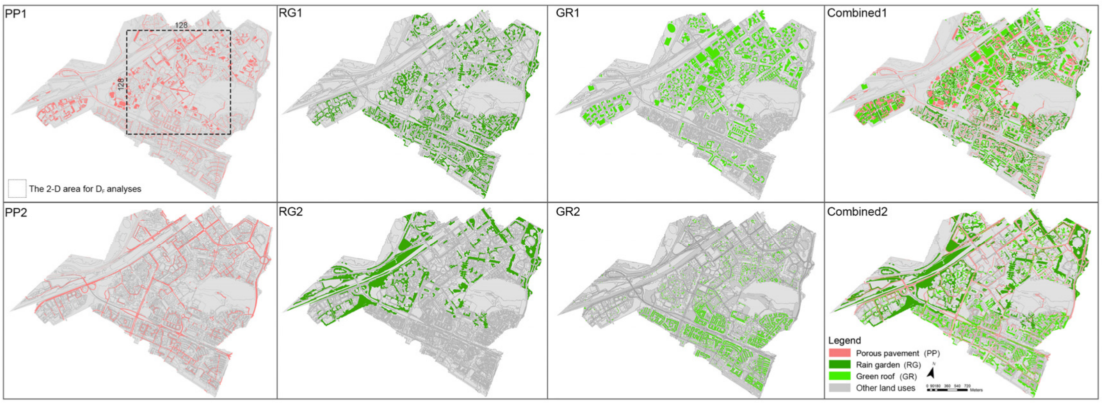

Figure 2.27: Spatial layouts of the first set and second set of NBS scenarios. The rectangular area that presented in the PP1 scenario is the example area for applying fractal analysis.

NBS types	**Scenario**	**Area (km^2)**	**D_F of NBS in small scale/ large scale (after rasterization)**	**Description of scenario**
Permeable pavement (PP)	PP3	0.147	0.42/1.6	PPs are implemented on some of non-driveways (width equal and less than 2.5 m), and some parking lots.
	PP4	0.293	0.73/1.64	
	PP5	0.440	0.9/1.68	
	PP6	0.587	1.1/1.77	PPs were implemented on all non-driveways (width equal and less than 2.5 m), and all parking lots.
Rain garden (RG)	RG3	0.108	0.24/1.54	The low elevation greenbelts around houses and public buildings are implemented by RGs.
	RG4	0.215	0.59/1.59	
	RG5	0.323	0.79/1.61	
	RG6	0.430	0.95/1.64	The low elevation greenbelts around all houses and some public buildings are implemented by RGs.
Green roof (GR)	GR3	0.119	0.42/1.53	Extensive GRs are implemented on some flat roofs and some roofs with light slope (≤15°).
	GR4	0.239	0.67/1.59	
	GR5	0.358	0.85/1.60	
	GR6	0.478	1.03/1.61	Extensive GRs are implemented on all flat roofs and some roofs with light slope (≤15°).
NBS combinations	PP6+RG6	0.802	1.26/1.78	A combination of GR4 and RG4.
	PP6+GR6	1.064	1.28/1.79	A combination of PP4 and GR4.
	RG6+GR6	0.693	1.19/1.74	A combination of RG4 and GR4.
	PP6+RG6+GR6	1.279	1.31/1.80	A combination of PP4, RG4 and GR4.

NBS types	Scenario	Area (km^2)	D_F of NBS in small scale/ large scale (after rasterization)	Description of scenario
Permeable pavement (PP)	PP (upstream)	0.183	0.99/1.47	PPs were implemented on some non-driveways, secondary roads, and parking lots that located in the upstream of the catchment.
	PP (downstream)	0.183	0.93/1.49	PPs were implemented on some non-driveways, secondary roads, and parking lots that located in the downstream of the catchment.
Rain garden (RG)	RG (upstream)	0.430	0.95/1.53	Some upstream low elevation greenbelts around public buildings were implemented by RGs.
	RG (downstream)	0.430	1.05/1.5	Some downstream low elevation greenbelts around houses and public buildings were implemented by RGs.
Green roof (GR)	GR (upstream)	0.253	1.08/1.48	Extensive GRs are implemented on the flat roofs and the roofs with slightly slope (≤15°) that located in the upstream of the catchment.
	GR (downstream)	0.253	1.0/1.53	Extensive GRs are implemented on the flat roofs and the roofs with slightly slope (≤15°) that located in the downstream of the catchment.

NBS types	**Scenario**	**Area (km^2)**	**D_F of NBS in small scale/ large scale (after rasterization)**	**Description of scenario**
NBS combinations	Combined (upstream)	0.867	1.44/1.68	A combination of PP (upstream), RG (upstream) and GR (upstream).
	Combined (downstream)	0.867	1.4/1.69	A combination of PP (downstream), RG (downstream) and GR (downstream).
Extensive green roof	Extensive GR	0.441	1.07/1.56	Extensive GRs are only implemented on some flat roofs.
Semi-intensive green roof	Semi-intensive GR	0.441	1.07/1.56	Semi-intensive GRs are only implemented on some flat roofs.

Table 2.11: The details of simulation: the third to sixth sets of NBS scenarios.

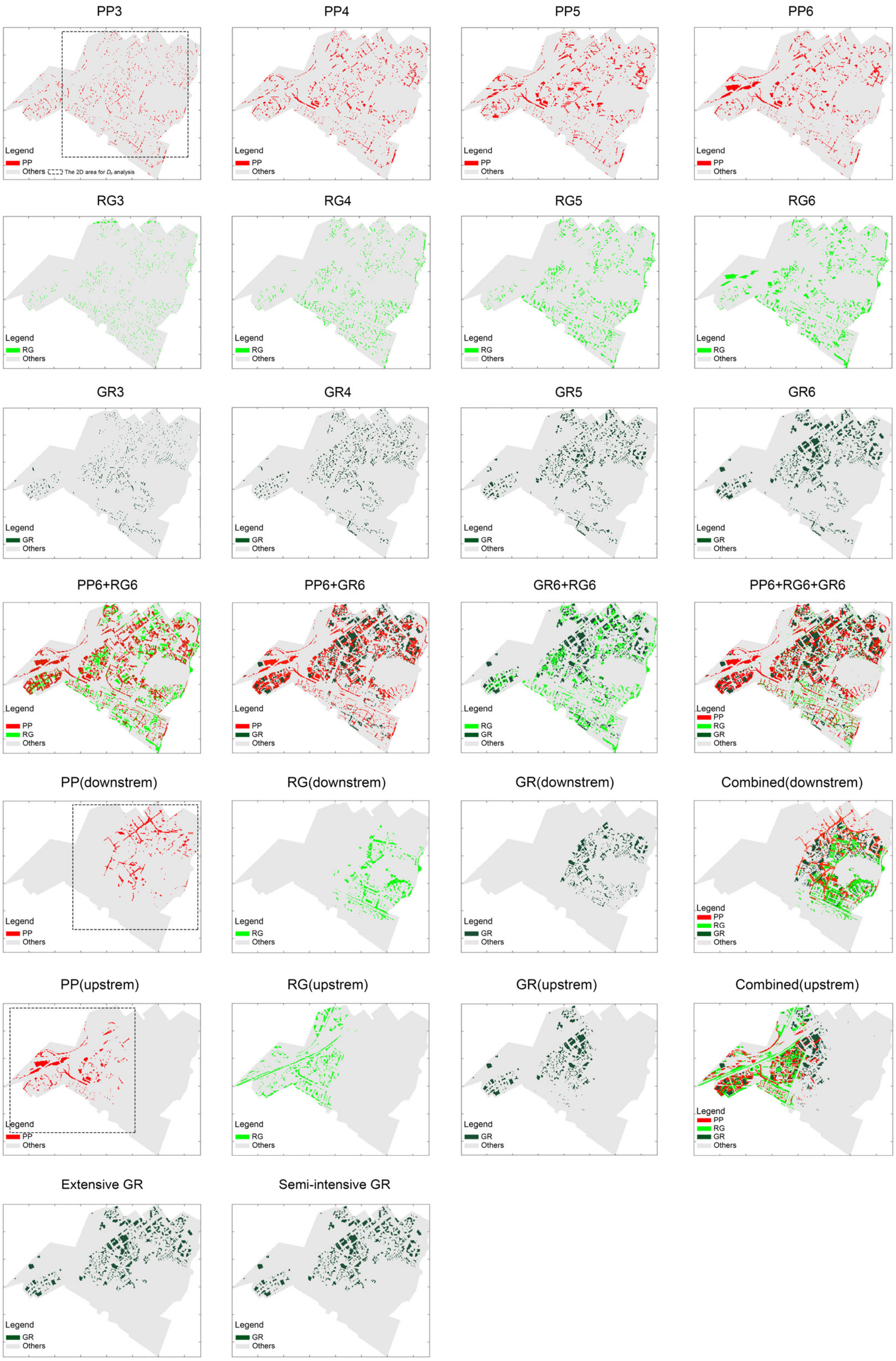

Figure 2.28: Spatial layouts of the third to sixth sets of NBS scenarios.

Scenarios	**Substrate thickness (m)**	**Initial substrate saturation**	**Porosity**	**Hydraulic conductivity (m/h)**	**Field capacity**
GR1 – GR2	0.03	10 %	0.395	1.2	0.3
GR3 – GR6 PP6+GR6 RG6+GR6 PP6+RG6+GR6 GR upstream GR downstream	0.05	10 %	0.395	1.2	0.2
Extensive GR	0.1	10 %/25 %/50 %	0.395	1.2	0.39
Semi-intensive GR	0.2	10 %/25 %/50 %	0.395	1.2	0.79

Table 2.12: The selected parameters for the first – sixth sets of GR scenarios based on the experimental sites of Cerema and ENPC green wave.

Chapter 3

Space-time variability and multifractals

The urban context, especially the rainfall, is a very complex system which can be hardly represented using a deterministic equations' system. Multifractal has been developed (Schertzer and Lovejoy, 1987; Schertzer and Lovejoy, 1989; Schertzer and Lovejoy, 1993) and widely applied to analyse and simulate geophysical fields exhibiting extreme variability over a wide range of scales, such as rainfall (Lovejoy and Schertzer, 1990; Gupta and Waymire, 1993; Fraedrich, 1993; Harris et al., 1996; Olsson and Niemczynowicz, 1996; Marsan et al., 1996; Marsch et al., 1996 ; De Lima and Grasman, 1999; Deidda, 2000; Pathirana and Herath, 2002; Biaou et al., 2003; Ferraris et al., 2003; Pathirana et al., 2003; Macor et al., 2007; Royer et al., 2008; Nykanen, 2008; De Montera et al., 2009; Langousis et al., 2009; Hoang, 2010; Tchiguirinskaia et al., 2011; Gires et al., 2013; Alves de Souza et al., 2018; Paz et al., 2018; Paz et al., 2019; Paz et al., 2020), wind turbulence (see Schertzer and Lovejoy, 2011 for review) , river flow (Tessier et al., 1996; Pandey et al., 1998), topography (Lovejoy et al., 1995; Tchiguirinskaia et al., 2000; Gagnon et al., 2006; Lovejoy and Schertzer, 2007) and soils (Tarquis et al., 2011; Aguado et al., 2014; Stanić et al., 2020; Rodríguez-Sinobas et al., 2021;). In this chapter, the theory of fractal, multifractal, and universal multifractals are presented. The multifractal framework is an appropriate approach to analyse the small scale rainfall variability in a wide range of scales. This theory is applied for analysing six rainfall events from two different types of radar data (i.e., C-band radar data and X-band radar data) in Section 3.8.2. As discussed by Schertzer and Lovejoy (1987), the coupled cascades of turbulent wind and water content are the main reason resulting in the complex structure of rainfall and clouds, and the generic output of cascade processes is multifractal. In addition, the basic characteristics of multifractal fields are in agreement with that of the precipitation. That is, more and more activities in these fields are concentrated on an increasing number of the embedding spaces with a smaller fraction. Therefore, with multifractal, the basic feature of precipitation in a wide range of scales can be quantified.

Furthermore, because one of the objectives of this thesis is to find a multi-scale resilience alternation for the future urban development, the UM framework is also applied for analysing the 2D simulated overland flow of different NBS scenarios in Section 4.3. As mentioned previously, multifractal has been widely used in different research fields. However, multifractal is more generally applied in urban hydrology, especially the questions on precipitation have been analysed by multifractal in a theoretical framework. Therefore, many questions can be taken into account with statistical physics, instead of being only analysed with different case studies. For instance, Schertzer and Lovejoy (1992) indicated that the question of extremes was related to multifractal phase transitions. Furthermore, Schertzer and Lovejoy (1987) and Schertzer and Lovejoy (1997) proposed the number of relevant parameters to stochastic universality (see Section 3.4 for discussion). Schertzer and Lovejoy (2004) investigated the forecast limitations to intrinsic predictability limits. Several recent developments of multifractal formalism can be found (Schertzer and Lovejoy, 2011; Schertzer and Tchiguirinskaia, 2015).

In Section 4.3, a scale independent singularity is proposed for evaluating the performances of NBS based on UM framework. To be more specific, the UM is initially used for investigating the potential multifractal characteristics of the 2D simulated overland flow in a semi-urban catchment under different rainfall conditions and land use scenarios. The UM parameters (intermittency C_1 and multifractality α) are used to describe the spatial variability of the 2D simulated overland flow over a wide range of scales. Furthermore, the maximum probable singularity γ_s based on the UM framework is compared with the maximum singularity γ_{max} based on the simulated overland flow at the maximum resolution of the 2D analysed field. With the comparison of the two singularities obtained by different methods, the performances of NBS can be overall grasped rely on the γ_s without focusing on a specific point. Thus, γ_s is considered to be a scale invariance indicator to evaluate the hydrological performances of NBS in terms of stormwater management and to estimate the extremes of the resilience of cities in multi-scale.

3.1 Fractal dimension

The classical geometry describes the objects with regular form. However, some objects with very irregular or fragmented shape are not able to be introduced by classical geometry, and they were named as “fractals” by Mandelbrot (1977).

The significant features of a fractal object are irregular and scale-invariant. The scale-invariant feature means that the form of a fractal object remains the same at different observation scales. Namely, a fractal object has the properties of self-similarity and self-affinity. For instance, the Cantor set (Figure 3.1a) and the Sierpinski triangle (Figure 3.1b) are two classic cases for fractal geometry.

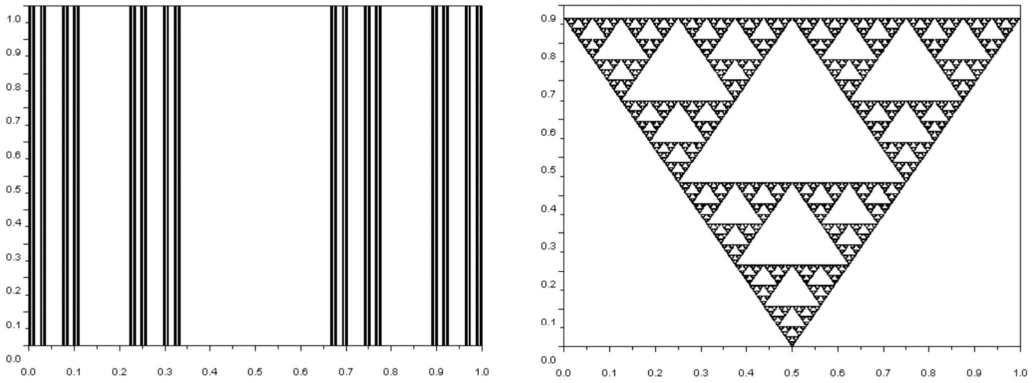

(a) (b)

Figure 3.1: (a) Cantor set; (b) Sierpinski triangle (Paz, 2018).

Regarding the classical geometry, dimensions can only be described as an integer. As shown in Figure 3.2, a regular space with straight lines (1D), planar figures (2D) or volumes (3D). Let's assume an object embedded in a Euclidian dimension with a linear size L, then it can be covered by N small objects of linear size l, with a given resolution λ $(\lambda = \frac{L}{l})$. We obtain:

$$N = \lambda^D, \ D = \frac{log(N)}{log(\lambda)} \tag{3.1}$$

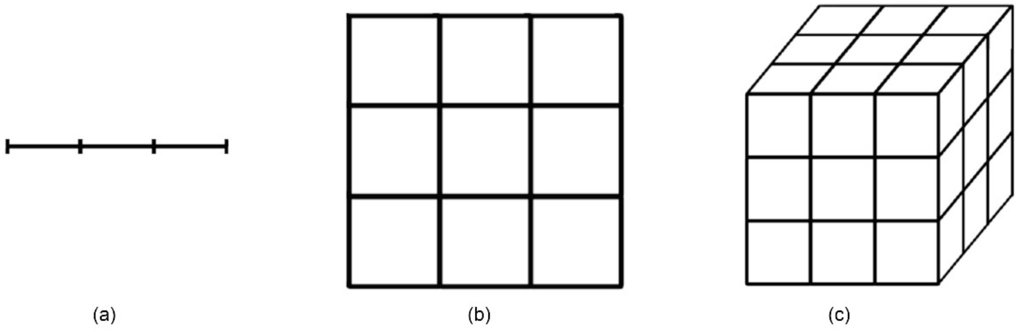

Figure 3.2: $l = L/3 \Rightarrow \lambda = 3$; (a) D = 1; (b) D = 2; (c) D = 3.

For the fractal objects or sets, their dimension is no longer adaptable by an integer, and Mandelbrot (1977) introduced it as the fractal dimension (D_F) (Mandelbrot and Pignoni, 1983; Falconer, 1988; Hastings and Sugihara, 1993; Feder, 2013; Barnsley, 2014). D_F has been often used in meteorology, hydrology and geology (e.g. Schertzer and 220 Lovejoy, 1984; Fraedrich, 1986; Schertzer and Lovejoy, 1987; Schertzer and Lovejoy, 1991; Lavallée et al., 1993; Tarquis et al., 2007; Tarquis et al., 2008; Gires et al., 2013; Gires et al., 2017; Ichiba et al., 2017; Paz et al., 2020; Versini et al., 2020; Rivas-Tabares et al., 2020). To compute the D_F, a theoretical approach is to compute the Hausdorff dimension, which is rather complex. However, the box-counting method is an easier way to compute the D_F, which was widely applied (Hentschel and Procaccia, 1983; Lovejoy et al., 1987; Schertzer and Lovejoy, 1987; Hubert and Carbonnel, 1989).

In practice, it assumes that there is a power-law relation between the fractal dimension and the number of “non-empty” pixels of the set (N_λ) at the resolution λ:

$$N_\lambda \approx \lambda^{D_F} \tag{3.2}$$

where the exponent D_F is the fractal dimension, the symbol $\approx$ means an asymptotic relation (i.e. for large resolution λ and possibly up to a proportionality prefactor).

When N_λ and λ are plotted in a log-log plot, the fractal dimension D_F can be defined as follows:

$$D_F \approx \frac{ln(N_\lambda)}{ln\,\lambda} \tag{3.3}$$

The application of the box-counting method on the different land use scenarios (i.e., the baseline and NBS) is presented in the following section.

3.1.1 Fractal dimension of NBS scenarios

To quantify the multi-scale space heterogeneity of NBS in each NBS scenario, the concept of fractal dimension (D_F) is applied.

Because the spatial distributions of NBS in each set of NBS scenario are heterogeneous, for adapting different modelling experiments, the size of selected area for computing the fractal dimension of the first and second sets of NBS scenarios is different from the third – sixth sets of NBS scenarios. For the first and second set of NBS scenarios, a square area of 128 x 128 pixels was extracted from the catchment to make the fractal analysis (see the example of the PP1 scenario in Figure 2.27).

As shown in Figure 3.3, all the NBS scenarios are presented with two scaling behaviour regimes, with a scale break roughly at 80 m. For each regime, the scaling is robust, with linear regression coefficients (R^2) around 0.99. For the first regime corresponding to the small scale range (10 m

– 80 m) that related to the assets spatial distributions, the dimension D_F is around 1 for most of NBS scenarios. It is in contrast with the second regime, the large scale range (from 80 m to 1280 m) that exhibits a scaling behaviour with a D_F ranging from about 1.75 to 1.98. The fractal analysis is also applied on the impervious surface of the baseline scenario in the same selected area, and the same scale break at 80 m (the D_F of the baseline scenario in each regime are presented in Figure 3.3) was found. Therefore, it rather confirms that the spatial distribution of NBS is strongly constrained by the urbanisation level of the catchment.

The D_F of first and second sets of NBS scenarios is summarised in Table 2.10. The D_F measures the implementation level of NBS across scales. For instance, the D_F (large scale) of the two combined scenarios (Combined1 and Combined2) is close to 2, showing that NBS are rather homogeneously distributed. However, it is important to notice that, in spite of initially identical percentage at a given scale of the NBS implementation over the catchment, the resulting D_F could be quite different. It is simply because the percentage of the space is a scale dependent quantity, while D_F quantifies the propagation of the spatial heterogeneity for each of NBS scenarios, from the smallest scale to the outer scale of the catchment. This propagation remains scenario dependent and hence a subject to its optimisation.

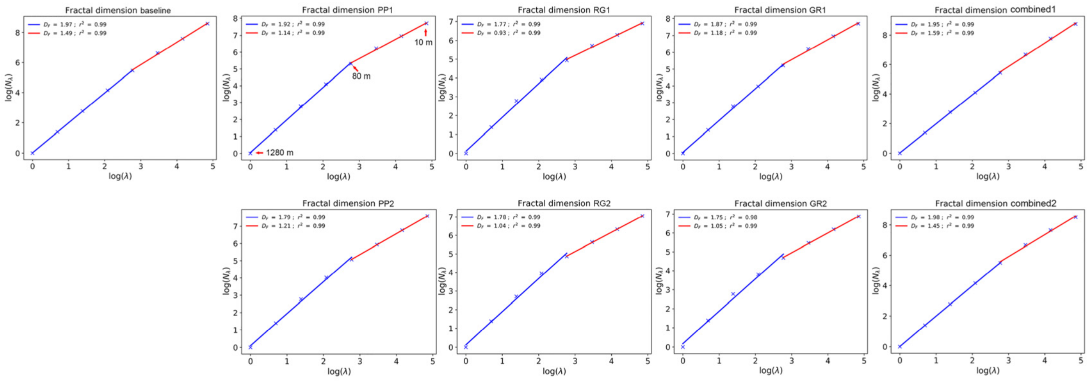

Figure 3.3: The fractal dimension of impervious surface of the baseline scenario and the fractal dimension of the first and second sets of NBS scenarios.

For the third - sixth sets of NBS scenarios, a square area of 256 x 256 pixels was extracted from the catchment to make the fractal analysis (see the example of the PP3 scenario in Figure 2.28) Here, for the fifth set of NBS scenario, the location of the selected square is slightly different from the other set of NBS scenarios because of the specific spatial layout of the NBS (see the example of the PP upstream and PP downstream scenario in Figure 2.28).

The D_F of the four sets of NBS scenario are summarised in Table 2.11, and the corresponding figures are shown in Figure 3.4. All the NBS scenarios are characterised with two scaling behaviour regimes, with a scale break roughly at 40 m. For each regime, the scaling is robust, with a linear regression coefficients (R^2) around 0.99. For the first regime corresponding to the small scale range (10 m – 40 m, presented in the red line in Figure 3.4) related to the intrinsic 2D size and the spatial distributions of the NBS, it represents that the NBS performed on the selected areas (i.e., roads, roofs and low-elevation green belts) with size range between 100 m^2 to 1600 m^2. In this observation scale, for the third set of NBS scenario, the D_F of the four PP scenarios (i.e., PP3, PP4, PP5, and PP6) range from 0.42 to 1.05. Similarly, the D_F of the four of RG scenarios range from 0.24 to 0.95, and the D_F of the four GR scenarios range from 0.42 to 1.03. For the fourth set of NBS scenarios (four combined scenarios), the D_F range from 1.19 (RG6+GR6 scenario) to 1.31 (PP6+RG6+GR6 scenario). Concerning the fifth set of NBS scenario, the D_F is around 1.4 for the combined upstream and downstream scenarios, and the D_F is about 1 for the other NBS scenarios.

Regarding the large scale range (from 40 m to 2560 m), it typically presents the implementation levels of NBS in the catchment. Generally, it noticed that the D_F of all NBS scenarios in this range of scales tends to 2 (the dimension of the 2D studied space). However, as the NBS are embedded in the environmental context that containing other types of land use (e.g. parking, water, green space), it exhibits a scaling behaviour with the D_F less than 2 for all NBS scenarios. For instance, the D_F (large scale range) of the third set of NBS scenarios range from 1.5 to 1.7, which means the spaces are gradually filled by NBS in this observation scale.

Overall, it is noticed that the D_F of NBS scenarios in small scale range and large scale range increases with increasing the proportion of the NBS implementation in the catchment, which presents that the D_F can reflect the implementation level of NBS over a wide range of scales. Indeed, such scale-invariance indicator contains the information across scales and represents the spatial layout of NBS in the catchment, while the initial percentage that defined at the maximum resolution is not able to present the heterogynous spatial distribution of NBS explicitly.

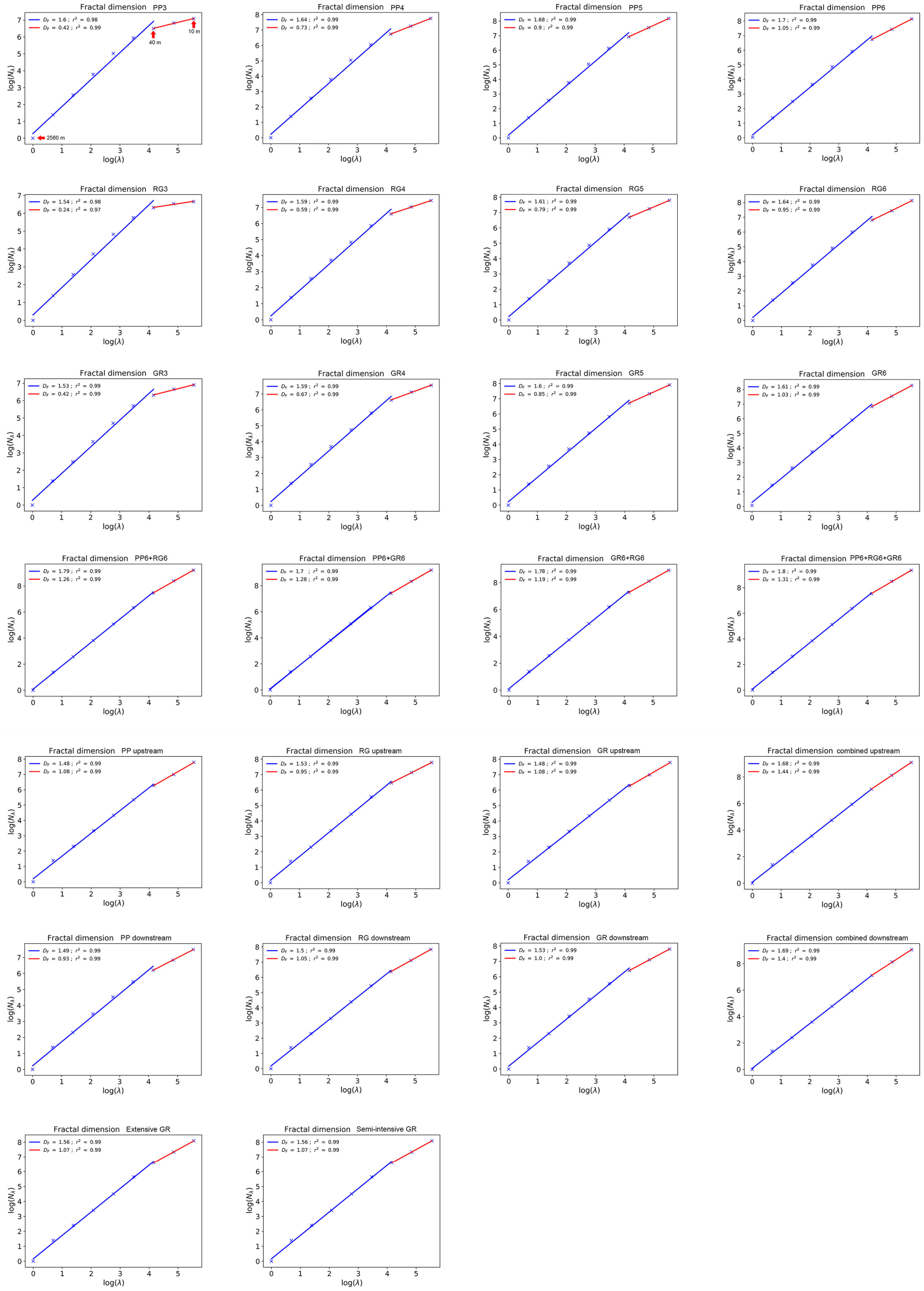

Figure 3.4: Fractal dimension of the third – sixth sets of NBS scenarios (the red line is corresponding to the small scale range, and the blue line is corresponding to the large scale range).

3.2 Codimension

Several researchers used the concept of codimension to address the fractal behaviour of random sets (Mandelbrot 1967, 1977; Mandelbrot and Pignoni, 1983; Schertzer and Lovejoy, 1987, 1989; Falconer, 1988; Feder, 2013; Barnsley, 2014).

The codimension c is defined with the following equation:

$$c = D - D_F \tag{3.4}$$

where D is the Euclidean dimension, and D_F is the fractal dimension defined previously.

Based on Eq. 3.2, we obtain:

$$N_\lambda(A) \approx \lambda^{D_F(A)} \tag{3.5}$$

Therefore, the fractal codimension can be probabilistically defined based on Eq. 3.5, where the probability of a cube embedded in the Euclidean space R^D at the resolution λ is contained in the fractal set A, which is expressed as follows:

$$\frac{N_\lambda(A)}{N_\lambda} \approx \lambda^{D_F(A)-D} = \lambda^{-c} \tag{3.6}$$

As indicated by Schertzer et al. (2002a), the codimension can be more general for random multifractal fields, which enables $c > D$, and imply $D_F < 0$ based on Eq. 3.4.

3.3 Multifractal intersection theorem

Tchiguirinskaia et al. (2004) applied multifractal intersection theorem to the intersection of a rainfall with extreme space variability and a rain gauge network that provides quantitative estimates of this intersection. Figure 3.5, adapted from this paper, schematically represents the intersection at a given time of a (multifractal) rainfall, displaying quite variable pixel intensities ranging from light blue to dark brown (e.g. from 1 to 100 mm/h), with a heterogeneous rain gauge network (light brown pixels). The resulting measured rainfall field M is simply the product of the rainfall intensities R by the gauge characteristic function N (=1 if there is a gauge in this pixel, 0 otherwise). The intersection theorem states that for fractal objects, like for the usual (Euclidean) geometric ones, the codimension – i.e. the complement $c_M = d - D_M$ of the dimension D_M to the embedding space dimension d – of the measured field above a given intensity threshold is the sum of the codimensions of the network ($c_N = d - D_N$) and of the "real" field ($c_R = d - D_R$) above the same intensity threshold:

$$c_M = c_N + c_R \Leftrightarrow D_M = D_N + D_R - d \tag{3.7}$$

For instance, the intersection in a plane ($d = 2$) of two straight lines ($D_N = D_R = 1;\ c_N = c_R = 1$) corresponds to a point ($c_M = 2,\ D_M = 0$). Of particular interest is the case where the intersection is small that its codimension c_M is larger than the embedding dimension d, i.e. has a negative dimension D_M (Schertzer and Lovejoy, 1987). Due to Eq. 3.7, the codimension of the network c_N is thus the critical dimension of the (real) field under which the rainfall intensity is rarely measured by the network:

$$c_M > \mathrm{d} \Leftrightarrow D_M < 0 \Leftrightarrow D_R < c_N = d - D_N \tag{3.8}$$

More precisely, the smaller D_R is with respect to c_N, the lesser the real field R is measured. Let us mention that Paz et al., (2020) used this intersection theorem to determine when the adjustment of radar data by a rain gauge network becomes misleading instead of improving the data.

The assessment of the performance of an NBS network cannot be reduced to the binary question of presence or not of an NBS, like done for a rain gauge of a network. However, it is possible immediately state they will be more and more ineffective for rainfall intensity whose fractal dimension is more and more below the codimension c_N of the network. This is already an important information that can be used to design NBS and their networks. This also explains why in the previous subsection the fractal (co-) dimension of the NBS network was estimated, as well as the simulations resulting from spatially uniform rainfalls ($D_R = d,\ c_R = 0$) and spatially heterogeneous rainfalls ($D_R < d,\ c_R > 0$) are compare in Section 4.1.

Indeed, this theorem indicated why it is so much indispensable to take into account the multi-scale space variability of both the rainfall and the NBS distribution. For instance, both “hot spots” (extremes) of the rainfall and NBS are scarce and therefore could rarely coincide, i.e., rainfall spikes may fall more often elsewhere than on NBS. Similar questions can occur for less extreme events. The effective NBS performance could be therefore biased with respect to their potential performance due to this problem of intersection between rainfall intensity and NBS.

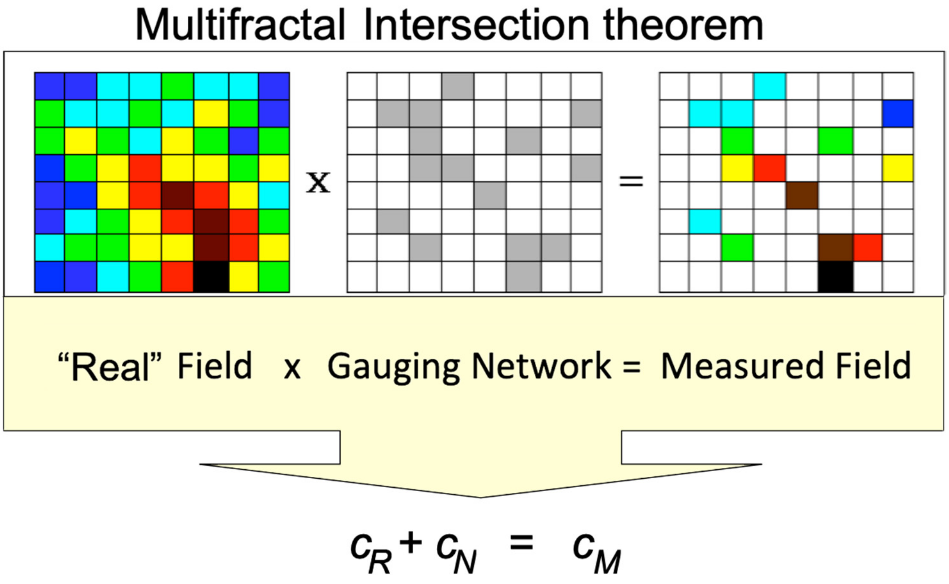

Figure 3.5: Schematic of the (multifractal) intersection theorem applied to the measured rainfall M by a rain gauge network N. The measured rainfall corresponds to the product of the "real" rainfall R by the gauge characteristic function (=1 if there is a gauge in this pixel, 0 otherwise) and the corresponding codimensions $\boldsymbol{c_R = d - D_R}$ and $\boldsymbol{c_N = d - D_N}$ add to yield the codimension of the measured rainfall $\boldsymbol{c_M = d - D_M}$. d is the embedding space dimension, D_R, D_N and D_M are the corresponding fractal dimensions (adapted from Tchiguirinskaia et al., 2004).

3.4 Universal Multifractals

The geophysical fields with different levels of intensity, irregular geometries and scale invariance, can be considered as fractal fields at different thresholds (singularities). Namely, it is possible to compute the fractal dimension in terms of each singularity (Schertzer and Lovejoy, 1984a). Based on the imposed threshold, the fields can be characterised by several fractal dimensions, and these fields are called "multifractals" by Parisi and Frisch (1985).

As mentioned, the fractal fields can be characterised by a hierarchy of fractal dimensions and codimensions. According to the concept of fractal codimension, for a given field ε_λ at a given resolution of λ, we can obtain the probability of a singularity of the order greater than or equal to γ:

$$Pr(\varepsilon_\lambda \geq \lambda^\gamma) = \frac{N_\lambda(\varepsilon_\lambda \geq \lambda^\gamma)}{N_\lambda} = \frac{\lambda^{D_F(\gamma)}}{\lambda^D} \tag{3.9}$$

where D is the domain dimension, $N_\lambda(\varepsilon_\lambda \geq \lambda^\gamma)$ is the number of boxes of size λ^{-1}

characterised by a singularity of order greater than or equal to γ, and N_λ is the total number of boxes, which must cover the whole space.

Based on Eq. 3.4, we can obtain:

$$D = D_F(\gamma) + c(\gamma) \tag{3.10}$$

Then:

$$Pr(\varepsilon_\lambda \geq \lambda^\gamma) \approx \lambda^{-c(\gamma)} \tag{3.11}$$

where γ is the singularity of scale invariant, and $c(\gamma)$ is the co-dimension function which is convex and increases with no superior limit.

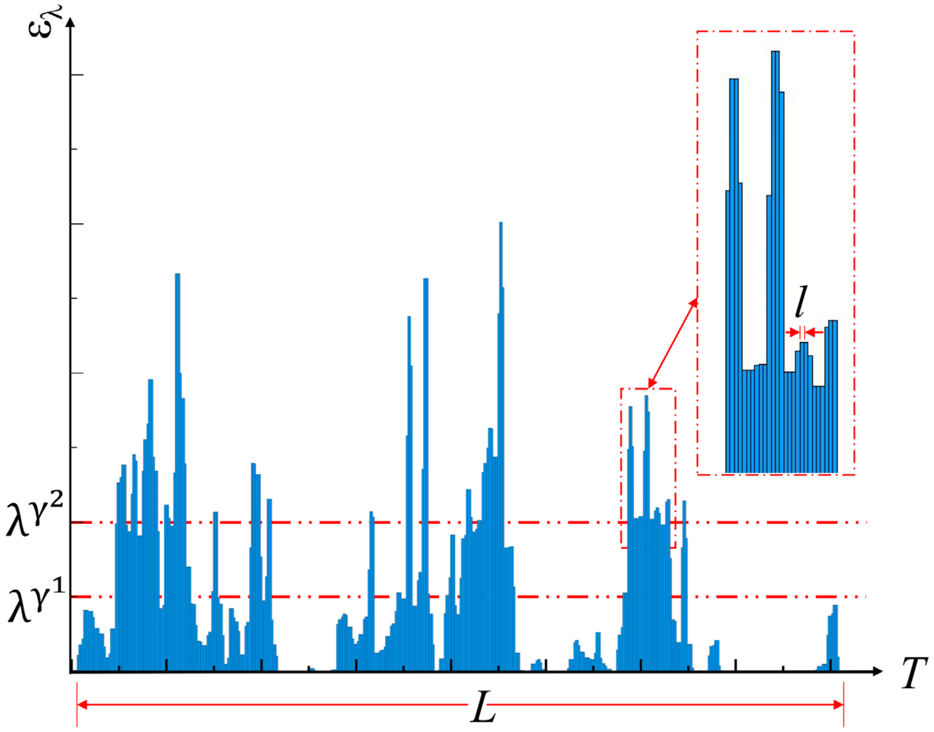

Figure 3.6: An example of 1 D (time series) multifractal field.

With respect to the Universal Multifractal framework (Schertzer and Lovejoy, 1987; Schertzer and Lovejoy, 1997), a pair of UM parameters can be used to express $c(\gamma)$: (i) the mean intermittency C_1; (ii) the multifractality α. If the field is conservative, $c(\gamma)$ can be obtained as follows:

$$c(\gamma) = \begin{cases} \frac{C_1}{\alpha-1}\left(\frac{\gamma}{C_1\alpha'}+\frac{1}{\alpha}\right)^{\alpha'} & \alpha \neq 1 \\ C_1 e^{\left(\frac{\gamma}{C_1}-1\right)} & \alpha = 1 \end{cases} \tag{3.12}$$

where $\frac{1}{\alpha'}+\frac{1}{\alpha}=1.$

In addition, another equivalent approach to describe the statistical properties of the multifractal field was proposed by Schertzer and Lovejoy (1987), which is based on the scaling of the statistical moments of order q:

$$\langle \varepsilon_\lambda^q \rangle \approx \lambda^{K(q)} \tag{3.13}$$

where $\langle \varepsilon_\lambda^q \rangle$ is the average statistical moment of order q, and $K(q)$ is the scaling moment function which is convex. The $K(q)$ function can be expressed with UM parameters in terms of the following equations:

$$K(q) = \begin{cases} \frac{C_1}{\alpha-1}(q^\alpha - q) & \alpha \neq 1 \\ C_1 q log(q) & \alpha = 1 \end{cases} \tag{3.14}$$

The Legendre transform (Parisi and Frisch, 1985) linked the functions of $K(q)$ and $c(\gamma)$, which means each singularity γ has a corresponding statistical order q, and vice versa (see Figure 3.7 for an illustration).

The equations are expressed as following:

$$c(\gamma) = max_q\big(q\gamma - K(q)\big) = q_\gamma\gamma - K(q_\gamma) \tag{3.15}$$

$$K(q) = max_\gamma\big(q\gamma - C(\gamma)\big) = q\gamma_q - c(\gamma_q) \tag{3.16}$$

The $K(q)$ function is widely applied for determining the C_1 and α, because its characteristic can be used for estimating UM parameters by different techniques (i.e., Trace Moment and Double Trace Moment). These techniques will be briefly introduced in Section 3.8. Regarding a single value of C_1, it can be calculated by the first derivative of Eq. 3.14 at $q = 1$:

$$\frac{dK(q)}{dq}|_{q=1} = C_1 \tag{3.17}$$

On the other hand, if only the value C_1 changes, the second derivative of Eq. 3.14 at $q = 1$ can be calculated by Eq. 3.18:

$$\frac{d^2K(q)}{dq^2}|_{q=1} = \alpha C_1 \tag{3.18}$$

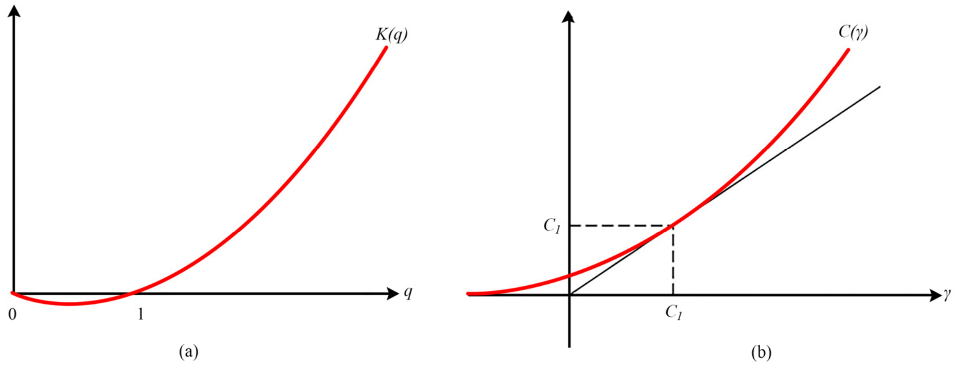

Figure 3.7: Statistical functions: (a) $K(q)$ and (b) $c(\gamma)$.

3.5 Critical values

Theoretical $K(q)$ function Eq. 3.14 is valid until to the certain critical value of moment order q_c. This critical value is linked with multifractal phase transition (Schertzer et al., 1993), and it can be estimated as $q_s = \min(q_s, q_D)$, where q_s is the maximal order moment estimated with a finite number of samples N_s, and q_D is the critical moment order of divergence. The value of q_s is linked with the maximal observable singularity γ_s by Legendre transform, and it can be calculated as follows:

$$q_s = \left(\frac{D+D_s}{C_1}\right)^{1/\alpha} \tag{3.19}$$

If the $D = 1$ (one-dimensional field), and $N_s = 1$, then, $D_s = 0$. The critical value of moment order is usually $q_c = q_s$. Thus, for $q \geq q_s$, a linear behaviour of empirical $K(q)$ can be obtained.

The moment order q_D represents the critical value of q at which extreme values of the field become dominant, thus the average statistical moment of order $q \geq q_D$ approaches to infinity:

$$\langle {\varepsilon_\lambda}^q \rangle = \infty, \; q \geq q_D \tag{3.20}$$

Moment order q_D can be determined with the following equation

$$K(q_D) = (q_D - 1)D \tag{3.21}$$

q_D represents the point where Eq. 3.14 intersects the linear regression $K(q) = (q\text{-}1)\,D$ obtained with Eq. 3.14 at $\alpha = 0$ and $C_1 = D$. If $q_c = q_D$, the empirical $K(q)$ function will quickly approaching infinity for $q > q_D$.

By increasing N_s, the value of q_s increases, thus, Eq. 3.14 is validated in a larger range of q. Therefore, the theoretical framework enables to simulate the studied field more accurately.

3.6 Physical meaning of UM parameters

According to the framework of Universal Multifractal proposed by Schertzer and Lovejoy (1987), three common exponents (α, C_1, and H) can be used to describe the multifractal field. With respect to the main characteristics of the function of $c(\gamma)$ and $K(q)$, the physical meaning of UM parameters is described as follows:

- *Multifractality index* α ($0 \leq \alpha \leq 2$), describes the deviation from the mean value of the field. A log-normal field corresponds to the highest variability ($\alpha = 2$), while the monofractal field secures no variability ($\alpha = 0$). See more details in Schertzer and Lovejoy (1992).

- *Mean intermittency* C_1, which measures how much sparseness varies with the change of the mean value of the field. $C_1 = 0$ means that the field is homogeneous. On the contrary, a higher value of C_1 provides a much smoother $c(\gamma)$, which is able to present higher extreme. In the case of $C_1 = D$, it presents the mean value is too sparse to be observed, resulting in $Pr(\varepsilon_\lambda \geq \lambda^{C_1}) = 0$. Therefore, the value of C_1 ranges between 0 and D.

- *Hurst's exponent* H, which measures the degree of non-conservation of the field. If the field is conservative, $H = 0$. If $H \neq 0$, it means the field is non-conservative. The value of H can be obtained with the slope of the energy spectrum of the studied field (more details about the spectral analysis can be found in Section 3.8.1).

To demonstrate the impact of a multifractality index α on the shape of statistical functions $K(q)$ and $c(\gamma)$ (see Figure 3.7), Eqs. 3.12 and 3.14 could be renormalized by the mean intermittency C_1. Next, Figures 3.8 and 3.9 show renormalized scaling functions, where each curve corresponds to the function of a unique parameter α. Such renormalisation will be used later in Section 4.3 to define an indicator of the percentage change in morphological variability.

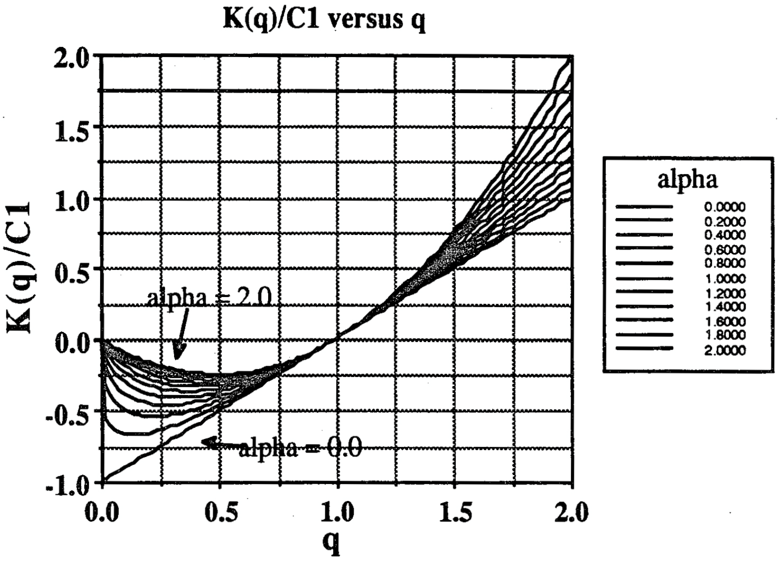

Figure 3.8: Universal $K(q)/C_1$ versus q, for different α=0 to 2 by increment $\Delta\alpha$=2 (adapted from Schertzer and Lovejoy, 1993).

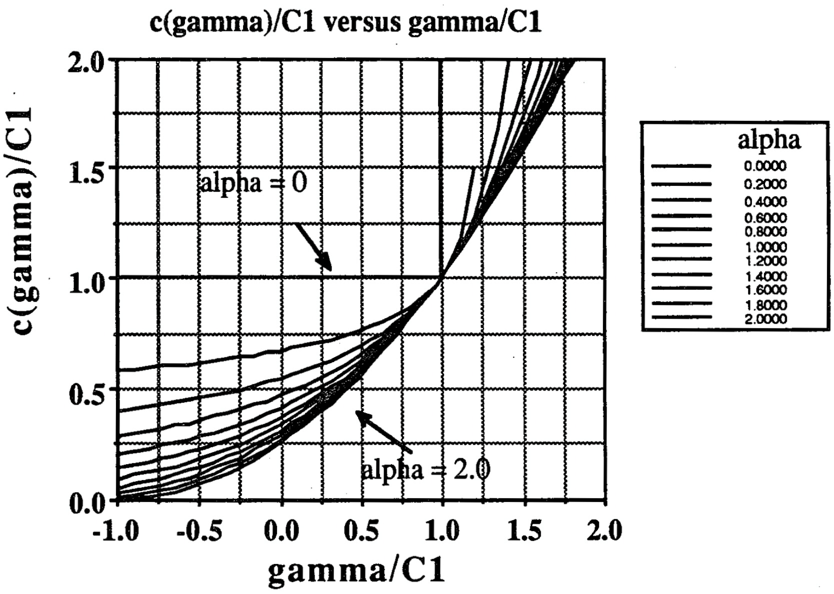

Figure 3.9: Universal $c(\gamma)/C_1$ versus γ/C_1, for different α=0 to 2 by increment $\Delta\alpha$=2 (adapted from Schertzer and Lovejoy, 1993).

3.7 Maximum probable singularity and Maximum singularity

To analyse the spatial variability of overland flow across scales over the whole catchment (i.e., the third set of modelling experiments studied in Section 4.3), the UM theoretical framework is applied (Scherzter and Lovejoy, 1987; Schertzer and Lovejoy, 1997). As mentioned before, for UM, the function of $K(q)$ and $c(\gamma)$ are defined by α and C_1. Great values of α and C_1 correspondingly to strong extremes. A general method for assessing the extremes of a field is to use the scale-independent indicator of maximum probable singularity γ_s (Hubert and Carbonnel, 1989; Douglas and Barros, 2003; Royer et al., 2008; Tchiguirinskaia et al., 2011; Gires et al., 2018).

To assess the extremes of a field (i.e., great values of α and C_1), the main properties of $c(\gamma_s)$ need to be introduced. For a unique sample, $c(\gamma_s)$ can be expressed as:

$$c(\gamma_s) = D \tag{3.22}$$

where D is the dimension of embedding space (in this study D =2).

An intrinsic characteristic of the maximum probable singularity is its scale-independence, while we intend to use it to describe overland flow maxima that are scale-dependent. To bridge this gap, we first define a multi-scale overland flow H_λ (as before the resolution $\lambda = \frac{L}{l}$ is the ratio of the involved scales), normalised by the mean overland flow $\langle H_\Lambda \rangle$ at its highest resolution Λ, as follows:

$$\frac{H_\lambda}{\langle H_\Lambda \rangle} = \lambda^\gamma \tag{3.23}$$

Then for the multifractal fields defined by the parameters α and C_1, one can expect that:

$$\max\{\mathrm{H}_\lambda\} \propto \lambda^{\gamma_s} \tag{3.24}$$

where, by combining Eqs. 3.12 and 3.22, the maximum probable singularity γ_s can be easily calculated with the following equation:

$$\gamma_s = \frac{\alpha}{\alpha-1} C_1 \left(\frac{D}{C_1}\right)^{\frac{\alpha-1}{\alpha}} - \frac{C_1}{\alpha-1} \tag{3.25}$$

Applying the idea of renormalisation by C_1 as presented in Section 3.6, the definition of the maximum probable singularity can be also re-written in its renormalized form:

$$D/C_1 = \left(\frac{\alpha-1}{\alpha}\left(\frac{\gamma_s}{C_1}\right) + \frac{1}{\alpha}\right)^{\frac{\alpha}{\alpha-1}} \tag{3.26}$$

where for a fixed pare (γ_s/C_1, D/C_1), there is a unique value of the multifractality index α that satisfies this equation.

To investigate whether the semi-theoretical γ_s can infer extremes of the spatial distribution of overland flow at the smallest modelled scale, the effective maximum singularity γ_{max} is obtained from the maximum value and mean value of the 2D simulated overland flow, at each time step t. In practice, we define the ratio of the largest overland flow value over a pixel at the highest resolution Λ (H_{max}, m) to the instant mean value of the overland flow (H_{mean}, m). Therefore, the γ_{max} can be determined as follows:

$$\gamma_{max}(t) = log_{\Lambda}\left(\frac{H_{max}(t)}{H_{mean}(t)}\right) \tag{3.27}$$

As already mentioned in Section 3.1, the highest spatial resolution of the investigated field is $\Lambda = 128$ for the study of Section 4.3. The explicit notation of time dependency, defining the effective maximum singularity (Eq. 3.27), will be omitted in what follows by simply referring to γ_{max}.

3.8 Techniques of multifractal analysis

To estimate the parameters α and C_1, two techniques can be used: Trace Moment (TM) and Double Trace Moment (DTM). The application of these two techniques on rainfall data analysis can be found in Section 3.8.2.

The TM technique is based on the scaling behaviour of average statistical moments of order q. The TM technique is based on Eq. 3.14, and the investigated field needs to be conservative. To apply the TM technique, the first step is to normalize to unity a studied field ε'_λ with the following equation:

$$\varepsilon_\lambda = \frac{\varepsilon'_\lambda}{\langle \varepsilon'_\lambda \rangle} \Longrightarrow \langle \varepsilon_\lambda \rangle = 1 \tag{3.28}$$

The field is up scaled by averaging n ($n = 2$ for 1-D field, $n = 4$ for 2-D field) neighbour values. The field is raised on the power q at each resolution λ. Then, λ gradually decreases to 1 (a uniform field). The average statistical moment of the field at a given order q is calculated as follows:

$$\langle {\varepsilon_\lambda}^q \rangle = \frac{\sum_1^\lambda {\varepsilon_\lambda}^q}{\lambda^D} \tag{3.29}$$

where D =1 corresponds to the one-dimensional field, and D = 2 for the two-dimensional field. Each $\langle {\varepsilon_\lambda}^q \rangle$ has a corresponding λ with different q values. If the graph is plotted in a log-log scale, $\langle {\varepsilon_\lambda}^q \rangle$ should follow a linear regression at each q value. The slopes of the linear regressions correspond to $K(q)$ values, therefore, the empirical $K(q)$ function can be obtained with different $K(q)$ values at the corresponding q. Finally, the α and C_1 can be calculated with the first and second derivatives of the empirical $K(q)$ function at $q = 1$ (Eqs. 3.17 and 3.18).

For applying the technique of Double Trace Moment (DTM), it also needs to first assume that the studied field is conservative. (Lavallée et al., 1993; Schmitt et al., 1994). Similar to the TM technique, the first step using the DTM technique is to renormalize the original field based on Eq. 3.28. DTM technique is able to directly estimate α and C_1 with Eq. 3.14, which considers that the average statistical moment $\langle \varepsilon_\lambda^{(\eta)q} \rangle$ is in correlation with λ:

$$\langle \varepsilon_\lambda^{(\eta)q} \rangle \approx \lambda^{K(q,\eta)} = \lambda^{\eta^\alpha K(q)} \tag{3.30}$$

Then, we can obtain:

$$K\ (q,\eta) = K\ (\eta q) - qK(\eta) \tag{3.31}$$

Therefore, the slope of the linear section of the log-log plot in terms of $K(q, \eta)$ and η is used for estimating α. C_1 can be estimated by $K(q,1)$, representing the intersection of the slope at $\log(\eta) = 0$. More applications of TM and DTM techniques on the rainfall data can be found in Section 3.8.2.

3.8.1 Spectral analysis

In this section, the main objective is to quantitatively compare the C-band and X-band radar data. Hence, the Universal Multifractal framework was applied to analyse the temporal evolutions of the rainfall rates of all available C-band and X-band radar products (i.e., by spatially averaging the rainfall rate over the whole studied catchment at each time step) for six selected events.

Multifractal comparison of C-band and X-band radar data

Before directly applying the TM and DTM analysis, the first step is to check the scaling behaviour of the data. In general, if the analysed field is scaling, its power spectra E exhibits a power-law relation in terms of the wave number k (Scherzter and Lovejoy, 1985a; Lovejoy and Schertzer, 1995):

$$E(k) \approx k^{-\beta} \tag{3.32}$$

where β is the exponent of spectral.

When Eq. 3.32 is plotted in a log-log scale, a straight line can be obtained (see Figure 3.10 for an example). The β is linked to the Hurst's exponent (H), which can be approximated by the following equation:

$$\beta = 1 - K(2) + 2H \tag{3.33}$$

where K is the second moment scaling function of the conservative part of the field.

Lovejoy and Scherter (2013) indicated for a D-dimensional field, Eq. 3.33 can be expressed as:

$$\beta = D - K(2) + 2H \tag{3.34}$$

Indeed, regarding a conservative field, the value of β should be less than the dimension D of the embedding field ($D = 1$ for temporal analysis, and $D = 2$ for spatial analysis). If $\beta > D$, the field needs to be differentiated before directly applying TM and DTM analysis, in order to assumes the field is conservative (Nykanen, 2008). Here, the spectral analysis is applied for the temporal evolution of rainfall rate of each rainfall product for six rainfall events (1-D time series). It was noticed that the values of β of the original series are larger than D. Hence, for obtaining a conservative field, one of the simplest methods (Lavalée et al., 1993) is to take the absolute value of the fluctuations of the field at the maximum resolution.

Accordingly, the conservative proxies of rainfall time series were obtained by $|\Delta R(t)| = |R(t_{i+1}) - R(t_i)|$ priory to performing the 1D spectral analysis, and the corresponding values of β are summarised in Table 3.1.

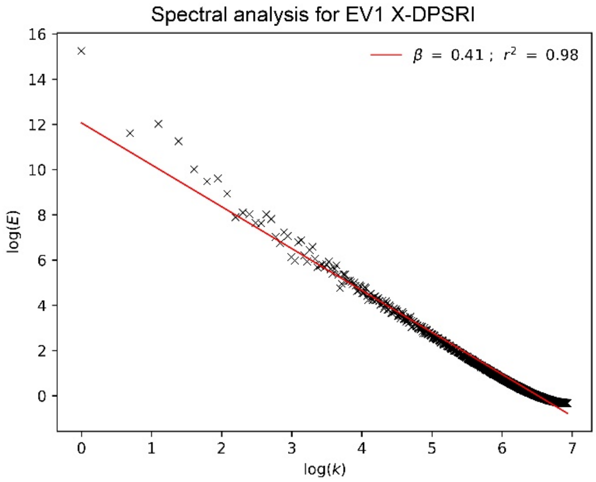

Figure 3.10: An example of spectral analysis for the EV1 of X-band DPSRI data.

Rainfall data	**EV1**	**EV2**	**EV3**	**EV4**	**EV5**	**EV6**
C- CALAMAR	0.1	0.16	0.15	0.27	0.13	0.14
C-ZPHI	N/A	N/A	N/A	0.12	0.13	0.27
C-MeteoGroup	N/A	N/A	N/A	0.33	0.08	0.15
X-SRI	N/A	N/A	N/A	0.57	0.64	0.37
X-DPSRI	0.41	0.53	0.64	0.75	0.69	0.42
X-SRIMP	N/A	N/A	N/A	N/A	N/A	0.46

Table 3.1: The β values of the six selected rainfall events and all the rainfall data from C-band radar and X-band radar.

3.8.2 Trace Moment (TM) and Double Trace Moment (DTM)

In this section, the techniques of TM and DTM are used to analyse all the available rainfall data (1D time series) in the full range of scales (without scaling break) (see Figures 3.11, 3.12, 3.13, 3.14, 3.15, 3.16, 3.17, and 3.18). Regarding the TM analysis, a clear scaling break can be found for several rainfall products, especially for the C-band rainfall products (e.g. EV2 of CALAMAR). However, for the DTM analysis, the scaling behaviour can be found in full range of scales without a clear break for all the rainfall products and rainfall events. The values of UM parameters (C_1 and α) estimated based on these two methods are plotted in Figure 3.19 and summarised in Tables 3.2, 3.3, 3.4 and 3.5. As shown in Figure 3.19, the multifractality (α) estimated by TM and DTM is lower than 1.2 for all rainfall events. Regarding the SRI product for EV5, the values of α are highest (1.18 for TM analysis, and 1.03 for DTM analysis). Comparing the values of α of C-band radar products and X-band radar products of each rainfall event, the values for the former are relatively lower.

Furthermore, the mean value of α of each rainfall product estimated by TM and DTM technique is lower than 0.8 for all rainfall events, which presents that the multifractality of these rainfall events is relatively weak. For the TM analysis, the lower mean value of α was obtained for the EV1 and EV4 (around 0.44 and 0.48, respectively). The reason may be related to that these rainfall events include a large number of zero values which biased the estimation. Correspondingly, the highest mean value of α is estimated for the EV5 (about 0.68). For the other rainfall events, the mean values of α are around 0.6. Concerning the DTM analysis, the lowest mean value of α is also computed for EV4 (around 0.49). This result is consistent with the result of TM analysis. For the other rainfall events, the mean values of α range from 0.65 to 0.75.

The parameter of C_1 of each rainfall product estimated by TM and DTM analysis is lower than 0.6 for all rainfall events (the difference is less than 0.3). Furthermore, the mean value of C_1 of all rainfall events ranges from 0.3 to 0.5. This result indicates that each rainfall product, as well as the rainfall events, has very similar degrees of homogeneity.

Overall, these results are consistent with the classical metrics (Section 2.4.3.3), which presents that the products of SRI, SRIMP and DPSRI have very similar performances. In general, the estimated α for the X-band radar products is higher than that of the C-band radar products for most of the rainfall events. This result indicates that the X-band radar is able to detect higher singularities than the C-band radar, which highlights the significance of the rainfall data resolution.

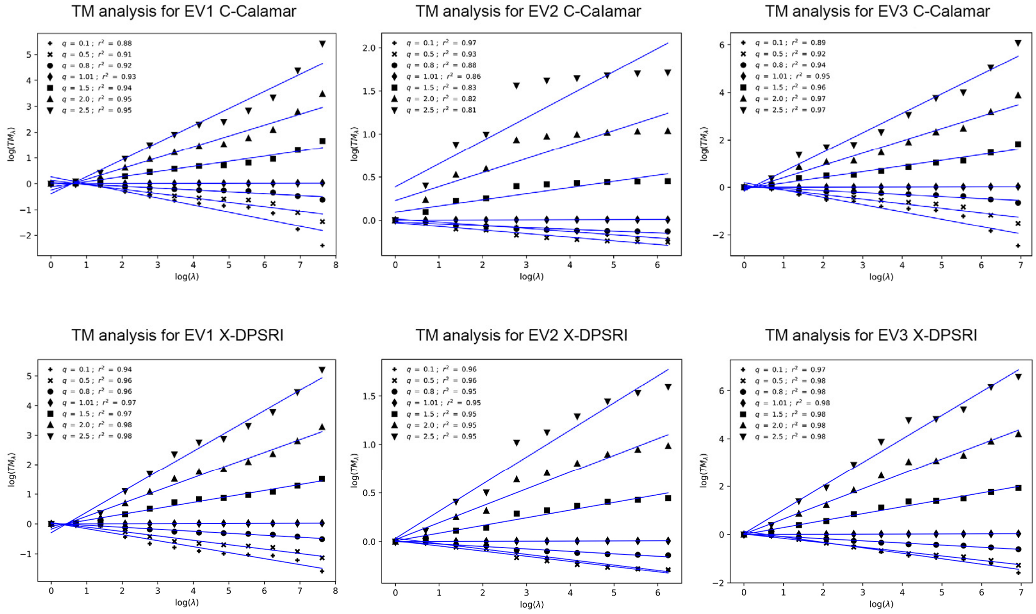

Figure 3.11: TM analysis of the three rainfall events of 2015 (EV1, EV2, and EV3) in the full range of scales (top: C-band radar data, bottom: X-band radar data).

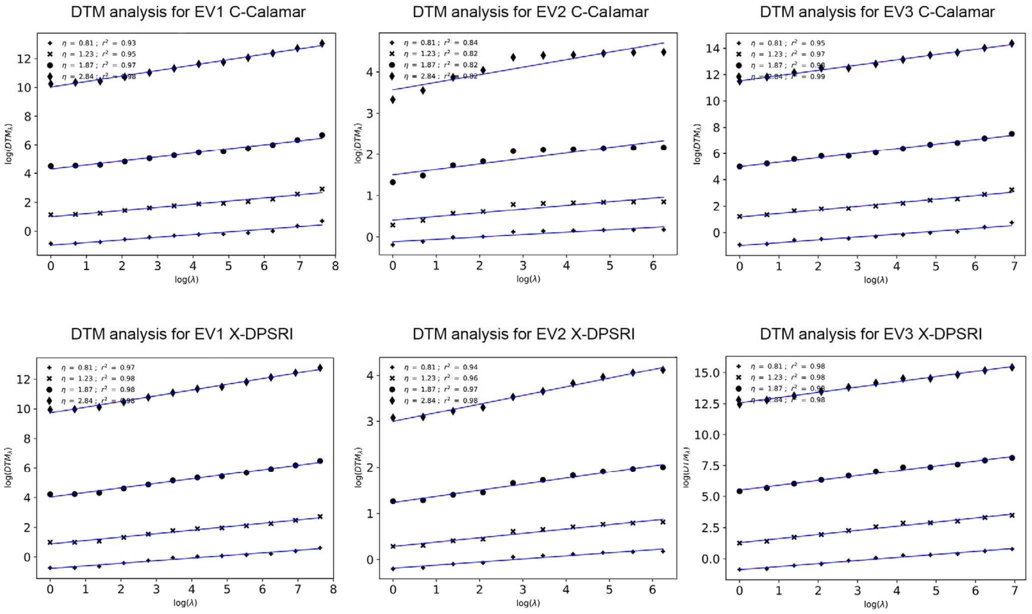

Figure 3.12: DTM analysis of the three rainfall events of 2015 (EV1, EV2, and EV3) in the full range of scales (top: C-band radar data, bottom: X-band radar data).

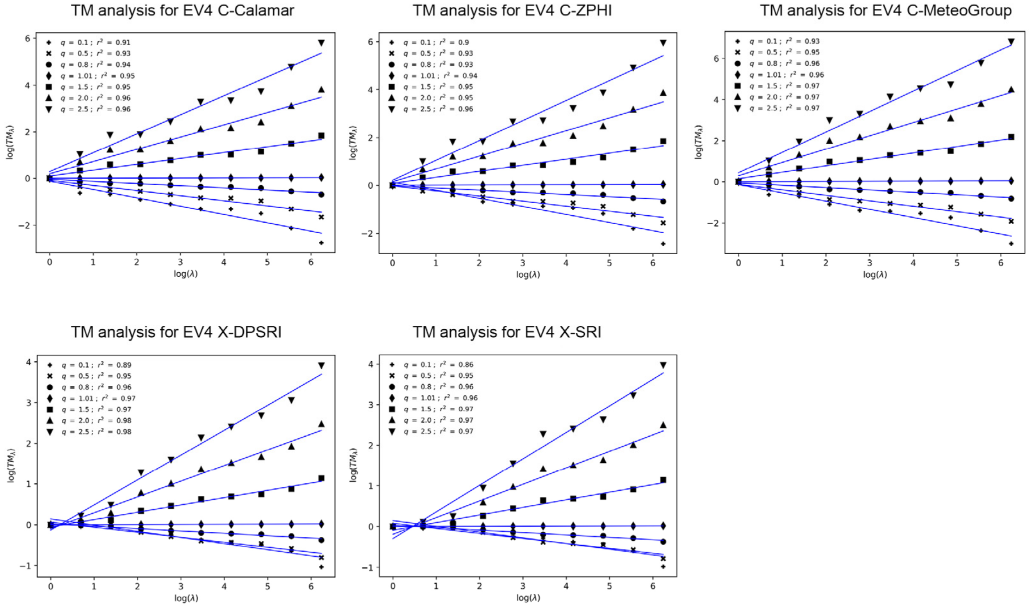

Figure 3.13: TM analysis of all the rainfall data of the EV4 in the full range of scales (top: C-band radar data, bottom: X-band radar data).

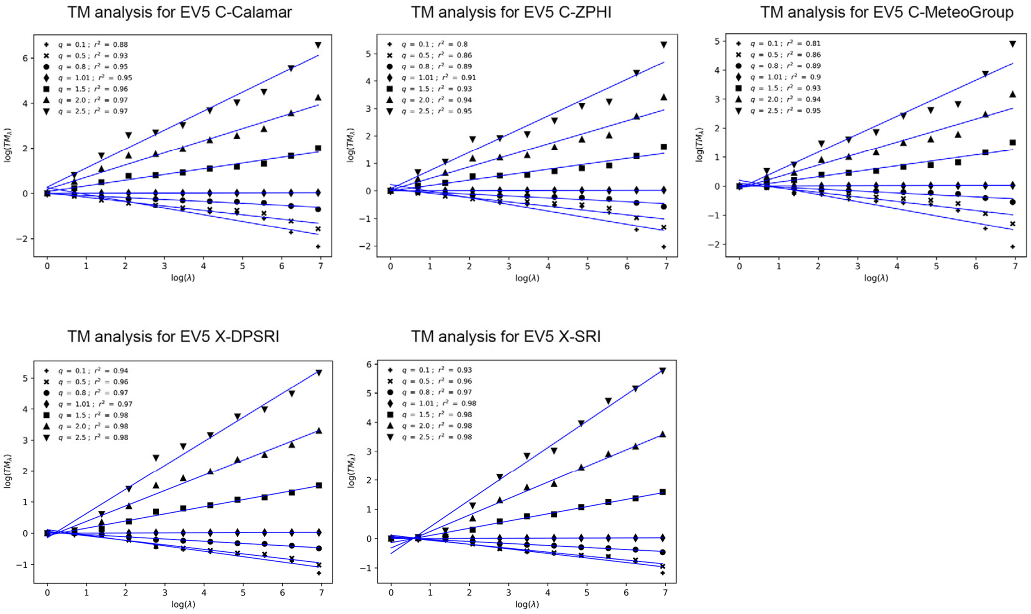

Figure 3.14: TM analysis of all the rainfall data of the EV5 (top: C-band radar data, bottom: X-band radar data).

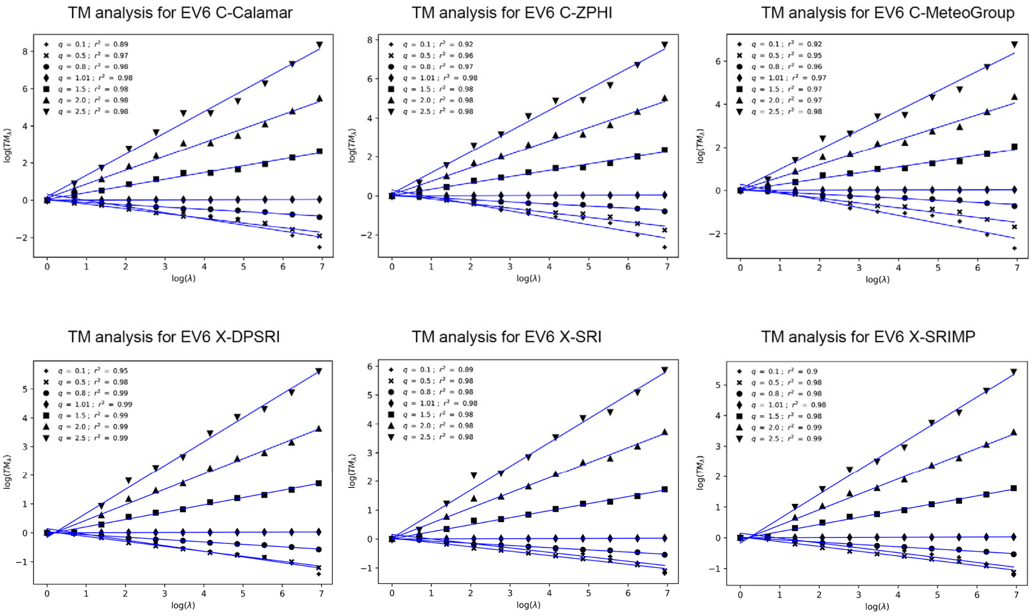

Figure 3.15: TM analysis of all the rainfall data of the EV6 (top: C-band radar data, bottom: X-band radar data).

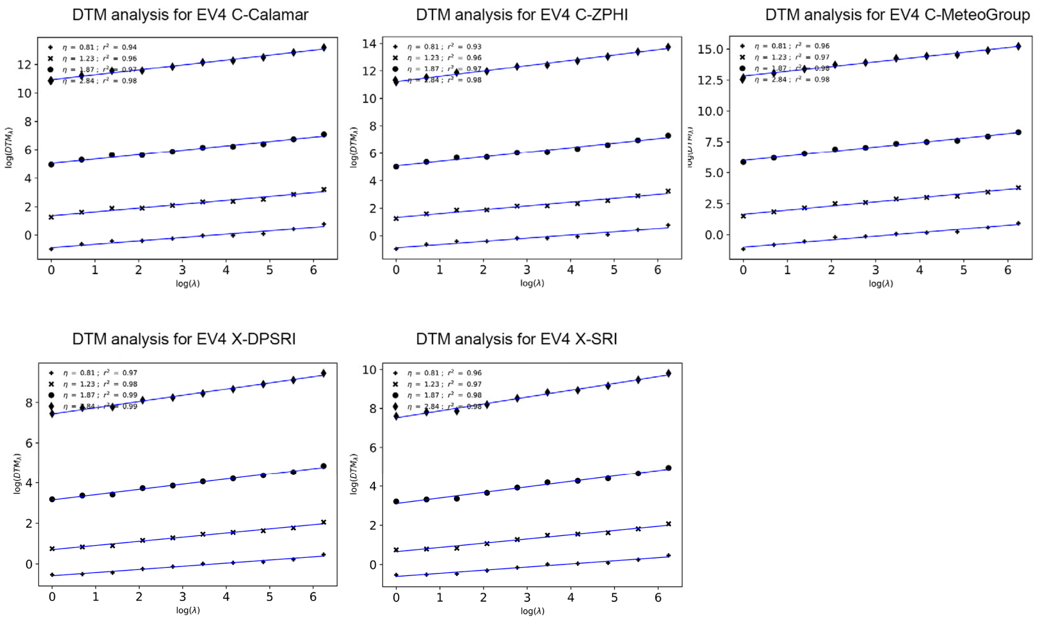

Figure 3.16: DTM analysis of all the rainfall data of the EV4 (top: C-band radar data, bottom: X-band radar data).

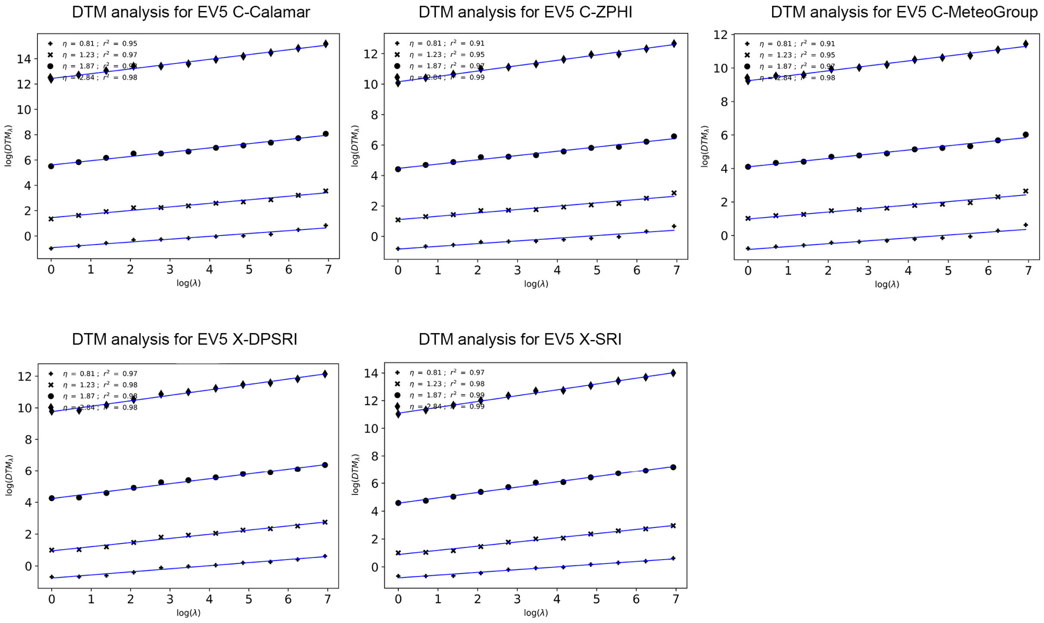

Figure 3.17: DTM analysis of all the rainfall data of the EV5 (top: C-band radar data, bottom: X-band radar data).

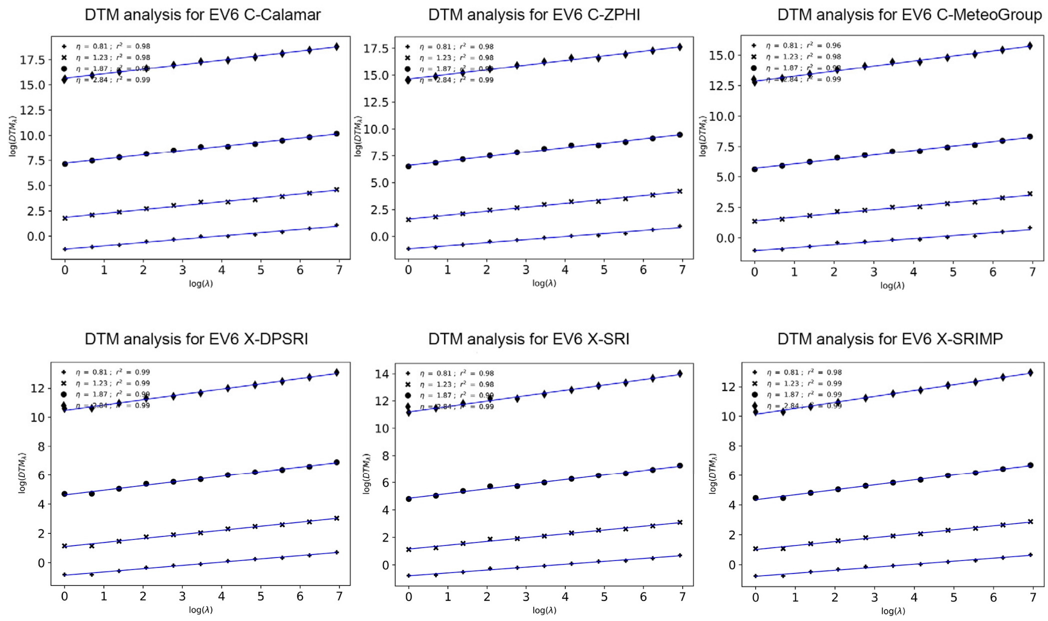

Figure 3.18: DTM analysis of all the rainfall data of the EV6 (top: C-band radar data, bottom: X-band radar data).

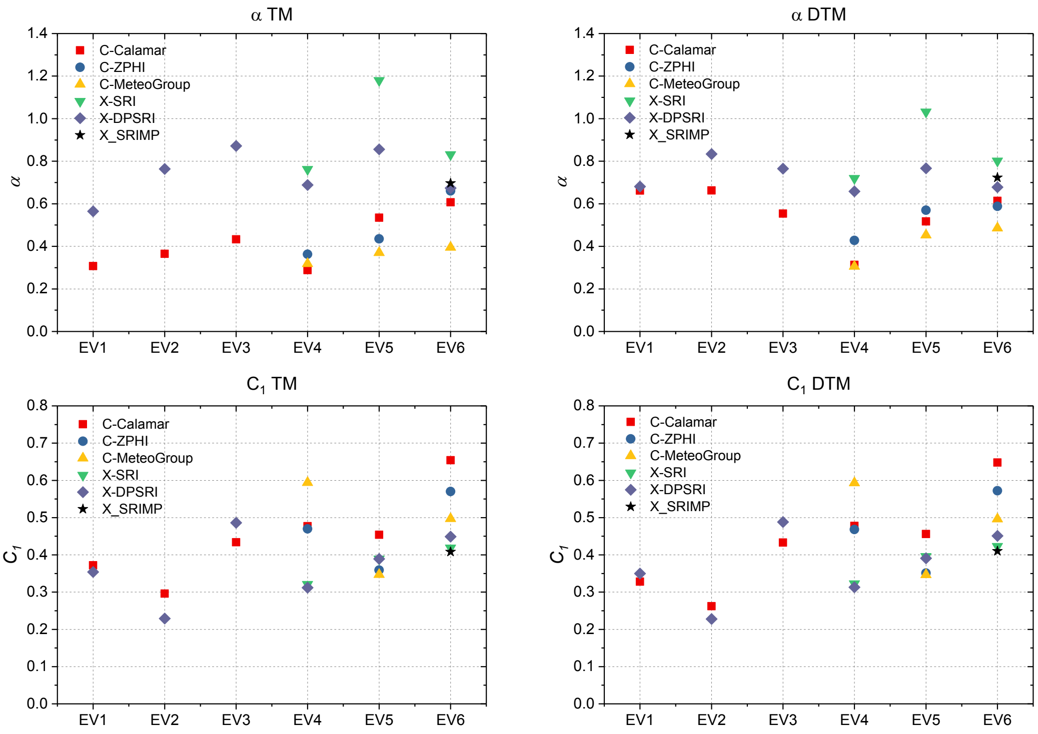

Figure 3.19: Representation of the UM parameters of the six selected rainfall events and all the rainfall data from C-band radar and X-band radar (The ■, ●, ▲,▼, ◆ and ★ represents the product of CALAMAR, ZPHI, MeteoGroup, SRI, DPSRI, and SRIMP, respectively).

Rainfall data	EV1	EV2	EV3	EV4	EV5	EV6
C- CALAMAR	0.31	0.37	0.43	0.29	0.54	0.61
C-ZPHI	N/A	N/A	N/A	0.36	0.44	0.66
C-MeteoGroup	N/A	N/A	N/A	0.32	0.37	0.4
X-SRI	N/A	N/A	N/A	0.76	1.18	0.83
X-DPSRI	0.57	0.76	0.87	0.69	0.86	0.67
X-SRIMP	N/A	N/A	N/A	N/A	N/A	0.7
Mean	0.44	0.57	0.65	0.48	0.68	0.65

Table 3.2: The α values (TM) of the six selected rainfall events and all the rainfall data from C-band radar and X-band radar.

Rainfall data	EV1	EV2	EV3	EV4	EV5	EV6
C- CALAMAR	0.66	0.66	0.55	0.31	0.52	0.61
C-ZPHI	N/A	N/A	N/A	0.43	0.57	0.59
C-MeteoGroup	N/A	N/A	N/A	0.31	0.45	0.49
X-SRI	N/A	N/A	N/A	0.72	1.03	0.8
X-DPSRI	0.68	0.83	0.77	0.66	0.77	0.68
X-SRIMP	N/A	N/A	N/A	N/A	N/A	0.72
Mean	0.67	0.75	0.66	0.49	0.67	0.65

Table 3.3: The α values (DTM) of the six selected rainfall events and all the rainfall data from C-band radar and X-band radar.

Rainfall data	EV1	EV2	EV3	EV4	EV5	EV6
C- CALAMAR	0.37	0.3	0.43	0.48	0.45	0.65
C-ZPHI	N/A	N/A	N/A	0.47	0.36	0.57
C-MeteoGroup	N/A	N/A	N/A	0.59	0.35	0.5
X-SRI	N/A	N/A	N/A	0.32	0.39	0.42
X-DPSRI	0.35	0.23	0.49	0.31	0.39	0.45
X-SRIMP	N/A	N/A	N/A	N/A	N/A	0.41
Mean	0.36	0.27	0.46	0.43	0.39	0.5

Table 3.4: The C_1 values (TM) of the six selected rainfall events and all the rainfall data from C-band radar and X-band radar.

Rainfall data	EV1	EV2	EV3	EV4	EV5	EV6
C- CALAMAR	0.33	0.26	0.43	0.48	0.46	0.65
C-ZPHI	N/A	N/A	N/A	0.47	0.35	0.57
C-MeteoGroup	N/A	N/A	N/A	0.59	0.35	0.5
X-SRI	N/A	N/A	N/A	0.32	0.4	0.42
X-DPSRI	0.35	0.23	0.49	0.31	0.39	0.45
X-SRIMP	N/A	N/A	N/A	N/A	N/A	0.41
Mean	0.34	0.25	0.46	0.43	0.39	0.5

Table 3.5: The C_1 values (DTM) of the six selected rainfall events and all the rainfall data from C-band radar and X-band radar.

Chapter 4

Numerical investigation of the nature-based solutions scenarios

4.1 First set of modelling experiments

The main objective of the first set of modelling experiments is to investigate the uncertainty of hydrological responses in various NBS scenarios resulting from the spatial variability in rainfall and the heterogeneous distribution of NBS at the urban catchment scale, and thus not those associated to the model structure, hypothesis or parameterization for instance. For these modelling experiments, the rainfall inputs of EV1 – EV3, EV1U – EV3U, and the EV1S – EV4S are used (see Chapter 2 for more details). The baseline scenario and the first and second sets of NBS scenarios are adopted. The variability and resulting uncertainties in hydrological responses of the catchment are quantified by considering the peak flow and the total runoff volume in the drainage conduits. It is important to mention here that a precise quantitative evaluation of NBS performances, e.g. peak discharge reduction, total runoff volume reduction, or both, is not the goal of the present study. The aim of this section is to first deepen the knowledge on the impact of spatial variability of the rainfall on hydrological responses of several NBS scenarios, and that in turn helps to clarify whether the nature-based solutions could be randomly implemented in semi-urban catchments or not.

The overall target of the study is to investigate the impacts of spatial variability in rainfall, the spatial arrangement of NBS, and their intersection on the hydrological responses of NBS scenarios at the urban catchment scale. For this purpose, four subsets modelling experiments were prepared, and two indexes (PD_{Qp}, percentage difference in peak flow; PD_V, percentage difference in total runoff volume) were used for quantifying the uncertainty associated to rainfall and NBS spatial distribution in the hydrological response of the catchment. Figure 4.1

presents the flow chart of the four subsets of modelling experiments. In addition, the corresponding descriptions are presented as follows:

The first subset is used to investigate the impact of spatial variability in rainfall on the hydrological responses of NBS scenarios. In this first subset, the following scenarios are adopted: baseline, PP1, RG1, GR1, and Combined1. These five scenarios are simulated under the distributed X-band rainfall data (EV1 – EV3) and uniform rainfall data (EV1U – EV3U). Then, the ratio on peak flow (Eq. 4.1), and the PD_{Qp} and PD_V (Eq. 4.2 and Eq. 4.3) indexes for each scenario under two different kinds of rainfall inputs were computed.

The second subset is used to analyse the impact of the spatial distribution of NBS on the hydrological responses of NBS scenarios. In this experiment, the first and second sets of NBS scenarios mentioned in the Section 2.6 (GR1 vs GR2 for instance) were compared. The eight scenarios were only simulated with the uniform rainfall in order to avoid the impact of spatial variability in rainfall and to focus on the uncertainty associated with the spatial arrangement of NBS.

The third subset is used to analyse the intersection impact of spatial variability in rainfall and the spatial distribution of NBS on the hydrological responses of the catchment. In this experiment, the eight mentioned NBS scenarios were simulated under the distributed and uniform rainfall, respectively. Then, the PD_{Qp} and PD_V of each NBS scenario were computed by comparing the results obtained for the two different kinds of rainfall inputs (distributed and uniform). Finally, the difference of PD_{Qp} and the difference of PD_V between the NBS scenarios characterised by the same solutions/measures were compared.

The fourth subset is used to analyse further the intersection impact of spatial variability in rainfall and the spatial distribution of NBS on the hydrological responses of the NBS scenarios. In this experiment, the GR1 and GR2 scenarios have been selected, and they are simulated under the synthetic rainfall of EV1S – EV4S. The reason is the difference of D_F between GR1 and GR2 is larger compare to the other NBS scenarios. Thus, the intersection effects can be more significant for these two scenarios. Here, the GR1 scenario was taken as the reference scenario, assuming that the extremes of rainfall (hot spots) only falls on the GRs of the GR1 scenario. With this respect, the rainfall was re-distributed in a binary manner in space during the 3 min that lasted at the largest rainfall peak of the EV3U, as illustrated in Figure 2.15 (c-f). Namely, the ‘hot spots’ of the EV1S – EV4S are strictly intersected with the distributions of GRs in GR1, while the GR2 scenario is not. Contrary to EV1S-EV3S, EV4S corresponds to the ‘no rain’ situation on GR1 during the same 3 min.

The peak flow ratio and the two indexes are especially calculated for the sum of four highlighted conduits connected to the catchment outlet (Figure 2.5 with Eqs. 4.1, 4.2 and 4.3):

$$\text{Ratio} = \frac{Q_{\mathrm{p}_1}}{\mathrm{Q}_{\mathrm{p}_2}} \tag{4.1}$$

$$\mathrm{PD}_{Q_\mathrm{p}}(\%) = \frac{|Q_{\mathrm{p}_1} - Q_{\mathrm{p}_2}|}{\frac{(Q_{\mathrm{p}_1} + Q_{\mathrm{p}_2})}{2}} \times 100 \tag{4.2}$$

$$\mathrm{PD}_\mathrm{V}(\%) = \frac{|V_1 - V_2|}{\left(\frac{V_1 + V_2}{2}\right)} \times 100 \tag{4.3}$$

where Q_{p_1} and Q_{p_2} refer to the peak flow of scenarios under distributed rainfall and uniform rainfall respectively for the first and third subsets modelling experiments. For the second subset experiment, they represent the peak flow of the first set of NBS scenarios and the second set of NBS scenarios, respectively. For the fourth subset experiment, they represent the peak flow of the GR1 scenario and GR2 scenario, respectively. Correspondingly, for the first and third subsets modelling experiments, V_1 and V_2 refer to the total runoff volume of scenarios under the distributed and uniform rainfall respectively. For the second subset modelling experiment, they represent the total runoff volume of the first set of NBS scenarios and the second set of NBS scenarios, respectively. For the fourth subset experiment, they represent the total runoff volume of the GR1 scenario and GR2 scenario, respectively.

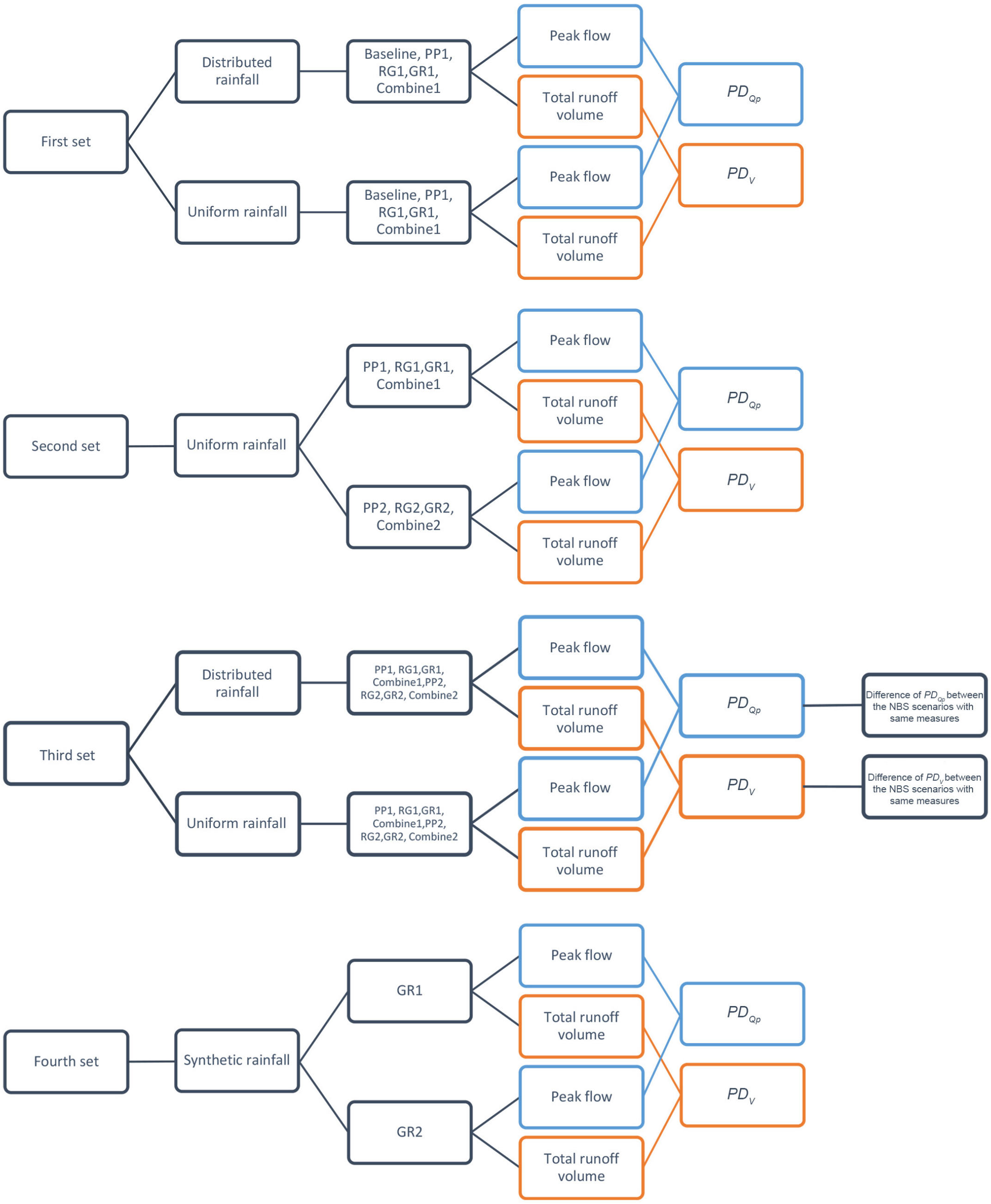

Figure 4.1: Flow chart of the four subsets of modelling experiments.

4.1.1 Impacts of spatial variability in rainfall

The impact of spatial variability in rainfall on the hydrological responses of each NBS scenario over the whole catchment was evaluated integrally in terms of the sum of flow in four conduits (highlighted in the Figure 2.5). These four conduits are chosen because they collect the runoff from the whole catchment and finally merge into the storage unit representing the outlet of the drainage system. To be more specific, the PD_{Qp} and the PD_V computed for the first subset of modelling experiments are presented in the following section.

4.1.1.1 Baseline scenario

Before going on, it is important to evaluate the ‘baseline’ scenario under both distributed and uniform rainfalls, by using the simulations already performed to validate the Multi-Hydro implementation in the Guyancourt catchment. As shown in the hydrographs (Figure 4.2), the higher peak flow was generated by the distributed rainfall in EV1 and EV2. Hence, the peak flow ratio computed by comparing distributed rainfall and uniform rainfall is larger than 1 (see the first column of Figure 4.2c), but this ratio is around 0.9 in EV3. The reason is that during the largest rainfall peak of EV1 and EV2, the rainfall intensity of all radar pixels in distributed rainfall is higher than those of uniform rainfall. While in EV3, the rainfall intensity of around 30 % radar pixels in uniform rainfall is about 28 mm/h higher than that of the distributed rainfall.

As shown in Figure 4.4a, the PD_{Qp} of baseline scenario in EV1, EV2 and EV3 is about 9.4 %, 16.2 %, and 10.9 %, respectively. According to the SD of the rainfall intensity at the largest rainfall peak of each event (see Table 2.1 in Section 2.4.3), the spatial variability of the rainfall intensity of EV2 is more pronounced than that of EV1 and EV3. Accordingly, the PD_{Qp} of baseline scenario in EV2 is the highest. Regarding the total runoff volume (Figure 4.4b), the PD_V of the baseline scenario for the three rainfall events range from 1 % to 3.8 %. Contrary to the PD_{Qp}, the PD_V of the baseline scenario is not correlated to the SD of the total rainfall depth. For the baseline scenario, it is noticed that the PD_{Qp} is more pronounced than PD_V for all rainfall events. These results can be explained by the fact that the spatial variability in rainfall intensity at the largest rainfall peak is strong in all three rainfall events, while the total rainfall volume for the distributed and uniform rainfall inputs is the same. This small PD_V is influenced by the differences on the grid scale (storage capacity, infiltration, etc.), which are differently modelled when the input is uniform or non-uniform.

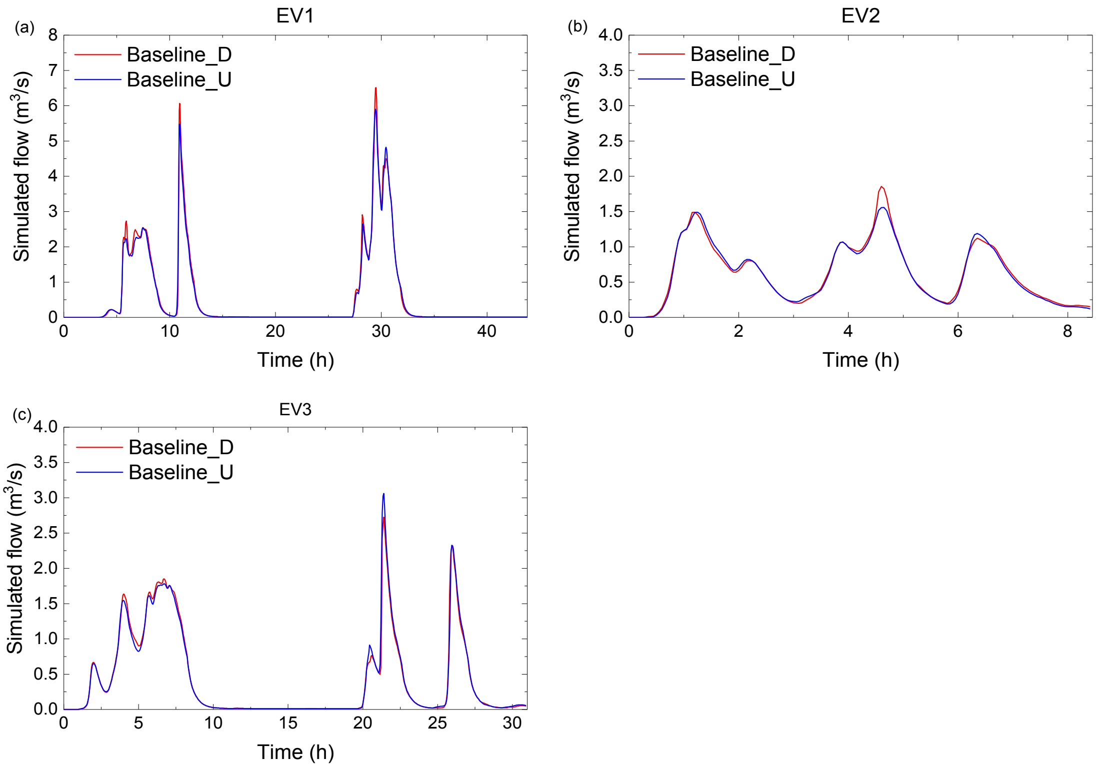

Figure 4.2: Simulated flow (m^3/s) of the baseline scenario under three distributed rainfall events and three uniform rainfall events: (a) EV1; (b) EV2; (c) EV3.

4.1.1.2 NBS scenarios

Figure 4.3 presents the simulated flow of the first set of NBS scenarios under the three distributed and uniform rainfall events. The results are generally consistent with the results of the baseline scenario. Indeed, as shown in Figure 4.3c, the peak flow ratios between distributed rainfall and uniform rainfall simulations for the four NBS scenarios are larger than 1 for EV1 and EV2, and around 0.8 for EV3 for the reason mentioned in the previous section.

As shown in Figure 4.4a, the results of $PD_{Q\text{p}}$ for PP1, RG1, and Combined1 scenarios are generally in agreement with the baseline scenario: $PD_{Q\text{p}}$ is the lowest for EV1, and the highest for EV2. For these three NBS scenarios, $PD_{Q\text{p}}$ range from about 8 % to 18 % for the three rainfall events. The relationship between the SD of the rainfall intensity at the largest rainfall peak and the $PD_{Q\text{p}}$ of each NBS scenario (Figure 4.5a) show that $PD_{Q\text{p}}$ (the uncertainty related to the peak flow) computed for PP1, RG1, and Combined1 scenarios increase simultaneously with the increase of the SD of the rainfall intensity. The results computed for GR1 scenario do not depict the same tendency: PD_{Qp} computed for EV3 is higher than those computed for the two other events. The reason is related to various factors. Namely, it may be affected by the intersection effects of the spatial variability in rainfall and the spatial arrangement of green roofs in the catchment. The reason can be explained by the fact that, in the GR1 scenario, the green roofs are mainly implemented on the locations with high distributed rainfall intensities. As demonstrated by many previous studies (Qin et al., 2013; Palla and Gnecco, 2015; Ercolani et al., 2018), GR are usually more effective for intense but short rainfall peaks. In the case of the GR1 scenario under the distributed rainfall of EV3, GR measures effectively stored more runoff than in the uniform rainfall during the main rainfall peak. This enlarges the variability of the hydrological response in terms of peak flow.

Regarding the percentage differences on total runoff volume, it is noticed that the computed PD_V are lower than 6 % for all NBS scenarios under the three rainfall events, especially in EV3, where they are lower than 2 %. This demonstrates that the resulting uncertainty on the total runoff volume is little influenced by the spatial variability of the rainfall. The reason is that the spatial variability of total rainfall depth is less pronounced with respect to the spatial variability of the rainfall intensity, and also there is no highly localised storm cell in studied events. Figure 2.8 (right) displays the rainfall intensity at the largest rainfall peak (per radar pixel) over the Guyancourt catchment area for the three studied rainfall events. It is noticed that the highest rainfall peak of the distributed rainfall is very variable in space, which enlarged the discrepancy with the corresponding uniform rainfall data, resulting in a significant impact on the peak flow of each NBS scenario that simulated with two different rainfall data. However, the cumulative rainfall of the distributed rainfall data is not very variable in space (see Figure 2.9 right). For instance, the standard deviation (SD) of the cumulative rainfall of the three rainfall events is around 1 mm, which indicates that the spatial variability of the distributed rainfall is not very pronounced at most of the time steps. Thus, the difference between distributed rainfall data and uniform rainfall data is relatively small during the whole rainfall period. Finally, the simulated flow of NBS scenarios under two different rainfall data is similar in most time steps, resulting in the percentage difference in the total runoff volume of NBS scenarios is not significant. As illustrated in Figure 4.5b, the relationship between the SD of total rainfall depth and the PD_V of NBS scenarios is nonlinear. This can be explained by the fact that the three rainfall events are relatively long, and the hydrological performances of NBS are gradually changed during the event (e.g. they can efficiently infiltrate or store water at the beginning, and be saturated after a long rainfall period). Comparing the PD_V of each NBS scenario for all three rainfall events (Figure 4.4b), those computed for GR1 and Combined1 appear to be the highest for EV2. It could be also related to the intersection effects of spatial location of GR measures and the spatial variability in rainfall. Indeed, these GR measures (considered in the GR1 and Combined1 scenarios) are mainly located in the north side of the catchment. In this area, the first distributed precipitation of EV2 (1-3.5 h), is relatively weak and variable (i.e., there is no rainfall or the rainfall with very low intensity in some localization pixels). Furthermore, as the initial moisture condition of GR measures are considered as unsaturated in both distributed and uniform rainfall, the GR measures are more efficient at the beginning of the distributed rainfall than in the uniform rainfall, and finally enlarge the uncertainty associated with precipitation variability (i.e., the corresponding PD_V). More discussion about the intersection effects is presented in Section 4.1.3.

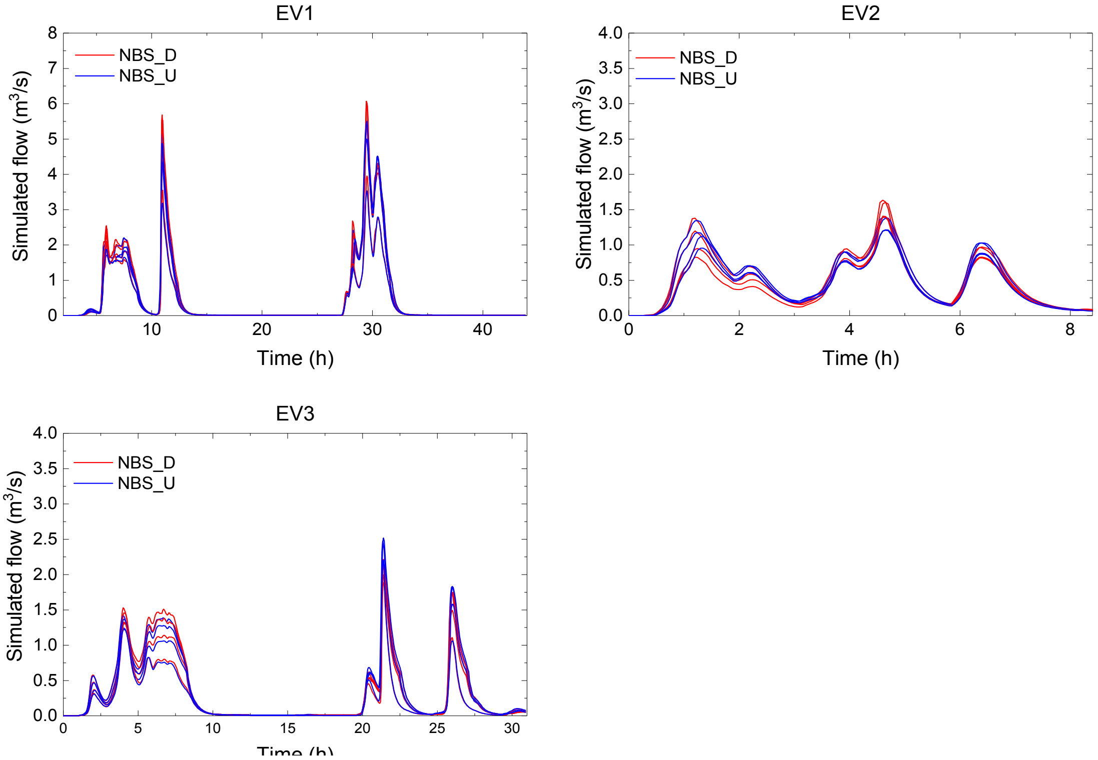

Figure 4.3: Simulated flow (m^3/s) of the first set of NBS scenarios under three distributed rainfall events and three uniform rainfall events (the red hydrographs represent the NBS scenarios simulated with distributed rainfall, and the blue hydrographs represent the NBS scenarios simulated with uniform rainfall).

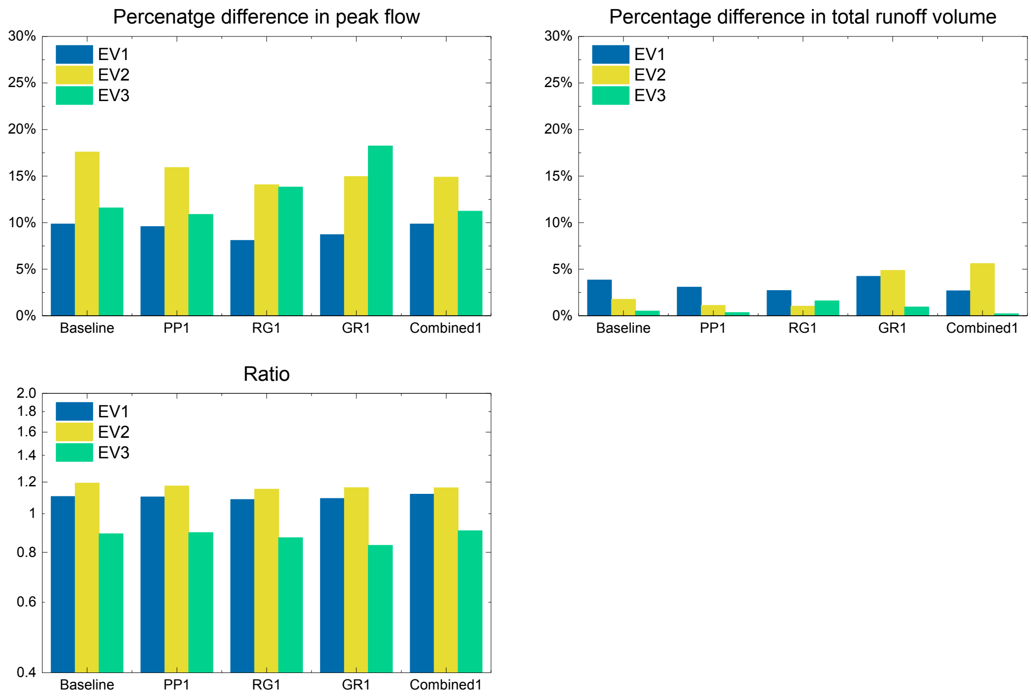

Figure 4.4: (a) Percentage difference in peak flow of the baseline scenario and the first set of NBS scenarios under the three distributed rainfall events and the three uniform rainfall events; (b) percentage difference in total runoff volume of the baseline scenario and the first set of NBS scenarios under the three distributed rainfall events and the three uniform rainfall events; (c) the ratio of peak flow between the scenarios under the distributed rainfall and the scenarios under the uniform rainfall.

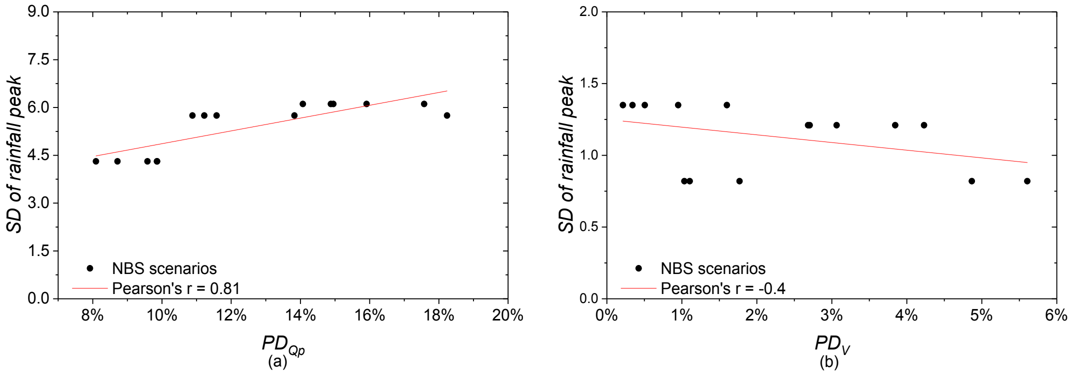

Figure 4.5: (a) Relationship between the SD of rainfall intensity at the largest rainfall peak and PD_{Qp} of NBS scenarios; (b) Relationship between the SD of total rainfall depth and PD_V of NBS scenarios.

4.1.2 Impacts of the spatial distribution of NBS

In order to analyse the impacts of the spatial distribution of NBS on the hydrological responses of NBS scenarios, the results of the second subset of modelling experiment (described in Section 4.1) are presented as follows. As shown in Figure 4.6a, the $\mathrm{PD}_{Q_\mathrm{p}}$ of all NBS scenarios are lower than 5 %, and the PD_V of all NBS scenarios are lower than 8 %, which indicates that the hydrological responses of NBS scenarios are little affected by the spatial distribution of NBS in the catchment. This result is generally consistent with the observation of Versini et al., (2016), who pointed out that the impact of the spatial distribution of green roofs on the catchment response is minimal. However, comparing the $\mathrm{PD}_{Q_\mathrm{p}}$ of each NBS scenario, those computes for PP and GR scenarios range from about 2 % to 5 %, which are slightly higher than those related to other scenarios, especially for EV1 and EV3. The reason can be explained by two factors: (i) the infiltration or detention capacity of PP and GR measures are less effective for rainfall characterised by strong intensity and long duration (Qin et al., 2013; Palla and Gnecco, 2015), whereas the RG measures are artificial depressed green areas (simulated with a 0.3 m depression depth) with higher retention capacity (Dussaillant et al., 2004); (ii) the differences of D_F (large scale; i.e., the second regime) between PP1 and PP2 scenarios as well as between GR1 and GR2 scenarios are larger than that of the other NBS scenarios (Table 2.10). Figure 4.7a shows the difference of D_F between the same types of NBS scenarios is proportional to the corresponding $\mathrm{PD}_{Q_\mathrm{p}}$. It is found that the larger the difference of D_F, the higher the $\mathrm{PD}_{Q_\mathrm{p}}$ is. Regarding the PD_V of NBS scenarios for the three uniform rainfall events (Figure 4.6b), those comparing PP1 and PP2 scenarios (which ranges from about 4 % to 8 % for the three rainfall events, especially higher for the two strong and long events) are slightly higher than those related to the other scenarios. Because permeable pavements are infiltration-based measures (they do not retain water for a limited period), their performances are more related to the heterogeneity of their performed location. Namely, some PP measures are implemented in drained areas may suffer more from surface runoff, are therefore more easily saturated (see Figure 2.27 for a comparison of the spatial arrangement of PP measures for two PP scenarios). As shown in Figure 4.7b, the difference of D_F between the same types of NBS scenarios has a moderate positive correlation (r =0.61) with the corresponding PD_V. This study hypothesizes that the rather weak correlation is related to the complexity of rainfall with several peaks and dry periods, the retention/infiltration capacity of NBS changes with the rainfall intermittency.

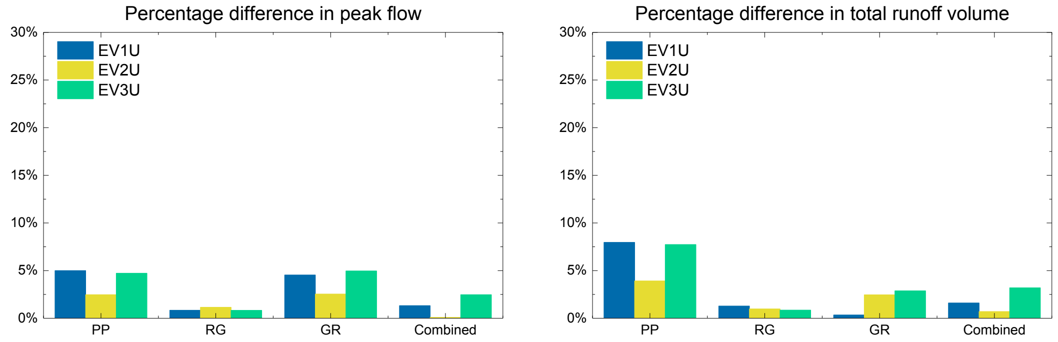

Figure 4.6: (a) Percentage difference in peak flow between the same types of NBS scenarios under the three uniform rainfall events. (b) Percentage difference in total runoff volume between the same types of NBS scenarios under the three uniform rainfall events.

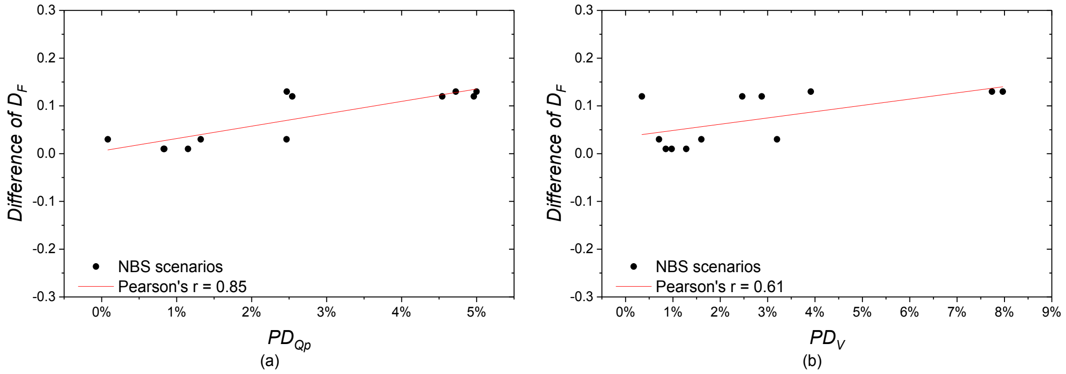

Figure 4.7: (a) Relationship between the difference of D_F of the same types of NBS scenarios and PD$_{Qp}$ of the same types of NBS scenarios. (b) Relationship between the difference of D_F of the same types of NBS scenarios and PD$_V$ of the same types of NBS scenarios.

4.1.3 Intersection effects of spatial variability in rainfall and NBS

In the following, the results of the third and fourth subsets modelling experiments are described and discussed. The aim is to analyse the potential intersection effects of spatial variability in rainfall and spatial distribution of NBS on the hydrological responses of NBS scenarios.

The resulting uncertainty on the peak flow and total runoff volume (PD$_{Qp}$ and PD$_V$) of the third subset of modelling experiments are shown in Figure 4.8. Firstly, it is found that the spatial variability in rainfall has a certain extent impact on the peak flow of each scenario, with the PD$_{Qp}$ ranging from about 8 % to 18 %. With the exception of GR1, all the NBS scenarios have a similar tendency: the $\mathrm{PD}_{Q\mathrm{p}}$ are the lowest for the first event, and the highest for the second one. Namely, for most of NBS scenarios, the $\mathrm{PD}_{Q\mathrm{p}}$ (uncertainty on peak flow) increases with the increase of the spatial variability in rainfall intensity. As shown in Figure 4.8a, comparing the $\mathrm{PD}_{Q\mathrm{p}}$ between scenarios of PP1 and PP2, RG1 and RG2, as well as Combined1 and Combined2 for the three rainfall events, the maximum difference is less than 3 % (Figure 4.8c). However, comparing the $\mathrm{PD}_{Q\mathrm{p}}$ between GR1 and GR2, the difference is larger, especially in EV3 (> 6 %). For the GR1 scenario, the $\mathrm{PD}_{Q\mathrm{p}}$ range from about 8.7 % to 18 % in all three rainfall events, and those of GR2 range from about 10.7 % to 16 %. Furthermore, for GR1, the largest $\mathrm{PD}_{Q\mathrm{p}}$ is in EV3, but for GR2, the largest $\mathrm{PD}_{Q\mathrm{p}}$ is computed for EV2. The difference of $\mathrm{PD}_{Q\mathrm{p}}$ between GR1 and GR2 scenarios demonstrated that the spatial variability in rainfall and the spatial arrangement of GR measures have some intersection effects on the peak flow of GR scenarios. However, it is not obvious for the other NBS scenarios. One of the reasons has been discussed in Section 4.1.1: in the GR1 scenario, GR measures are mainly implemented in the north part of the catchment, which coincidently received higher rainfall (distributed EV3); namely, the "hot spots" of the rainfall field were highly intersected by the GR measures due to their high fractal dimension. Therefore, the peak flow was effectively reduced by the GRs. On the contrary, for GR2 scenario, the GR measures are mainly located on the south side of the catchment, which scarcely intersected with the rainfall spikes. Therefore, the impervious roofs on the north side of the catchment intersected with the rainfall spikes and eventually generated more runoff. Another possible reason is GR has the lowest storage capacity in the studied NBS, as well as the studied rainfall events are not intense enough to saturate the other types of NBS (see Versini et al., 2016 for a comparison of different properties of GR). Her et al., (2017) also indicated the hydrological performances of NBS are sensitive to their configurations. Comparing with the $\mathrm{PD}_{Q\mathrm{p}}$ of the third subset of modelling experiments, the PD_{V} is much lower. The reason is the same as explained in Section 4.1.1.2.

Concerning the intersection impact on total runoff volume of NBS scenarios, the variations of PD_{V} among most of NBS scenarios pairs (PP1 and PP2, GR1 and GR2, as well as Combined1 and Combined2) are significantly different for the three rainfall events. The maximum discrepancy (higher than 5 %) is noticed between Combined1 and Combined2 in EV3, because the two combined scenarios mixed three types of NBS with different retention capacity, at the beginning of the rainfall periods, the unsaturated NBS can effectively reduce the flow if they largely intersected with the rainfall spikes. On the contrary, if the NBS are not effectively intersected with the rainfall spikes, the corresponding simulated flow is higher. Furthermore, the total rainfall depth (rainfall grid) is relatively more variable for EV3. Conversely, the difference of PD_{V} between RG1 and RG2 is relatively small, which is less than 1 %. The reason can be explained by the large retention capacity of RG measures, which has been mentioned in Section 4.1.2.

To further investigate the intersection effects, the fourth subset of modelling experiment is used. As shown in the hydrographs (Figure 4.9), the peak flow of GR1 scenario was expected to be less than that of GR2, and this is confirmed for EV1S, EV2S, and EV3S. For EV1S and EV2S, with the same maximum intensity of 55 mm/h, the hydrographs of these two events significantly differ, with the peak flow decreasing by a factor 2 for EV2S. However, the only difference in the rainfall inputs is that there is zero rainfall outside of the GRs during the 3 min rainfall peak. The percentage difference in peak flow ($PD_{Q\mathrm{p}}$) and total runoff volume (PD_V) of GR1 and GR2 scenario under the EV1S is around 5 %, and 4.3 %, respectively (see Figure 4.10). For EV2S, the $PD_{Q\mathrm{p}}$ and PD_V increase to 20.7 % and 7.8 %, respectively. This confirms that without the impact of runoff that generated by other land uses, the intersection effects increase considerably with the high rainfall intensity, also increasing the NBS effectiveness. For the EV3S, the maximum rainfall intensity during the 3 min has been decreased to 17 mm/h. This was sufficient to further reduce the peak flow during the principal rainfall peak. For this event, the $PD_{Q\mathrm{p}}$ and PD_V values drop to 3.5 % and 1.8 %, respectively. This indicates that the intersection effects is less significant for the rainfall with low intensity. As expected in the EV4S, because of zero rainfall intersected with the GRs in GR1 scenario, the peak flow of GR2 remains slightly lower than that of the GR1, with the $PD_{Q\mathrm{p}}$ and PD_V values of only 2.1 % and 1.4 %, respectively.

Overall, the results demonstrate that the spatial variability in rainfall and the spatial arrangement of NBS can generate uncertainties on peak flow and total runoff volume estimations if they are not considered properly. In this specific case, they are more significant for GR scenarios, while less evident for RG scenarios. Therefore, the performances of NBS scenarios that evaluated by some studies with only applying uniform rainfall as input can be biased in terms of the intersection effects (Zahmatkesh et al., 2014; Ahiablame et al.,2016; Guo et al., 2019). In this specific study, the intersection effect is more significant for GR scenarios and combined scenarios in terms of peak flow and total runoff volume, respectively. However, the physical properties of NBS are indeed another significant factor for the overall performances of scenario (Gilroy and McCuen 2009), for example, the intersection effect is less evident for RG scenarios mainly due to their high storage capacity. Comparing to the impacts of spatial variability in rainfall on the hydrological responses of NBS, the intersection effects seem less significant. This results also further demonstrated the performances of NBS scenario is less influenced by the spatial distributions of NBS.

As the rainfall fields are always variable in space and time, to make the most of the benefits of NBS for stormwater management, the results suggest to implement NBS scattered in the catchment, but with a higher fractal dimension D_F. This will combine a lower investment with the maximum return, preventing NBS from concentrated in certain specific places.

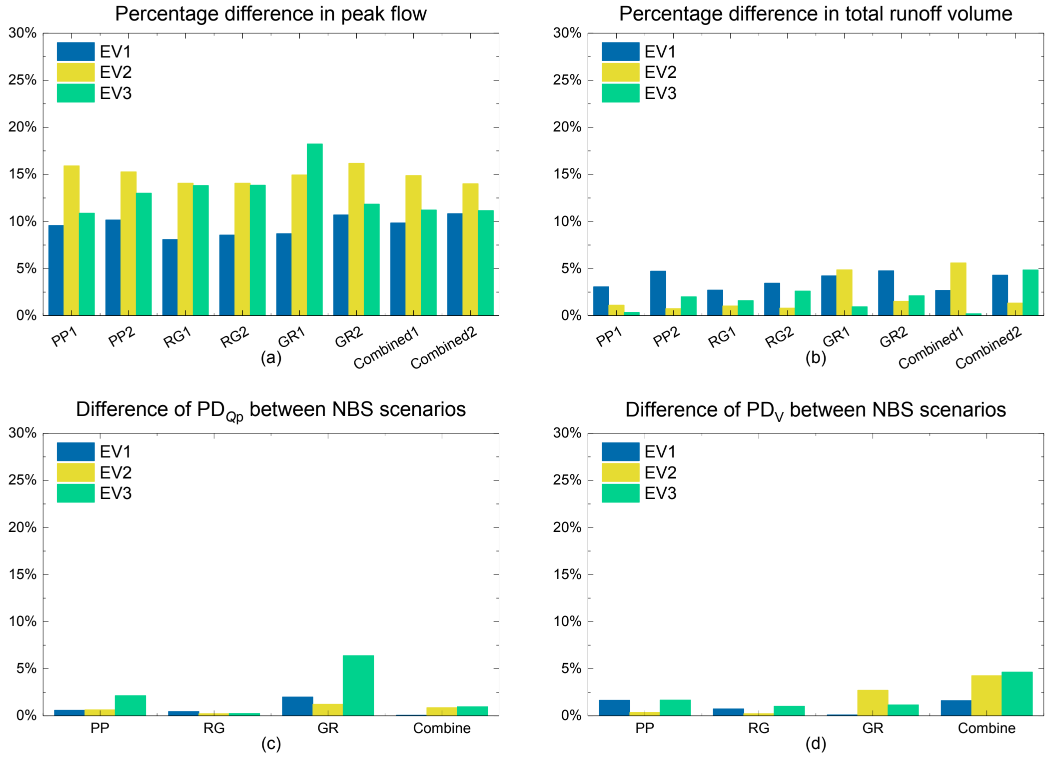

Figure 4.8: (a) Percentage difference in peak flow of all NBS scenarios under the three distributed rainfall events and the three uniform rainfall events. (b) Percentage difference in total runoff volume of all NBS scenarios under the three distributed rainfall events and the three uniform rainfall events. (c) Difference of PD_{Qp} between the same types of NBS scenario. (d) Difference of PD_V between the same types of NBS scenario.

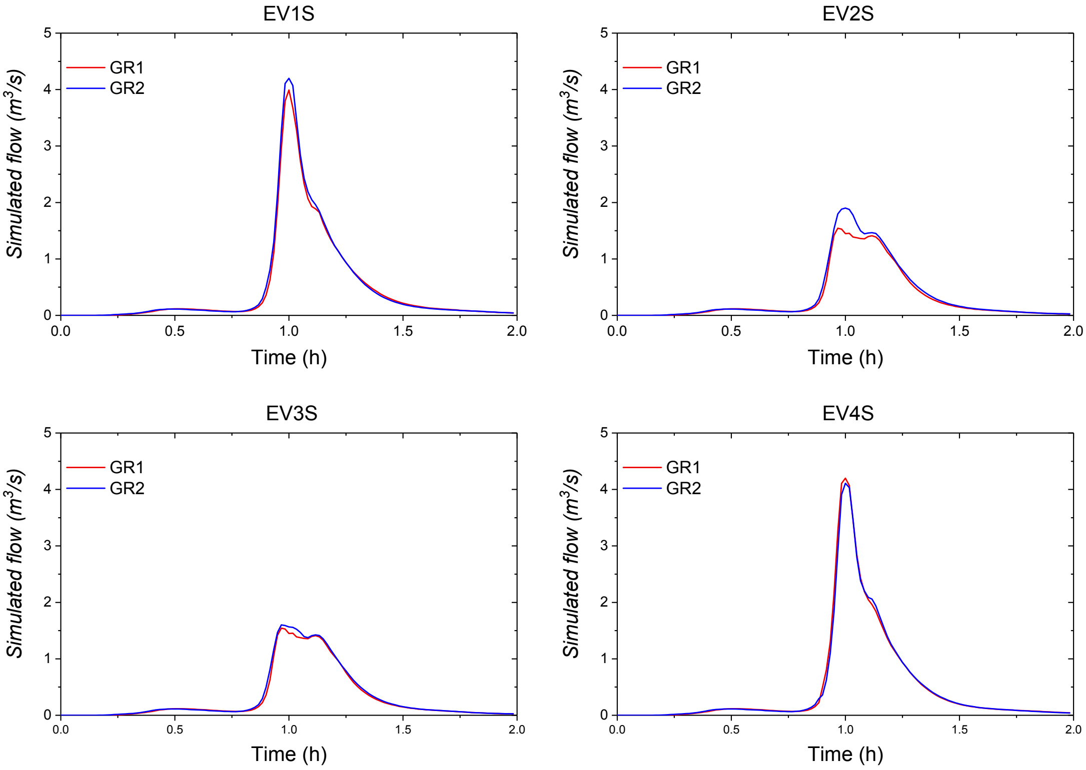

Figure 4.9: Simulated flow (m^3/s) of GR1 and GR2 scenarios under the four syntactic rainfall events.

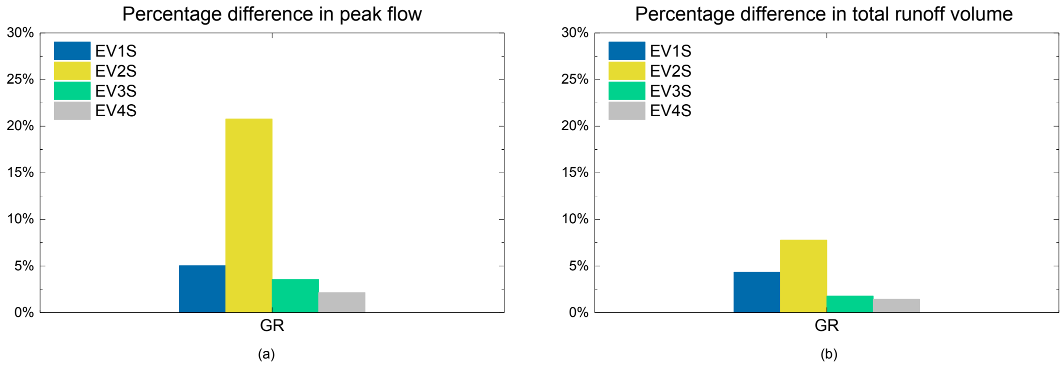

Figure 4.10: (a) Percentage difference in peak flow of GR scenarios under the four syntactic rainfall events; (b) Percentage difference in total runoff volume of GR scenarios under the four syntactic rainfall events.

4.1.4 Intermediate conclusions for Section 4.1

This section focuses on the variability of the hydrological responses of NBS scenarios resulting from the multi-scale spatial heterogeneity of both the rainfall and the NBS distribution. The principal findings are summarised as follows:

1. The spatial variability in rainfall has a significant impact on the peak flow of NBS scenarios for the three studied rainfall events. For instance, it makes the maximum $\mathrm{PD}_{Q\mathrm{p}}$ increase up to 18 % in GR1 scenario. Furthermore, the spatial variability of the rainfall intensity at the largest rainfall peak is almost linearly related to the $\mathrm{PD}_{Q\mathrm{p}}$ computed for all NBS scenarios (except for GR1): the more variable are the rainfall intensities, the higher are the $\mathrm{PD}_{Q\mathrm{p}}$. However, the resulting PD_{V} computed for all NBS scenarios show that the spatial variability in rainfall has much lower impact on the uncertainty related to total runoff volume: the average PD_{V} being of the order of 2.3 % only.

2. The impact of spatial arrangement of NBS on hydrological responses of the catchment is less obvious. For all the NBS scenarios, $\mathrm{PD}_{Q\mathrm{p}}$ and PD_{V} are lower than 5 % and 8 %, respectively. However, it is found that the difference of D_F between the same types of NBS scenarios has a fairly strong positive correlation to the related $\mathrm{PD}_{Q\mathrm{p}}$. Therefore, it suggests to implement NBS by optimizing D_F over the whole catchment to be the highest possible. Furthermore, mixing different NBS in the catchment, as presented in the two combined scenarios, can also efficiently reduce the uncertainty associated with the spatial arrangement of NBS.

3. The fractal dimension D_F appears as a useful tool to quantify the spatial heterogeneity of NBS across a range of scales. The D_F of each NBS scenario is associated with the urbanization level of the catchment, which confirms that the level of implementation of NBS is reasonable to match the catchment conditions. The fractal dimension combined with the fully-distributed model is an innovative approach that is easily transportable to other catchments.

4. The spatial distribution of rainfall and the spatial arrangement of NBS have intersection effects on the hydrological responses of NBS scenarios, especially significant for the peak flow of GR scenarios (with a maximum difference between the scenario of GR1 and GR2 reaching about 6 % on peak flow). The intersection effects on the total runoff volume of each NBS scenario is quite variable because the chosen NBS present some limitations in terms of infiltration or detention capacity during a long rainfall event with high intermittency. However, the RG scenarios appear to be less affected by the intersection effects, with a difference lower than 3 % on peak flow and lower than 1 % on total runoff

volume, mainly due to RG measures are artificial depressed green areas that characterised with higher retention capacity.

5. The results of synthetic experiment strengthened again the intersection effects on the GR scenarios. This intersection effects can be more significant for the strong rainfall events.

6. The study of hydrological response in various NBS scenarios resulting from the multi-scale spatial variability of precipitation and the heterogeneous distribution of NBS hints towards using fully distributed hydrological models over semi-distributed or lumped models. Indeed, the fully distributed model has been shown to be able to take into account these small scale heterogeneities and propagate their effects to watershed scales, while parameterizing or smoothing out some critical heterogeneity, as done in non-fully distributed models, may bias its predictions.

In this specific case, the GR scenarios are more sensitive to the spatial variability in rainfall and the spatial arrangement of GR measures, while the performances of RG scenarios and combined scenarios are more stable under any condition. Apparently, these findings already give some incites to decision-makers on Why they need to prioritize given NBS within the urban planning process.

Although the rainfall events selected for this study were not extreme events, they cover a rather broad spectrum of spatio-temporal variability in rainfall, and they are very typical precipitations in the Paris region. The simulation results can serve as a reference for future urban planning in this region. For example, the results of three different impacts (i.e., the spatial variability of precipitation, the spatial distribution of NBS, and the intersection effects) on the performance of NBS scenarios are useful for decision-makers, targeting for an actual project.

However, larger precipitation samples, including extreme rains, as well as NBS monitoring data will be helpful to get a better knowledge of somehow universal solutions and provide answers on How to prioritize these NBS. With respect to this perspective, the obtained results already demonstrated that new scale-independent indictors, like the fractal dimension D_F applied in this study, will be essential for more profound quantitative evaluation of the diversity of combined impacts, including for other heterogeneous catchments. Therefore, this study have an important potential impact, due to its originality with respect to the nonlinear tools used to address such practical issues, and its relevance in interdisciplinary applications. This suggests to pursue the development of original tools to get new insights into the scaling complexity of flows in urban hydrology.

4.2 Second set of modelling experiments

Following the first set of modelling experiments, there is a great interest to assess the hydrological responses of NBS scenarios in terms of the rainfall data with different spatial and temporal resolutions. Because the choice of the rainfall input strongly influences the simulated hydrological responses of NBS, and affects the assessment of the performances of NBS scenarios in the catchment scale. The main objective of this study is to analyse the variability of hydrological responses of NBS associated with the small scale rainfall variability. More precisely, the hydrological responses of the first set of NBS scenarios (GR1, PP1, RG1, and Combined1) are simulated by Multi-Hydro model under the EV4 – EV6 of different rainfall products of C-band and X-band radar (i.e., these rainfall products have been analysed by classical metrics and multifractal analysis in Section 2.4.3.3 and Section 3.8.2, respectively). The simulation results are presented with the sum of flow in the four conduits which finally merged in to the outlet of the catchment (Figure 2.5). Finally, the variability of hydrological responses of NBS associated with the small scale rainfall variability are quantified in terms of the peak flow reduction and total runoff volume reduction, by comparing with the baseline scenario.

4.2.1 Hydrological responses of baseline scenario

As shown in Figure 4.11, for the three rainfall events, the temporal evolution of the simulation flow of baseline scenario is in good agreement with the corresponding rainfall intensity for all rainfall products. Namely, the model is very sensitive to the rapid variations of the rainfall inputs (peaks).

The peak flows of baseline scenario simulated under CALAMAR and ZPHI are generally more pronounced than that of the other products, showing the highest peak flow up to 3.5, 4.5 and 8.6 m^3/s for EV4, EV5, and EV6, respectively. For the other rainfall products, the simulated peak flow is less significant compared to the CALAMAR and ZPHI. For EV4, the peak flow of the baseline scenario simulated under MeteoGroup is around 1.0 m^3/s, and that of the DPSRI and SRI is about 1.5 m^3/s. Concerning the EV5, the peak flow of the baseline scenario simulated under the X-band products has a higher peak flow than that of the C-band products at the first two rainfall peaks, with the maximum peak flow (about 3.5 m^3/s) computed for DPSRI. However, for the last peak flow of EV5, the simulated flow under ZPHI is about 3 m^3/s higher than that of the other products. Indeed, this result is in agreement with the high rainfall intensity (45.66 mm/h areal averaged) at the last rainfall peak of ZPHI data. Regarding the hydrograph of EV6, the largest peak flow for CALAMAR is 7 m^3/s, higher than that of the other rainfall products. This result is attributed to that the CALAMAR has a strong rainfall intensity at this peak (around 124 mm/h).

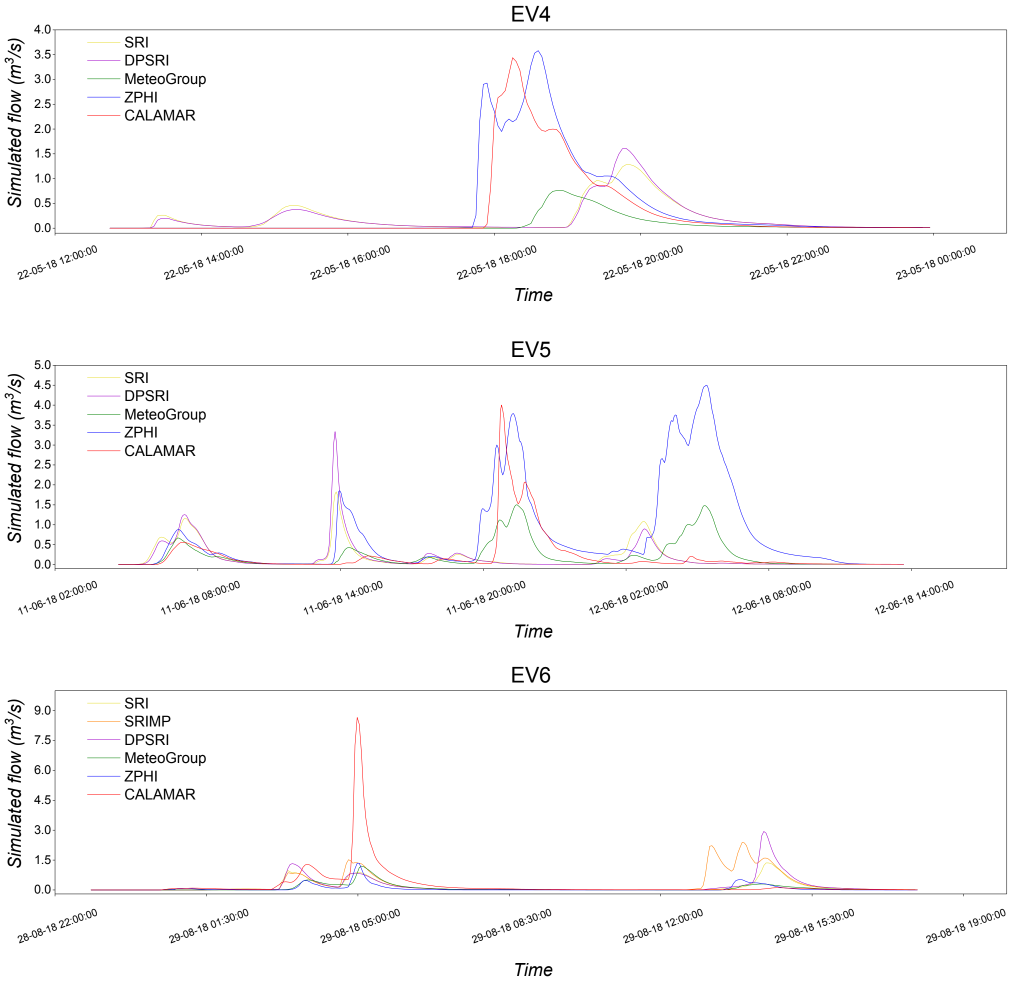

Figure 4.11: Comparison of simulated flow of baseline scenario under the three rainfall events (EV4, EV5 and EV6) of C-band and X-band radar data.

In order to statistically compare the quality of the simulation flows of baseline scenario under the different rainfall products of three rainfall events, two classical metrics are used: Nash Sutcliffe coefficient (Eq. 2.3) and correlation coefficient (Eq. 2.4).

Due to the lack of the local measurements, the simulated flows of baseline scenario from each product is taken as the reference values to compute the NSE coefficient and correlation coefficient, respectively. The results are summarised in Tables 4.1, 4.2, 4.3, 4.4, 4.5 and 4.6. For the three rainfall events, if the simulated flow of SRI is taken as the reference, the NSE values of DPSRI are range from 0.5 to 0.96. However, the NSE values of the most of C-band products are negative (-17.1 < NSE < -0.05), except for the MeteoGroup of EV6 (NSE = 0.39).

If the simulated flow of DPSRI is the reference one, the NSE values are positive for SRI (0.79 < NSE < 0.97), but negative for SRIMP (NSE = -0.01) and all C-band rainfall products (-11.5 < NSE < -0.03). For EV6, when the additional product SRIMP is taken as the reference one, the NSE values of all other products range from -0.26 to 0.33. If the reference is the simulated flow of MeteoGroup, the NSE values are negative for all available products except for ZPHI of EV6 (NSE = 0.65). If the simulated flow of ZPHI or CALAMAR considered as the reference data, the NSE values are generally negative for X-band products (except for the SRIMP), but the NSE values vary for the C-band products, depending on the rainfall event. Overall, the results of NSE significantly depend on the choice of the reference flow.

Regarding the results of correlation coefficient (Tables 4.4, 4.5 and 4.6), it is noticed that EV4 and EV6 are better than that of the EV5. For EV4 (see Table 4.4), the results of two X-band products show similar dynamics, with a correlation coefficient equal to 0.99. Furthermore, the results of CALAMAR and ZPHI are also consistent, with a correlation coefficient equal to 0.86. The results of EV6 present that the correlation coefficients of all rainfall products range between 0.28 and 0.94 (see Table 4.6). The highest correlation coefficient was computed between SRI and DPSRI, and the lowest correlation coefficient was found between CALAMAR and DPSRI. As mentioned before, for EV6, CALAMAR presents a very strong rainfall peak around 124 mm/h (areal averaged), around 7 times higher than that of the DPSRI. As shown in Table 4.5, for EV5, the correlation coefficients of all products range between -0.04 and 0.93, the negative values and the values approach to 0 are found between X-band products and C-band products (ZPHI and CALAMAR). Namely, the X-band products are not correlated to the C-band products for this rainfall event. Indeed, this can be explained by the fact that the third peak flow is very pronounced for ZPHI (> 4.5 m^3/s), while not obvious for those of the X-band radar products (< 1 m^3/s).

Nevertheless, for three rainfall events, the simulated flows of baseline scenario under two X-band radar products are correlated with each other, with the maximum NSE and correlation coefficient equal to 0.97 and 0.99, respectively. The simulated flow of baseline scenario under SRIMP matches with most of the rainfall products (except for CALAMAR), which demonstrates that the Z-R parameters (a and b) are significant for the estimation of rainfall intensity. The simulated flow of baseline scenario under MeteoGroup relatively less correlates with that of the other rainfall products, with the mean value of NSE equal to -5.68 for three rainfall events. Finally, the results (NSE and correlation coefficient) of CALAMAR and ZPHI are more dependent on the rainfall event.

Reference Simulated	X-SRI	X-DPSRI	C-MG	C-ZPHI	C- CALAMAR
X-SRI	1	0.97	-2.02	-0.15	-0.16
X-DPSRI	0.96	1	-2.64	-0.16	-0.18
C-MG	-0.04	-0.03	1	0.04	0.08
C-ZPHI	-7.73	-6.28	-20.27	1	0.66
C- CALAMAR	-5.84	-4.77	-14.96	0.74	1

Table 4.1: The NSE values of each rainfall product of EV4.

Reference Simulated	X-SRI	X-DPSRI	C-MG	C-ZPHI	C-CALAMAR
X-SRI	1	0.85	-0.71	-0.35	-0.39
X-DPSRI	0.77	1	-1.12	-0.38	-0.58
C-MG	-1.26	-0.82	1	0.24	0.33
C-ZPHI	-17.1	-11.05	-6.69	1	-3.92
C- CALAMAR	-3.15	-2.07	-0.52	-0.1	1

Table 4.2: The NSE values of each rainfall product of EV5.

Reference Simulated	X-SRI	X-SRIMP	X-DPSRI	C-MG	C-ZPHI	C-CALAMAR
X-SRI	1	0.33	0.79	-0.29	-0.83	0.17
X-SRIMP	-1.28	1	-0.01	-5.61	-6.65	0.04
X-DPSRI	0.5	0.3	1	-3.11	-0.43	0.03
C-MG	0.39	0.1	-0.19	1	0.57	0.25
C-ZPHI	-0.3	0.15	-0.15	0.65	1	0.23
C- CALAMAR	-8.05	-2.06	-3.44	-16.52	-20.9	1

Table 4.3: The NSE values of each rainfall product of EV6.

Reference Simulated	X-SRI	X-DPSRI	C-MG	C-ZPHI	C-CALAMAR
X-SRI	1	0.99	0.39	0.06	0.05
X-DPSRI	0.99	1	0.37	0.07	0.06
C-MG	0.39	0.37	1	0.56	0.51
C-ZPHI	0.06	0.07	0.56	1	0.86
C- CALAMAR	0.05	0.06	0.51	0.86	1

Table 4.4: The correlation coefficient of each rainfall product of EV4.

Reference Simulated	X-SRI	X-DPSRI	C-MG	C-ZPHI	C-CALAMAR
X-SRI	1	0.93	0.041	-0.01	-0.04
X-DPSRI	0.93	1	0.03	-0.003	-0.04
C-MG	0.041	0.03	1	0.89	0.58
C-ZPHI	-0.01	-0.003	0.89	1	0.38
C- CALAMAR	-0.04	-0.04	0.58	0.38	1

Table 4.5: The correlation coefficient of each rainfall product of EV5.

Reference Simulated	X -SRI	X-SRIMP	X-DPSRI	C -MG	C-ZPHI	C-CALAMAR
X-SRI	1	0.64	0.94	0.66	0.62	0.46
X-SRIMP	0.64	1	0.61	0.49	0.64	0.32
X-DPSRI	0.94	0.61	1	0.5	0.5	0.28
C-MG	0.66	0.49	0.5	1	0.82	0.8
C-ZPHI	0.62	0.64	0.5	0.82	1	0.84
C- CALAMAR	0.46	0.32	0.28	0.8	0.84	1

Table 4.6: The correlation coefficient of each rainfall product of EV6.

4.2.2 Hydrological responses of NBS scenarios

As shown in the hydrographs of Figures 4.12, 4.13 and 4.14, a typical hydrological response of NBS scenarios can be summarised for all rainfall products of three rainfall events: the simulated flows of NBS scenarios are lower than that of the baseline scenario, especially at the rainfall peaks. This result indicates that NBS can effectively attenuate the runoff under different rainfall conditions. Regarding the simulated flow of each NBS scenario for different rainfall products, the difference is significant for the same rainfall event. Firstly, the simulated flows of two C-band products (i.e., CALAMAR and ZPHI) are generally higher than that of the MeteoGroup and X-band radar products. For instance, the maximum simulated flows of NBS scenarios are around 8 m^3/s and 5 m^3/s for CALAMAR and ZPHI in EV6, respectively. However, the simulated flows of NBS scenarios under MeteoGroup and X-band radar products are around 50 % lower than that of the CALAMAR and ZPHI. Indeed, the reason is that the rainfall intensity of CALAMAR and ZPHI is much higher than that of the other products.

Concerning the hydrological responses of each type of NBS scenario, the GR scenario is very efficient at the beginning of the rainfall event with lower flow, compared with the PP and RG scenario. However, with the continuing of the rainfall, especially when the rainfall event consists of several peaks, the performance of GR is simultaneously attenuated. This is due to that the substrate of GR gradually saturated during the whole rainfall period. This performance is in agreement with the investigation by other researchers (Qin et al., 2013; Versini et al., 2016). Furthermore, it is noticed that performances of NBS are indeed less effective under the rainfall with high intensity (Figure 4.14). For instance, for EV6, the CALAMAR data is characterised with the highest rainfall peak around 124 mm/h. After this rainfall peak, some types of NBS are saturated, resulting in a higher flow than that of the baseline scenario (e.g. PP1, RG1, and GR1). Only the Combined1 scenario presents a lower flow than the baseline scenario. Namely, a combination of different NBS with a higher fractal dimension in the catchment is more effective under strong rainfall events.

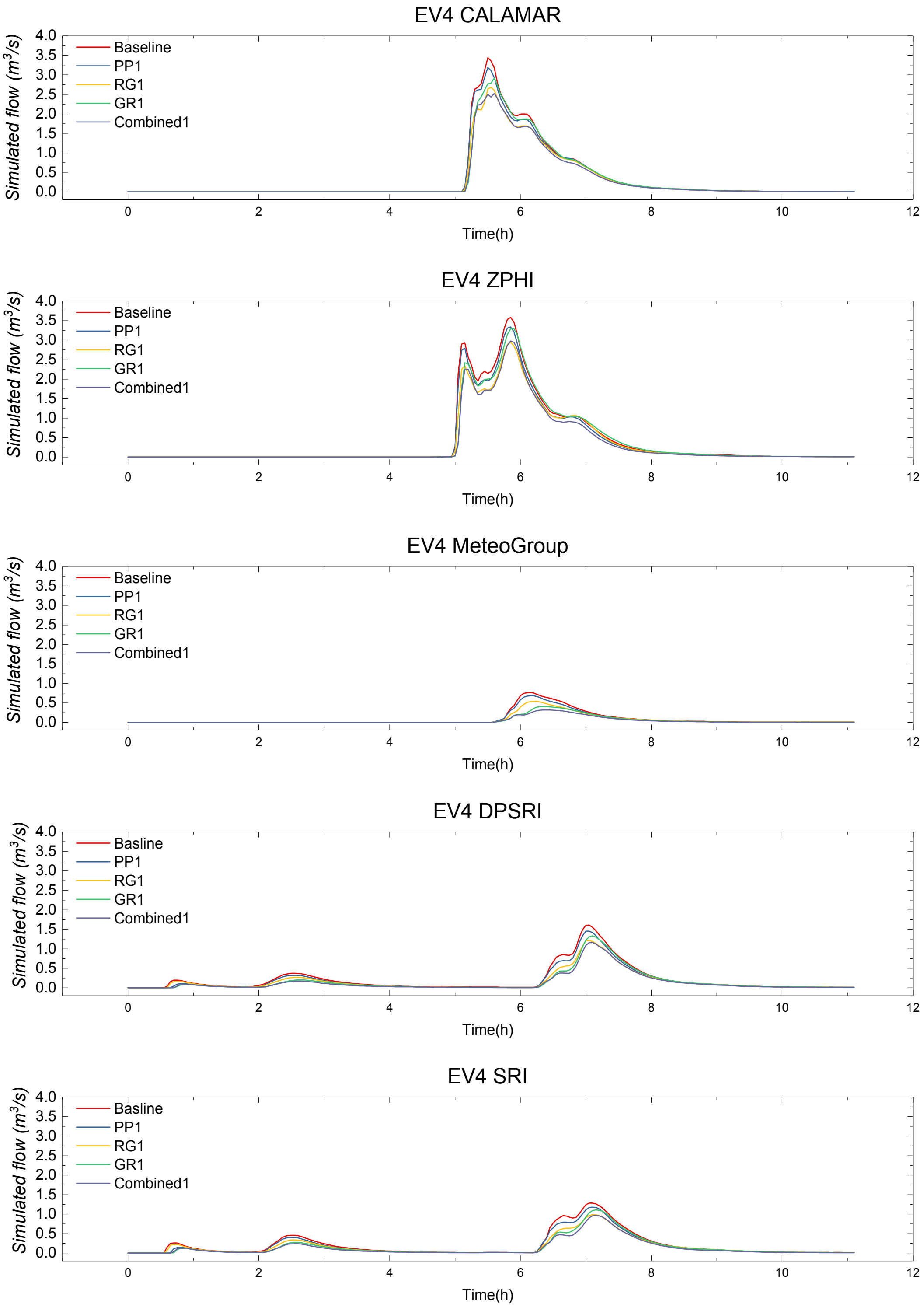
EV4 CALAMAR

EV4 ZPHI

EV4 MeteoGroup

EV4 DPSRI

EV4 SRI

Figure 4.12: Hydrographs of baseline scenario and NBS scenarios for each rainfall product of EV4.

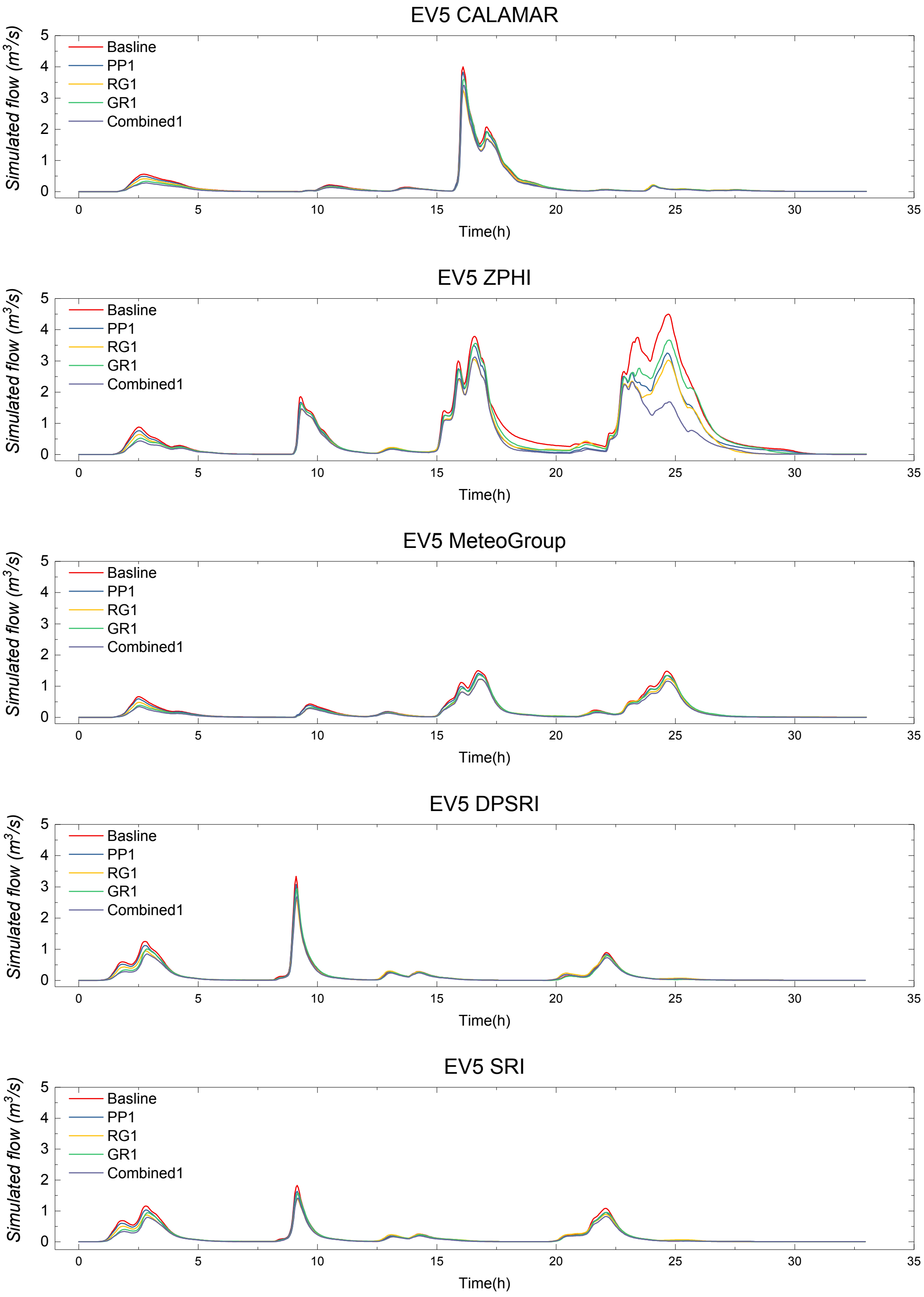

Figure 4.13: Hydrographs of baseline scenario and NBS scenarios for each rainfall product of EV5.

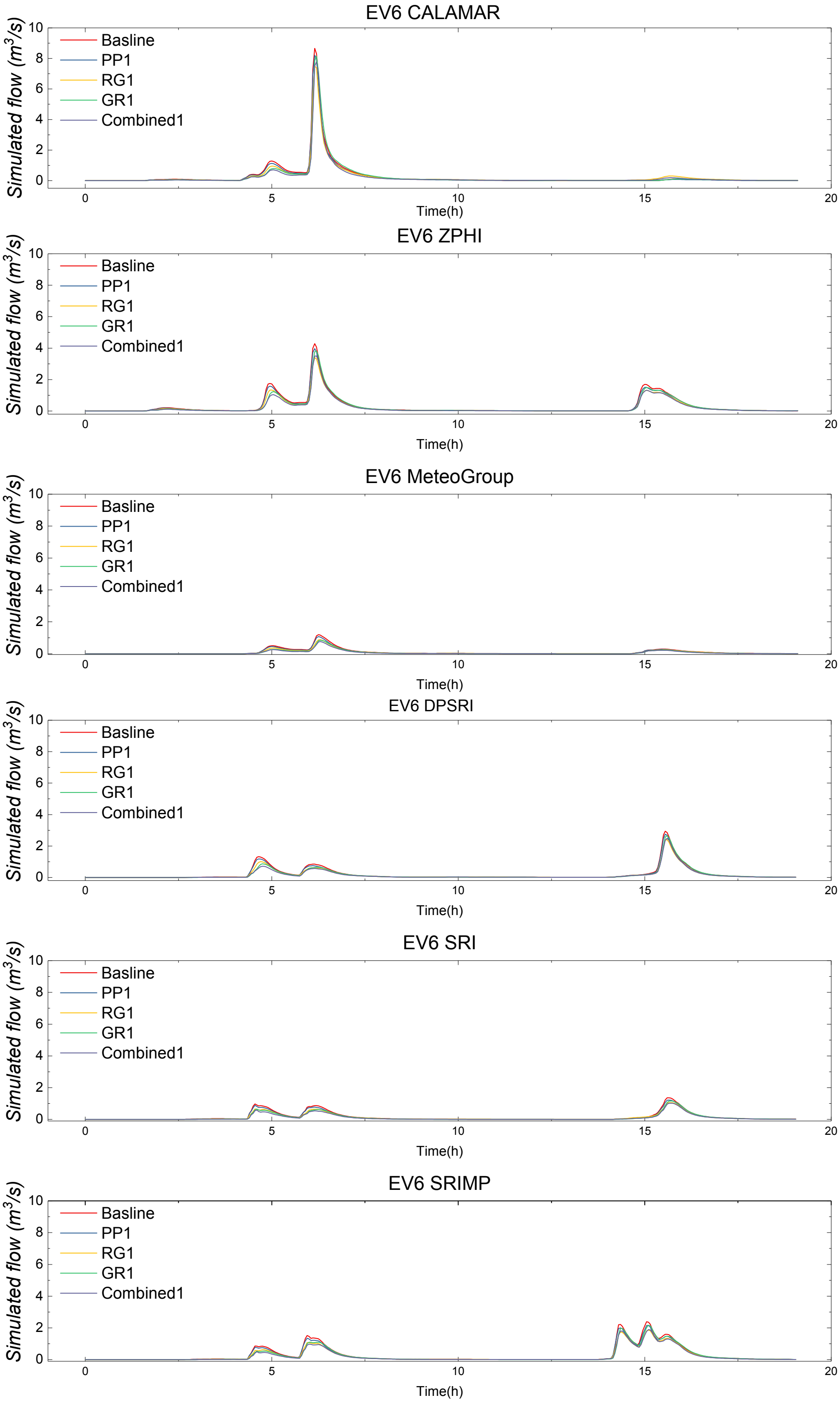
EV6 CALAMAR

EV6 ZPHI

EV6 MeteoGroup

EV6 DPSRI

EV6 SRI

EV6 SRIMP

Figure 4.14: Hydrographs of baseline scenario and NBS scenarios for each rainfall product of EV6.

4.2.3 Hydrological performances of NBS scenarios

4.2.3.1 Peak flow reduction

The hydrological performances of NBS scenarios are evaluated and compared with the baseline scenario. More precisely, the two hydrologic performance indexes, peak flow reduction (ΔQp) and total runoff volume reduction (ΔV), are computed for each NBS scenario under different rainfall products of three rainfall events. The peak flow reduction is calculated as the relative percentage error between the peak flow of the baseline scenario and NBS scenarios (Eq. 4.4); total runoff volume reduction is computed similarly (Eq. 4.5).

$$\Delta Q\mathrm{p}(\%) = \frac{Q_{P_{\mathrm{base}}} - Q_{p_{\mathrm{NBS}}}}{Q_{P_{\mathrm{base}}}} \times 100 \tag{4.4}$$

$$\Delta \mathrm{V}(\%) = \frac{V_{\mathrm{base}} - V_{\mathrm{NSB}}}{\mathrm{V}_{\mathrm{base}}} \times 100 \tag{4.5}$$

where $\mathrm{Q}_{P_{\mathrm{base}}}$ and $\mathrm{V}_{\mathrm{base}}$ refer to the peak flow and total runoff volume of the baseline scenario, respectively. Correspondingly, $\mathrm{Q}_{p_{\mathrm{NBS}}}$ and V_{NBS} are those for different NBS scenarios, respectively.

Regarding the peak flow reduction of the NBS scenarios for different rainfall products of three rainfall events, the performances of each NBS scenario vary under different rainfall products. For instance, in EV4 and EV6, the peak flow reduction of GR1 is higher than that of PP1 and RG1 in terms of the MeteoGroup data. However, for the other rainfall products, the peak flow reduction of GR1 is lower than that of the RG1. Similarly, the peak flow reduction of Combined1 scenario is generally higher than that of the other NBS scenarios, because this scenario combining different types of NBS, presents a higher fractal dimension (see more details about the fractal dimension in Section 3.1.1). However, for EV5, the peak flow reductions of Combined1 under the CALAMAR and DPSRI data are slightly lower than that of the RG1.

As shown in Figure 4.15, for all the rainfall products of EV4, the peak flow reduction of PP1 scenario ranges from 7 % to 11 %, while that of the RG1 scenario ranges from 17 % to 29 %. For these two scenarios, the difference between the minimum and maximum peak flow reduction is around 4 % and 12 %, respectively. This result presents the performances of RG1 scenario is more variable than that of the PP1 scenario simulated under different rainfall inputs of EV4. Regarding the scenarios of GR1 and Combined1, this difference is even more significant (> 39 %). The minimum peak flow reduction of GR1 and Combined1 scenario was found for the ZPHI data, around 8 % and 17 % respectively. Similarly, the maximum peak flow reduction of GR1 and Combined1 scenario was found for MeteoGroup, which is approximately 47 % and 60 %, respectively. Indeed, the difference is more significant for GR1 and Combine1 scenario may related to the storage capacity of GRs.

Regarding the EV5, the peak flow reduction of NBS scenarios simulated under different rainfall product is also very variable. For instance, the difference between the minimum and maximum peak flow reduction of Combined1 scenario, and PP1 scenario is around 48 % and 24 %, respectively. Concerning the EV6, the peak flow reduction of Combined1 scenario is more variable than that of the other NBS scenarios. The difference between the minimum and maximum peak flow reduction of Combined1 scenario is about 25 %. Similar to the EV4, the peak flow reduction of PP1 scenario under each rainfall product of EV6 is less variable, compared with the other NBS scenarios.

For the same rainfall event, the peak flow reductions of NBS scenarios have significant differences due to the small scale rainfall variability. In these rainfall events, the difference in peak flow reduction is most significant for Combined1 scenario, reaching 48 % in EV5. This indicates the small scale rainfall variability has an essential impact on the hydrological performances of NBS scenarios, especially for a combination of different types of NBS.

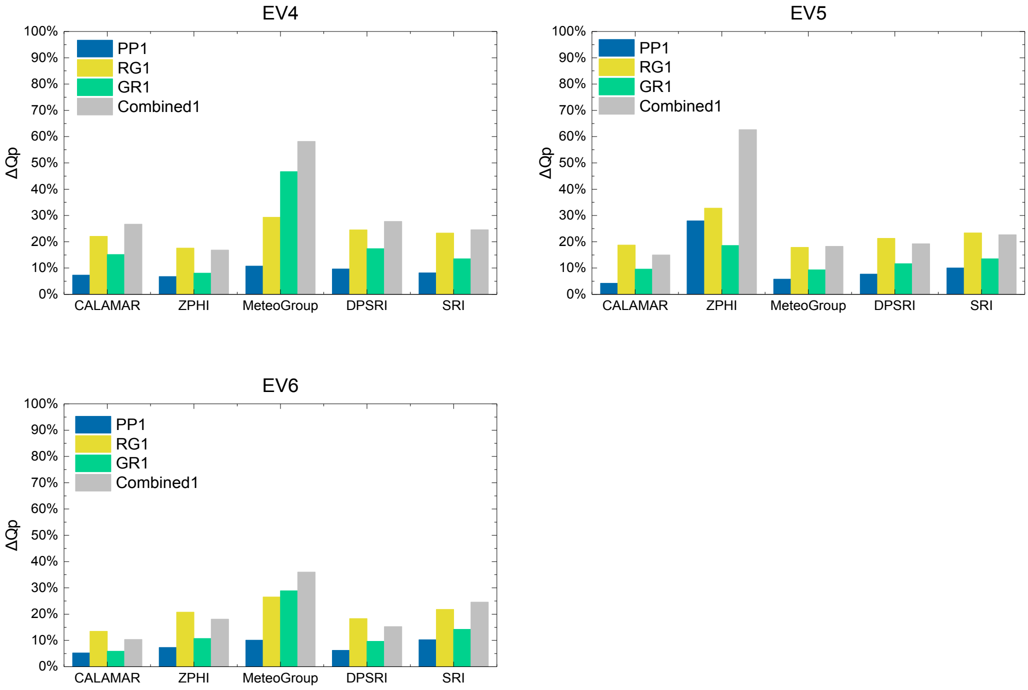

Figure 4.15: Peak flow reduction of NBS scenarios for each rainfall product of three rainfall events.

4.2.3.2 Total runoff volume reduction

Regarding the total runoff volume reduction of each NBS scenario for all rainfall products of three rainfall events, Combined1 scenario is higher than that of the other NBS scenarios, and the PP1 scenario is relatively lower than that of the other scenarios (except for ZPHI of EV5, PP1 scenario has higher total runoff volume reduction than that of the GR1 scenario). For the scenario of GR1 and RG1, the total runoff volume reduction of the latter is generally higher than that of the former for most of the rainfall products. For instance, in EV4 and EV6, the total runoff volume reductions of RG1 scenario are higher than that of the GR1 under the products of CALAMAR, ZPHI, DPSRI, SRI and SRIMP. However, for MeteoGroup data, the total runoff volume reduction of the RG1 scenario is lower than that of the GR1. These results indicate that green roof is more effective in terms of the total runoff volume reduction under the rainfall events with lower rainfall intensity.

For EV4 (see Figure 4.16), the total runoff volume reduction of PP1 scenario ranges from 5 % to 14 % under each rainfall product, while that of the RG1 scenario ranges from 14 % to 25 %. For the GR1 scenario, the difference of total runoff volume reduction between each product is relatively more significant than that of PP1 and RG1 scenario. For the CALAMAR and ZPHI, the total runoff volume reduction of GR1 scenario is around 7 %, while about 40 %, 25 % and 24 % for MeteoGroup, DPSRI and SRI, respectively.

For EV5, it is found that the total runoff volume reduction of PP1 scenario under DPSRI is the lowest (7 %), while that of the highest one (24 %) is under ZPHI. The total runoff volume reduction of Combined1 scenario under each rainfall product in EV5 also varies in a large range. For instance, the highest total runoff volume reduction of Combined 1 scenario is found for ZPHI (44 %), while that of the lowest one is found for DPSRI (around 21 %). The total runoff volume reduction of GR1 scenario is relatively stable under all rainfall products, which ranges from 12 % to 16 %.

For the EV6, the total runoff volume reduction of PP1 scenario for each rainfall product is less variable, compared with the other rainfall events. The difference in total runoff volume reduction between each product is around 1 %. For the RG1 scenario, only the total runoff volume reduction for CALAMAR is about 10 %, lower than that of the other rainfall products. For the GR1 and Combined1 scenario, the difference of total runoff volume reduction between each rainfall product is relatively higher (e.g. the difference between CALAMAR and MeteoGroup is the largest, about 20%).

Overall, the NBS scenarios simulated with different radar data with different spatial and temporal resolution result in the evaluation of hydrological performances of NBS scenario have significant discrepancies. Apparently, this discrepancy is more pronounced for the scenario of GR1 and Combined1.

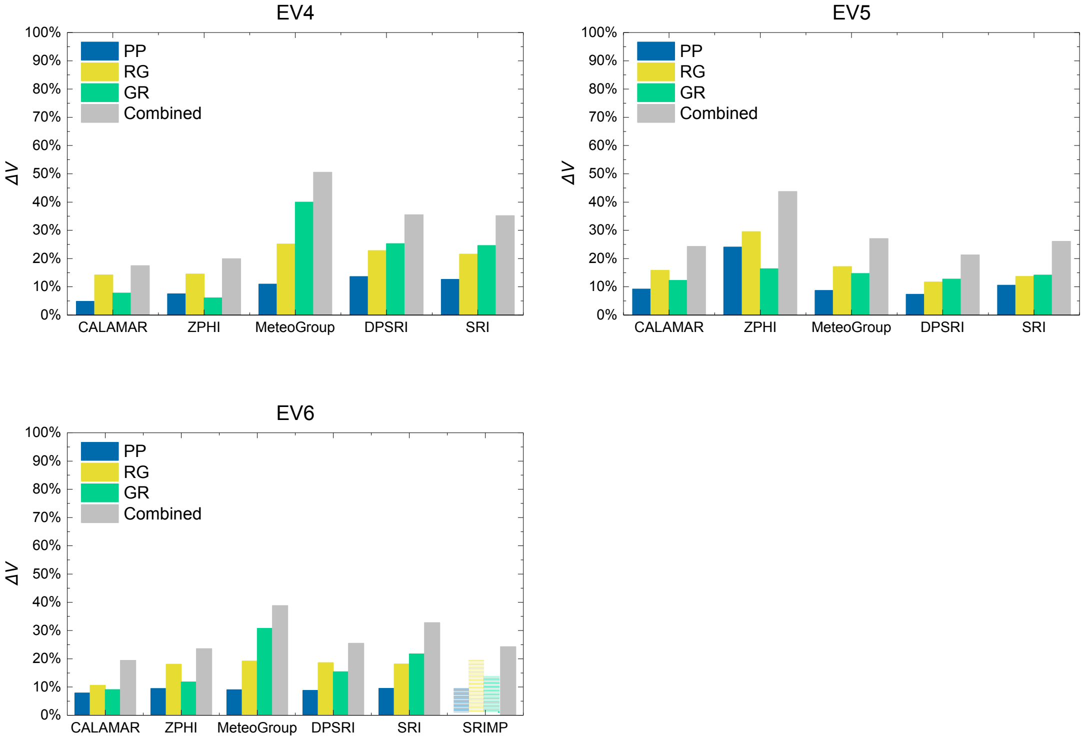

Figure 4.16: Total runoff volume reduction of NBS scenarios for each rainfall product of three rainfall events.

4.2.4 Statistical analysis of NBS scenarios

The statistical analysis of performances of NBS scenarios is based on the correlation coefficient of peak flow reduction / total runoff reduction of NBS scenarios for each rainfall product. The results are plotted by scatter matrix (see Figures 4.17, 4.18, 4.19, 4.20, 4.21, and 4.22 for more information), which consists of several pair-wise scatter plots of variables presented in a matrix format. The aim is to determine whether the performances of NBS under different rainfall products are correlated and the correlation is positive or negative.

As shown in Figures 4.17 and 4.19, for EV4 and EV6, the peak flow reductions of NBS scenarios for MeteoGroup are not correlated with that of the other rainfall products. The results of the other four rainfall products (i.e., CALAMAR, ZPHI, DPSRI, and SRI) are quite correlated. Namely, the performances of NBS scenarios simulated under the MeteoGroup may have a particular discrepancy with their real performance. Indeed, the rainfall intensity and cumulative rainfall of MeteoGroup is relatively lower than that of the other products (Figure 2.10). Furthermore, as discussed in Chapter 3, the multifractality (α) of MeteoGroup (DTM analysis) is lower than that of the other rainfall products, which means some rainfall spikes may not be detected by this rainfall product. Therefore, the performances of NBS scenarios simulated by MeteoGroup have a quite different behaviour, compared to that of the other rainfall products.

For EV5 (see Figure 4.18), the peak flow reduction of NBS scenario for ZPHI is not correlated with the other rainfall products. This can be explained by that the rainfall intensity of ZPHI is much higher than that of the other rainfall products at the highest rainfall peak.

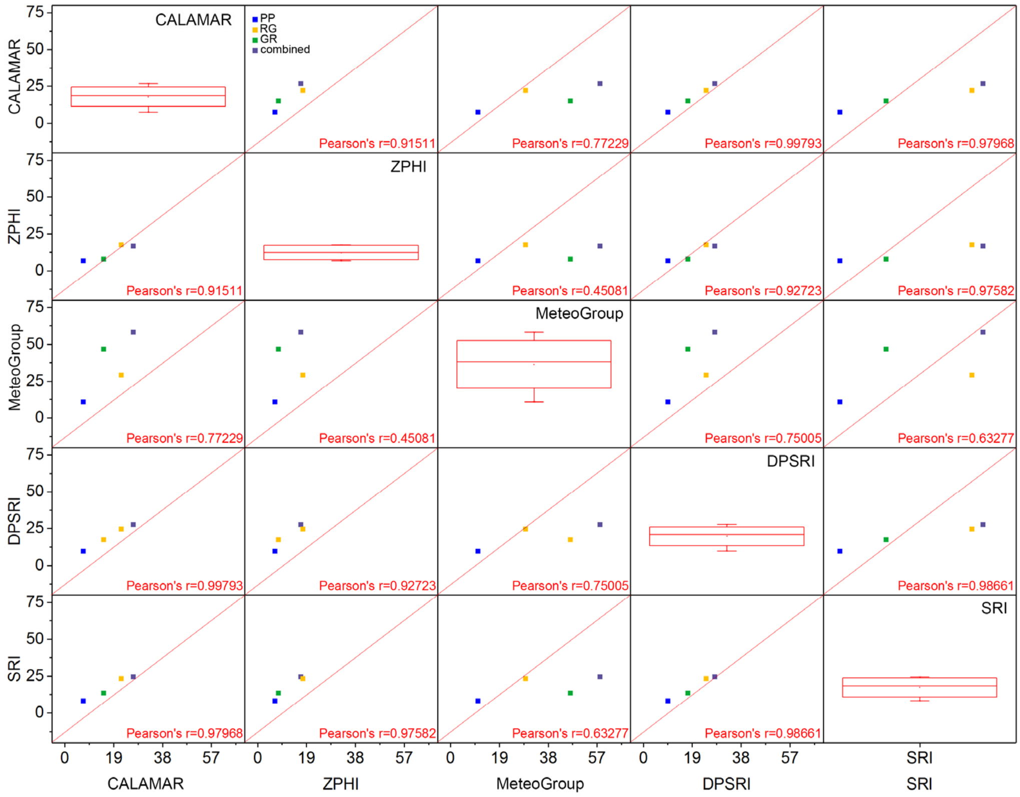

Figure 4.17: Scatter matrix of peak flow reduction of NBS scenarios for each rainfall product of EV4.

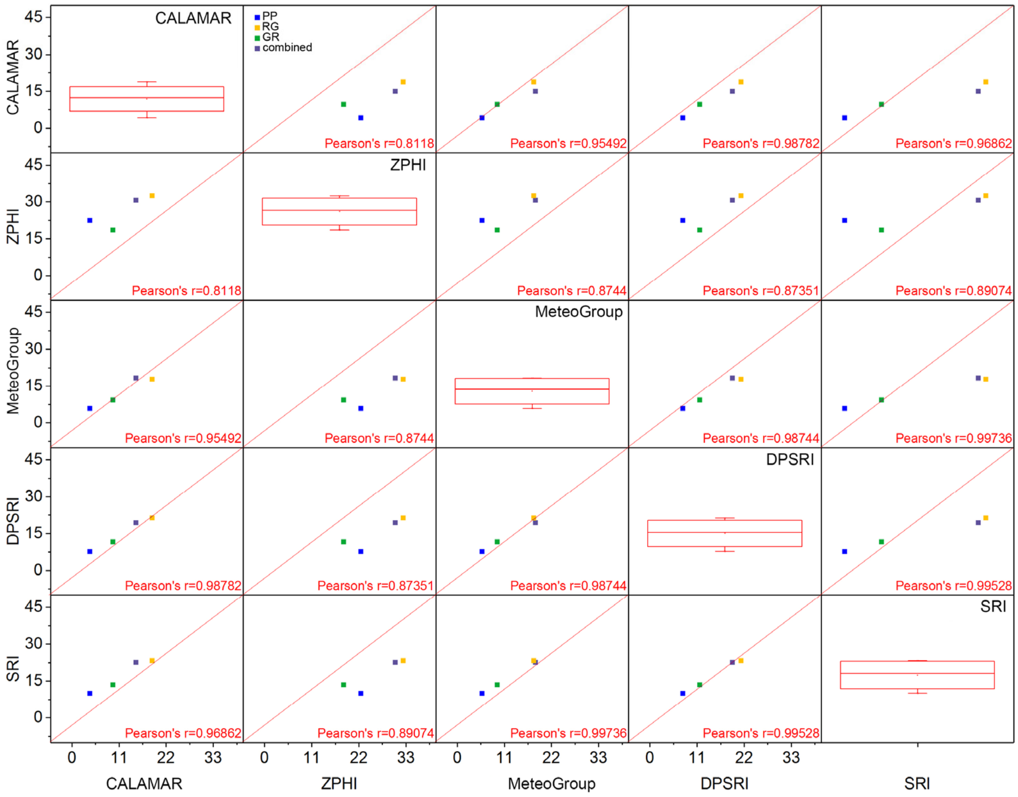

Figure 4.18: Scatter matrix of peak flow reduction of NBS scenarios for each rainfall product of EV5.

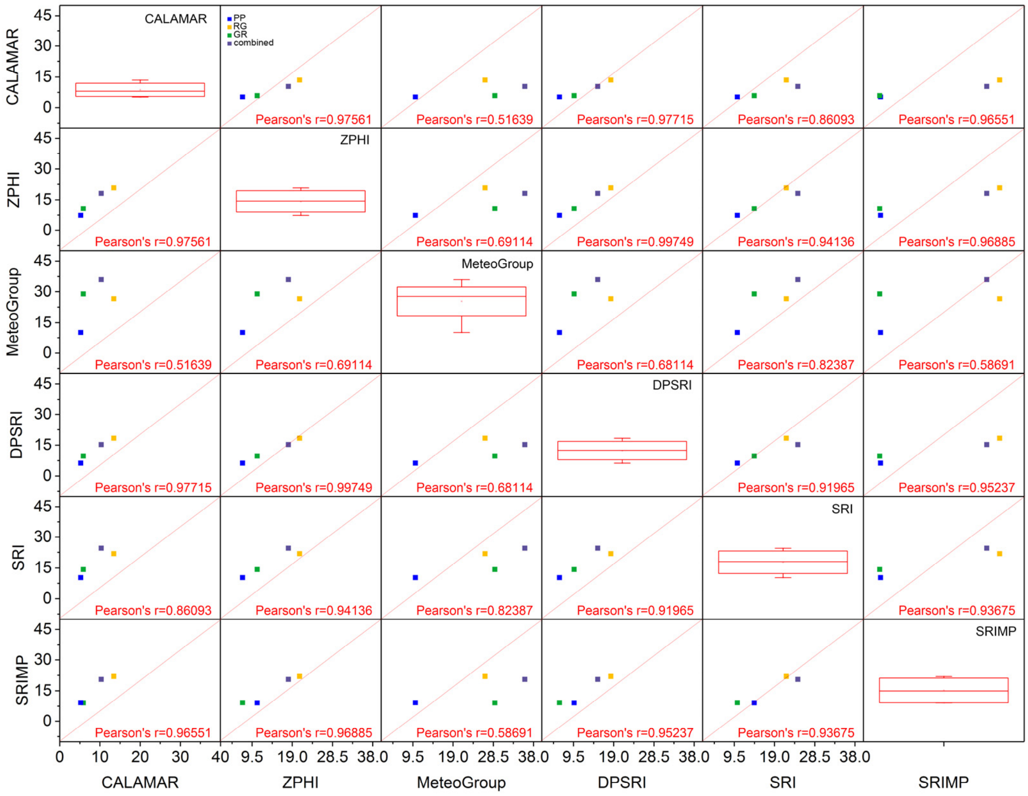

Figure 4.19: Scatter matrix of peak flow reduction of NBS scenarios for each rainfall product of EV6.

Regarding the total runoff volume reduction of NBS scenarios under each rainfall product of EV4, it is noticed that the performances of NBS scenarios simulated under MeteoGroup are not correlated with that of CALAMAR and ZPHI. This reason is the same as that mentioned previously. Furthermore, the total runoff volume reduction of NBS scenarios for ZPHI is less correlated with DPSRI and SRI. The reason can be explained by the fact that the cumulative rainfall of ZPHI is 50 % higher than the other rainfall products. Thus, the NBS simulated with this data is easier to be saturated, and the total runoff reduction is far less than that of the NBS scenario simulated with other rainfall products.

For EV5, the performances of NBS scenarios simulated with ZPHI are less correlated with that of the other rainfall products. As discussed in Section 3.8.2, this event has a higher multifractality than EV4 and EV6 (mean value of $\alpha = 0.67$). For the first two rainfall peaks, ZPHI has relatively lower rainfall intensities. Thus, NBS may not be saturated during this period. Then, ZPHI has two extreme rainfall peaks, which finally increased the cumulated rainfall. Because NBS simulated under the ZPHI are not saturated at the beginning, the total runoff volume reduction of NBS scenario is higher for this product. For the other rainfall products, the total runoff volume reductions of NBS scenarios under each rainfall product are correlated, which may be due to that the spatial distribution of cumulative rainfall of these products are relatively uniform (Figure 2.13).

For EV6, the performances of NBS scenarios simulated with MeteoGroup are not correlated with that of CALAMAR, ZPHI, and SRIMP. The reason is similar to that mentioned previously: the cumulative rainfall of MeteoGroup is much lower than that of the CALAMAR, ZPHI and SRIMP. Furthermore, the α of MeteoGroup is also lower than that of the other rainfall products, and the simulated flows of NBS scenarios may be smoothed under this product, especially for some peak flows.

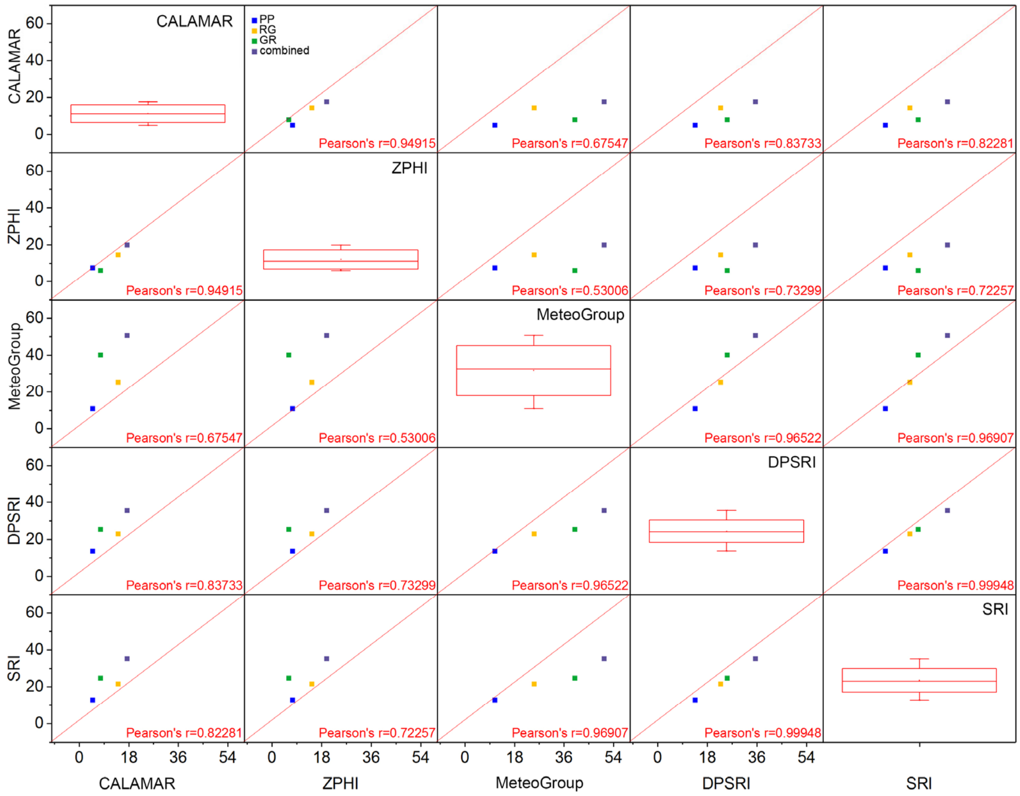

Figure 4.20: Scatter matrix of total runoff volume reduction of NBS scenarios for each rainfall product of EV4.

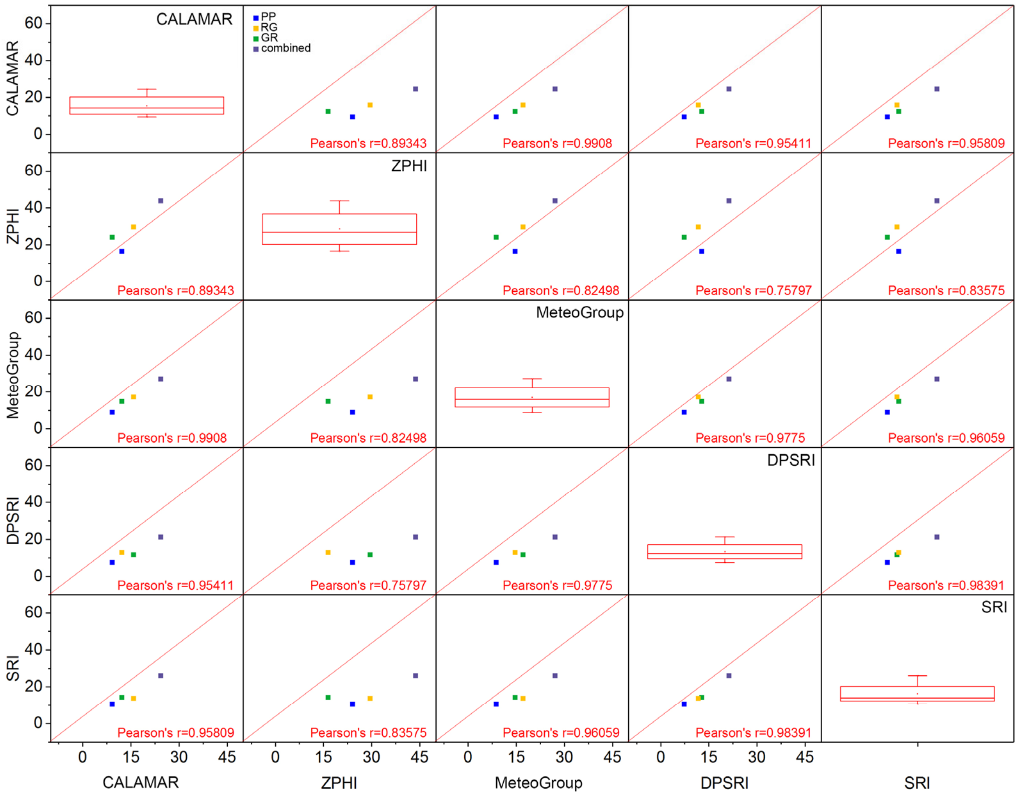

Figure 4.21: Scatter matrix of total runoff volume reduction of NBS scenarios for each rainfall product of EV5.

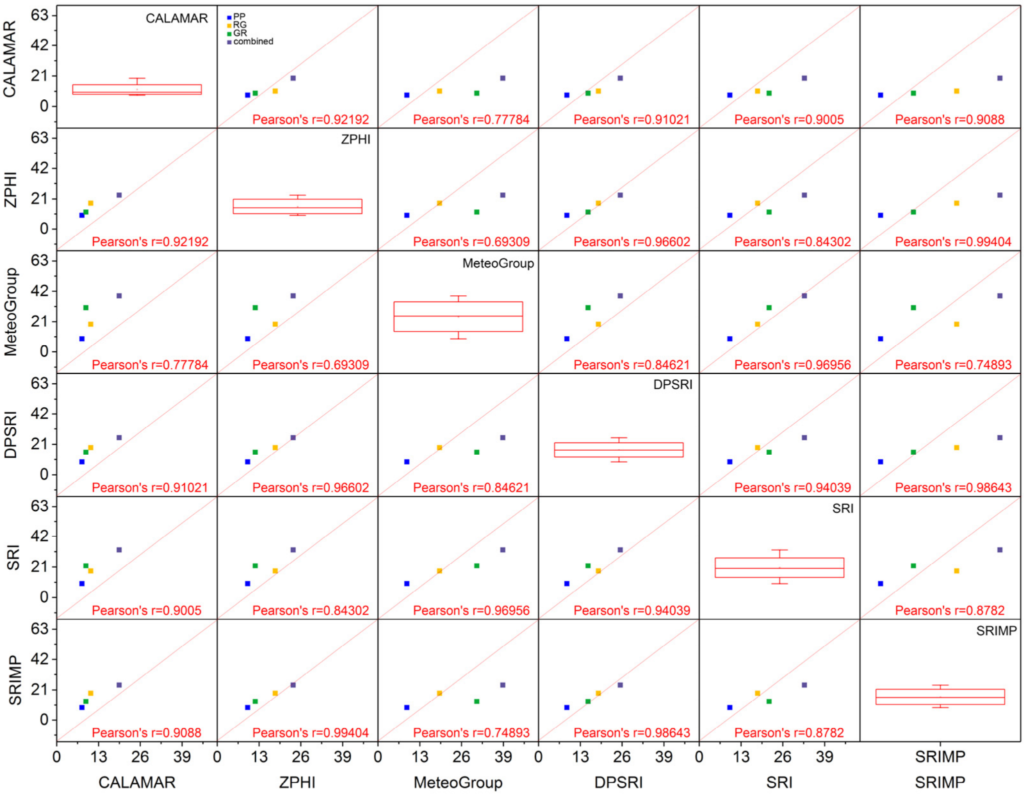

Figure 4.22: Scatter matrix of total runoff volume reduction of NBS scenarios for each rainfall product of EV6.

4.2.5 Intermediate conclusions for Section 4.2

In this section, the impacts of small scale rainfall variability on the hydrological responses of NBS were investigated. Six different rainfall products from C-band radar and X-band radar characterised with different spatio-temporal resolutions were used as the rainfall inputs for the modelling experiments. The first set of NBS scenarios were investigated: PP1, RG1, GR1 and Combined1. Several main findings can be summarised as follows:

(i) The temporal evolution of the simulated flow of baseline scenario is mostly in agreement for all rainfall products. For the three rainfall events, the simulated flows of baseline scenario under two X-band radar products are correlated with each other. The simulated flow of baseline scenario under SRIMP is correlated with most of the rainfall products (except for CALAMAR), which demonstrates that the *Z*-*R* parameters (*a* and *b*) are significant for the estimation of rainfall intensity. The simulated flow of baseline scenario under MeteoGroup is relatively less correlated with that of the other rainfall products.

(ii) The performances of NBS scenarios vary under different rainfall products. For the same rainfall event, the peak flow reduction and total runoff volume reduction of NBS scenarios have significant differences under different rainfall inputs. For the three studied rainfall events, the most significant difference of peak flow reduction was found for Combined1 scenario, which is around 48 %. This indicates that the small scale rainfall variability has an essential impact on the evaluation of the performances of NBS scenarios.

(iii) The hydrological performances of NBS scenarios simulated under the MeteoGroup are less correlated with that of the other rainfall products. The reason is due to that the rainfall intensity, cumulative rainfall, and rainfall intermittency of this product are relatively lower, compared with that of the other products. Furthermore, the low multifractality of this product results in several spikes of the simulated flow are smoothed. Finally, the hydrological performances of NBS scenarios simulated under MeteoGroup may be overestimated, compared with that of the other rainfall products.

Overall, the rainfall data plays an essential role in the reliability of the hydrological responses of the catchment and NBS scenarios. The spatio-temporal resolution, rainfall data processing process, and the selection of the best products are the factors which influence the hydrological responses. This study shows that the hydrological performances of NBS scenarios simulated with X-band radar data are more stable than that of the C-band radar for three rainfall events, which is related to the impacts of higher resolution of rainfall data. This was investigated by performing universal multifractals analysis on C-band and X-band radar data, which indicates that value of multifractality index α for the X-band radar products is higher than that of C-band radar products for the three studied rainfall events. This result indicates that to improve the resolution of the rainfall input is significant for the hydrological modelling of NBS. For the future studies, the impact of the small scale rainfall variability on the hydrological performances of NBS needs to be further studied. Furthermore, there is a strong need to find a scale-independent indicator to evaluate the performances of NBS across range of scales (see next section for detailed information), because the hydrological performances of NBS scenarios simulated with hydrological models strongly related to the scale, which will greatly affect the final cost-effective design of NBS scenarios in a catchment scale (see Chapter 5 for the cost-effective analysis of NBS scenarios).

4.3 Third set of modelling experiments: multifractal characterisation of overland flow

As introduced in Chapter 3, the Universal Multifractal is a stochastic approach used widely in geophysics to characterise extremely variable fields over a wide range of scales. Following the studies of Sections 4.1 and 4.2, this section intends to use UM framework for investigating the potential multifractal characteristics of overland flow in Guyancourt catchment under different rainfall events (i.e., the EV1-EV3, EV4S and EV5S) and to evaluate the hydrological performances of NBS scenarios (i.e., the first set). This time, in terms of an eventual improvement of the morphological functioning of the catchment. This should complete the study on the NBS efficiency across the scales for the stormwater management in resilience cities.

4.3.1 Multifractal analysis of 2D overland flow maps

In this study, the baseline and NBS scenarios were firstly simulated by Multi-Hydro model with the spatial resolution of 10 m and the time step of 3 min. More precisely, the baseline scenario was simulated under five rainfall events (EV1, EV2, EV3, EV5S and EV6S), and then the first set of NBS scenarios was simulated under the EV2.

The 2D maps of overland flow are the outputs of Multi-Hydro model. An example is shown in Figure 4.23, the last time step of the 2D overland flow map of the baseline scenario that simulated under the EV2 with z-axis plotted in log-scale. For avoiding the no data areas that may biased the results of UM analysis, the area of 128 × 128 pixels (each pixel with the size of 10 m × 10 m) was extracted from the overland flow map. This square area will be analysed with the help of UM framework. In order to obtain the temporal evolutions of the UM parameters and the critical singularities (see Sub-section 4.3.3 for details), the same square area in the 2D overland flow map at each time step are analysed.

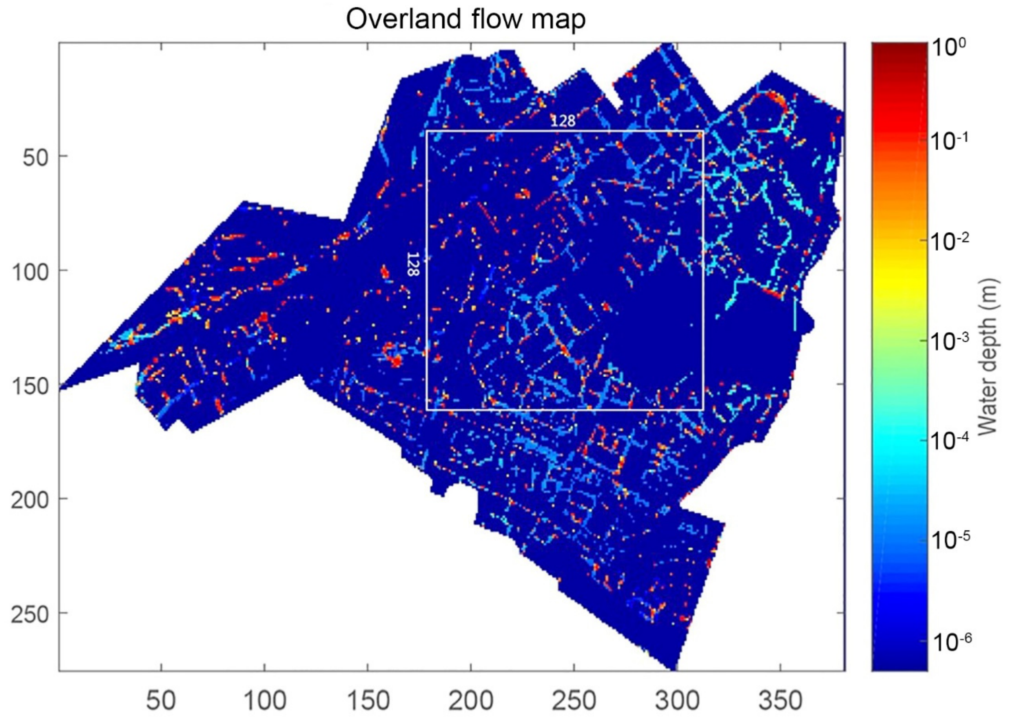

Figure 4.23: The last time step of 2D overland flow map under the EV2, the z-axis plotted in log-scale.

4.3.2 Temporal evolution of UM parameters

The 2D maps of the overland flow of baseline scenario under three rainfall events are analysed by the TM technique. Figure 4.24 displays the log-log plot of the TM ensemble analysis of the 2D overland flow maps for over all the time steps of three rainfall events. It is noticed that there exists a scaling break roughly at the 80 m, which indicates a possible physical interpretation. The reason may be related to the land use distributions of the catchment. Indeed, the location of the scaling break is the same as the fractal analysis of the NBS scenarios (see Chapter 3 for more discussions). This indicates the break is driven by the impacts of the imperviousness of the catchment.

Here, the coefficient of determination r^2 for the linear regression of q = 1.5 is regarded as an indicator to evaluate the scaling quality. Figure 4.25 shows the temporal evolution of r^2 for the linear regression of q = 1.5 in TM analysis for the three rainfall events. On the whole, the temporal evolution of r^2 in all range of scales is relatively variable, and the mean value of r^2 of three rainfall events is around 0.84, 0.85, and 0.86, respectively. Associated with the rainfall rate of each event, the scaling quality has a sudden decrease at the rainfall peaks, which reflects that the estimation of UM parameters is less reliable at these moments. However, in order to compare the temporal evolution of maximum probable singularity γ_s and effective maximum singularity γ_{max}, they are kept for the following analysis. Furthermore, as two scaling regimes were found in TM analysis, they are also used for investigating the multifractal characteristics of the overland flow in small-scale (10-80 m) and large scale (80-1280 m).

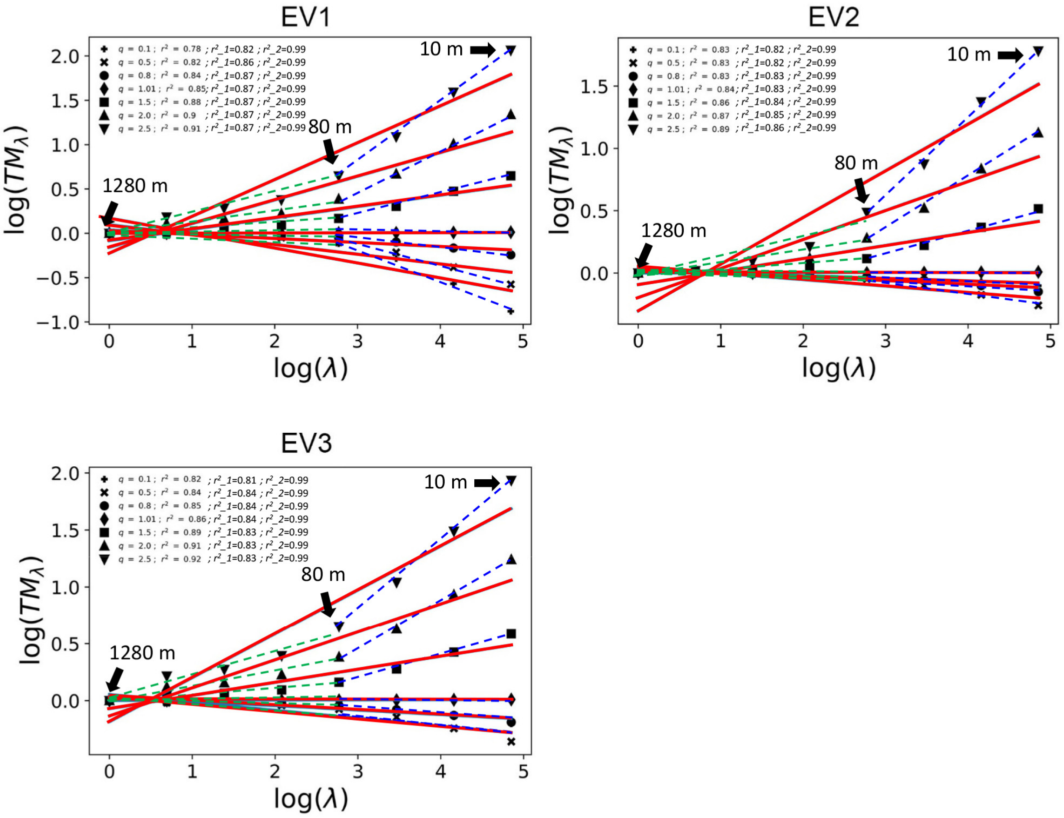

Figure 4.24: Ensemble TM analysis of 2D overland flow maps over all the time steps under three rainfall events (the linear regression of full, small scale and large scale range is represented in solid red line, blue dash line and green dash line, respectively).

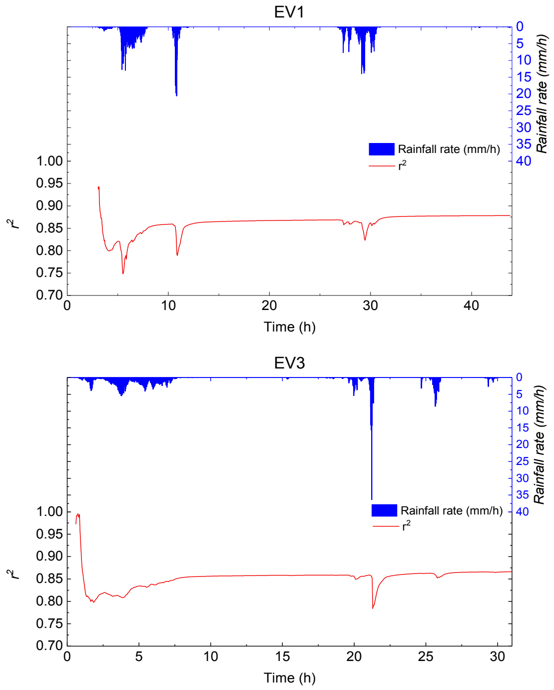

Figure 4.25: Temporal evolution of coefficient of determination r^2 for the linear regression of $q = 1.5$ under three rainfall events of 2015.

As shown in Figures 4.26 and 4.27, the temporal evolutions of C_1 and α in full range, small scale range, and large scale range have an opposite trend (α increasing and C_1 decreasing, vice versa) for three rainfall events. Indeed, these two parameters measure the variability of the overland flow of the field from different aspects. It is noticed that the temporal evolution of UM parameters is strongly affected by the rainfall intermittency. During the intensive rainfall periods, the UM parameters are very variable. For instance, at the largest rainfall peak of EV1 and EV3, the values of α and C_1 approach to 2 and 0, respectively. Namely, at this moment, overland flow exists in most pixels, and some pixels additionally accumulate very high surface flow, resulting in maximised α and minimised C_1. These results demonstrate that the extremes of overland flow depend on both α and C_1. Besides, during the periods when the rainfall already stopped, the UM parameters may stay constant due to a residual distribution of water depth. The mean values of C_1 (full range) for three rainfall events are 0.68, 0.83, and 0.67, respectively. Correspondingly, the mean values of α (full range) are 0.38, 0.61, and 0.39, respectively. These mean values suggest that EV2 is characterised by the strongest extremes among these three events.

Comparing the UM parameters estimated over the full, small scale and large scale ranges, it is noticeable that the small scale range exhibits much stronger intermittency, supported by much higher estimates of C_1, than that of the full or large scale ranges. The values larger C_1>1 indicates that the phenomena is so sparse that almost surely cannot be observed over a 1D cut of the field. This reflects the intrinsic variability of the 2D overland flow over the range small scales of the catchment. As already mentioned, the physical meaning of UM parameters (see Chapter 3), implies that for a given value of α, an increase of the intermittency C_1 responds by a sparser overland flow, thus, amplifying the intensity of extremes, as a certain amount of overland flow concentrates on a smaller set. Similarly, for a given value of C_1, an increase of multifractality α responds by higher variability of overland flow, also amplifying to extremes. Hence, if the UM parameters vary in the same direction, their impacts on the overland flow extremes reinforce each other. Conversely, if UM parameters vary in an opposite direction, like in the case of this study, their impact on the overland flow will tend to compensate each other, and the resulting response of extremes will sensitivity depend on which of the two parameters is dominant.

The decrease of C_1 and simultaneous increase of α during rainfall peaks indicates that the overland flow gradually increases over the field, and they are continuously concentrated on pixels of given land uses, especially on some impervious surfaces (see Figure 4.23). When the rainfall peaks get over, the C_1 values are increased and α values are decreased during the concentration time of the catchment, and these two parameters stay constant during the intermediate no rainfall periods, while the overland flow gradually decreases and its variability among the different land uses is getting smaller.

The hydrological parameters that uses Multi-Hydro intend to encompass the diversity of major classes of land uses (see Table 2.8 for more information). In particular, the property of hydrological conductivity, strongly influences the infiltration process. Furthermore, the spatial variability in rainfall may result in higher affection of some land uses by higher intensity rainfall. Therefore, the fluctuations of UM parameters suggests that the variation of overland flow is also subject to the intersection effects of spatial variability in rainfall and the spatial distribution of land uses, supporting the intermediate conclusions of Section 4.1.

Finally, the scale-independent parameter γ_s (maximum probable singularity) will be compared in the following section with the effective maximum singularity γ_{max}, which could be directly estimated from the (scale-dependent) maxima of 2D flow fields. By inter-comparing the temporal dynamics of these two maximum singularities, obtained by quite different approaches, we also intend to define an indicator to deduce the morphological impacts of NBS on extremes of the overland flow in the catchment.

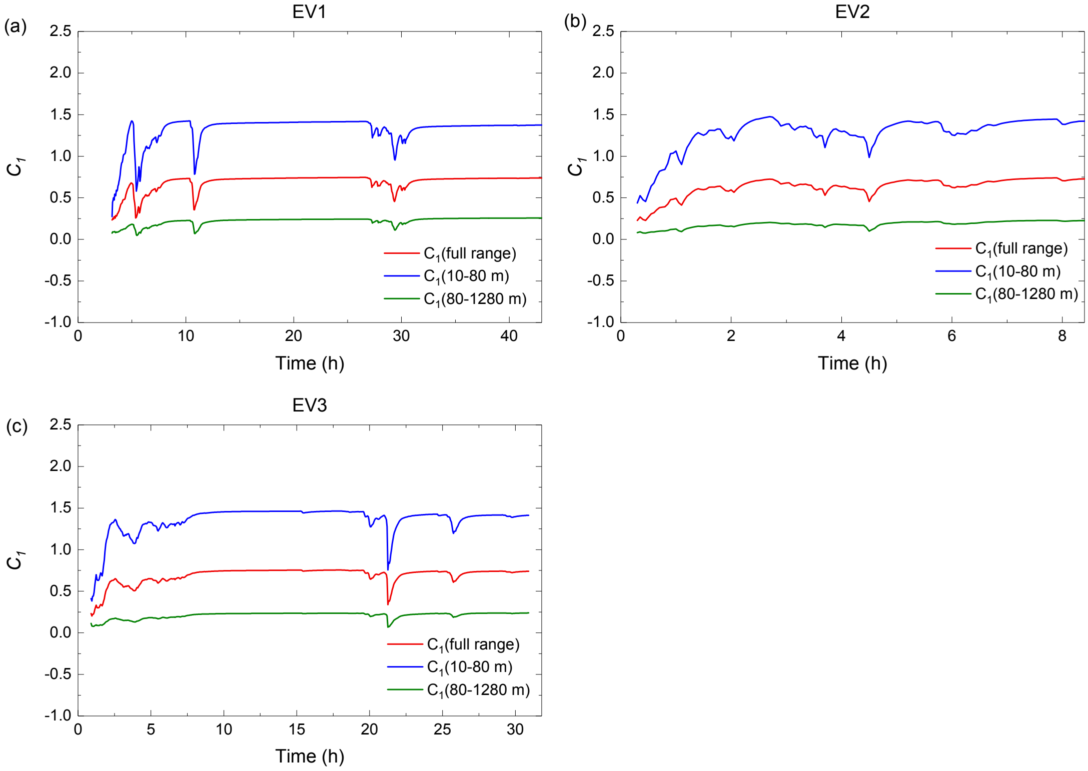

Figure 4.26: Temporal evolution of C_1 under the EV1 (a); EV2 (b); and EV3 (c); the red line presents the full range; the blue line presents the small scale range; the green line presents the large scale range.

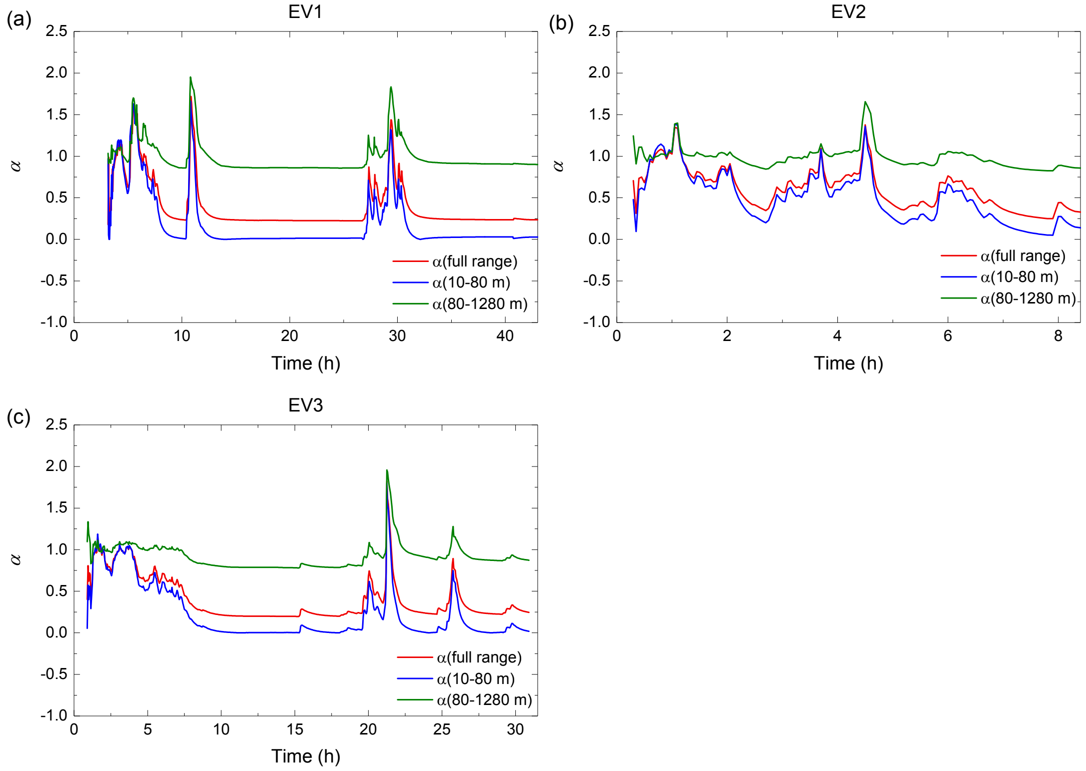

Figure 4.27: Temporal evolution of α under the EV1 (a); EV2 (b); and EV3 (c); the red line presents the full range; the blue line presents the small scale range; the green line presents the large scale range.

4.3.3 Comparison of maximum probable singularity and maximum singularity

Figure 4.28 displays the temporal evolutions of γ_s in full range, small scale range and large scale range, and γ_{max} of overland flow for three rainfall events (i.e., EV1, EV2, and EV3). This comparison aims to investigate whether γ_s is possible to infer the extremes of the distribution of overland flow. According to the results of three rainfall events (full range), four characteristics can be summarised: (i) at the beginning of three rainfall events (1-2 hours), the values of γ_s fits well with the values of γ_{max}; (ii) the values of γ_s are more variable than that of the γ_{max} at the rainfall peaks; (iii) γ_s overestimates γ_{max} during the intensive rainfall periods, while underestimates γ_{max} during the periods of rainfall stopped; (iv) at some rainfall peaks, it is noticed that γ_s and γ_{max} tend to vary in an opposite tendency. According to Eq. 3.25, γ_s is the composite parameter affected by the C_1 (intermittency) and α (multifractality). Therefore, the evolution of extreme behaviour can be decomposed into the contributions of C_1 and α. The results of EV1 and EV3 suggest that the evolution of γ_s is mainly influenced by the evolution of the multifractality, which is only partly compensated by the evolution of intermittency. These results could be explained by three reasons: (1) the non-stationary evolution of UM parameters leads to γ_s very variable; (2) UM parameters are less reliable during the rainfall peaks because of the scaling behaviour has a sudden decrease; (3) a certain number of pixels are zero values or very small values close to zero, which may result in an underestimation of α values (see Gires et al., 2012 for more details). However, for the result of EV2, it seems that the trend of C_1 is ultimately dominant. Namely, the rainfall intermittency and intensity may have strong impacts on the UM parameters. In order to statistically quantify the deviation of γ_s from γ_{max} for three rainfall events, the Root-Mean-Square Error (*RMSE*) was used. The *RMSE* of EV1, EV2 and EV3 is 0.13, 0.14, and 0.2, respectively. Nevertheless, the temporal evolutions of γ_s are generally proportional to that of the γ_{max}, but not close at some rainfall peaks.

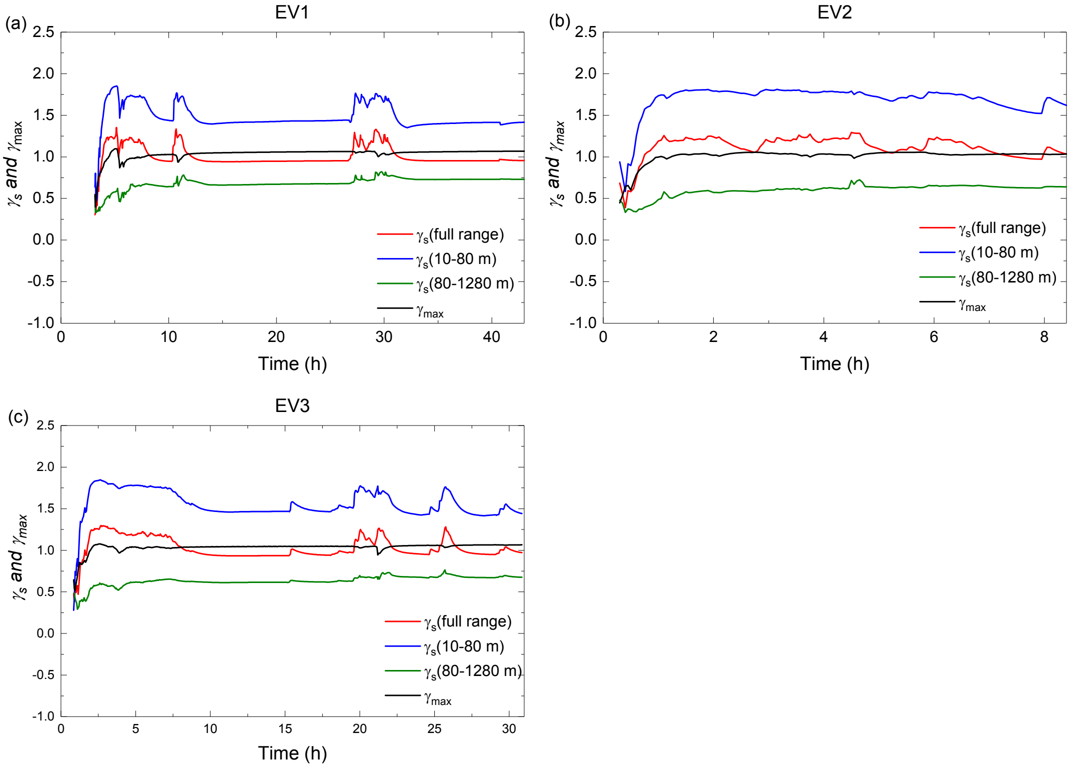

Figure 4.28: Temporal evolution of γ_s and γ_{max} under the EV1 (a); EV2 (b); and EV3 (c); the black line presents the γ_{max}; the red line, blue line, and green line present the γ_s in the full range, small scale range, and large scale range, respectively.

While the γ_s estimated over the full range of scales remains in overall good agreement with γ_{max}

(see Figure 4.28), these estimates are not supported by a unique scaling behaviour. Indeed, two distinct scaling regimes were observed, as illustrated by Figure 4.24, with a much steeper scaling moments over the small scale range, resulting also in widen singularities with higher γ_s values. The reason was mentioned earlier: the small scale range reflects the inherent complexity of the overland flow. However, with the integrative nature of surface runoff, the hydrological performance of urban watersheds could potentially be improved through interventions focused on the intelligent deployment of NBS on a given range of scales. This opens up new horizons in urban design, but how to detect and characterize the morphological changes inherent in improvements?

Similarly to Figure 3.9, at each time step t, we can define a renormalized pare (γ_s/C_1, D/C_1) (see Figure 4.29). However, this time, each of these pares corresponds to a given value of the nonlinear (and non-analytical) function with a unique value of the multifractality index α (see Eq. 3.26). Figure 4.29 illustrates the distribution of renormalized maximum probable singularities (RMPS) during the rainfall event EV2. As expected, RMPS are stronger over large scales, consistent with the general trend of the α estimates. However, the quantitative changes in RMPS are induced by the two parameters, α and C_1, and thus, they characterise the consequent changes in the overall morphological variability of the field.

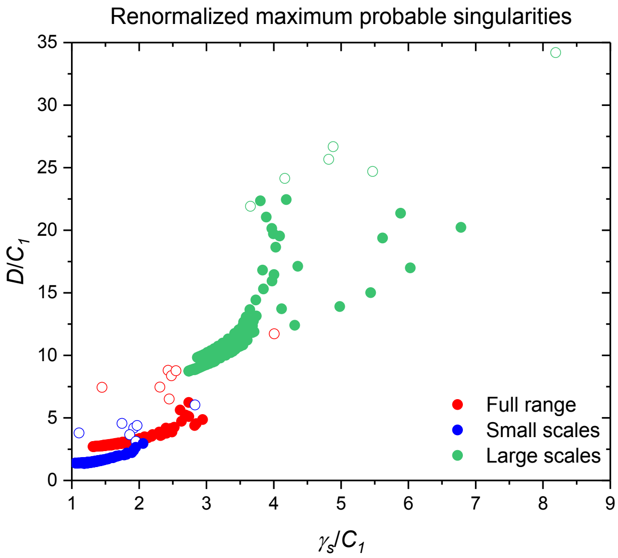

Figure 4.29: Ensemble of renormalized maximum probable singularities during the rainfall event EV2, estimated over the three ranges of scales at each time step t: red circles represent the full range of scales; blue circles correspond to the small scales (10-80 m); green circles correspond to the large scales (80-1280 m). The empty circles indicate the estimates during the concentration time steps, i.e., seven steps (21 minutes) at the beginning of the event.

At each time step of the rainfall event, we then plot the RMPS estimated over the full range of scales versus the RMPS estimated over a sub-range of scales to quantify the changes induced by the difference in scales. Then, the RMPS indicator (RI) is obtained as a linear approximation of their correspondence (see Figure 4.30 for EV2). Since no changes would correspond to the unit slope, this indicator can also be easily understood in terms of the percentage change in the resulting morphological variability, using the linear regression coefficient (LRC):

$$RI = (LRC - 1) \cdot 100\% \tag{4.6}$$

A positive sign of this coefficient indicates an increase, while a decrease corresponds to a negative value. For example, morphological variability over large scales increased by about 62 % compared to that over the full range of scales, while morphological variability over small scales decreased by about 42 %.

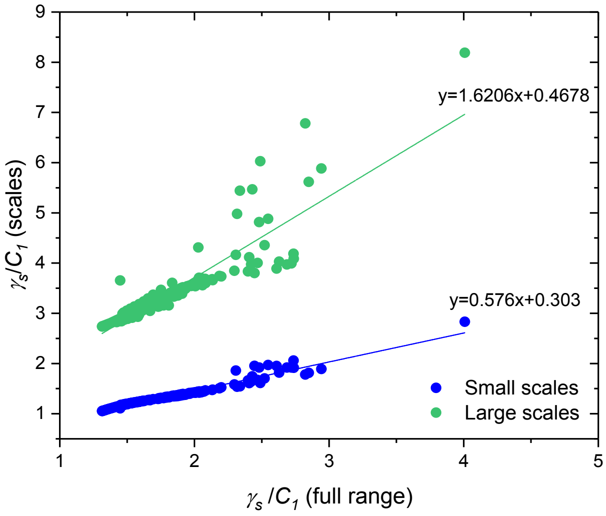

Figure 4.30: RMPS indicator: blue circles correspond to the small scales (10-80 m); green circles correspond to the large scales (80-1280 m); and the linear approximations by straight lines of the same colour.

In Subsection 4.3.5, the RI will also be used, but on the same range of scales, to quantify the percentage change in morphological variability induced by the implementation of different NBS scenarios.

4.3.4 Results of the EV5S and EV6S

Comparing the UM parameters of overland flow of the EV2 (Figures 4.26b and 4.27b) with that of the EV5S (Figures 4.31a and 4.31b), the mean value of C_1 (full range) of the EV5S event is about 0.23, which is 30 % lower than that of the EV2. Concerning the mean value of α (full range) of the EV5S event, it is 0.4 higher than that of the EV2. This result indicates that the strong rainfall results in a higher and more homogeneous overland flow over the analysed field. Namely, most of the areas are filled with the overland flow, and they are accumulated in certain land use covers. As shown in Figure 4.31c, the two singularities increase with the increase of rainfall intensity. For the EV2, the values of γ_s (full range) range from 0.4 to 1.3, and that of γ_{max} ranges from 0.4 to 1.0. For the EV5S, γ_s (full range) is range from 0.6 to 1.2, and that of γ_{max} is between 0.7 and 1.0. Indeed, the values of γ_s are closer to the values of γ_{max} in EV5S than the EV2. By checking the values of RMSE of γ_s and γ_{max} of the EV5S and EV2, it is found that the *RMSE* of the EV5S is 0.12, which is slightly lower than that of the EV2. Furthermore, with this strong synthetic rainfall, the UM parameters and γ_s in small scale and large scale ranges are less distinct.

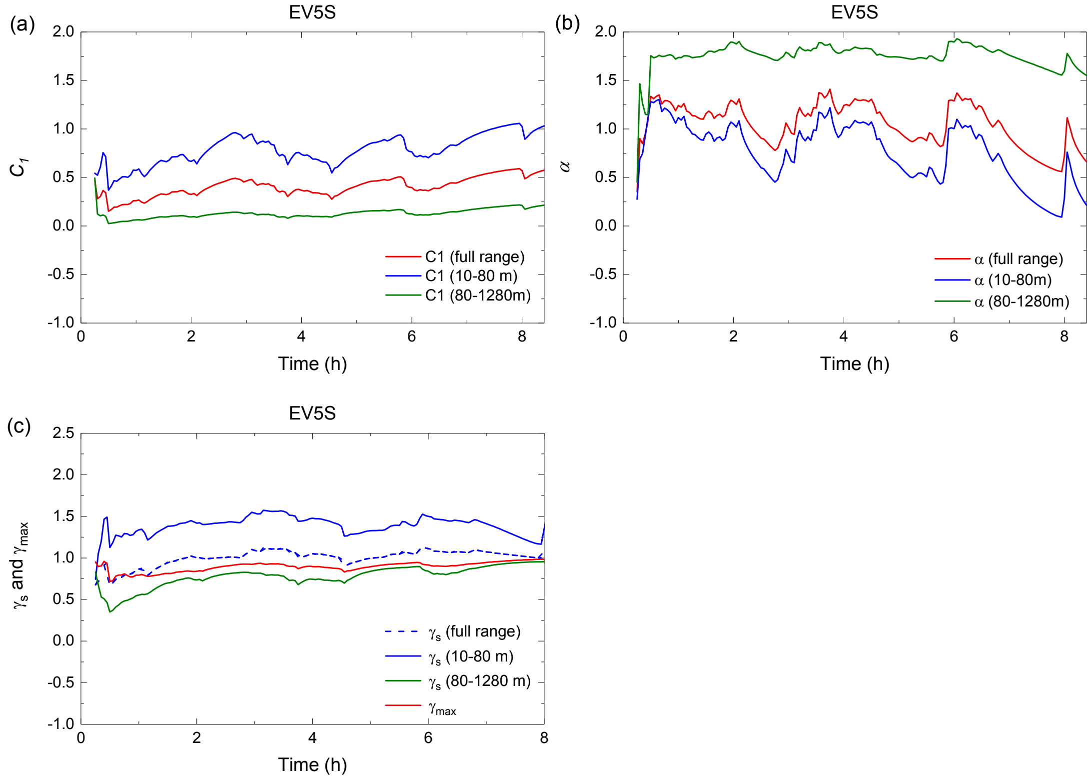

Figure 4.31: Temporal evolution of α (a), C_1 (b), γ_s and γ_{max} (c) under the EV5S.

The results of EV6S are shown in Figure 4.32. The value of C_1 (full range) starts from 1.2 at the beginning of the event, while decreasing to 0.1 at the highest rainfall peak. On the contrary, the value of α (full range) starts at 0, then increases to 1.5 at the highest rainfall peak. For the C_1 in small scale range, the value starts from 1.5 at the beginning of the event, while decreasing to 0.25 at the highest rainfall peak. The values of α (small scale) are very close to that of the α in full range. For the large scale range, the values of C_1 is almost constant (around 0), but the values of α approach to 2 at the rainfall peak. Namely, for this large scale range, the field is relatively homogeneous during most of the time, but the overland flow are indeed concentrated at some locations at the rainfall peak. The variation of UM parameters indicates that the overland flow in the field is very variable during the rainfall period and the field approach to homogeneous at the rainfall peak. Comparing the temporal evolution of γ_s and γ_{max} (see Figure 4.32c), the long-term evolution of γ_s (full range) fits the trend of γ_{max}, where the value of *RMSE* is 0.1.

Overall, the results obtained by the EV5S and the EV6S indicate that the rainfall intensity and duration have a significant impact on the estimation of UM parameters. For these two events, the trend of C_1 exhibits a dominant impact on the temporal evolution of γ_s. In addition, with the higher rainfall intensity, the values of γ_s are closer to that of the γ_{max}. The reason could be attributed to the fact that the overland flow in the field increases with high rainfall intensity, thus reduces the impacts of the extreme small values on the estimation of UM parameters.

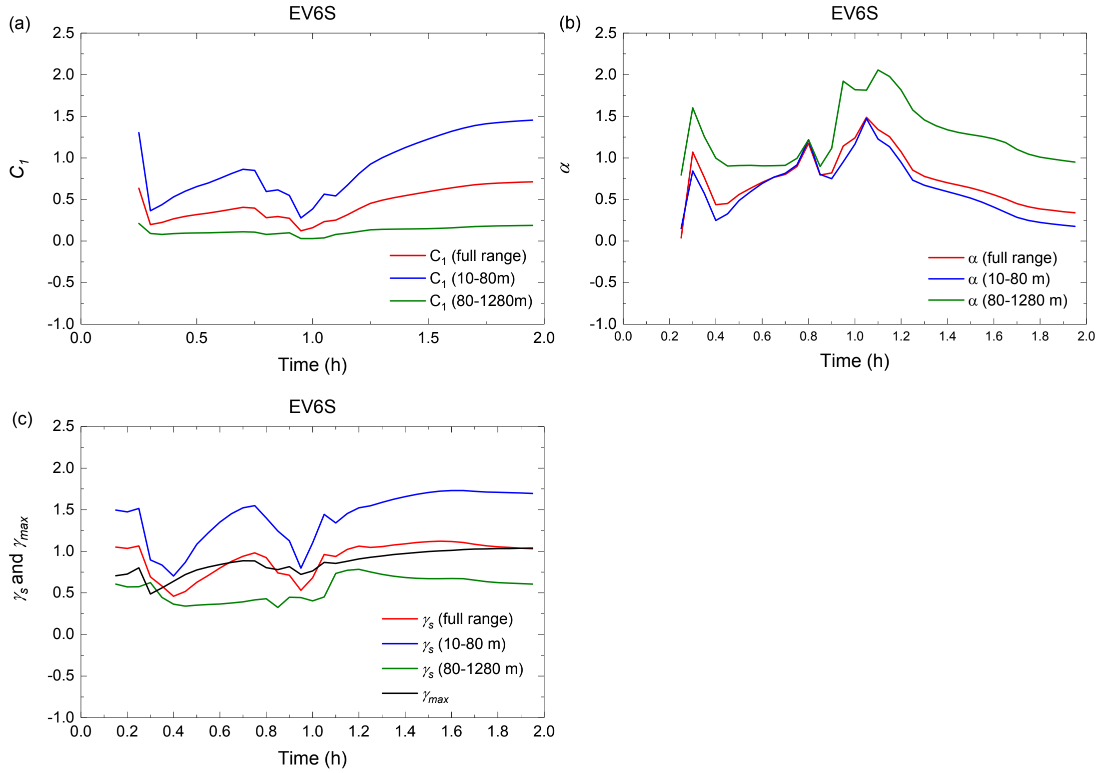

Figure 4.32: Temporal evolution of α (a), C_1 (b), γ_s and γ_{max} (c) under the EV6S.

4.3.5 Multifractal characterisation of overland flow of different NBS scenarios

In order to assess the hydrological performance of the NBS, the multifractal characteristics of the overland flow of the first set of NBS scenarios are compared with that of the baseline scenario under the EV2. This rainfall event was selected because it is relatively stable and consecutive, furthermore, the mean values of C_1 and α (full range) suggest the EV2 has the strongest extremes among three original events. The mean values of UM parameters, as well as γ_s and γ_{max} of the five scenarios are summarised in Table 4.7. As shown in Table 4.7 and Figure 4.33, the mean values and the time evolution of C_1 of Combined1 and PP1 are higher than that of the other scenarios, whatever the selected scale range. However, the RG1 and GR1 are more dependent on the selected scale range. The mean values of α (full and large scale range) of the five scenarios from the highest to the lowest, are: RG1, GR1, baseline, Combined1 and PP1, all of which are less than unity, implying a weak multifractality with bounded extremes. However, for the small scale range, intermittency increases almost twice for all scenarios, while multifractality increases slightly for GR1 and Combined1 scenarios only. Overall, flows become sparser and more variable at the rainfall peaks, but still with bounded extremes. Regarding the large scale range, the values of α of GR1, RG1 and baseline scenarios are significantly higher than those of the other scenarios, also accompanied by a much lower C_1 which reduces intermittency. This opposite trend makes it difficult to evaluate the overall impact on large scale extremes.

	Baseline	**PP1**	**RG1**	**GR1**	**Combined1**
C_1 (full range)	0.63	0.77	0.69	0.66	0.84
C_1 (10-80m)	1.27	1.35	1.27	1.26	1.35
C_1 (80-1280m)	0.18	0.35	0.18	0.22	0.39
α (full range)	0.61	0.52	0.72	0.72	0.56
α (10-80m)	0.50	0.47	0.50	0.61	0.56
α (80-1280m)	0.99	0.64	1.00	1.08	0.69
γ_s (full range)	1.12	1.23	1.24	1.21	1.33
γ_s (10-80m)	1.69	1.74	1.69	1.71	1.76
γ_s (80-1280m)	0.60	0.73	0.6	0.73	0.82
γ_{max}	1.01	1.13	1.09	1.04	1.19

Table 4.7: Mean value of temporal evolution of UM parameters, γ_s in full range, small scale range (10 – 80 m), and large scale (80-1280 m) and γ_{max} of five scenarios.

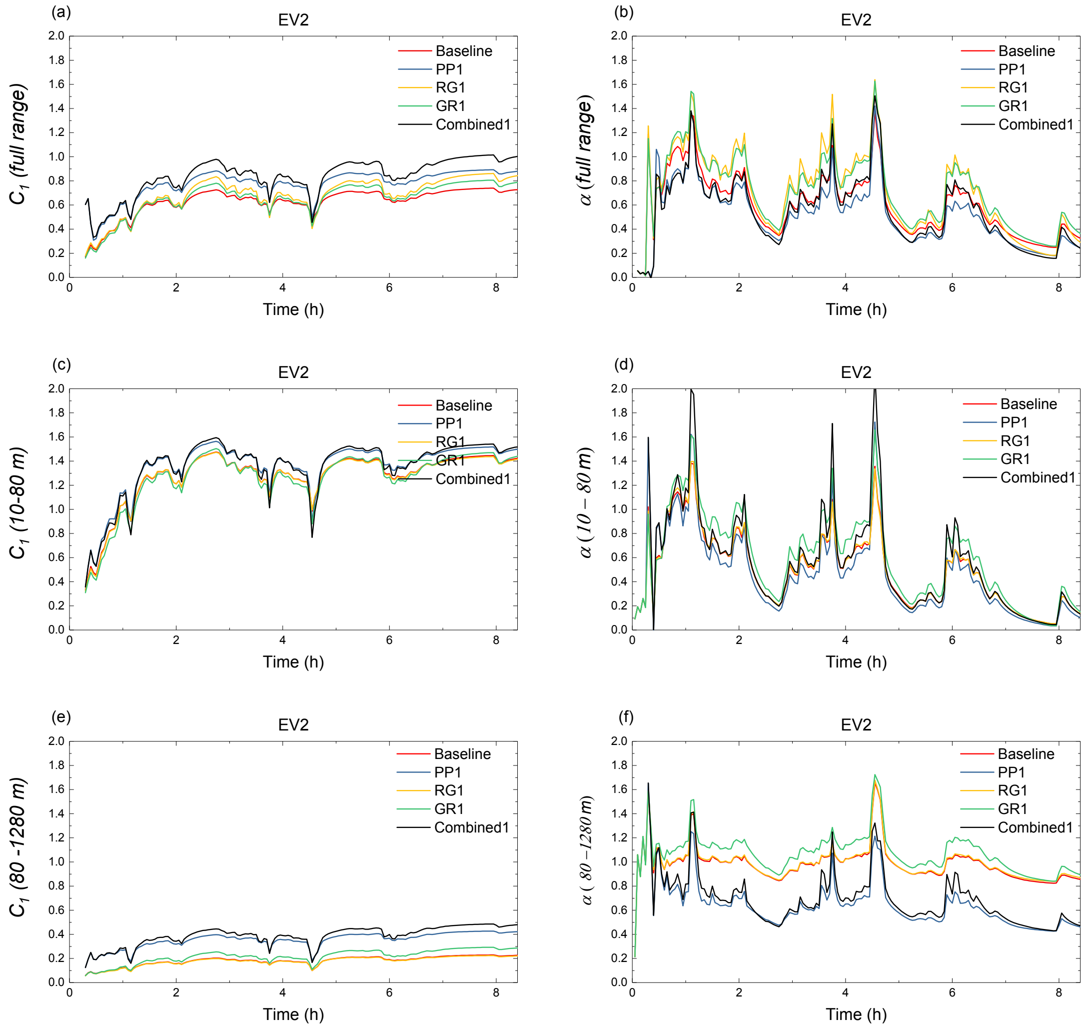

Figure 4.33: Temporal evolution of C_1, and α, in full range (a, b), small scale range (c, d), and large- scale range (e, f) under the EV2.

The differences between the four NBS scenarios are mainly due to the different infiltration and retention capacities of each type of NBS. As indicated in Chapter 3, three types of NBS implemented in the Combined1 scenario result in the fractal dimension of NBS that reaches 1.95 (at the large scale range). This estimate reflects that the infiltration capacity of the Combine1 scenario is very remarkable. As the rainfall intensity decreases, the overland flow in these pixels representing NBS infiltrates quickly. The PP1 scenario has C_1 and α values slightly lower than those of Combined1 scenario, and α of the Combined1 scenario increases very rapidly during periods of heavy rains (see Figure 4.33b). This could be explained by the fact that the RGs and GRs have impacts on the Combined1 scenario. As presented in Chapter 1, RG is a kind of low-lying human-made greenbelt, which means that the runoff can be accumulated in the RGs for some time. Likewise, for GR, it is characterised by a retention capacity of substrate. However, for the PP1 scenario, the reservoir layer of PP comprised of coarse aggregate provides a structure for temporarily retention of water inside the porous media and gradually discharging water into the underlying layers. Hence, runoff may slowly seep into the subsoil or flow directly into the drainage system. The RG1 scenario and GR1 scenario have higher C_1 and α values than those of the baseline scenario, in particular at certain rainfall peaks. These reasons can be explained in two aspects: (i) the substrates of RGs and GRs retained surface runoff during the periods of intense rains; (ii) the land use type of road was kept as original in the RG1 and GR1 scenarios, which may result in the overland flow being mainly concentrated at the pixels that represent the road.

Figure 4.34 presents that the values of γ_s and γ_{max} at the same time in NBS scenarios are higher than that of the baseline and Combined1 scenario is the highest. The comparison of mean values of γ_s and γ_{max} in Table 4.7 shows the similar tendency. According to the Eq. 3.27, γ_{max} is determined by the two parameters H_{max} and H_{mean} at the highest resolution Λ. The application of NBS can effectively reduce the overland flow all over the catchment, thus H_{max} and H_{mean} both decrease. However, compared with that in the baseline scenario, the decrease of H_{mean} is more significant than H_{max} in NBS scenarios, further resulting in larger γ_{max}. By comparing the temporal evolutions of γ_s (full range) and γ_{max} of each scenario (e.g. Figure 4.34a), γ_s generally follows the trend of γ_{max}, but γ_s has some overestimation of γ_{max}. These results indicate that the γ_s and γ_{max} can reflect the effects of NBS on the reduction of overland flow in the catchment. According to Figure 4.34a, the temporal evolution of γ_s of the PP1 scenario is slightly higher than that of the RG1 scenario at the start of the rains. In addition, the values of γ_s of the PP1 scenario become lower than those in the RG1 scenario at peak precipitation. The similar observations are obtained in Figures 4.34b and 4.34c. This can be explained by the fact that at the onset of the rains, the PPs quickly infiltrated the overland flow into the subsoil. With the continuous rainfall, the infiltration capacity of the PPs have gradually diminished, which results in an increase in extreme flows.

Note that while the γ_s (full range) is overall in good agreement with γ_{max}, there is clearly no convincing scaling behaviour over the full range of scales. This immediately implies that any morphological change, i.e., a change affecting the multifractal structure or the properties of the complex urban watershed, introduced at one of two distinct scale regimes, currently has an indefinite impact on whole system.

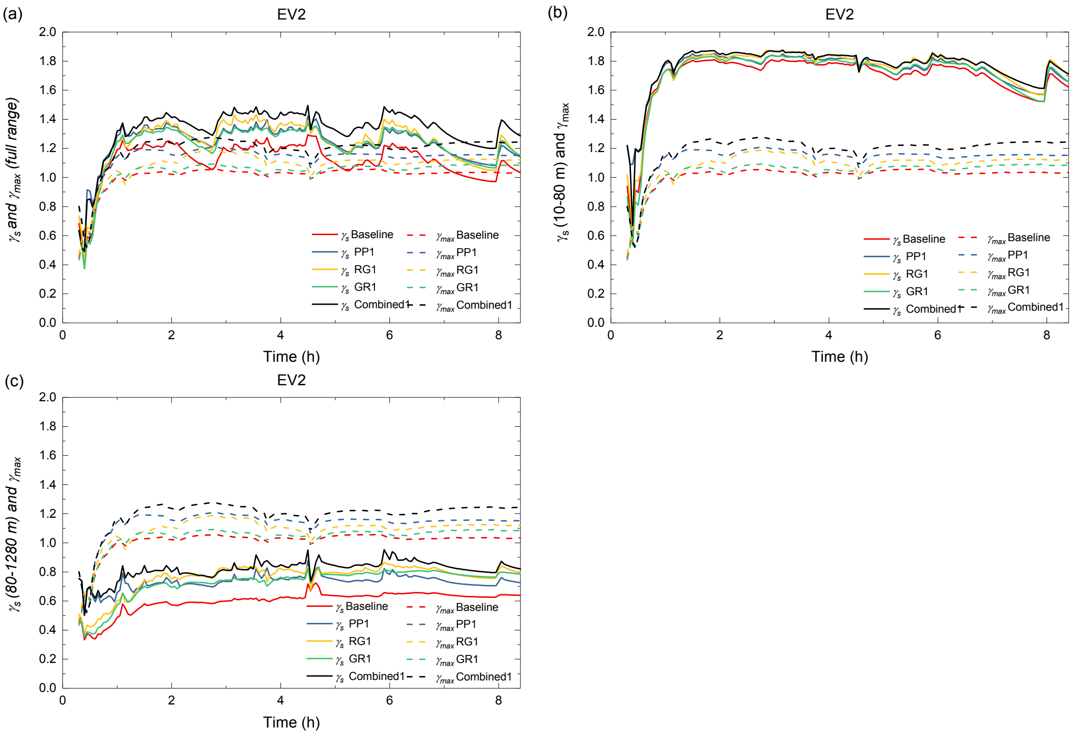

Figure 4.34: Temporal evolution γ_s in full range (a), small scale range (b), and large- scale range (c) and γ_{max} of the baseline scenario and NBS scenarios under the EV2.

To detect and better understand the morphological changes inherent in the improvements, we use the *RI* to quantify the percentage of change in morphological variability induced by the implementation of different NBS scenarios, on each range of scales. Similar to Figure 4.29, we define a time series of renormalized pares (γ_s/C_1, D/C_1) for each scenario, on the three scale ranges: full, small and large. Figure 4.35 (a-c) displays the resulting distributions of renormalized maximum probable singularities on each of the scale ranges, as well as their superposition on Figure 4.35d. As previously, each of these points corresponds to a given value of the non-linear, non-analytical function corresponding to a unique value of the multifractality index α. Note that the most distinct points for each of the sets correspond to several time steps during the concentration time at the start of the rain. Since $D = 2$ for all the points, the vertical shift depends only on the trend of C_1. Larger offsets of C_1 shift down towards unity, which corresponds to the limit $C_1 = D$. The horizontal shift towards unity corresponds to the limit $C_1 = \gamma_s$. The two limits correspond to the (mono)fractal β-model with $\alpha = 0$. For the RMPS over the full range of scales (Figure 4.35a), the GR1 seems to have only an increase in intermittency, while for all other scenarios, an increase in intermittency is accompanied by a decrease in multifractality. On the small scale range (Figure 4.35b), the differences between the scenarios become vaguely distinguishable, with some points closely approaching the β-model. In agreement with the observations made for the baseline scenario, RMPS remain stronger over large scale range for all scenarios (Figure 4.35c), in accordance with the general trend of the α estimates. Over this range of scales, the PP1 and Combined1 scenarios stand out strongly among other scenarios, offering a good example of the consequent changes in the overall morphological variability of the field. We then quantify all the changes with the RI (see Figure 4.36).

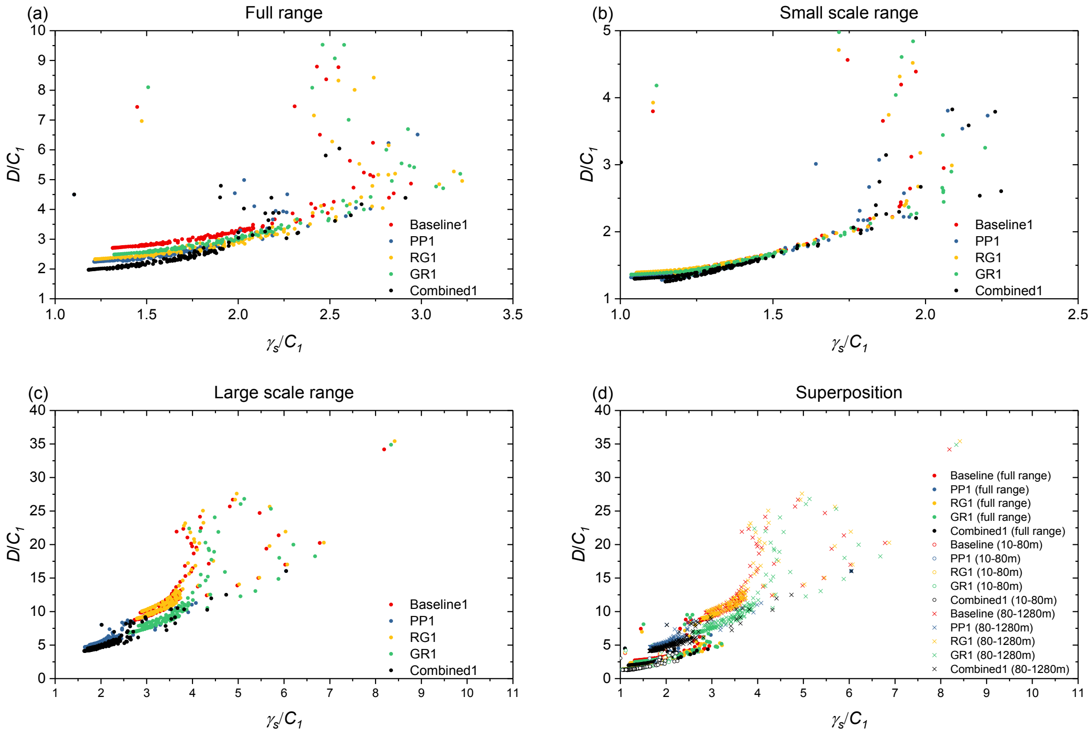

Figure 4.35: Ensemble of renormalized maximum probable singularities during the rainfall event EV2, estimated over the three ranges of scales at each time step t for baseline and NBS scenarios: (a) full scale; (b) small scales (10-80 m); (c) large scales (80-1280 m); and (d) their superposition.

The relationship of the RMPS of baseline scenario and NBS scenarios are shown in Figure 4.36, reflecting the morphological variability of each NBS scenario in different scale ranges. The first seven time steps (21 min concentration-time) are not considered because they may bias the estimation. Here, the RG1 and GR1 scenarios present a higher morphological variability than that of PP1 and Combined1, especially for full range and large scale range, indicating the overland flow in these two scenarios are relatively more heterogeneous than that of PP1 and Combined1. According to the RI indicator, the morphological variability of RG1 and GR1 scenarios increased by about 19.6 % and 14.3 % in full range, and about 1.1 % and 11.1 % in a large scale range. For the PP1 and Combined1 scenario, the morphological variability decreased by about 19.3 % and 14.7 % in full range, and 33.1 % and 20.6 % in large scale range. Namely, this two scenarios reduced the morphological variability of the field. For the small scale range, the difference between these NBS scenario is less significant, with the morphological variability of the PP1 scenario decreased by about 6.0 %, while the other three NBS scenarios increased by about 1.0 %, 18.2 % and 6.9 %, respectively.

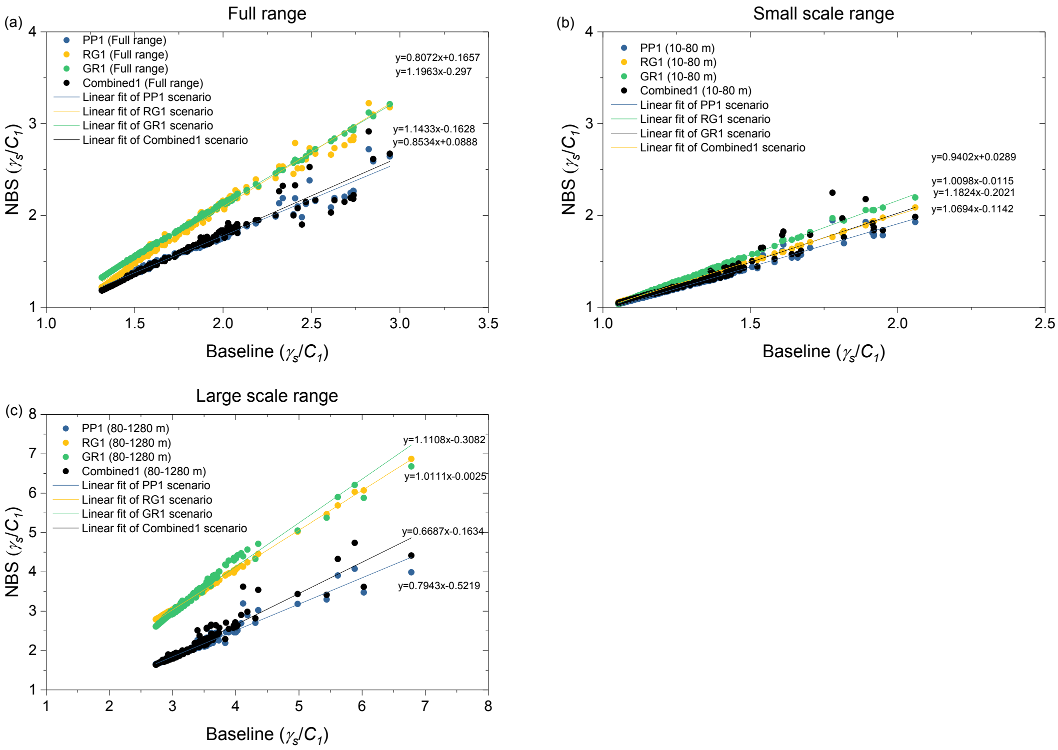

Figure 4.36: RMPS indicator of NBS scenarios versus baseline scenario in (a) full range; (b) small scale range; and (c) large scale range.

As presented by the results, the intrinsic characteristics of the overland flow of the NBS scenarios can be comprehensively understood using universal multifractals across the range of scales. More precisely, within the UM framework, the general performance of the NBS scenarios in terms of urban waterlogging mitigation can be clearly described. Moreover, when comparing γ_s with γ_{max} of each scenario, the multi-scale understanding is necessary and useful to distinguish the NBS that can efficiently mitigate overland flow, and RI (%) is a scale-independent indicator that can be used to estimate the change in resilience capacity of a watershed under a given scenario. This new morphological understanding complements the more classical approaches studied in the previous sections. This opens up new opportunities in the design of urban interventions focused on the intelligent deployment of NBS on the most appropriate range of scales.

4.3.6 Intermediate conclusions for the Section 4.3

The standard method for characterising the variability of overland flow focused primary on a single scale, usually the smallest scale available (i.e., highest resolution). However, the extremes of overland flow are generally variable over a wide range of scales. Thus, the smallest scale has no specific hydrological significance, and a scale-independent characterisation is more physically relevant. In this study, the 2D maps of overland flow at each time step of the baseline scenario and the NBS scenarios were obtained by the Multi-hydro model and analysed within the Universal Multifractal theoretical framework. This study investigated the spatial variability of overland flows and evaluated the hydrological performance of the NBS in terms of a possible improvement of the morphological functioning of the catchment at several scales. The main findings are summarised as follows:

1. For the baseline scenario under three rainfall events of 2015, the UM parameters are highly variable during the periods of intensive rainfall and remain constant during the periods of no rainfall, indicating that the spatiotemporal variability of rainfall has significant impacts on the overland flow. Over the full range of scales, the temporal evolution of γ_s generally follows the trends of γ_{max}, but not close at some rainfall peaks, which may be related to the estimation of the UM parameters, not being supported by the corresponding scaling regime.

2. For the baseline scenario under the synthetic rains EV5S and EV6S, the values of γ_s are closer to that of the γ_{max} than the three original rainfall events. This reveals that the estimation of multifractal parameters and γ_s are strongly linked to the break of scales observed at 80 m, which decreases with a higher rainfall intensity. Therefore, the intrinsic characteristics of overland flow are best presented with higher intensity and short duration precipitation.

3. The study demonstrated that NBS can quickly infiltrate or store the overland flow during the period of short heavy rains. Overall, the Combined1 scenario seems to be the best alternation for the Guyancourt catchment, considering only the hydrological impact, which has the highest γ_s. The PP1 scenario has higher C_1 and γ_s but a lower α than that of RG1 and GR1 scenarios, because the PP infiltrate the overland flow directly to the porous medium or discharge the runoff into the drainage system, while the RG and GR retain runoff in their substrates for a certain period.

4. For the NBS scenarios, the variability of overland flow over the full range, small and large scales was first described by the variation of the UM parameters. Then, by comparing the γ_s and γ_{max}, it is confirmed that the NBS scenarios can effectively reduce the overland flow in the catchment. The multifractal exponent γ_s can be considered as the scale-independent indicator to infer the observed extremes. In turn, the newly defined indicator of percentage

change in morphological variability of the overland flow (*RI*), successfully quantifies the relative performance of NBS scenarios in terms of urban flood resilience across scales.

Overall, this study provides new means to describe and generalize the spatial variability of overland flow across scales. With this new method, the overland flow extremes over the catchment can be quantified without being limited to a single scale or to certain specific values. Apparently, it might be useful to make a macroscopic description of the spatial variability of overland flow, to evaluate the hydrological performance of the NBS and the resulting morphological changes, aimed at increasing the city's resilience for stormwater management at multiple scales.

Chapter 5

Cost-effective design of nature-based solutions

5.1 Integrating hydrological impacts and Life cycle costs

Following the numerical investigations of NBS scenarios in Chapter 4, the main novelty of the study in this section is to focus on integrating both technical and economic criteria to design a cost-effective alternation for future urban planning. More preciously, the technical indicator based on the reduction of peak flow and total runoff volume of NBS scenarios under different rainfall conditions. The economic indicator is corresponding to the life cycle cost (LCC) of each NBS scenario. For achieving this study, the third – sixth sets of NBS scenarios are adopted and simulated under the synthetic rainfall events of EV7S – EV14S (more details about these rainfall events and NBS scenarios can be found in Section. 2.4.4.4 and Section 2.6). Correspondingly, to quantify the heterogeneity of spatial distributions and implementation levels of these NBS scenarios in a range of scales, the scale-invariance indicator of fractal dimension is used, and the results are discussed in Section 3.1.1.

5.1.1 Evaluation criteria

5.1.1.1 Technical criteria

The hydrological performances of NBS are firstly assessed concerning the simulated flow in all conduits (in total 4474) of the drainage network. All conduits are selected to investigate the impact on any conduit of the drainage network. Then, a percentage error is computed between the baseline scenario and each NBS scenario. In detail, two indictors, reduction of peak flow and total runoff volume are considered. These two indicators are computed with the Eqs. 4.4 and 4.5.

5.1.1.2 Economic criteria: Life cycle costs

Life cycle costs is the economic indicator for evaluating the performances of NBS scenarios with considering all the related costs throughout the lifetime of the NBS (Spatari et al., 2011). In detail, three stages in terms of construction, operation, and the end of life should be taken into consideration (Fuller and Peterson, 1996). The associated cost corresponds to the three aspects: (i) the capital expenses; (ii) operation and maintenance expenses; (iii) salvage value.

To consider all the related costs, it requires a transformation based on a proper discount rate. The present values of cost (PVC) is applied to compute the LCC with the following equation:

$$PVC = C_0 + \left(\frac{C_a\left((1+r)^{T+1}-1\right)}{r(1+r)^T}\right) - \frac{SV}{(1+r)^T} \tag{5.1}$$

where PVC is the present value of LCC (€/m^2), C_0 is the capital cost (€/m^2), T is the lifespan (year), C_a is the annual operation and maintenance cost (€/m^2), r is the discounting rate (5 % in this study), t is the time variation (year), and SV is the salvage value at the end of the year of the lifespan (€/m^2).

The salvage value (SV) refers to the residual life of NBS at the end of their lifespan. The residual life of NBS needs to be taken into account because NBS may not be entirely exhausted at the end of the design year. The SV is computed by using the following equation:

$$SV = \left(1 - \frac{L_A}{T}\right) \times C_a \tag{5.2}$$

where L_A is the time span from the year of last maintenance to the end of the year of lifespan (generally, NBS are maintained at each year, thus, L_A equal to 1 in this study).

5.1.1.3 Cost-effective evaluation (criteria)

The process of the cost-effective evaluation of NBS scenarios takes into account the two hydrological indicators (ΔQp and ΔV) and the economic indicator of LCC of each NBS scenario by using the following equation:

$$\mathrm{CE} = \frac{(\Delta Qp+\Delta V)/2}{PVC \times A} \tag{5.3}$$

where $\Delta Q\mathrm{p}$ and ΔV is the peak flow reduction and total runoff volume reduction of NBS scenarios, respectively. PVC is the present value of LCC (€/m^2), and A is the total implementation area of NBS in each NBS scenario (m^2).

5.1.2 Impact of the implementation level of NBS scenarios

Here, the local reductions of peak flow and total runoff volume of each set of NBS scenario are presented with the box-plots in terms of the flow in all conduits (4470) of the drainage system. Because the hydrological performances of the three types of NBS vary under different rainfall conditions, their specific characters are firstly presented and discussed.

5.1.2.1 PP scenarios

As summarised in Table 5.1, for the PP3 scenario (D_F: 0.42/1.6), the mean values of peak flow reduction range from about 10 % to 15.2 % for the 8 rainfall events. With the increase of the D_F of PP scenarios, the mean values of peak flow reduction increases by around 0.5 % to 1 %. Regarding the 75 % quartile of the peak flow reduction of each PP scenario, the PP3 scenario ranges from 10.9 % to 22 %, and that of the PP6 scenario (D_F: 1.1/1.77) ranges between 14.2 % and 25 %.

Regarding the mean values of total runoff volume reduction, the PP3 scenario ranges from 16.4 % to 21.2 %, around 1.7 – 7.3 % lower than that of the PP6 scenario. It is worth noting that the largest mean value of total runoff volume reduction was computed for the PP6 under the EV7S, around 7 % higher than that of the other PP scenarios (the D_F of the large scale regime lower than 1.7). Namely, in this short and weak rainfall event, the hydrological performance of PPs significantly increases with increasing their D_F.

5.1.2.2 RG scenarios

Although the reduction of peak flow and total runoff volume is almost positively linearly related to the D_F of RGs for all the studied rainfall events (expect for EV13S), the average difference between each RG scenario is less than 2 % (see Figure 5.1 and Figure 5.2) for each rainfall event. Namely, the hydrological responses of each RG scenario are similar. It indicates that enlarging the D_F of RGs over the whole catchment is not very significant for increasing the hydrological performance of the RG scenarios. However, as mentioned previously, the relationship between the performances ($\Delta Q\mathrm{p}$ and $\Delta \mathrm{V}$) of RGs are not merely linear with their

D_F in EV13S. The mean values of these two indicators of RG5 scenario are 0.8 – 1 % lower than that of the RG4 scenario and RG6 scenario. The reason could be related to the spatial layout of the RGs and the convey capacity of the conduits for flow routing, because some relevant conduits may overload in this rainfall event. This result is consistent with some previous studies (Fry and Maxwell, 2017; Ercolani et al., 2018), which shows that the relationship between peak flow reduction and GR percentage conversions is non-linear of 25 % of conduits exceeding 80 % of filling.

5.1.2.3 GR scenarios

For the 8 studied rainfall events, when the GR scenarios with D_F (large scale regime) larger than 1.6, the mean values of peak flow reduction range from 14 % to 25 %, and that of the total runoff volume reduction range from 18 % to 30 %. If the D_F (large scale regime) of GR scenarios lower than 1.6, the mean values of peak flow reduction are larger than 11 % but less than 20 %, and that of the total runoff volume reduction range from 15 % to 24 %. Regarding the 75 % quartile of these two indicators of each GR scenario, the peak flow reduction ranges from about 16.6 % to 50 %, and that of the total runoff volume reduction ranges between 20 % and 55 %, depending on the magnitude of the D_F. Concerning the two stronger rainfall events (EV8S and EV14S), the mean values of reduction of peak flow and total runoff volume of each GR scenario are lower than 20 %, even the scenario characterised with the highest D_F. This result is generally consistent with the previous studies, which shows that GRs are more effective for the smaller storms (Qin et al., 2013; Ercolani et al., 2018; Palla and Gnecco, 2015).

5.1.2.4 Overall performances

As shown in Figures 5.1 and 5.2, a similar result can be summarised for different types of NBS scenario: the peak flow reduction and total runoff volume reduction are generally positively linearly related to the D_F of NBS over the catchment for the 8 studied rainfall events.

Furthermore, the hydrological responses of each NBS scenario in terms of peak flow and total runoff volume reduction significantly depend on the rainfall event. However, in these modelling experiments, the performances of PP scenarios are relatively less effective than that of the RG scenarios and GR scenarios, especially in some stronger rainfall events.

In addition, the non-linearity relationship is found between the performances of the NBS scenario and the rainfall intensity. This result suggests that the non-linearity can be related to the intersection effects of the spatial variability in rainfall and the spatial distribution of the

NBS. For instance, the extremes of the precipitation and NBS are scarce and could rarely coincide, i.e., rainfall spikes may fall more often elsewhere than on NBS. The effective NBS performance could be therefore biased with respect to their potential performance due to this problem (see more details in Section 4.1.3). Comparing the peak flow reduction and total runoff volume reduction of each NBS scenario, the NBS is more efficient for decreasing total runoff volume than peak flow. The reason could be related to the selected rainfall events are characterised by short duration and low accumulation, which are not sufficient to entirely saturate these NBS.

NBS scenario	ΔQp (mean)	ΔQp (75% quartile)	ΔV (mean)	ΔV (75% quartile)
PP3	10 % - 15.2 %	10.9 % - 22 %	16.4 % - 21.2 %	20 % - 24.1 %
PP4	10.9 % - 15.9 %	11 % - 25 %	17.6 % - 22.1 %	21% - 25.7 %
PP5	11.6 % - 16.3 %	12.5 % - 25 %	17.5 % - 22.4 %	22.6 % - 26.3 %
PP6	12 % - 17.1 %	14.2 % - 25 %	18.1 % - 28.5 %	24.1 % - 41.3 %
RG3	14.4 % - 17.7 %	22 % - 30 %	18.3 % - 20.4 %	27.6 % - 32.9 %
RG4	14.6 % - 18.3 %	24 % - 31.5 %	18.6 % - 21.2 %	28.3 % - 34.4 %
RG5	13.8 % - 18.4 %	20 % - 31.5 %	17.7 % - 21.1 %	26.8 % - 34.7 %
RG6	14.6 %- 18.5 %	25 % - 31.8 %	18.6 % - 21.2 %	28.4 % - 35 %
GR3	11% - 15%	16 % - 25 %	15 % - 20 %	19.7 % - 28.9 %
GR4	13% - 19%	16.6 % - 33 %	16 % - 24 %	20.1 % - 36.6 %
GR5	13% – 22%	16.6 % - 40 %	17 % - 27 %	23.8 % - 46.6 %
GR6	14% - 25%	17 % - 50 %	18 % - 30 %	26.3 % - 55.0 %
PP6+RG6	17.5 % - 29.4 %	28.5 % -41.7 %	19 % - 30.1 %	28.1 % - 42.1 %
PP6+GR6	25.6 % - 37.3 %	38.4 % - 66.6 %	23.2 % - 41.3 %	45.4 % - 75.1 %
RG6+GR6	22.3 % - 34.1 %	33.3 % - 60 %	19.7 % - 37.1 %	33.3 % - 66.6 %
PP6+RG6+GR6	26.8 % - 44 %	40 % - 68 %	20.1 % - 48.3 %	50 % - 77 %
Extensive GR_10%	22.3 % - 25.7 %	42.9 % - 50 %	25.9 % - 30 %	42.9 % - 55 %
Extensive GR_25%	22.3 % - 25.7 %	42.9 % - 50 %	25.9 % - 30 %	42.8 % - 55 %
Extensive GR_50%	10.7 % - 25.4 %	14.3 % - 50 %	18 % - 29.9 %	25 % - 54.9 %
Semi-intensive GR_10%	22.3 % - 25.7 %	42.9 % - 50 %	25.9 % - 30 %	42.9 % - 55 %
Semi-intensive GR_25%	22.3 % - 25.7 %	42.9 % - 50 %	25.9 % - 30 %	42.9 % - 55 %
Semi-intensive GR_50%	20.7 % - 25.7 %	35.7 % - 50 %	22 % - 30 %	33.7 % - 55 %
PP(upstream)	41.9 %	46.8 %	43.4 %	46 %
PP(downstream)	42 %	47.5 %	43.4 %	46.4 %
RG(upstream)	17.5 %	27.1 %	18.8 %	26.1 %
RG(downstream)	22.5 %	35.8 %	24.3 %	37.5 %
GR(upstream)	37 %	50 %	40.8 %	52.8 %
GR(downstream)	44.4 %	51.8 %	46.2 %	53.3 %
Combined(upstream)	28.6 %	46.3 %	30.1 %	46 %
Combined(downstream)	30.4 %	48.5 %	31.4 %	46.3 %

Table 5.1: The mean values and 75 % quartile of peak flow reduction and total runoff volume reduction of all NBS scenarios under the 8 rainfall events.

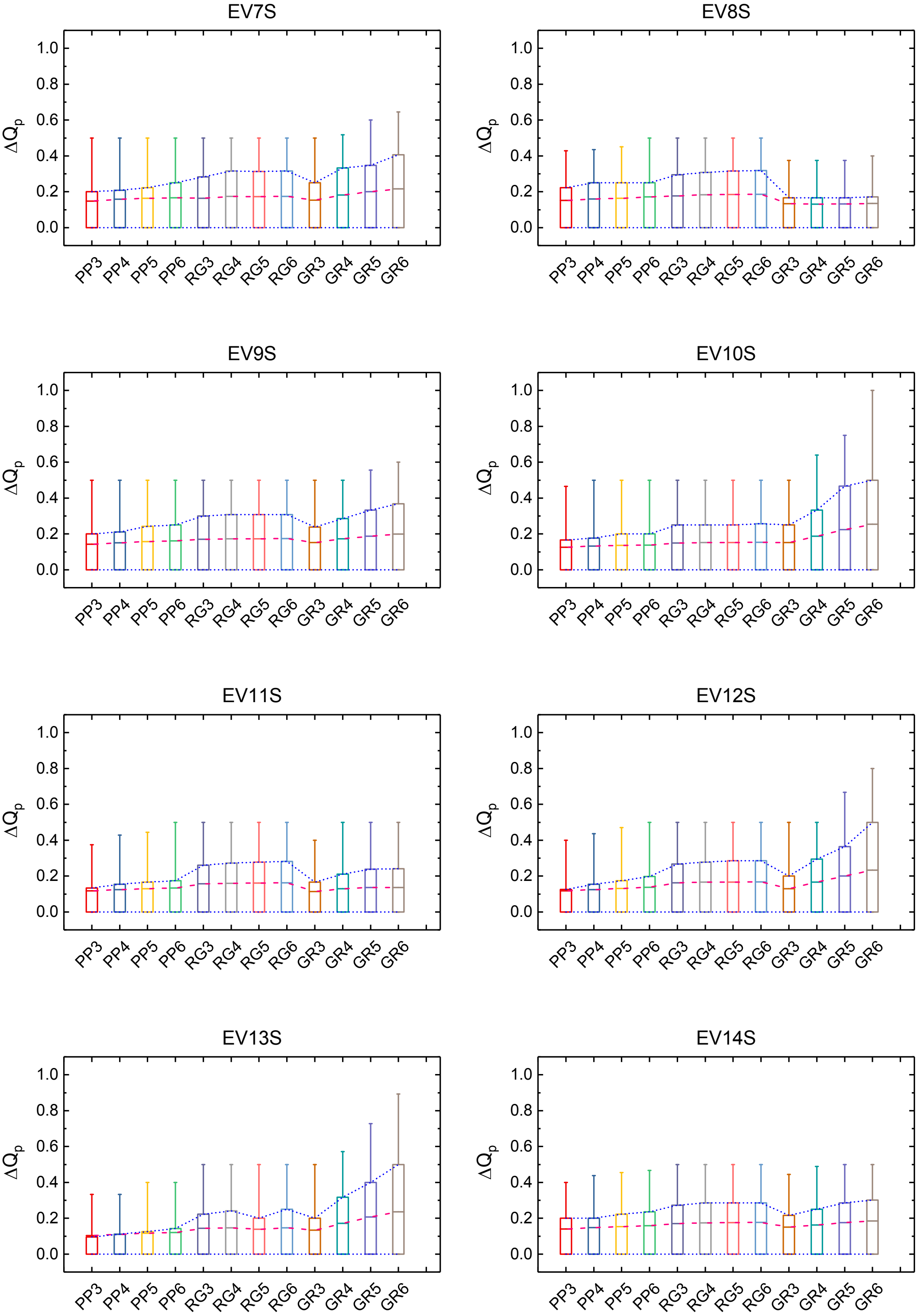

Figure 5.1: Peak flow reduction of the third set of NBS scenarios under the 8 rainfall events.

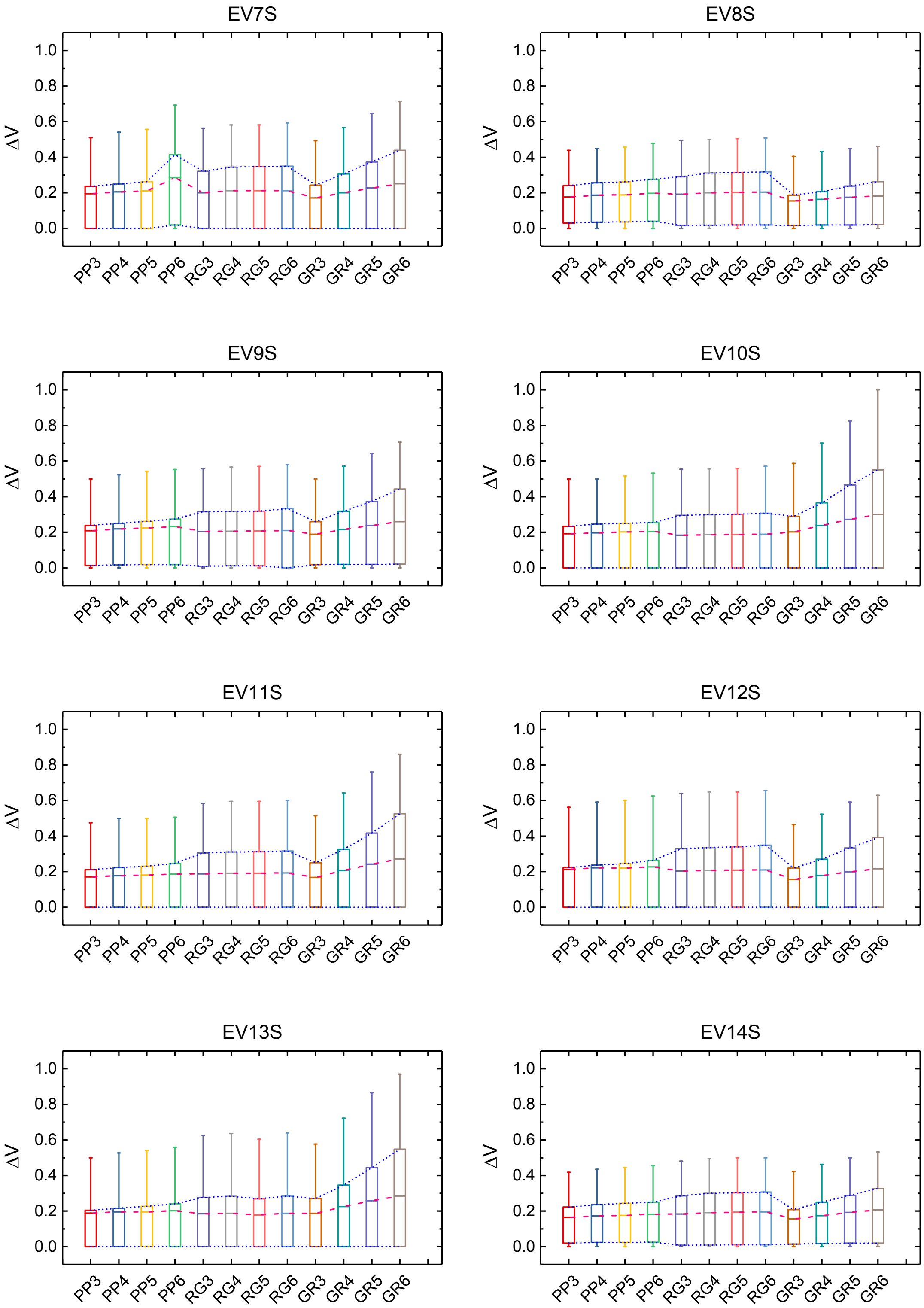

Figure 5.2: Total runoff volume reduction of the third set of NBS scenarios under the 8 rainfall events.

5.1.3 Combined scenarios

As shown in Figure 5.3, for the four different combined scenarios, the combination of three different NBS has the best performance in terms of the peak flow reduction. This result is generally in agreement with some previous studies (Ahiablame et al., 2013; Versini et al., 2018). For the 8 studied rainfall events, the mean values of peak flow reduction of PP6+RG6+GR6 scenario range from 26.8 % to 44 %. Correspondingly, that of the 75 % quartile ranges from 40 % to 68 %. Concerning the three other combined scenarios, the mean values of peak flow reduction of PP6+GR6 scenario range from 25.6 % to 37.3 %, and that of the 75 % quartile range from 38.4% to 66.6 %, which indicates the performance is better than the two others. The reason could be related to that the PP6+GR6 is characterised with a relatively higher D_F, and the RGs are less effective compared to the GRs under the short rainfall events.

Regarding the mean values of total runoff volume reduction of the four combined scenarios (Figure 5.4), the PP6+RG6+GR6 scenario also presents a higher value than the others, followed by PP6+GR6 scenario, GR6+RG6 scenario and PP6+RG6 scenario. However, in EV8S, the mean value of total runoff volume reduction of PP6+GR6 scenario is around 3 % higher than that of the PP6+RG6+GR6 scenario. The reason could be related to the complexity of the drainage system, for instance, in some locations, the flow direction may be modified in some conduits, which finally results in an unexpected increase of flow in the other parts of the drainage network.

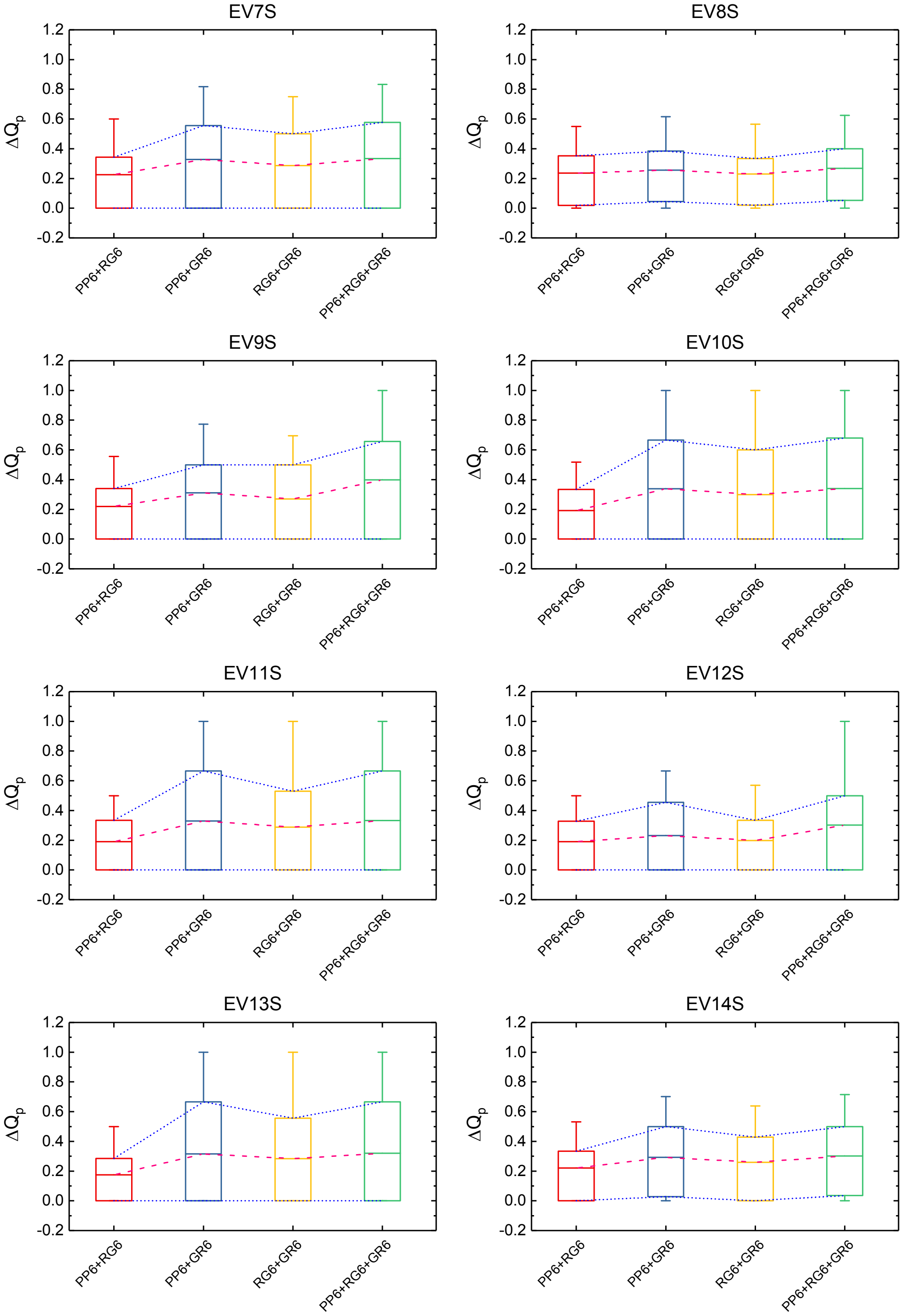

Figure 5.3: Peak flow reduction of the fourth set of NBS scenarios under the 8 rainfall events.

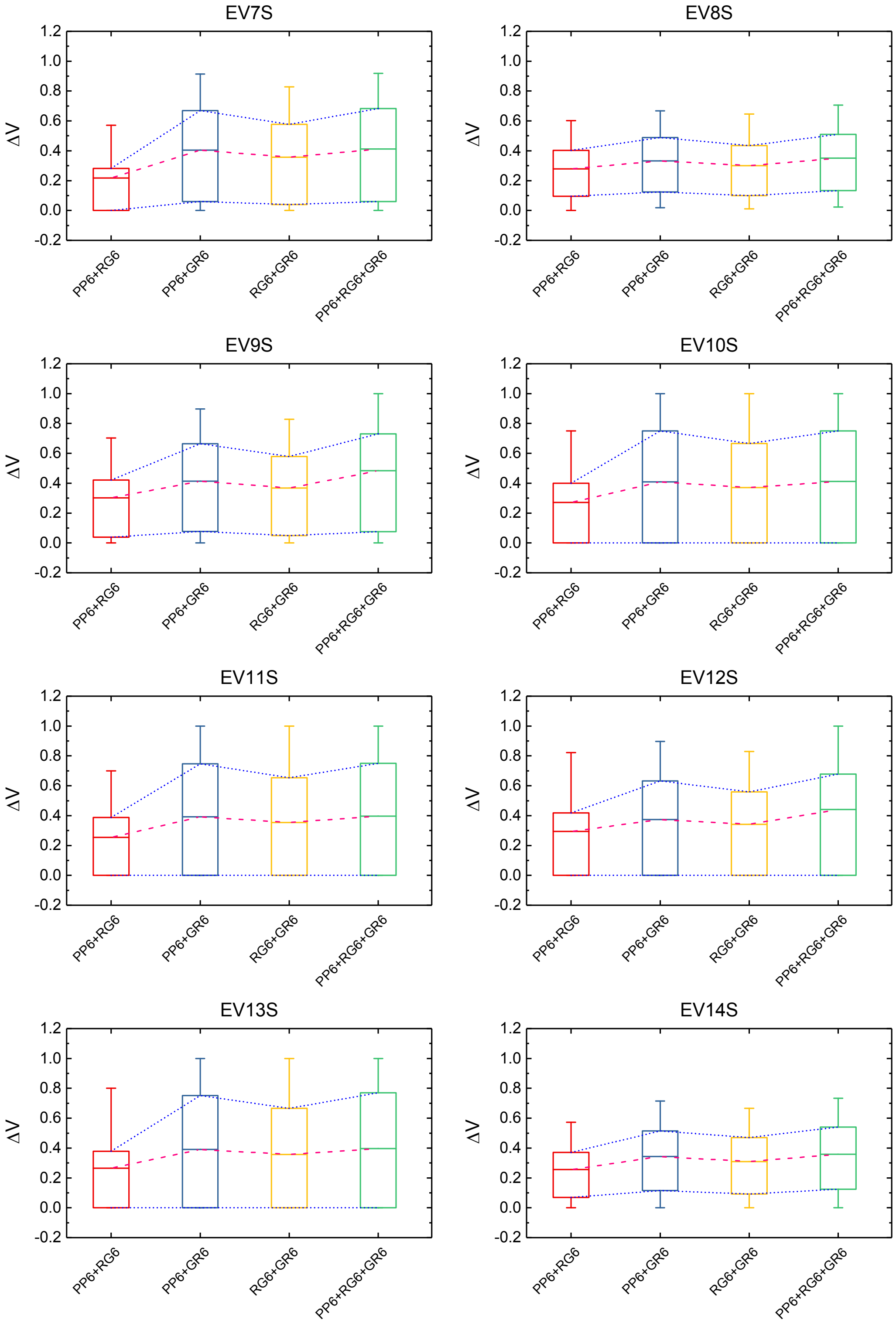

Figure 5.4: Total runoff volume reduction of the fourth set of NBS scenarios under the 8 rainfall events.

5.1.4 Location analysis of NBS scenarios

One of the significant advantages of Multi-Hydro is its ability to represent the specific spatial layout of NBS with a high resolution. Therefore, a location analysis for different NBS scenarios under the EV14S is performed. Here, the fifth set of NBS scenario was studied. The reasons for selecting EV14S is because this event has the strongest peak rainfall intensity, and the spatial variability of this rainfall event is more pronounced than that of the other rainfall event.

The results of the two hydrological indicators of the fifth set of NBS scenario are shown in Figure 5.5, and several findings can be summarised as follow:

(i) The scenarios with NBS at the downstream of the catchment have better performances than those of the scenarios by implementing NBS at the upstream. The reason could be related to the intersection effects of both the spatial variability of the rainfall and NBS distributions. As shown in Figure 2.21, the cumulated rainfall (per radar pixel) of EV14S at the downstream has some strong rainfall cells, the NBS that located in these areas are highly intersected with the rainfall spikes, which increases the performances of NBS scenarios. Furthermore, the downstream is the drained area that near to the outlet, and the NBS that implemented in these areas can be more effective to reduce the runoff. A similar finding was indicated by some previous studies, which suggested that the peak flow and total runoff volume can be reduced more significantly at the outlet of the catchment (Di Vittorio and Ahiablame., 2015; Helmi et al., 2019).

(ii) GR downstream scenario is the most effective one, with the mean values of peak flow reduction around 44 % and total runoff volume reduction around 46 %. Following the two PP scenarios. However, the hydrological performances of PP upstream scenario are almost as same as the PP downstream scenario. This may be related to the PP upstream scenario has very similar D_F with the PP downstream scenario. The two RG scenarios are less effective compared with the GR and PP scenarios, with peak flow reduction and total runoff volume reduction around 20 % lower than that of the GR and PP scenarios.

(iii) The reduction of peak flow and total runoff volume of two combined scenarios are around 30 %, which is less effective compared with the two GR and PP scenarios. The reason could be related to some RGs were saturated in this event, and finally decreased the performances of combined scenarios.

Overall, these results indicate that with a careful arrangement of individual NBS in space, a substantial reduction of peak flow and total runoff volume can be achieved.

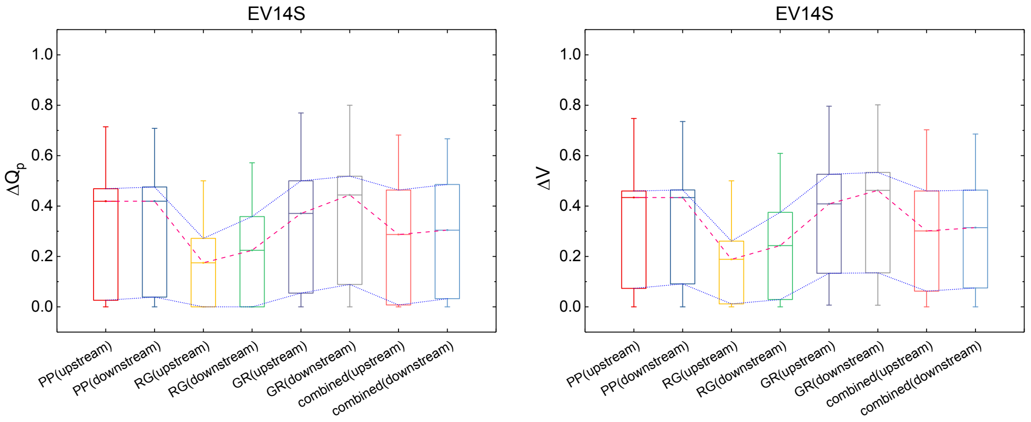

Figure 5.5: Peak flow reduction and total runoff volume reduction of the fifth set of NBS scenarios under the EV14S.

5.1.5 The different properties of GR scenarios

As described in Section 2.6, two different kinds of GR were studied (i.e., extensive and semi-intensive). For the 8 rainfall events, the two types of GR scenario with the *IS* of 10 % and 25 % have similar performances: the mean values of peak flow reduction and the total runoff volume reduction are almost unvaried (see Figures 5.6 and 5.7). However, when *IS* increases to 50 %, the performances of extensive GR scenario and semi-intensive GR scenario have a significant difference. For instance, the extensive GR scenario with *IS* of 50 %, the mean values of peak flow reduction range from 10.7 % to 25.4 %, and those of the corresponding semi-intensive GR scenario range from 20.7 % to 25.7 %. Regarding the mean values of total runoff volume reduction, the extensive GR scenario with *IS* of 50 % is averagely around 3 % lower than that of the semi-intensive GR scenario. The largest difference of the mean values of peak flow reduction and the total runoff volume reduction between the two types of GR scenario is found in EV12S, which is 10 % and 7.3 %, respectively. The reason is due to this rainfall event consecutively lasts around 2 hours, thus the extensive GRs with *IS* of 50 % are more easily saturated. Overall, the mean values of peak flow reduction and total runoff volume reduction of the semi-intensive GR scenario (*IS* = 50%) are higher than that of the extensive GR scenario (*IS* = 50%) under the stronger rainfall events (i.e., EV8S and EV14S, return period larger than 1 year). However, the performances of two types of GR scenarios (*IS* = 10 %, 25 % and 50 %) have no significant difference for some weak rainfall events with 1 month return period (i.e., EV10S, EV11S, EV13S). Therefore, these results reveal that the semi-intensive GR is more effective than the extensive GR only in strong and consecutive rainfall events.

The results of 75 % quartile of these two technical indicators are almost the same. The scenarios of extensive GR and semi-intensive GR with *IS* of 10 % and 25 %, the peak flow reduction ranges from 43 % to 50 %, and the total runoff volume reduction ranges from 43 % to 55 %. When *IS* increases to 50 %, the minimum peak flow reduction of the extensive GR scenario decreases to 14.3 % and that of the semi-intensive GR scenario decrease to 35.7 %. Correspondingly, the total runoff volume reduction of the extensive GR scenario (*IS* = 50 %) ranges from 25 % to 55 %, which is around 8.4 % lower than that of the semi-intensive GR scenario (*IS* = 50 %).

In total, it seems that the *IS* of GR is more sensitive than their substrate thickness. During the strong rainfall event, the hydrological performances of the semi-intensive GR scenario are more effective than that of the extensive GR scenario only when *IS* reaches 50 %.

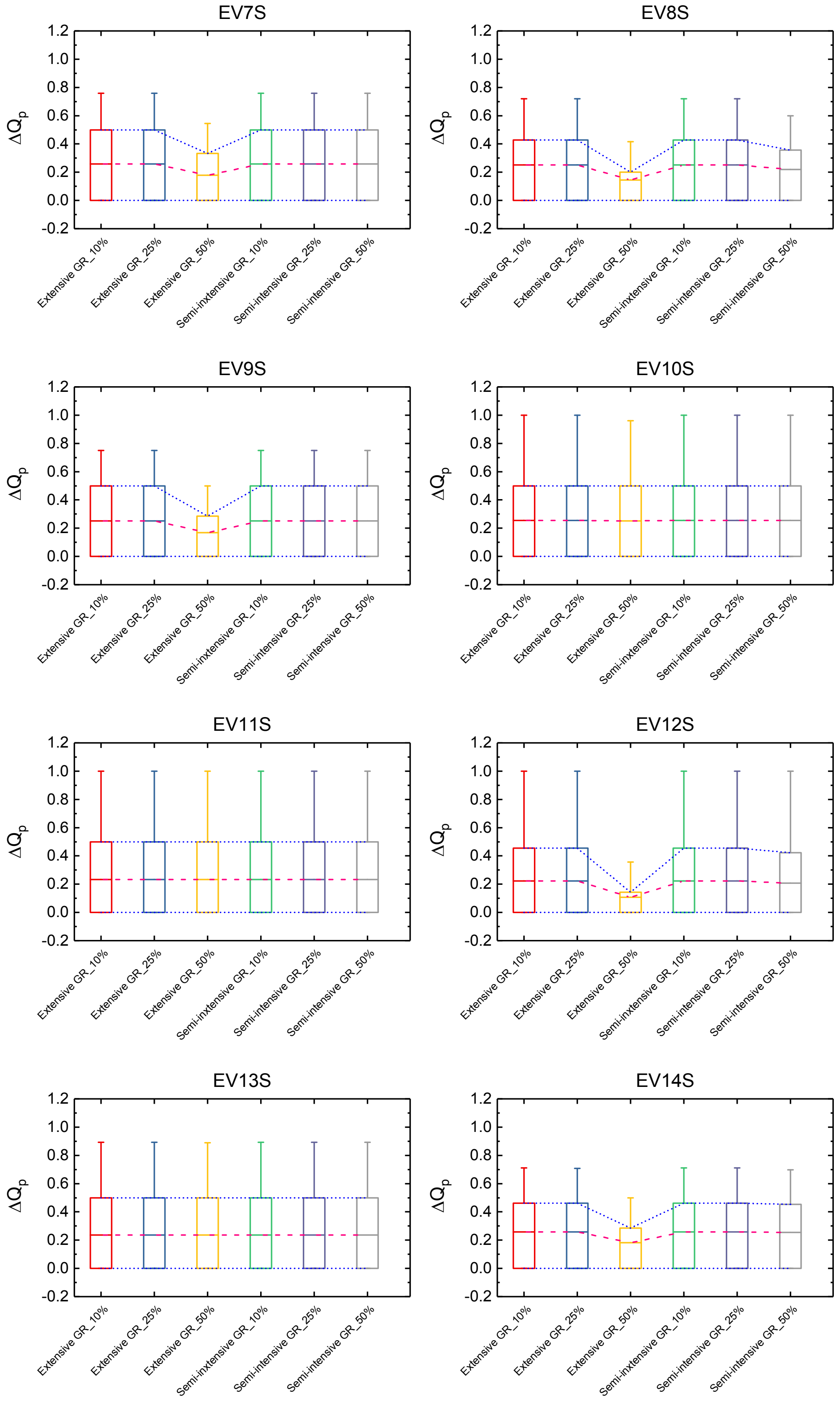

Figure 5.6: Peak flow reduction of the sixth set of NBS scenarios under the 8 rainfall events.

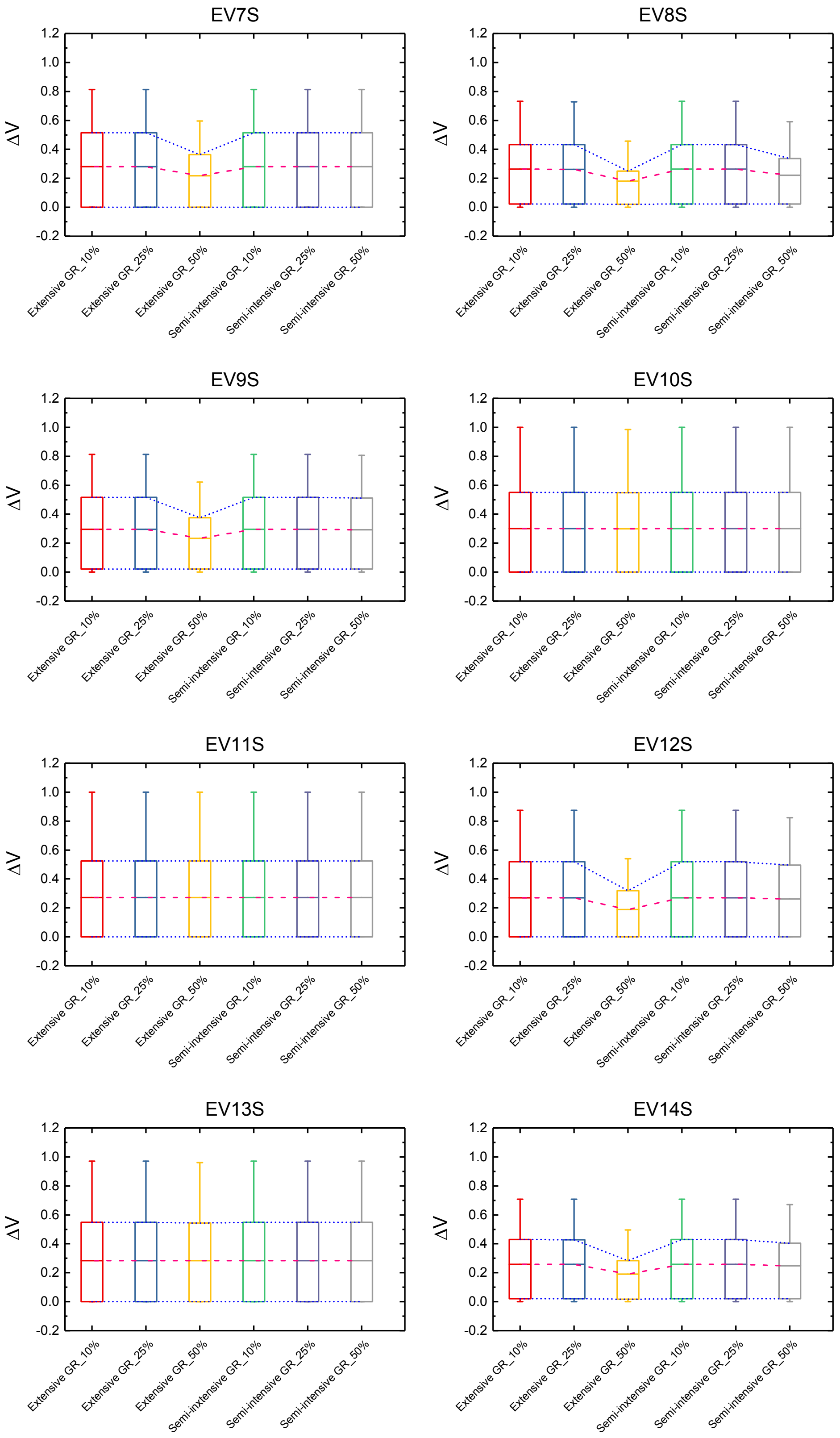

Figure 5.7: Total runoff volume reduction of the sixth set of NBS scenarios under the 8 rainfall events.

5.1.6 Life Cycle Costs analysis

In this study, based on the grid-based character of the Multi-Hydro model, the implementation areas of NBS can be calculated by counting the pixels that represent the NBS. The PVC of each NBS scenario is calculated based on Eq. 5.1, and the relative parameters (e.g. empirical cost, life span, and annual operation and maintenance costs) are obtained from the references (more details of the parameters can be found in Table 5.2). Here, the PVC (€/m^2) of each type of NBS is shown in Figure 5.8a, and the corresponding LCC (million €) of each NBS scenarios is shown in Figure 5.8b. According to Figure 5.8a, the highest PVC is computed for the semi-intensive GR, around 154.4 €/m^2. Correspondingly, the lowest one, is around 57 €/m^2 for RG. Concerning the LCC of each NBS scenario (Figure 5.8b), the combined scenarios are much higher than that of scenarios with single types of NBS. For instance, the scenario of PP6+RG6+GR6 has the highest LCC, which is around 93.5 million €. Correspondingly, the scenario of RG3 has the lowest LCC, which is approximately 6.1 million €.

NBS type	**Construction cost (C_0) (€/m^2)**	**Annual operation and maintenance Costs (C_a) (€/m^2)**	**Life span (T) (year)**	**Discount rate (r)**	**Reference**
Extensive GR	35	1.75	40	5%	Leimgruber et al., 2019
Semi-intensive GR	120	1.91	40	5%	https://www.travaux.com/couverture-toiture/guide-des-prix/combien-coute-une-toiture-vegetalisee
Permeable pavement	49.4	1.07	20	5%	Praticò et al. 2015; Montalto et al. 2007; Li et al. 2020
Rain garden	30	1.5	40	5%	Leimgruber et al. 2019

Table 5.2: The parameters of *PVC* of each type of NBS.

5.1.7 Cost-effective evaluation

The cost-effective evaluation of NBS scenarios is based on Eq. 5.3. For each NBS scenario, the mean value of CE of eight rainfall events is taken into account.

As shown in Figure 5.8 (c), for the third set of NBS scenarios, the RG scenarios are relatively more cost-effective than that of the GR and PP scenarios. The most cost-effective scenario is RG3, with the CE value around 2.9. In general, the scenarios with lower D_F are relatively more cost-effective (e.g. RG1, GR1, and PP1), because of their lower implementation level.

Regarding the fourth set of NBS scenarios (i.e., the 4 combined scenarios), the GR6+RG6 scenario is more cost-effective than the other combined scenarios. The PP6+RG6+GR6 scenario has the lowest CE (= 0.38), which again demonstrates that increasing the implementation level of NBS in the catchment may not be the best solution in terms of both economic and technical criteria.

Regarding the sixth set of GR scenarios, the extensive GR scenario is much more cost-effective than that of the semi-intensive GR scenario, with the averaged CE around 0.88 (here, the CE is only computed for two different GR scenarios with $IS = 10$ %). Comparing with the other NBS scenarios, the semi-intensive GR scenario is even less cost-effective than that of scenarios with combining two different kinds of NBS (i.e., PP6+RG6, PP6+GR6). Therefore, a high implementation level of semi-intensive GRs in the catchment is not appropriate in terms of the cost-effectiveness.

Concerning all NBS scenarios under the EV14S, the most cost-effective scenarios are the PP (upstream) and PP (downstream) scenarios, with the CE value around 3.7. The results demonstrate that in some specific rainfall conditions, concentrating the single type of NBS in some specific locations in the catchment (e.g. the downstream in our studied catchment) is more cost-effective than heterogeneous implementing NBS over the whole catchment.

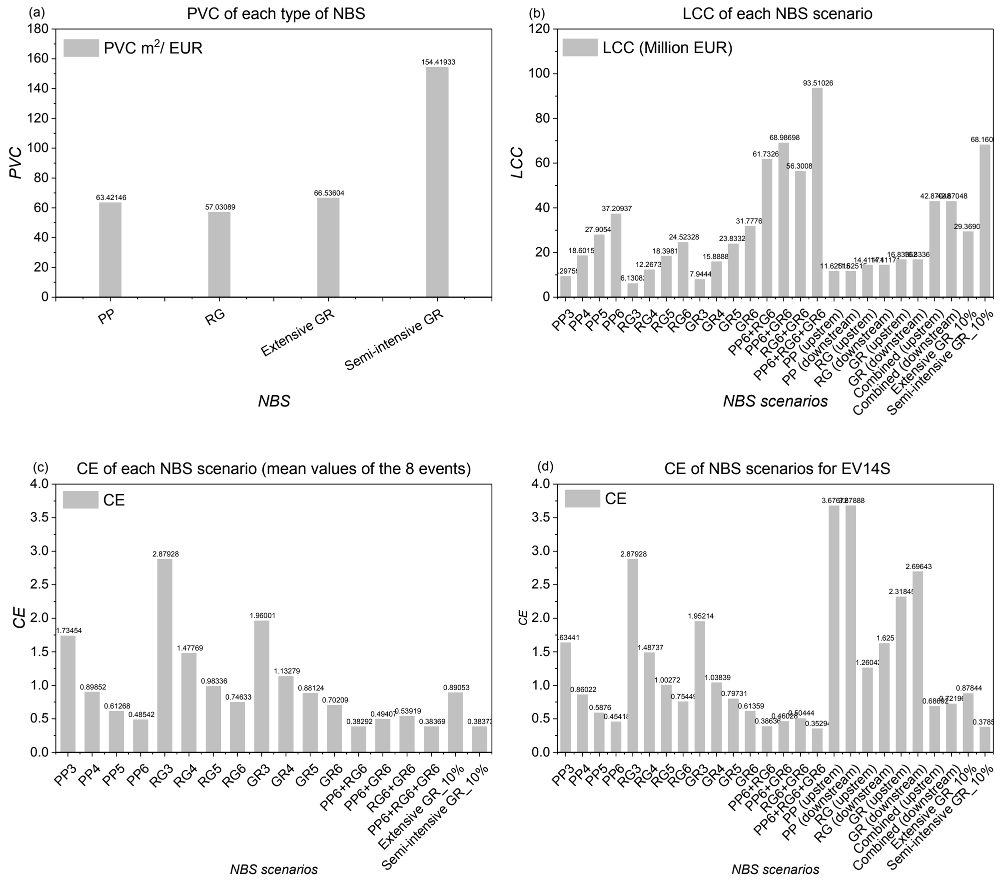

Figure 5.8: (a) PVC of each type of NBS; (b) LCC of each NBS scenario; (c) The mean value of CE of each NBS scenario under the 8 rainfall events; (d) CE of each NBS scenario under the EV14S.

5.1.8 Intermediate conclusions for Section 5.1

This study focuses on the cost-effective design of NBS scenarios with integrating both technical and economic indicators in terms of different rainfall conditions. The hydrological performances of NBS scenarios are evaluated by technical indicators with the help of numerical modelling. The LCC is considered as the economic indicator and integrated with technical indicators for the cost-effective design of NBS scenarios. The main findings are summarised as follows:

1. With the help of the fractal dimension, the spatial distributions and implementation levels of NBS over the catchment were quantified in a wide range of scales. For different types of NBS scenario, their hydrological performances are indeed improved with the increase

of the D_F of NBS. However, due to some intersection effects of both the spatial rainfall variability and NBS distributions, the non-linear relationship is found between the performances of NBS and the rainfall intensity.

2. The hydrological performances of NBS scenarios are generally better with the combination of three different types of NBS (PP6+RG6+GR6 scenario), which represents the highest D_F. However, in the strong rainfall event of EV8S, the total runoff volume reduction of the PP6+RG6+GR6 scenario is lower than that of the PP6+GR6 scenario.
3. The spatial locations of NBS have certain impacts on their performances. In some specific rainfall conditions, with implementing NBS in the downstream of the catchment is more effective than that of the upstream.
4. The extensive GR scenarios have the same hydrological responses as the semi-intensive GR scenarios when *IS* of GRs lower than 50 %. When the *IS* of two types of GR reaches 50 %, the hydrological performance of semi-intensive GR scenario is significantly better than that of the extensive GR scenario under the strong rainfall events.
5. Concerning the eight studied rainfall events, the most cost-effective NBS scenario is the RG3 scenario with a relatively low D_F. The combination of three types of NBS in the watershed is less cost-effective compared with the other NBS scenarios. Regarding the NBS scenario in the strongest event (EV14S), the most cost-effective NBS scenarios are the PP upstream and PP downstream. In this rainfall condition, concentrating single type of NBS in some specific locations can be more cost-effective than heterogeneous implementation NBS all over the catchment.
6. Considering both hydrological performances and economic costs, the cost-effective NBS scenario has a relatively lower implementation level. The D_F of these NBS scenarios ranges from 1.5 to 1.6 (large scale). The NBS scenarios are less cost-effective when their D_F higher than 1.6. Under the given economic investments, by quantifying the optimal D_F of NBS, the hydrological performance of NBS can be improved and that of the life cycle costs can be reduced, so as to realize the spatial non-uniform distribution optimization.

Overall, these results can provide some effective guidelines for the future urban planning. In addition, this proposed method in this study can be easily transferred from one catchment to other, which is helpful to find a universal solution for different catchments. Future work will be conducted for evaluating the cost-effective of NBS scenarios in a wide range of scales with the help of a scale-independent indicator based on the Universal Multifractal framework.

5.2 A scale-independent framework for cost-effective design of NBS scenarios

In Section 4.3, to evaluate the hydrological performances of NBS scenarios in terms of the 2D overland flow across scales, the scale-independent indicator of maximum probable singularity γ_s that based on UM theoretical framework was applied (Scherzter and Lovejoy, 1987; Schertzer and Lovejoy, 1997). The results of Section 4.3 indicated that γ_s is an effective indicator for assessing the extremes of a field. Thus, this indicator can be integrated with the economic indicator (i.e., LCC) as the scale-independent cost-effectiveness indicator (SICE) for designing cost-effective NBS scenarios over a wide range of scales.

To investigate whether the SICE within the UM framework can effectively predict the cost-effective NBS scenarios across scales, another SICE is proposed and used as the reference to compare with it. With this respect, the scale-dependent singularity γ_{max} is integrated with the LCC at different resolutions as the reference SICE. The procedure for computing γ_s and γ_{max} are detailed in Section 3.7, and the approach for calculating LCC of different NBS scenarios can be found in Section 5.1.

This study takes the last time step of the simulated overland flow of the third – sixth sets of NBS scenarios under the EV14S as an example. Because this rainfall event characterised by a very pronounced rainfall peak and results in the field with the higher overland flow (see Chapter 2 for more information about the NBS scenarios and the rainfall event). Furthermore, the last time step reflects the eventually hydrological response of the catchment.

For comparing the SICE of NBS scenarios by two different methods, the first step is to compute the corresponding γ_{max} and γ_s. Here, a 256 × 256 rectangle area of the last time step (t_n) of the 2D simulated overland flow map of each NBS scenario under the EV14S is selected from the outputs of Multi-Hydro (see Figure 5.9 for an example of PP3 scenario). Then, this rectangle area is up-scaled from the initial smallest scale $\lambda_8 = 256$ to the larger scale $\lambda_1 = 2$ (see Figure 5.10 for an example of the up-scaling process). Here, the field is not up-scaled to the largest scale $\lambda_0 = 1$, because the overland flow in this resolution is not evident. According to the box-counting method (Eq. 3.2), the up-scaling process is first to count the number of pixels containing the overland flow, by starting with the smallest pixel size (l = 10 m in this study), then continuously increasing the pixel size by simply merging the 4 adjacent pixels, this procedure is repeated until reaching the largest pixel size (L). Thus, the resolution is decreased by λ_1 times. Here, it is important to mention that the fifth set of NBS scenarios (i.e., upstream and downstream NBS scenarios) take different rectangle area because of the particular implementation location of the NBS (see Figure 2.28 for the PP upstream scenario and PP downstream scenario for more details on the selected area).

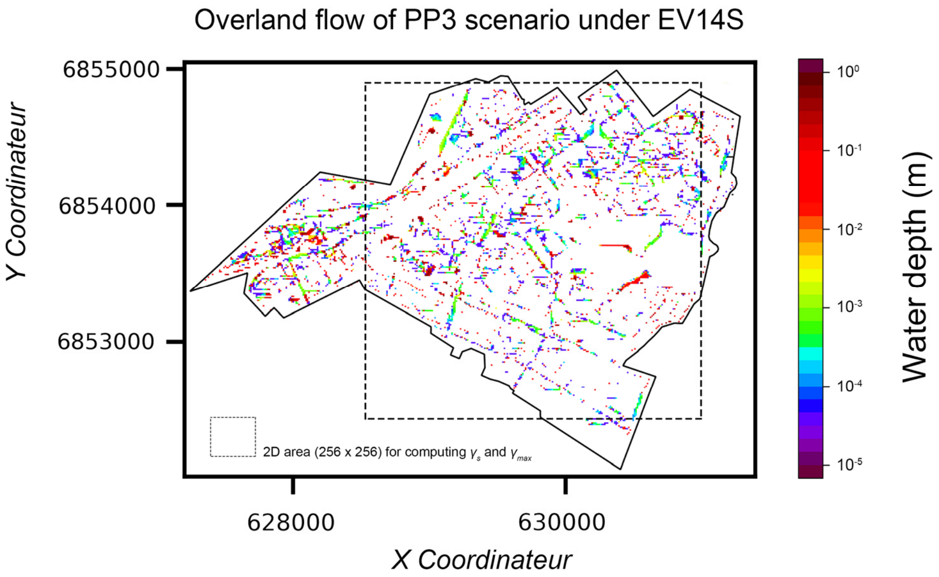

Figure 5.9: The overland flow map of PP3 scenario under the EV14S; z-axis plotted in log scale.

As shown in Figure 5.10, the up-scaling process is illustrated with an example of the last time step of simulated overland flow of PP3 scenario under the EV14S. Each bar represents a value of the overland flow on the selected field. Starting from the highest resolution $\lambda_8 = 256$, the fluctuations of the field are gradually reduced with the decrease of the resolution, and the number of pixels representing overland flow decreases compared to the initial resolution. Since a large number of overland flow pixels are surrounded by pixels without overland flow (i.e., zero values), the pixels with overland flow reduce after averaging adjacent pixels. By repeating the up-scaling procedure iteratively, the pixels with overland flow gradually disappear as resolution decreases. However, it is noticed that the overland flow pixels grouped in the west part of the field resist the up-scaling process up to the resolution λ_4, indicating that the higher values of overland flow are concentrated at that location, which is consistent with the 2D overland flow map presented in Figure 5.9.

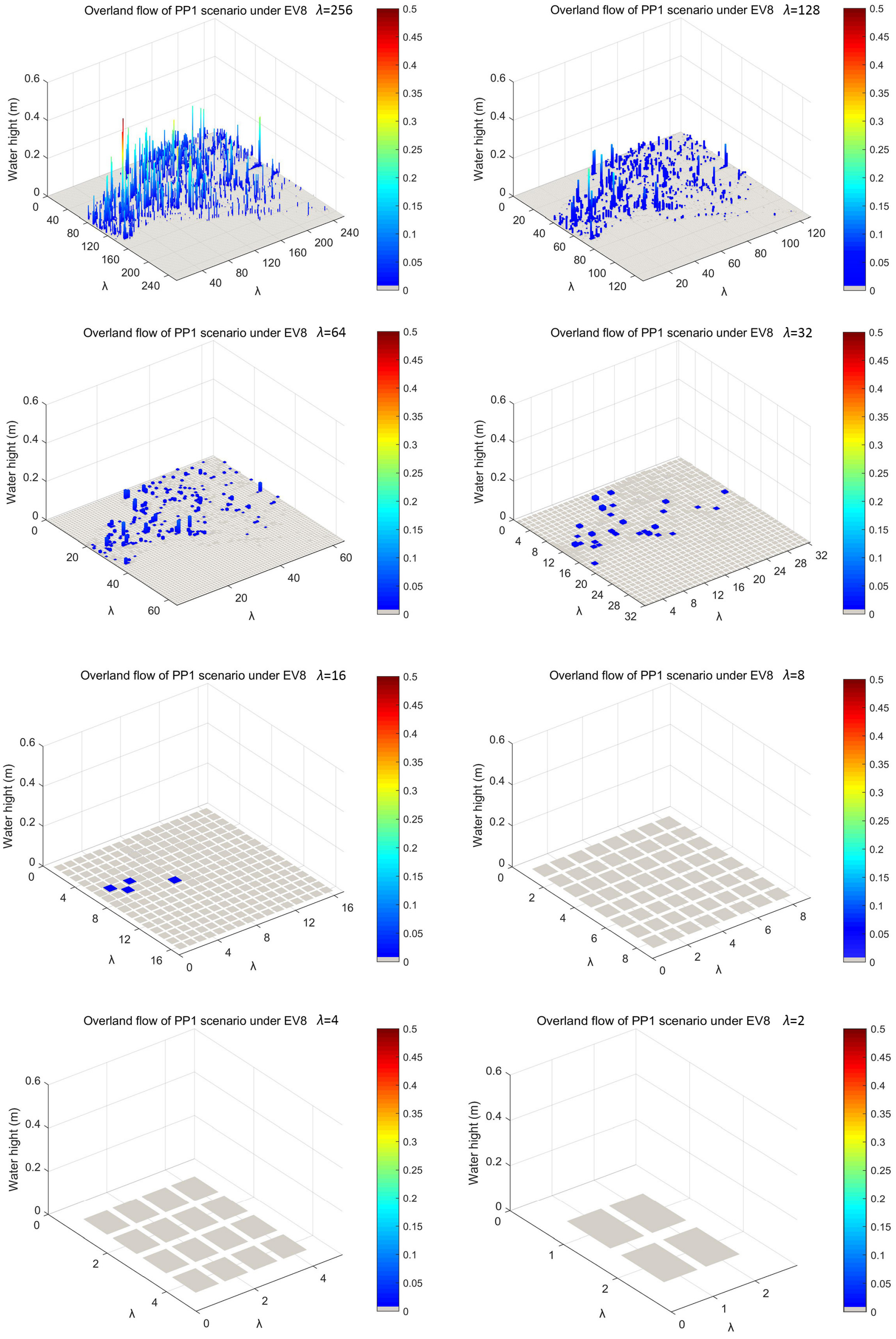

Figure 5.10: An example of the up-scaling process of the last time step of the overland flow map of PP3 scenario under the EV14S.

Similarly, for up-scaling the land use map, the same rectangle area shown in the 2D simulated overland flow map (Figure 5.9) is selected from the rasterised NBS land use maps (the fifth set of NBS scenarios takes different rectangle areas were shown in Figure 2.28). This area is also up-scaled from the initial scale λ_8 to the larger scale λ_1 in order to obtain the total implementation area of NBS at each resolution (i.e., λ_8, λ_7, $\lambda_6 \ldots \lambda_1$). Figure 5.11 presents an example of the up-scaling process of the land use of permeable pavement (PP3 scenario). Similar to the up-scaling process of the 2D simulated overland flow, the initial resolution of the land use map starts from λ_8 (the red pixels represent the permeable pavements). With decreasing the resolution, the pixel size of the permeable pavements is enlarged, and the analysed field was gradually filled with permeable pavements.

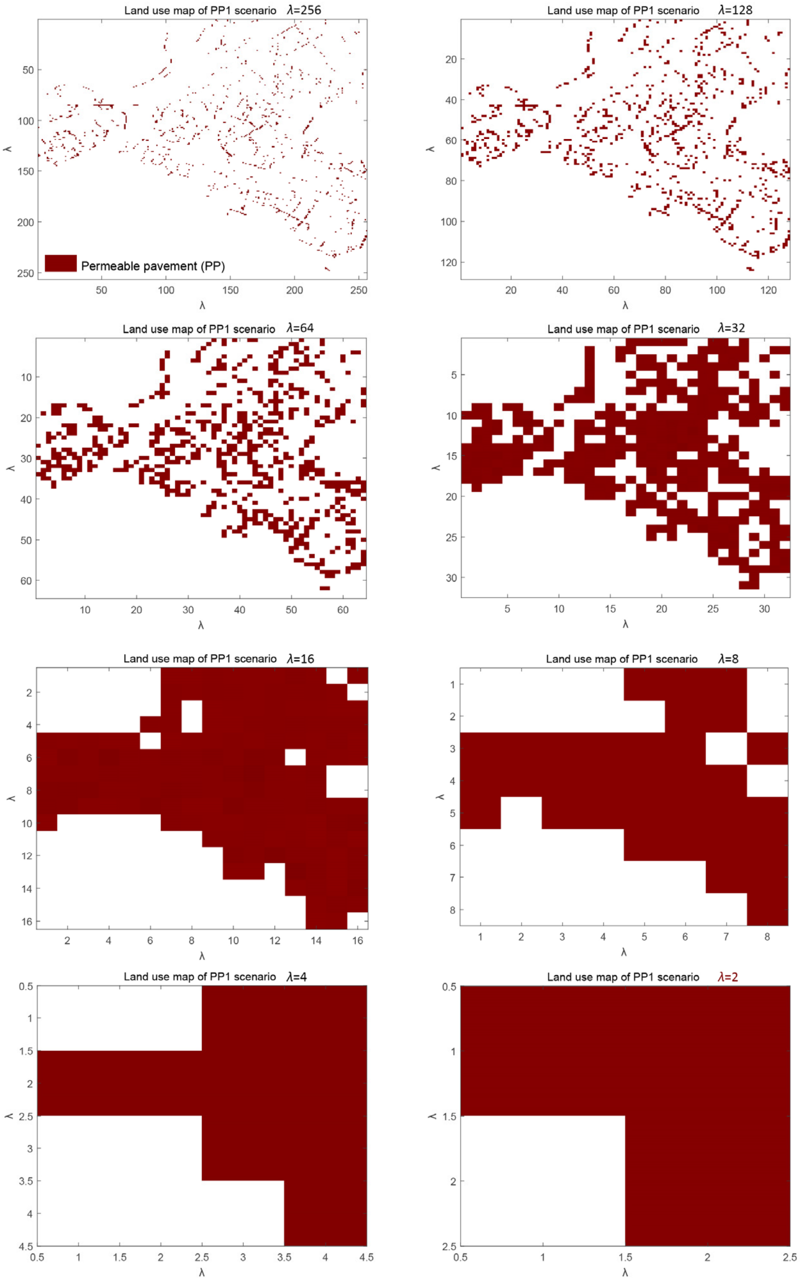

Figure 5.11: An example of up-scaling process of the rasterised land use data of PP3 scenario.

As the PVC of each type of NBS (i.e., PP, RG, and GR) has been computed in Section 5.1 (see Table 5.2), they are directly used in this section. The LCC of NBS scenarios at different resolutions can be expressed as:

$$\mathrm{LCC}\,(\lambda) = PVC\ \times A_l \tag{5.4}$$

where A_l (m^2) is the total implementation area of NBS in each NBS scenario at each scale l. Because the Multi-Hydro is a grid-based model, the A_l can be easily computed by multiplying the number of pixels representing the NBS by the size of a pixel at each l.

5.2.1 Scale-independent cost-effectiveness indicators

As γ_{max} is a scale-dependent singularity, the value changes with the change of λ. Thus, the value of γ_{max} is computed at different λ for the last time step (t_n) of the simulated overland flow by using the following expression:

$$\gamma_{max,t_n}\,(\lambda) = log_\lambda\left(\frac{H_{max,t_n}(\lambda)}{H_{mean,t_n}(\lambda)}\right) \tag{5.5}$$

where $\gamma_{max,t_n}(\lambda)$ is the effective maximum singularity at the resolution λ.

Combining Eq. 5.4 and Eq. 5.5, the reference SICE can be expressed as:

$$CE_{\gamma_{max}}(\lambda) = \frac{\gamma_{max,t_n}(\lambda)}{LCC(\lambda)} \tag{5.6}$$

Based on the UM framework (Scherzter and Lovejoy, 1987; Schertzer and Lovejoy, 1997), γ_s is computed by using Eq. 3.25, which is a scale-independent indicator for inferring the extremes and evaluating the hydrological performances of NBS scenarios (see Section 4.3 for more information). Therefore, the estimated SICE is based on the scale-independent indicator γ_s and the LCC of each NBS scenario at different resolution by using the Eq. 5.7:

$$CE_{\gamma_s}(\lambda) = \frac{\gamma_s}{LCC(\lambda)} \tag{5.7}$$

Before computing the γ_s, the first step is to estimate UM parameters. The spectral analysis (Eq. 3.32) is first applied to check whether the field is conservative. Figure 5.12 (a) displays the scaling quality (i.e., the coefficient of determination r^2 for the linear regression) of the last time step of the simulated overland flow of all NBS scenarios. The r^2 of all NBS scenarios ranges from 0.76 to 0.92. Furthermore, as shown in Figure 5.12 (b), the spectral slope of all NBS scenarios is less than D (i.e., the values of β range from 0.26 to 0.54), which indicates that the analysed fields are conservative. Therefore, it is possible to directly apply the DTM analysis to the field (see Chapter 3 for a review of the DTM technique).

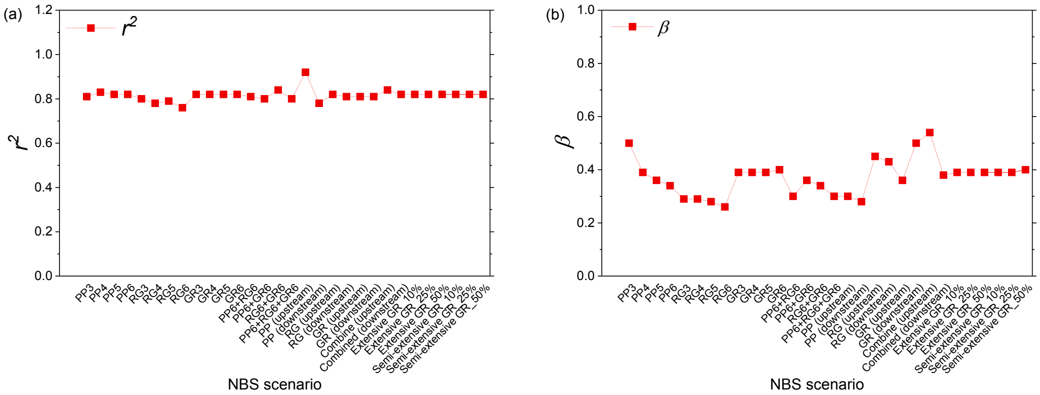

Figure 5.12: r^2 (a) and β (b) of spectral analysis of the last time step of the simulated overland flow of NBS scenarios under the EV14S.

Figure 5.13 displays the DTM analysis performed on the last time step of the 2D simulated overland flow map of NBS scenarios under the EV14S. For all NBS scenarios, one scaling regime from 10 m to 2560 m can be identified and the r^2 for q = 1.5 is higher than 0.9, which indicates the scaling quality of the UM field is satisfied, and the estimated UM parameters are reliable across the whole range of scales.

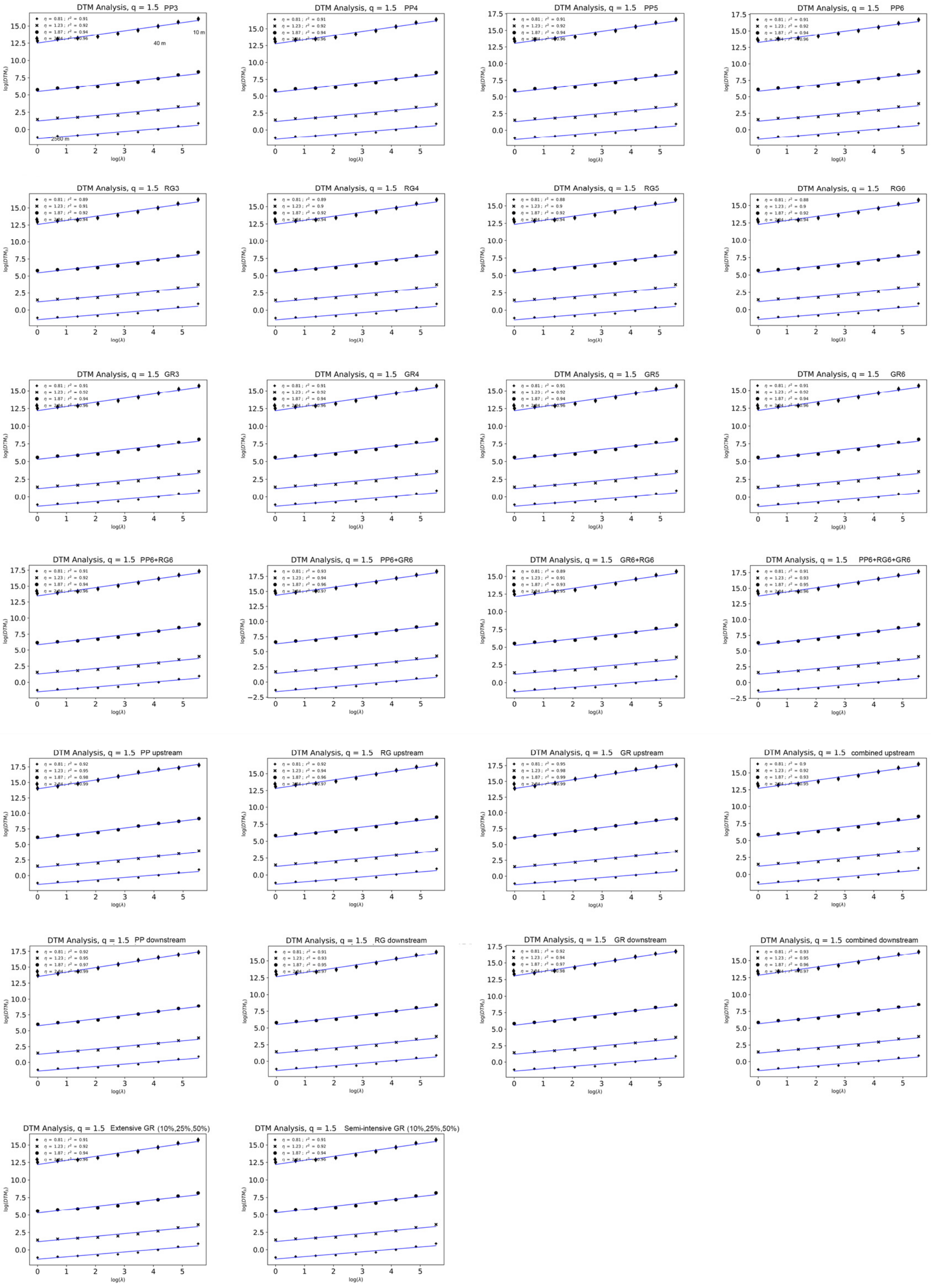

Figure 5.13: DTM analysis of the last time step of the simulated overland flow of NBS scenarios under the EV14S (Eq. 3.14 in log-log plot).

The values of UM parameters are shown in Figure 5.14, which α and C_1 present an opposite trend. The value of α of NBS scenarios ranges from 0.39 to 0.64, which presents that the multifractality of the overland flow of NBS scenarios is relatively weak. Correspondingly, the value of C_1 ranges between 0.55 and 0.75 indicates the overland flow of NBS scenarios has very similar degrees of homogeneity. For the third set of NBS scenarios, it is noticed that the α decreases with increasing D_F of NBS scenario, and the C_1 increases with increasing D_F of NBS scenario. For the fourth set of NBS scenarios, the fluctuation of UM parameters of RG6 + GR6 scenario is more significant than that of the other combined scenarios. For the fifth set of NBS scenarios, the NBS downstream scenarios have higher value α but lower C_1 value than that of the NBS upstream scenarios. Concerning the sixth set of NBS scenarios, the α and C_1 of extensive GR scenario and semi-intensive GR scenario are the same when the IS = 10 % and 25 %. When the IS increases to 50 %, the semi-extensive GR scenario has a lower α but higher C_1 than the extensive GR scenario.

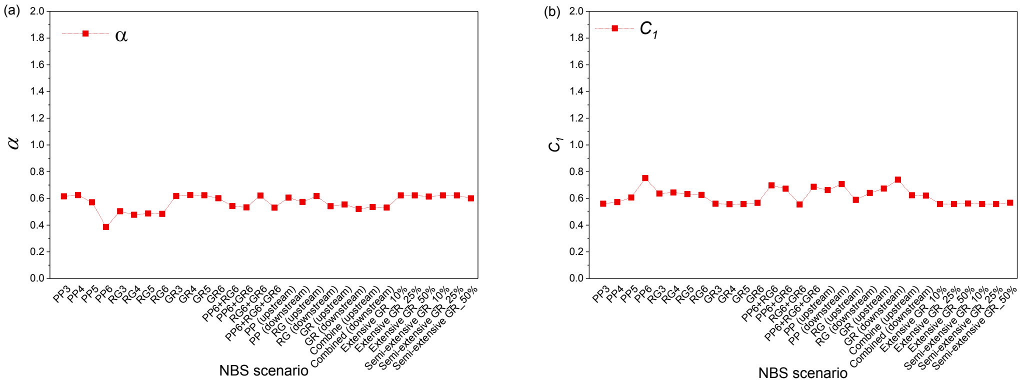

Figure 5.14: UM parameters of the last time step of the simulated overland flow of NBS scenarios under the EV14S (a) values of α; (b) values of C_1.

5.2.2 Hydrological performances of NBS scenarios

Figure 5.15 displays the $\gamma_{max,t_n}(\lambda)$ and γ_s of the last time step of the overland flow of NBS scenarios under EV14S at different scales. The values of γ_s range from 1 to 1.22 across the range of scales. Correspondingly, the values of $\gamma_{max,t_n}(\lambda)$ at the highest resolution λ_8 is strongly correlated with that of γ_s. With increasing the resolution of the field, the discrepancy between $\gamma_{max,t_n}(\lambda)$and γ_s becomes larger. However, at each level of resolution, γ_s is almost proportional to the $\gamma_{max,t_n}(\lambda)$.

Regarding the resolution from 256 to 128 (small scale), it is noticed that the values of $\gamma_{max,t_n}(\lambda)$ and γ_s of the third set of NBS scenario are very similar, which indicates these scenarios have similar hydrological performances. Regarding the fourth set of NBS scenarios in this range of scale (i.e., 256 to 128), the values of $\gamma_{max,t_n}(\lambda)$ and γ_s of RG6+GR6 scenario are lower than that of the other combined scenarios, which indicates the hydrological performances of this scenario are relatively less effective than those of the other combined scenarios. The results of the fifth set of NBS scenario present that the performance of NBS implemented in the downstream of the catchment is more effective than that of the NBS implemented in the upstream (i.e., the values of $\gamma_{max,t_n}(\lambda)$ and γ_s are higher for the NBS downstream scenarios). This finding is in agreement with the result presented in Section 5.1. Regarding the sixth set of NBS scenarios, the values of $\gamma_{max,t_n}(\lambda)$ and γ_s are almost same for the extensive GR scenario (*IS* = 10 %, 25 % and 50 %) and semi-extensive GR scenario (*IS* = 10 %, 25 % and 50 %). Thus, the extensive GR scenarios have the similar performance as the semi-extensive GR scenarios for mitigating the waterlogging under the EV14S.

Concerning the resolution from 64 to 2 (large scale), the values of $\gamma_{max,t_n}(\lambda)$ of NBS scenarios are more variable than that at the small scale range. For the third set of NBS scenarios, the values of $\gamma_{max,t_n}(\lambda)$ of four PP scenarios are more variable than that of the RG scenarios and the GR scenarios. As shown in Figure 5.14, the values of α and C_1 of the third set of NBS scenarios indicate that the overland flow of PP scenarios are more variable than RG scenarios and GR scenarios over the whole range of scales. Therefore, during the up-scaling process, some extreme values of the overland flow of PP scenarios are maintained and result in that $\gamma_{max,t_n}(\lambda)$ of PP scenarios are more variable than RG scenarios and the GR scenarios at the larger scale. The value of $\gamma_{max,t_n}(\lambda)$ generally increases with increasing of the D_F of NBS scenario, which shows that the hydrological response of the catchment is improved with a higher implementation level of NBS. For the fourth set of NBS scenarios, the values of $\gamma_{max,t_n}(\lambda)$ of RG6+GR6 scenario are still lower than that of the other NBS scenario. This result is consistent with the result at the small scale range. For the fifth set of NBS scenario, it is noticed that the values of $\gamma_{max,t_n}(\lambda)$ of NBS downstream scenarios are higher than that of the NBS upstream scenarios. These results are also in agreement with the results of the small scale range. At the resolution of λ_5 and λ_4 (i.e., 32 and 16), the values of $\gamma_{max,t_n}(\lambda)$ and γ_s are very pronounced for the scenarios of PP downstream and GR downstream. With increasing the resolution, the $\gamma_{max,t_n}(\lambda)$ of the combined downstream is more pronounced than that of the other NBS scenarios. This result indicates the combined downstream scenario is more effective in the large scale range. Concerning the sixth set of NBS scenarios, the value of $\gamma_{max,t_n}(\lambda)$ of extensive GR scenario (*IS* = 10 %, 25 % and 50 %) and semi-extensive GR scenario (*IS* = 10 %, 25 % and 50 %) remains almost the same for each resolution. Thus, for the whole range of scales, the performances of GRs are not significantly improved with increasing their substrate thickness under the EV14S.

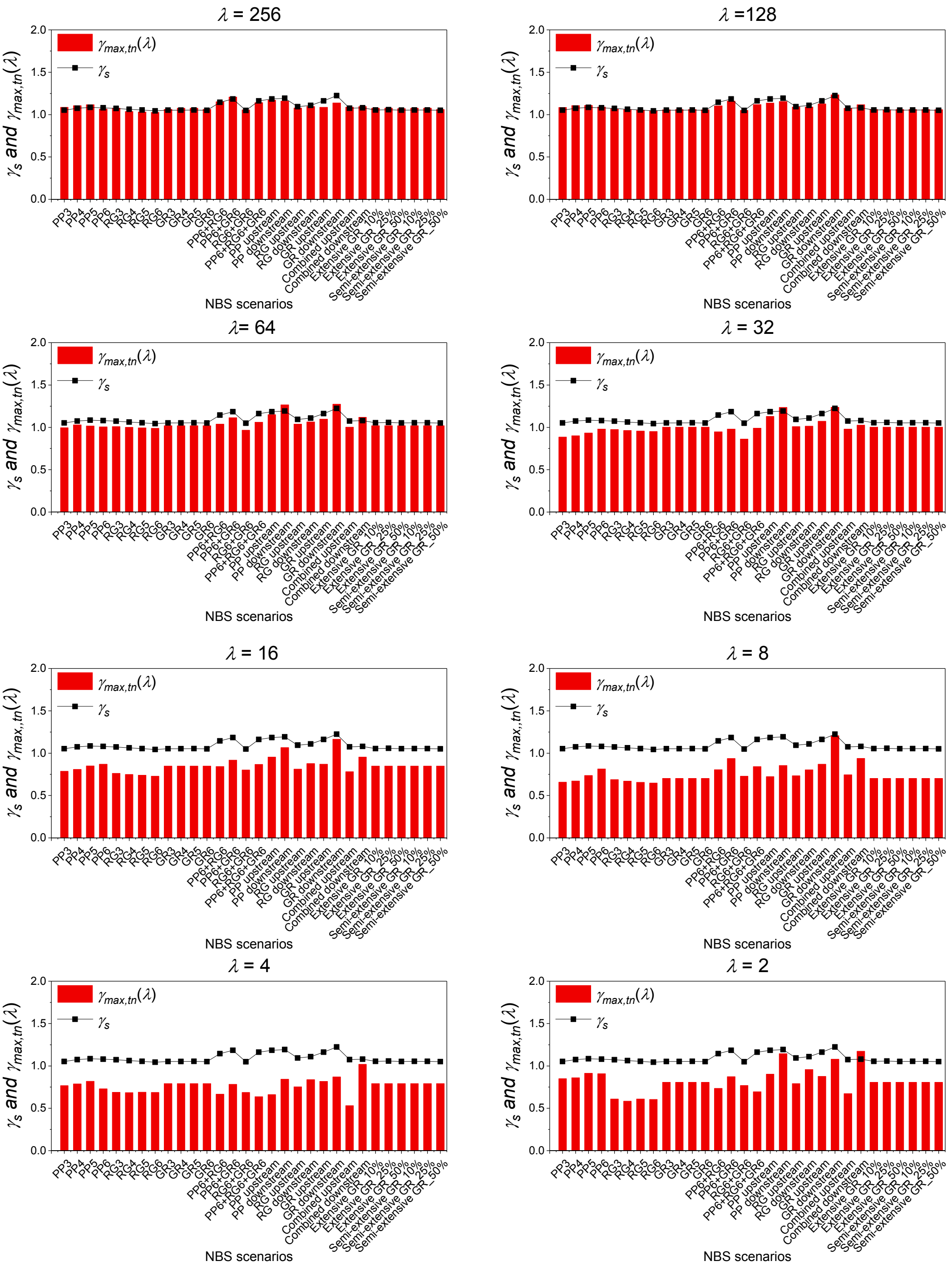

Figure 5.15: The γ_s and $\gamma_{max,t_n}(\lambda)$ of the four sets of NBS scenarios under the rainfall event EV14S.

5.2.3 LCC of NBS scenarios

As shown in Figure 5.16, the LCC of NBS scenarios in the small scale range (256 to 128) is very variable. Generally, the NBS scenarios characterised with higher D_F has higher LCC. Therefore, the LCC of the combined scenarios is much higher than that of the other NBS scenarios. For instance, at the highest resolution, the PP6+RG6+GR6 scenario has the highest LCC (around 71.7 million/€), while the RG3 has the lowest LCC, approximately 4.4 million/€. Furthermore, the LCC of semi-extensive GR scenario is also very pronounced (about 56.2 million/€) because the PVC of semi-extensive GR is more than two times higher than that of the other types of NBS.

In the large scale range (64 to 2), the LCC of NBS scenarios become more and more homogeneous, only the LCC of semi-extensive GR scenario is very pronounced, which is around two times higher than that of the other NBS scenarios. As shown in Figure 5.11, with decreasing the resolution, the area representing the NBS is increased, and finally occupied the whole catchment at the lowest resolution. Thus, for each NBS scenario, the total implementation area of NBS is more and more similar with decreasing the resolution. Finally, the LCC of each NBS scenario (except semi-extensive GR scenario) at the resolution λ_1 is very close.

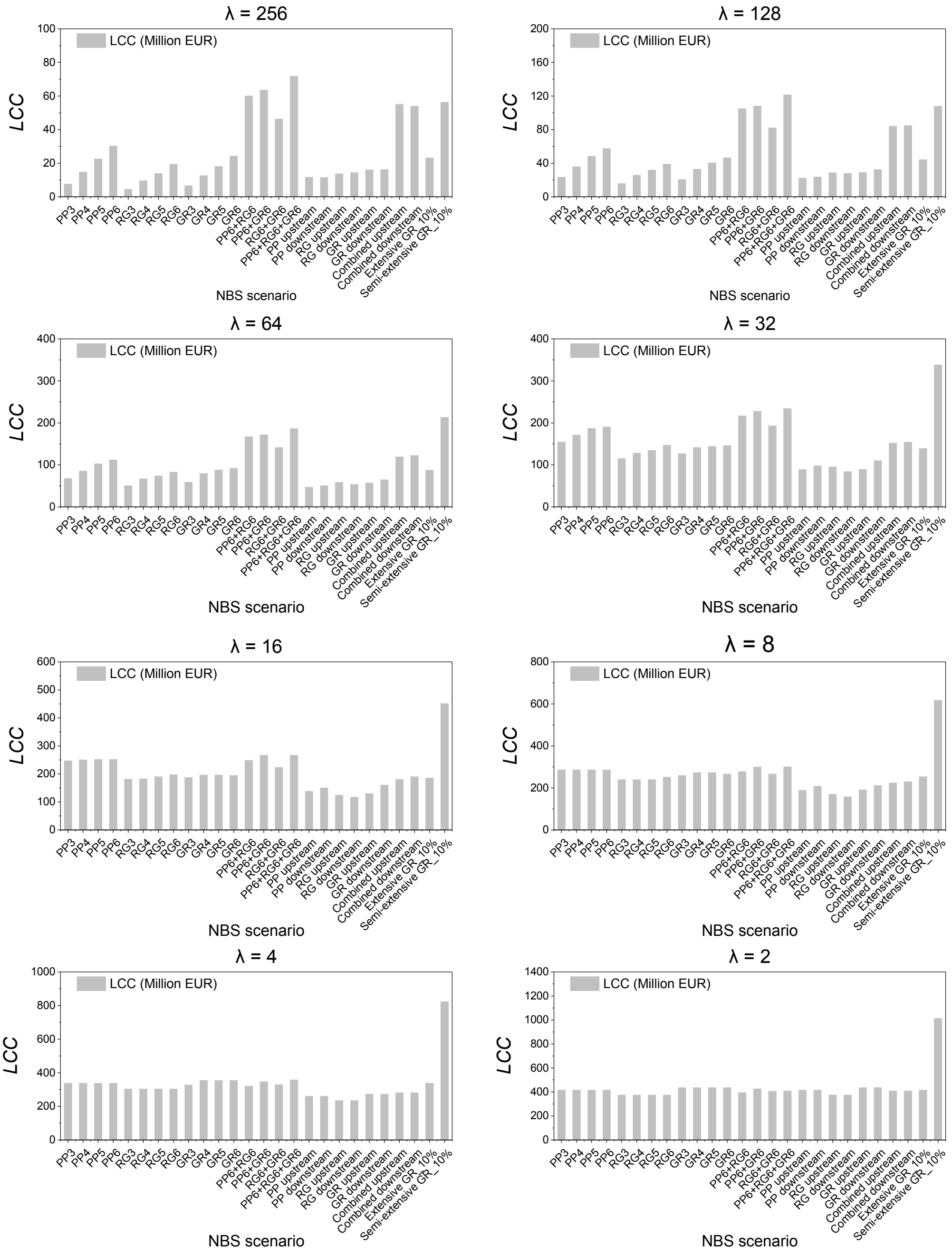

Figure 5.16: LCC of NBS scenarios at different resolution (from 256 to 2).

5.2.4 Towards the scale-independent cost-effective design

The results of two SICEs of NBS scenarios at each resolution are shown in Figure 5.17. The results of the reference SICE are in agreement with the estimated one, especially at the small scale range (258–128). The reason may be related to that the small scale range reflects the intrinsic feature of the performances of NBS scenarios. Nevertheless, the cost-effective NBS scenario changes with the change of the scale.

For the scale of λ_8 and λ_7, the cost-effective NBS scenarios are characterised with a low D_F. For instance, regarding the third set of NBS scenario, the scenario of PP3, RG3 and GR3 is more cost-effective than the scenario of PP6, RG6 and GR6, respectively. Thus, the combined scenarios that characterised with a high D_F are less cost-effective than that of the other NBS scenarios at these scales. Concerning all NBS scenarios, the most cost-effective one is RG3.

For the scale from λ_6 to λ_2, the reference SICE are proportional to the estimated SICE, and they are more pronounced for the fifth set of NBS scenarios (i.e., the upstream and downstream NBS scenarios). The reason may be related to the D_F of the NBS scenarios at this range of scales. In Section 3.1.1, two ranges of scales were quantified for the fractal dimension of all NBS scenarios: (a) the small scale range from 10 m to 40 m; (b) the large scale range from 40 m to 2560 m. For instance, the D_F of the PP3 scenario at the small scale range and the large scale range are 0.42 and 1.6, respectively. Correspondingly, the D_F of the PP upstream scenario at the small scale range and the large scale range is 0.99 and 1.47, respectively. Comparing these two scenarios, at the small scale range, the D_F of the PP upstream scenario is higher than that of the PP3 scenario. Therefore, at the small scale range, the two SICEs of the PP3 scenario is relatively higher than that of the PP upstream scenario due to the low D_F. On the contrary, at the large scale range, the D_F of PP3 scenario is higher than that of the PP upstream scenario. Thus, the two SICEs of the PP3 scenario gradually decreased, and finally lower than that of the PP upstream scenario due to the high D_F.

At the resolution of λ_6, the most cost-effective scenarios are the PP upstream and PP downstream. From the resolution of λ_5 to λ_2, the two SICEs are very pronounced for the RG downstream scenario and GR downstream scenario. The main reasons for these two scenarios with the highest CE are slightly different. For the RG downstream scenario, the reason is mainly due to the LCC of RG downstream scenario are lower than that of the other NBS scenarios. For the GR downstream scenario, the reason is mainly related to the hydrological performances of GRs. As shown in Figure 5.15, the $\gamma_{max,t_n}(\lambda)$ and γ_s of GR downstream scenario are the highest at the resolution from λ_5 to λ_2.

Regarding the largest resolution of λ_1, the two SICEs of each NBS scenario are homogeneous. At this scale, the CE of each NBS scenario is close to zero.

Overall, the SICE based on the UM framework is highly correlated with the reference SICE computed at each resolution. This new indicator can predict the cost-effective NBS scenario across a wide range of scales.

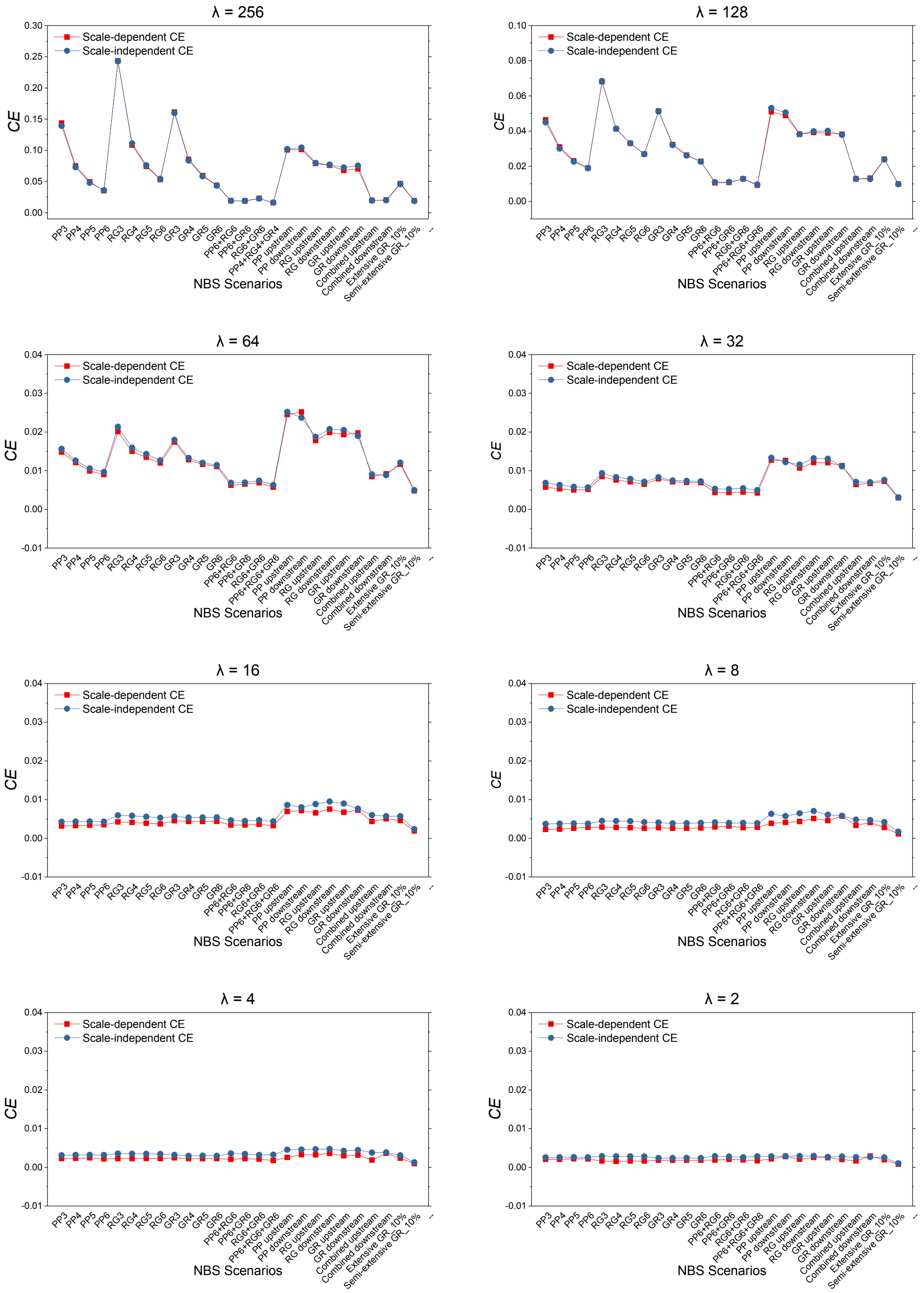

Figure 5.17: Reference SICE and estimated SICE of NBS scenarios at different resolution (from 256 to 2).

5.2.5 Intermediate conclusions for Section 5.2

In this section, the main objective is to investigate whether scale-independent cost-effectiveness indicators (SICE) can predict cost-effective NBS scenarios across a range of scales. With this respect, the maximum probable singularity γ_s of the last time step of the simulated overland flow of NBS scenarios is initially integrated with the LCC of NBS scenarios across scales as the estimated SICE for designing the cost-effective NBS scenarios. Correspondingly, the maximum singularity $\gamma_{max,t_n}(\lambda)$ of the last time step of the simulated overland flow of NBS scenarios is integrated with LCC of NBS scenarios at different resolutions, which is considered as the reference SICE to compare with the estimated SICE. The main findings of this study are summarised as follows:

(i) The γ_s of the simulated overland flow of NBS scenarios is strongly correlated to that of the $\gamma_{max,t_n}(\lambda)$, especially at the highest resolution. With increasing the resolution of the field, the discrepancy between $\gamma_{max,t_n}(\lambda)$ and γ_s becomes more remarkable. However, at each scale, the $\gamma_{max,t_n}(\lambda)$ is almost proportional to the γ_s. Therefore, γ_s is an appropriate the scale-independent indicator to evaluate the hydrological performances of NBS scenarios.

(ii) At the resolution of λ_8 to λ_7, the LCC of NBS scenario is very variable, and it decreases with increasing the D_F of the NBS scenario. For the resolution from λ_6 to λ_1, the LCC of each NBS scenario becomes more and more homogeneous, only the LCC of semi-extensive GR scenario is around two times higher than that of the other NBS scenarios.

(iii) The results of reference SICE are generally in agreement with the results of the estimated SICE for the whole range of scales. Especially, these two indicators are highly correlated at the small scale range (i.e., 258–128). The cost-effective NBS scenarios change with changing the scale. Furthermore, the cost-effective NBS scenarios estimated with the two SICEs are highly related to the fractal dimension of NBS scenarios. At the small scale range, the most cost-effective scenario is RG3 scenario. At the large scale range, the NBS downstream scenarios are more cost-effective than the other NBS scenarios.

Overall, this study presents a new approach for designing cost-effective NBS scenario. This approach is based on UM framework which estimated the cost-effective NBS scenario across range of scales. With the help of this scale-independent CE, the cost-effective NBS scenario can be easily quantified for different resolutions. This approach can effectively support urban planning and helps stakeholders to design cost-effective NBS scenarios in multi-scale.

Conclusions

An increasing number of highly urbanised cities are faced with the waterlogging risks due to the rapid urbanisation process and climate change (Fry and Maxwell, 2017; Ercolani et al., 2018). In the last decade, the interest has been raised up to mitigate the waterlogging and to improve the city resilience by employing nature-based solutions (NBS). With this respect, the main objective of this PhD thesis is multi-scale assessment of hydrological responses of nature-based solutions with the help of the fully-distributed hydrological model to improve urban resilience.

The Guyancourt catchment was selected as the case study in this thesis. The fully-distributed and physically-based hydrological model Multi-Hydro was used to simulate the hydrological responses of varies NBS scenarios under different rainfall conditions. In addition, two kinds of radar data (ENPC X-band radar data and Météo-France C-band radar data) characterised with different spatio-temporal resolutions were used as the main rainfall inputs for different modelling experiments. Chapter 1 presents the research background, NBS, and hydrological models. Three types of NBS are introduced: permeable pavement (PP), rain garden (RG), and green roof (GR). The Guyancourt catchment, geographic data, precipitation forcing, Multi-Hydro model and six sets of NBS scenarios were detailed in Chapter 2. Chapters 3 first quantified the fractal dimension (D_F) of each NBS scenario, then presented the Multifractal framework and its applications on the selected rainfall events. Chapter 4 devotes to the numerical investigation of the hydrological performances of various NBS scenarios in terms of urban flood resilience, and Chapter 5 respects to design the cost-effective NBS scenarios from catchment scale to multi-scale. The main findings are summarised as follows:

The hydrological responses of NBS scenarios (model outputs) largely depend on: (i) the highly spatially variable rainfall fields; (ii) the spatial distribution of NBS; and (iii) their intersection. Thus, in Chapter 4, the first objective is to investigate the variability of the hydrological responses of NBS scenarios, resulting from the multi-scale spatial heterogeneity of both the rainfall and the NBS distribution. To illustrate the importance of this objective, the heterogeneous spatial distributions of two sets of NBS scenarios (PP1, PP2, RG1, RG2, GR1, GR2, Combined1 and Combined2) were quantified with the help of their fractal dimension. The fully-distributed and physically-based hydrological model Multi-Hydro was applied, considering the Guyancourt catchment and these NBS scenarios with a spatial resolution of 10

m. A total of two approaches for processing rainfall data were considered for three rainfall events, namely gridded and catchment-averaged (i.e., distributed and uniform). The simulation results show that the impact of spatial variability in rainfall on the uncertainty of peak flow of NBS scenarios is about 8 % to 18 %, which is more pronounced than that of the total runoff volume. In addition, the spatial variability of the rainfall intensity at the largest rainfall peak responds almost linearly to the uncertainty of the peak flow of NBS scenarios. However, the hydrological responses of NBS scenarios are less affected by the heterogonous spatial distribution of NBS. For all the NBS scenarios, the uncertainties of peak flow and total runoff volume are lower than 5 % and 7 %, respectively. However, the difference of D_F between the same types of NBS scenarios has a fairly strong positive correlation to the corresponding uncertainties of peak flow. Therefore, this study suggests implementing NBS by optimizing D_F over the whole catchment to be the highest possible without considering the economic costs. Furthermore, to mix different NBS in the catchment, as presented in the two combined scenarios, can also efficiently reduce the uncertainties associated with the spatial arrangements of NBS.

Furthermore, the intersection effects of the spatial variability in rainfall and the spatial distributions of NBS are more pronounced for the peak flow of green roof scenarios and the total runoff volume of combined scenarios (with a maximum difference between the scenario of GR1 and GR2 reaching about 5 % on peak flow). The intersection effects on the total runoff volume of each NBS scenario is quite variable because the chosen NBS presents some limitations in terms of the infiltration or detention capacity during a long rainfall event with high intermittency. However, the RG scenarios appear to be less affected by the intersection effects, with a difference lower than 3 % on peak flow and lower than 1 % on total runoff volume, mainly due to their high retention capacity.

Following the modelling experiments in Section 4.1, the impacts of small scale rainfall variability on the hydrological responses of NBS were further investigated in Section 4.2. In this Section, six different rainfall products from C-band radar and X-band radar characterised with different spatio-temporal resolutions were used as the rainfall inputs for modelling the hydrological responses of NBS scenarios. Four different NBS scenarios were investigated: PP1, RG1, GR1 and Combined1. This study indicates the rainfall data plays an essential role in the reliability of the hydrological responses of the catchment and NBS scenarios. The spatio-temporal resolution, rainfall data processing process, and the selection of the best products are the factors which influence the obtained hydrological responses of NBS. This study shows that the hydrological performances of NBS scenarios simulated with X-band radar data are more stable than that of the C-band radar for three rainfall events, which is related to the impacts of the higher resolution of rainfall data. This was investigated by performing Universal

Multifractal framework on C-band, and X-band radar data, which indicates that value of multifractality index α for the X-band radar products is higher than that of C-band radar products for the three studied rainfall events. Thus, to improve the resolution of the rainfall input is significant for the prediction of hydrological performances of NBS.

As indicated by Eckart et al. (2017), the hydrological performances of NBS are strongly related to the site conditions and the studied scales. Therefore, the studies present the hydrological responses of NBS vary in different catchments (Qin et al., 2013; Versini et al., 2015; Ahiablame and Shakya, 2016). For assessing the hydrological performances of NBS on the mitigation of urban waterlogging to improve urban flooding resilience in multi-scales, this thesis investigated the intrinsic complexity of the heterogeneity of overland flow across the range of scales with the help of the UM framework (Schertzer and Lovejoy, 1987), which is considered as an appropriate technique to investigate the scale issue.

Based on the modelling studies in Sections 4.1 and 4.2, the Section 4.3 investigated the multifractal characterisation of the overland flow under various rainfall conditions and NBS scenarios. In this study, the 2D maps of overland flow of the baseline scenario and NBS scenarios were obtained by using Multi-hydro model. The Universal Multifractal theoretical framework was used innovatively to investigate the characteristics of the overland flow of different land use scenarios under varies rainfall conditions. To be more specific, the temporal evolution of maximum probable singularity γ_s was compared with the effective maximum singularity γ_{max} to infer the extremes of the overland flow in the field across scales and to evaluate the hydrological performances of NBS. The results reflect that γ_s is a scale-independent indicator that generally corresponds to the γ_{max} in a wide range of scales. With this new method, the observable extremes of overland flow on the catchment can be quantified without being limited to a single scale or certain specific values. In turn, the newly defined indicator of percentage change in morphological variability of the overland flow, RI, successfully quantifies across scales the relative performance of NBS scenarios in terms of improving urban flood resilience. For instance, the morphological variability of RG1 and GR1 scenarios in full range increased by about 19.6 % and 14.3 %, while that of the PP1 and Combined1 scenario decreased by about 19.3 % and 14.7 %, respectively.

In addition, to design cost-effective NBS scenarios and achieve multi-scale urban resilience, this thesis considered both hydrological impacts and economic costs of NBS. In Section 5.1, the study focused on the cost-effective design of NBS scenarios under different rainfall conditions by integrating the technical indicator (i.e., peak flow reduction and total runoff volume reduction) and economic indicator (i.e., LCC). The hydrological performances of NBS scenarios were explored with respect to the spatial variability in rainfall and spatial heterogonous distributions of NBS. The most cost-effective NBS scenario in eight studied rainfall events is the RG3 scenario, which presents a relatively low D_F. Compared with the other NBS scenarios, the combination of three types of NBS in the watershed is less cost-effective. In the strongest event (EV14S), the most cost-effective NBS scenarios are the PP upstream and PP downstream. This result demonstrated that in some specific rainfall conditions, concentrating single type of NBS in some specific locations is more cost-effective than heterogeneous implementation NBS all over the catchment.

Following the study of Section 5.1, Section 5.2 proposed a scale-independent CE indicator based on the UM framework. This indictor was compared with the reference scale-independent CE indicator at different scales to design the cost-effective NBS scenarios. The results indicated the scale-independent CE can effectively predict the cost-effective NBS scenarios across a range of scales. In Guyancourt catchment, the most cost-effective NBS scenario at the small scale range is RG3 scenario. In the large scale range, the NBS downstream scenarios are more cost-effective than the other NBS scenarios. Indeed, this new framework can be easily applied in some other catchments without repeating the simulations for different scales. Overall, the results obtained from Section 5.2 can provide some suggestions for future urban planning to help the city achieving multi-scale resilience.

In summary, the results obtained in this thesis have five aspects:

(i) The study of hydrological response in various NBS scenarios resulting from the multi-scale spatial variability of precipitation and the heterogeneous distribution of NBS hints towards using fully distributed hydrological models over semi-distributed or lumped models. Indeed, the fully distributed model has been shown to be able to take into account these small scale heterogeneities and propagate their effects to watershed scales, while parameterizing or smoothing out some critical heterogeneity, as done in non-fully distributed models, may bias its predictions.

(ii) The hydrological performances of NBS are significantly influenced by the intersection effects of spatial variability in rainfall and spatial distributions of NBS. Therefore, with only consider the hydrological performances of NBS, the study suggests to implement NBS decentralise over the catchment, but with a relatively higher fractal dimension. The small scale rainfall variability has a strong impact on the hydrological responses of NBS. To improve the resolution of the rainfall input is significant for better predicting the hydrological responses of NBS.

(iii) The scale-independent indicator γ_s is able to infer the extremes of overland flow on the catchment in a wide range of scales. The *RI* indicator reflects the morphological variability of the overland flow across the scales and estimates the changes in the resilience capacity of NBS. With these new scale-independent indicators, the efficiency of NBS can be quantified across the scales for stormwater management in resilience cities.

(iv) The technical indicators, especially the scale-independent technical indicator, integrated with the LCC for cost-effective design of NBS scenario, can be broadly applied in the future urban planning to achieve multi-scales resilience of a city.

For the perspectives, this thesis presents a typical example in Guyancourt catchment. In the future, the method used in this thesis can be easily applied in some other catchments with different environmental conditions. The results obtained from different catchments can be compared and it will be helpful to improve the overall urban flood resilience.

Bibliography

Arrowsmith, D. K. (1990). An introduction to dynamical systems. Cambridge University Press.

Adeyemo, O. J., Maksimovic, C., Leitao, J., & Butler, D. (2008). Sensitivity Analysis of Surface Runoff Generation for Pluvial Urban Flooding. *11th International Conference on Urban Drainage*, 1–10.

Ahiablame, L. M., Engel, B. A., & Chaubey, I. (2012). Effectiveness of low impact development practices: literature review and suggestions for future research. *Water, Air, & Soil Pollution*, *223*(7), 4253-4273.

Ahiablame, L. M., Engel, B. A., & Chaubey, I. (2013). Effectiveness of low impact development practices in two urbanized watersheds: Retrofitting with rain barrel/cistern and permeable pavement. *Journal of Environmental Management*, *119*, 151–161.

Aguado, P. L., Monte, J. P. Del, Moratiel, R., & Tarquis, A. M. (2014). Spatial Characterization of Landscapes through Multifractal Analysis of DEM. The Scientific World Journal, 2014.

Ahiablame, L., & Shakya, R. (2016). Modeling flood reduction effects of low impact development at a watershed scale. *Journal of Environmental Management*, *171*, 81–91.

Alves de Souza, B., da Silva Rocha Paz, I., Ichiba, A., Willinger, B., Gires, A., Amorim, J. C. C., de Miranda Reis, M., Tisserand, B., Tchiguirinskaia, I., & Schertzer, D. (2018). Multi-hydro hydrological modelling of a complex peri-urban catchment with storage basins comparing C-band and X-band radar rainfall data. *Hydrological Sciences Journal*, *63*(11), 1619–1635.

Blöschl, G., & Sivapalan, M. (1995). Scale issues in hydrological modelling: A review. *Hydrological Processes*, *9*(3–4), 251–290.

Biaou, A., Hubert, P., Schertzer, D., Hendrickx, F., BIAOU, A., HUBERT, P., Tchigurinsskaia, I., & Bendjoudi, H. (2003). Fractals, multifractals et previsions des precipitations. *2IE, Institut International d'Ingénierie de l'Eau et de l'Environnement*.

Brattebo, B. O., & Booth, D. B. (2003). Long-term stormwater quantity and quality performance of permeable pavement systems. *Water Research*, *37*(18), 4369–4376.

Bhaduri, B., Harbor, J. O. N., Engel, B., & Grove, M. (2008). Assessing Watershed-Scale , Long-Term Hydrologic Impacts of Land-Use Change Using a GIS-NPS Model, *Environmental management, 26(6),* 643–658.

Balica, S., & Wright, N. G. (2010). Reducing the complexity of the flood vulnerability index

Reducing the complexity of the flood vulnerability index, *Environmental Hazards*, *9*(4), 321-339.

Berndtsson, J. C. (2010). Green roof performance towards management of runoff water quantity and quality : A review. *Ecological Engineering*, *36*(4), 351–360.

Bianchini, F., & Hewage, K. (2012). How " green " are the green roofs ? Lifecycle analysis of green roof materials. *Building and Environment*, *48*, 57–65.

Burszta-Adamiak, E., & Mrowiec, M. (2013). Modelling of Green roofs' hydrologic performance using EPA's SWMM. *Water Science and Technology*, *68*(1), 36–42.

Barnsley, M. F. (2014). Fractals everywhere. Academic press.

Berretta, C., Poë, S., & Stovin, V. (2014). Moisture content behaviour in extensive green roofs during dry periods: The influence of vegetation and substrate characteristics. *Journal of Hydrology*, *511*, 374-386.

Baek, S. S., Choi, D. H., Jung, J. W., Lee, H. J., Lee, H., Yoon, K. S., & Cho, K. H. (2015). Optimizing low impact development (LID) for stormwater runoff treatment in urban area, Korea: Experimental and modeling approach. *Water Research*, *86*, 122–131.

Bell, C. D., Mcmillan, S. K., Clinton, S. M., & Jefferson, A. J. (2016). Hydrologic response to stormwater control measures in urban watersheds. *Journal of Hydrology*, 541, 1488-1500.

Bloorchian, A. A., Ahiablame, L., Osouli, A., & Zhou, J. (2016). Modeling BMP and Vegetative Cover Performance for Highway Stormwater Runoff Reduction. In *Procedia Engineering* (Vol. 145, pp. 274–280).

Bozovic, R., Maksimovic, C., Mijic, A., Smith, K. M., Suter, I., & van Reeuwijk, M. (2017). Blue Green Solutions: A Systems Approach to Sustainable, Resilient and Cost-Efficient Urban Development, (April), 52.

Brunetti, G., Šimůnek, J., Turco, M., & Piro, P. (2017). On the use of surrogate-based modeling for the numerical analysis of Low Impact Development techniques. *Journal of Hydrology*, *548*, 263–277.

Bai, Y., Zhao, N., Zhang, R., & Zeng, X. (2019). Storm Water Management of Low Impact Development in Urban Areas Based on SWMM. *Water*, *11*(1), 33.

Chow, V. T. (1964). Handbook of applied hydrology.

Carter, T.L., & Rasmussen, T.C. (2007). Hydrologic Behavior of Vegetated Roofs. *JAWRA Journal of the American Water Resources Association*, *42*(5), 1261-1274.

Cole, S. J., & Moore, R. J. (2009). Distributed hydrological modelling using weather radar in gauged and ungauged basins. *Advances in Water Resources*, *32*(7), 1107–1120.

Cashman, A. C. (2011). Case study of institutional and social responses to flooding: Reforming for resilience? *Journal of Flood Risk Management*, *4*(1), 33–41.

Cohen-Shacham, E., Walters, G., Janzen, C., & Maginnis, S. (2016). Nature-based solutions to address global societal challenges. *IUCN: Gland, Switzerland*, *97*.

Cipolla, S.S., Maglionico, M., & Stojkov, I. (2016). A long-term hydrological modelling of an extensive green roof by means of SWMM. *Ecological Engineering*, *95*, 876-887.

Chui, T. F. M., Liu, X., & Zhan, W. (2016). Assessing cost-effectiveness of specific LID practice designs in response to large storm events. *Journal of Hydrology*, *533*, 353–364.

Chan, F. K. S., Griffiths, J. A., Higgitt, D., Xu, S., Zhu, F., Tang, Y. T., ... & Thorne, C. R. (2018). " Sponge City " in China — A breakthrough of planning and flood risk management in the urban context. Land Use Policy " Sponge City " in China — A breakthrough of planning and fl ood risk management in the urban context. *Land Use Policy*, (March), 0–1.

Cai, D., Fraedrich, K., Guan, Y., Guo, S., Zhang, C., & Zhu, X. (2019). Urbanization and climate change: Insights from eco-hydrological diagnostics. *Science of the Total Environment*, *647*, 29–36.

De Lima, M. I. P., & Grasman, J. (1999). Multifractal analysis of 15-min and daily rainfall from a semi-arid region in Portugal. *Journal of Hydrology*, *220*(1–2), 1–11.

Dutta, D., Herath, S., & Musiake, K. (2000). Flood inundation simulation in a river basin using a physically based distributed hydrologic model. *Hydrological Processes*, *14*(3), 497–519.

Deidda, R. (2000). Rainfall downscaling in a space-time multifractal framework. *Water Resources Research*, *36*(7), 1779–1794.

Davis, A. P., Shokouhian, M., Sharma, H., & Minami, C. (2001). Laboratory study of biological retention for urban stormwater management. *Water Environment Research*, *73*(1), 5-14.

Davis, A. P., Shokouhian, M., Sharma, H., Minami, C., & Winogradoff, D. (2003). Water Quality Improvement through Bioretention : Lead , Copper , and Zinc Removal, 73–82. *Water Environment Research*, *75*(1), 73-82.

Dussaillant, A.R., Wu, C.H., & Potter, K.W. (2004). Richards Equation Model of a Rain Garden. *Journal of Hydrologic Engineering*, *9*(3), 219-225.

Dietz, M. E. (2007). Low impact development practices: A review of current research and recommendations for future directions. *Water, Air, and Soil Pollution*, *186*(1–4), 351–363.

Davis, A. P. (2008). Field performance of bioretention: Hydrology impacts. *Journal of Hydrologic Engineering*, *13*(2), 90-95.

De Montera, L., Barthès, L., Mallet, C., & Golé, P. (2009). The effect of rain-no rain intermittency on the estimation of the universal multifractals model parameters. *Journal* *of Hydrometeorology*, *10*(2), 493–506.

Diss, S., Testud, J., Lavabre, J., Ribstein, P., Moreau, E., & Parent du Chatelet, J. (2009). Ability of a dual polarized X-band radar to estimate rainfall. *Advances in water resources*, *32*(7), 975-985.

Di Vittorio, D., & Ahiablame, L. (2015). Spatial Translation and Scaling Up of Low Impact Development Designs in an Urban Watershed. *Journal of Water Management Modeling*, 1–9.

El Tabach, E., Tchiguirinskaia, I., Mahmood, O. & Schertzer, D. (2009): Multi-Hydro: a spatially distributed numerical model to assess and manage runoff processes in peri- urban watersheds. Poster session presentation at the Final Conference of the COST Action C22, Road map towards a flood resilient urban environment, Paris, France.

Emmanuel, I., Andrieu, H., & Tabary, P. (2012). Evaluation of the new French operational weather radar product for the field of urban hydrology. *Atmospheric Research*, *103*, 20-32.

European Commission. (2015). Towards an EU Research and Innovation policy agenda for Nature-Based Solutions & Re-Naturing Cities, Final Report of the Horizon 2020 Expert Group on 'Nature-Based Solutions and Re-Naturing Cities', Luxembourg: Publications Office of the European Union.

Eckart, K., McPhee, Z., & Bolisetti, T. (2017). Performance and implementation of low impact development – A review. *Science of the Total Environment*, *607–608*, 413–432.

Ercolani, G., Chiaradia, E. A., Gandolfi, C., Castelli, F., & Masseroni, D. (2018). Evaluating performances of green roofs for stormwater runoff mitigation in a high flood risk urban catchment. *Journal of Hydrology*, *566*(September), 830–845.

Frisch, U., & G. Parisi. (1985). "A Multifractal Model of Intermittency." Turbulence and Predictability in Geophisical Fluid Dynamics and Climate Dynamics, 84–88.

Fuller, S.K., & Petersen, S.R. (1996). *LIFE-CYCLE COSTING MANUAL for the Federal Energy Management Program, NIST Handbook 135, 1995 Edition* (No. Handbook (NIST HB)-135).

Falconer, K. J. (1988, March). The Hausdorff dimension of self-affine fractals. In Mathematical Proceedings of the Cambridge Philosophical Society (Vol. 103, No. 2, pp. 339-350). Cambridge University Press.

Fraedrich, K. (1986). Estimating the Dimensions of Weather and Climate Attractors. *Journal of the Atmospheric Sciences*, *43*(5), 419–432.

Fraedrich, K. (1993). Scaling regimes of composite rainfall time series.pdf. *Tellus A: Dynamic*

Meteorology and Oceanography, *45(4)*, 289–298.

Fraedrich, K., Kleidon, A., & Lunkeit, F. (1999). A green planet versus a desert world: Estimating the effect of vegetation extremes on the atmosphere. *Journal of Climate*, *12*(10), 3156–3163.

Ferraris, L., Gabellani, S., Parodi, U., Rebora, N., Von Hardenberg, J., & Provenzale, A. (2003). Revisiting multifractality in rainfall fields. *Journal of Hydrometeorology*, *4*(3), 544–551.

Fassman, E. A., & Blackbourn, S. (2010). Urban runoff mitigation by a permeable pavement system over impermeable soils. *Journal of Hydrologic Engineering, 15*(6), 475-485.

Folke, C., Carpenter, S. R., Walker, B., Scheffer, M., Chapin, T., & Rockstrom., J. (2010). Resilience thinking: integrating resilience, adaptability and transformability. Ecology and Society 15(4): *Nature Nanotechnology*, *15*(4), 20.

Freni, G., Mannina, G., & Viviani, G. (2010). Urban storm-water quality management: Centralized versus source control. *Journal of Water Resources Planning and Management*, *136*(2), 268–278.

Flo-2D manual, 2012. Reference Manuals. http://www.flo-2d.com/download.

Figueras i Ventura, J., Boumahmoud, A.A., Fradon, B., Dupuy, P., & Tabary, P. (2012). Long-term monitoring of French polarimetric radar data quality and evaluation of several polarimetric quantitative precipitation estimators in ideal conditions for operational implementation at C-band. *Quarterly Journal of the Royal Meteorological Society*, *138*(669), 2212-2228.

Feder, J. (2013). Fractals. Springer Science & Business Media.

Fletcher, T. D., Andrieu, H., & Hamel, P. (2013). Advances in Water Resources Understanding , management and modelling of urban hydrology and its consequences for receiving waters : A state of the art. *Advances in Water Resources*, *51*, 261–279.

Faivre, N., Fritz, M., Freitas, T., de Boissezon, B., & Vandewoestijne, S. (2017). Nature-Based Solutions in the EU: Innovating with nature to address social, economic and environmental challenges. *Environmental research*, *159*, 509-518.

Fry, T. J., & Maxwell, R. M. (2017). Evaluation of distributed BMPs in an urban watershed—High resolution modeling for stormwater management. *Hydrological Processes*, *31*(15), 2700–2712.

Fry, T. J., & Maxwell, R. M. (2018). Using a distributed hydrologic model to improve the green infrastructure parameterization used in a lumped model. *Water*, 10(12), 1756.

Green, W. H., & Ampt, G. A. (1911). Studies on Soil Phyics. *The Journal of Agricultural Science, 4*(1), 1-24.

Geiger, W. (1987) Flushing effects in combined sewer systems. In *Proceedings of the 4th International Conference Urban Drainage, Lausanne, Switzerland, 1987* (pp. 40-46).

Gupta, V. K., & Waymire, E. C. (1993). A statistical analysis of mesoscale rainfall as a random cascade. *Journal of Applied Meteorology*, *32*(2), 251-267.

Galderisi AC. (2005). Integrated vulnerability assessment: the relevance "to" and "of" regional and urban planning. ARMONIA project coference"multi Hazards: challenges for risk assessment ,mapping and management, Barcelona, Naples, Italy: Department of Urban and Regional Planning, University of Naples Federico II.

Gagnon, J., Lovejoy, S., Schertzer, D., Gagnon, J., Lovejoy, S., Multifractal, D. S., & Processes, N. (2006). Multifractal earth topography. *Nonlinear Processes in Geophysics*, *13*, 541–570.

Gilroy, K. L., & McCuen, R. H. (2009). Spatio-temporal effects of low impact development practices. *Journal of Hydrology*, *367*(3–4), 228–236.

Gires, A., Tchiguirinskaia, I., Schertzer, D., & Lovejoy, S. (2012). Influence of the zero-rainfall on the assessment of the multifractal parameters. *Advances in water resources*, *45*, 13-25.

Gires, A., Tchiguirinskaia, I., Schertzer, D., & Lovejoy, S. (2013). Multifractal analysis of a semi-distributed urban hydrological model. *Urban Water Journal*, *10*(3), 195–208.

Giangola-Murzyn, A. (2013). Modélisation et paramétrisation hydrologique de la ville, résilience aux inondations, Ph.D. thesis, Ecole des Ponts ParisTech, Université Paris-Est, France, 260 pp.

Grebel, J.E., Mohanty, S.K., Torkelson, A.A., Boehm, A.B., Higgins, C.P., Maxwell, R.M., Nelson, K.L., & Sedlak, D.L. (2013). Engineered infiltration systems for urban stormwater reclamation. *Environmental Engineering Science*, *30*(8), 437-454.

Gires, A., Tchiguirinskaia, I., Schertzer, D., & Lovejoy, S. (2013). Development and analysis of a simple model to represent the zero rainfall in a universal multifractal framework. *Nonlinear Processes in Geophysics*, *20*, 343–356.

Gires, Auguste, Giangola-Murzyn, A., Abbes, J. B., Tchiguirinskaia, I., Schertzer, D., & Lovejoy, S. (2015). Impacts of small scale rainfall variability in urban areas: a case study with 1D and 1D/2D hydrological models in a multifractal framework. *Urban Water Journal*, *12*(8), 607–617.

Gülbaz, S., & Kazezyilmaz-Alhan, C. M. (2017). An evaluation of hydrologic modeling performance of EPA SWMM for bioretention. *Water Science and Technology*, *76*(11), 3035–3043.

Gao, L., Zhang, L., Li, X., & Zhou, S. (2019). Evaluating Metropolitan Flood Coping

Capabilities under Heavy Storms. *Journal of Hydrologic Engineering*, *24*(6), 1–13.

Gires, Auguste, Tchiguirinskaia, I., Schertzer, D., Ochoa-Rodriguez, S., Willems, P., Ichiba, A., … & Ten Veldhuis, M. C. (2017). Fractal analysis of urban catchments and their representation in semi-distributed models: Imperviousness and sewer system. *Hydrology and Earth System Sciences*, *21*(5), 2361–2375.

Gires, Auguste, Abbes, J. B., da Silva Rocha Paz, I., Tchiguirinskaia, I., & Schertzer, D. (2018). Multifractal characterisation of a simulated surface flow: A case study with Multi-Hydro in Jouy-en-Josas, France. *Journal of Hydrology*, *558*, 482–495.

Guo, X., Du, P., Zhao, D., & Li, M. (2019). Modelling low impact development in watersheds using the storm water management model. *Urban Water Journal*, *16*(2), 146–155.

Horton, R. E. (1919). Rainfall interception. Monthly weather review, 47(9), 603-623.

Horton, R. E. (1933). The role of infiltration in the hydrologic cycle: Transactions of American Geophysical Union, v. 14.

Holling, C. S. (1973). Resilience and stability of ecological systems. *Annual review of ecology and systematics*, *4*(1), 1-23.

Hentschel, H. G. E., & Procaccia, I. (1983). The infinite number of generalized dimensions of fractals and strange attractors. *Physica D: Nonlinear Phenomena, 8*(3), 435-444.

Hubert, P., & Carbonnel, J. P. (1989). Dimensions fractales de l'occurrence de pluie en climat soudano-sahélien. *Hydrologie continentale*, *4*(1), 3-10.

Healy, R.W. (1990). Simulation of solute transport in variably saturated porous media with supplemental information on modifications to the US Geological Survey’s computer program VS2D. U.S. Geol. Surv. Water-Resources Investig. Rep. 90-4025.

Hastings, H. M., & Sugihara, G. (1993). Fractals. A user's guide for the natural sciences. fusg.

Harris, D., Menabde, M., Seed, A., & Austin, G. (1996). Multifractal characterization of rain fields with a strong orographic influence. *Journal of Geophysical Research Atmospheres*, *101*(21), 26405–26414.

Holman-Dodds, J. K., Bradley, A. A., & Potter, K. W. (2003). Evaluation of hydrologic benefits of infiltration based urban storm water management. *Journal of the American Water Resources Association*, *39*(1), 205–215.

Hunt, W. F., Davis, A. P., & Traver, R. G. (2012). Meeting hydrologic and water quality goals through targeted bioretention design. *Journal of Environmental Engineering, 138*(6), 698-707.

Hoang, T. (2011) Prise en compte des fluctuations spatio-temporelles pluies-débits pour une meilleure gestion de la ressource en eau et une meilleure évaluation des risques. Ph.D.

Thesis, Earth Sciences, Université Paris-Est, Champs-sur-Marne, France.

Hakimdavar, R., Culligan, P.J., Finazzi, M., Barontini, S., & Ranzi, R. (2014). Scale dynamics of extensive green roofs: Quantifying the effect of drainage area and rainfall characteristics on observed and modeled green roof hydrologic performance. *Ecological Engineering*, *73*, 494-508.

Hu, M., Sayama, T., Zhang, X., Tanaka, K., Takara, K., & Yang, H. (2017). Evaluation of low impact development approach for mitigating flood inundation at a watershed scale in China. *Journal of Environmental Management*, *193*, 430–438.

Her, Y., Jeong, J., Arnold, J., Gosselink, L., Glick, R., & Jaber, F. (2017). A new framework for modeling decentralized low impact developments using Soil and Water Assessment Tool. *Environmental modelling & software*, *96*, 305-322.

Hamidi, A., Farnham, D.J., & Khanbilvardi, R. (2018). Uncertainty analysis of urban sewer system using spatial simulation of radar rainfall fields: New York City case study. *Stochastic Environmental Research and Risk Assessment*, *32*(8), 2293-2308.

Helmi, N. R., Verbeiren, B., Mijic, A., van Griensven, A., & Bauwens, W. (2019). Developing a modeling tool to allocate Low Impact Development practices in a cost-optimized method. *Journal of Hydrology*, *573*(March), 98–108.

Hua, P., Yang, W., Qi, X., Jiang, S., Xie, J., Gu, X., Li, H., Zhang, J., & Krebs, P. (2020). Evaluating the effect of urban flooding reduction strategies in response to design rainfall and low impact development. *Journal of Cleaner Production*, *242*, 118515.

IPCC. (2014). Climate Change 2014. Synthesis Report. Contribution of Working Groups I, II and III to the Fifth Assessment Report of the Intergovernmental Panel on Climate Change [Core Writing Team, R.K. Pachauri and L.A. Meyer (eds.)]. IPCC, Geneva, Switzerland, 151 pp.

Ichiba, A. (2016) X-Band Radar Data and Predictive Management in Urban Hydrology. Ph.D. Thesis, Ecole des Ponts ParisTech, Université Paris-Est, Champs-sur-Marne, France, 272 pp.

Ichiba, A., Gires, A., Tchiguirinskaia, I., Schertzer, D., Bompard, P., & Veldhuis, M. C. Ten. (2018). Scale effect challenges in urban hydrology highlighted with a distributed hydrological model. *Hydrology and Earth System Sciences*, *22*(1), 331–350.

International Union for Conservation of Nature – IUCN: Commission on Ecosystem Management. Available online: https://www.iucn.org/commissions/ (accessed on 29 February 2020).

Institut National de la Statistique et des Etudes Economiques – INSEE: Dossier complet –

Commune de Guyancourt (78297). Available online: https://www.insee.fr/fr/statistiques/2011101?geo=COM-78297#chiffre-cle-5 (accessed on 29 February 2020).

Imhoff, R. O., Van Verseveld, W. J., Van Osnabrugge, B. & Weerts, A. H. (2020) Scaling Point-Scale (Pedo) transfer Functions to Seamless Large-Domain Parameter Estimates for High-Resolution Distributed Hydrologic Modeling : An Example for the Rhine River, Water Resourse Research, 56(4), 1–28.

James, W., Rossman, L. A., & James, W. R. C. (2010). User's guide to SWMM 5:[based on original USEPA SWMM documentation]. CHI.

Jia, H., Lu, Y., Yu, S.L., & Chen, Y. (2012). Planning of LID-BMPs for urban runoff control: The case of Beijing Olympic Village. *Separation and Purification Technology*, *84*, 112-119.

Jia, H., Yao, H., Tang, Y., Shaw, L. Y., Field, R., & Tafuri, A. N. (2015). LID-BMPs planning for urban runoff control and the case study in China. *Journal of Environmental Management*, 149, 65-76.

Jato-Espino, D., Sillanpää, N., Charlesworth, S.M., Andrés-Doménech, I. (2016). Coupling GIS with stormwater modelling for the location prioritization and hydrological simulation of permeable pavements in urban catchments. *Water (Switzerland) 8*.

Khader, O., & Montalto, F. A. (2009). Development and calibration of a high resolution SWMM model for simulating the effects of LID retrofits on the outflow hydrograph of a dense urban watershed. In *Low Impact Development for Urban Ecosystem and Habitat Protection* (pp. 1-9).

Kuang, X., Sansalone, J., Ying, G. and Ranieri, V. (2011). Pore-structure models of hydraulic conductivity for permeable pavement. *Journal of hydrology*, 399, 148–157.

Kelman, I. (2015). Climate change and the Sendai framework for disaster risk reduction. *International Journal of Disaster Risk Science*, *6*(2), 117-127.

Kwak, D., Kim, H., & Han, M. (2016). Runoff Control Potential for Design Types of Low Impact Development in Small Developing Area Using XPSWMM. *Procedia engineering*, *154*, 1324-1332.

Kamali, M., Delkash, M., & Tajrishy, M. (2017). Evaluation of permeable pavement responses to urban surface runoff. *Journal of Environmental Management*, *187*, 43–53.

Linsley, R. K., Kohler, M. A., & Paulhus, J. L. P. (1949). Applied hydrology. Civil Engineering Series (USA) eng.

Linsley Jr, R. K., Kohler, M. A., & Paulhus, J. L. (1975). Hydrology for engineers.

Li, R. M., Simons, D. B., & Stevens, M. A. (1976). Solutions to Green-Ampt infiltration equation. *Journal of the Irrigation and Drainage Division, 102*(2), 239-248.

Lappala, E. G., Healy, R. W. & Weeks, E. P. (1987). Documentation of computer program VS2D to solve the equations of fluid flow in variably saturated porous media.

Lovejoy, S. D. A. A., Schertzer, D., & Tsonis, A. A. (1987). Functional box-counting and multiple elliptical dimensions in rain. *Science, 235*(4792), 1036-1038.

Lovejoy, S., & Schertzer, D. (1990). Multifractals, universality classes and satellite and radar measurements of cloud and rain fields. *Journal of Geophysical Research*, *95*(D3), 2021–2034.

Lavallée, D., Lovejoy, S., Schertzer, D., & Ladoy, P. (1993). Nonlinear variability and landscape topography: analysis and simulation. *Fractals in geography*, 158-192.

Lovejoy, S, Lavallée, D., Schertzer, D., Ladoy, P., Lovejoy, S., Lavallée, D., … The, P. L. (1995). The 11 / 2 law and multifractal topography : theory and analysis. *Nonlinear Processes in Geophysics., 2*, 16–22.

Lee, J. G., Heaney, J. P., & Asce, M. (2004). Estimation of Urban Imperviousness and its Impacts on Storm Water Systems, *Journal of Water Resources Planning and Management, 129(5), 419-426.*

Lovejoy, S., & Schertzer, D. (2007). Scaling and multifractal fields in the solid earth and topography. *Nonlinear Processes in Geophysics*, *14*(4), 465–502.

Langousis, A., Veneziano, D., Furcolo, P., & Lepore, C. (2009). Multifractal rainfall extremes: Theoretical analysis and practical estimation. *Chaos, Solitons and Fractals, 39(3), 1182–1194.*

Loukas, A., Llasat, M.C., & Ulbrich, U. (2010). Extreme events induced by weather and climate change: Evaluation, forecasting and proactive planning. *Natural Hazards and Earth System Sciences, 10(9), 1895-1897.*

Lovejoy, S, & Schertzer, D. (2013). The weather and climate: Emergent laws and multifractal cascades. Cambridge University Press.

Liao, Z.L., He, Y., Huang, F., Wang, S., & Li, H.Z. (2013). Analysis on LID for highly urbanized areas' waterlogging control: Demonstrated on the example of Caohejing in Shanghai. *Water science and technology*, *68*(12), 2559-2567.

Liu, Y., Ahiablame, L. M., Bralts, V. F., & Engel, B. A. (2015). Enhancing a rainfall-runoff model to assess the impacts of BMPs and LID practices on storm runoff. *Journal of environmental management, 147.*

Liu, X., Mijic, A., & Maksimovic, C. (2015). A Conceptual Model for Simulating the

Hydrologic Performance of Extensive Green Roof Systems, (July), 27–29.

Luo, P., Mu, D., Xue, H., Ngo-Duc, T., Dang-Dinh, K., Takara, K., Nover, D., & Schladow, G. (2018). Flood inundation assessment for the Hanoi Central Area, Vietnam under historical and extreme rainfall conditions. *Scientific reports*, *8*(1), 1-11.

Liang, C. Y., You, G. J. Y., & Lee, H. Y. (2019). Investigating the effectiveness and optimal spatial arrangement of low-impact development facilities. *Journal of Hydrology*, *577*(July).

Liu, X., & Chui, T. F. M. (2019). Evaluation of green roof performance in mitigating the impact of extreme storms. *Water (Switzerland)*, *11*(4).

Leimgruber, J., Krebs, G., Camhy, D., & Muschalla, D. (2019). Model-based selection of cost-effective low impact development strategies to control water balance. *Sustainability*, *11*(8), 2440.

Li, Y., Huang, J.J., Hu, M., Yang, H., & Tanaka, K. (2020). Design of low impact development in the urban context considering hydrological performance and life-cycle cost. *Journal of Flood Risk Management*, 13, 1–15.

Marshall, J. S., & Palmer, W. M. K. (1948). The distribution of raindrops with size. *Journal of meteorology*, *5*(4), 165-166.

Mandelbrot, B. (1967). How long is the coast of britain? statistical self-similarity and fractional dimension. *Science, 156*(3775):636–638.

May, R. M. (1973). Qualitative stability in model ecosystems. Ecology, pages 638–641.

Mandelbrot, B. B. (1983). The fractal geometry of nature/Revised and enlarged edition. *whf.*

Mandelbrot, B. B. (1989). Multifractal measures, especially for the geophysicist. *Fractals in geophysics* (pp.5-42). Birkhäuser, Basel.

Marsan, D., Schertzer, D., & Lovejoy, S. (1996). Causal space ‐ time multifractal processes: Predictability and forecasting of rain fields. *Journal of Geophysical Research: Atmospheres*, *101*(D21), 26333-26346.

Marsch, E., Tu, C. Y., & Rosenbauer, H. (1996, March). Multifractal scaling of the kinetic energy flux in solar wind turbulence. *Annales Geophysicae 14*, No. 3, pp. 259-269.

Macor, J., Schertzer, D., & Lovejoy, S. (2007). Multifractal methods applied to rain forecast using radar data.

Martin, C., Ruperd, Y., & Legret, M. (2007). Urban stormwater drainage management: The development of a multicriteria decision aid approach for best management practices. *European journal of operational research*, *181*(1), 338-349.

Montalto, F., Behr, C., Alfredo, K., Wolf, M., Arye, M., & Walsh, M. (2007). Rapid assessment of the cost-effectiveness of low impact development for CSO control. *Landscape and urban planning*, *82*(3), 117-131.

Nykanen, D. K. (2008). Linkages between orographic forcing and the scaling properties of convective rainfall in mountainous regions. *Journal of Hydrometeorology, 9*(3), 327-347.

Moradkhani, H., & Sorooshian, S. (2009). General review of rainfall-runoff modeling: model calibration, data assimilation, and uncertainty analysis. *Hydrological modelling and the water cycle 63,* 1-24.

Morison, P. J., & Brown, R. R. (2011). Landscape and Urban Planning Understanding the nature of publics and local policy commitment to Water Sensitive Urban Design. *Landscape and Urban Planning*, *99*(2), 83–92.

Maksimović, Č., Kurian, M., & Ardakanian, R. (2015). Rethinking infrastructure design for multi-use water services. Springer International Publishing.

Miller, J. D., & Hutchins, M. (2017). The impacts of urbanisation and climate change on urban flooding and urban water quality: A review of the evidence concerning the United Kingdom. *Journal of Hydrology: Regional Studies*, *12*(January), 345–362.

Massoudieh, A., Maghrebi, M., Kamrani, B., Nietch, C., Tryby, M., Aflaki, S., & Panguluri, S. (2017). A flexible modeling framework for hydraulic and water quality performance assessment of stormwater green infrastructure. *Environmental Modelling & Software*, *92*,

Météo-France: Climat des Yvelines. Available online: https://www.meteofrance.com/accueil (accessed on 29 February 2020).

Niachou, A., Papakonstantinou, K., Santamouris, M., Tsangrassoulis, A., & Mihalakakou, G. (2001). Analysis of the green roof thermal properties and investigation of its energy performance, *Energy and buildings, 33*(7), 719-729.

Nash, J. E., & Sutcliffe, J. V. (1970). River flow forecasting through conceptual models part I - A discussion of principles. *Journal of Hydrology*, 10(3), 282–290.

Newcomer, M.E., Gurdak, J.J., Sklar, L.S., & Nanus, L. (2014). Urban recharge beneath low impact development and effects of climate variability and change. *Water Resources Research*, *50*(2), 1716-1734.

Nardi, L., & Rinaldi, M. (2015). Spatio-temporal patterns of channel changes in response to a major flood event : the case of the Magra River (central – northern Italy). *Earth Surface Processes and Landforms*, *40*(3), 326-339.

Newburn, D. A., & Alberini, A. (2016). Household response to environmental incentives for rain garden adoption. *Water Resources Research*, *52*(2), 1345-1357.

Olsson, J., & Niemczynowicz, J. (1996). Multifractal analysis of daily spatial rainfall distributions. *Journal of Hydrology*, *187*(1–2), 29–43.

Penman, H. L. (1948). Natural evaporation from open water, bare soil and grass. Proceedings of the Royal Society of London. *Series A. Mathematical and Physical Sciences*, *193*(1032), 120-145.

Pimm, S. and Lawton, J.H. (1977). Number of trophic levels in ecological communities. Nature, 268(5618) :329–331.

Prince George's County. (1993). Design manual for use of bioretention in stormwater management. Prince George's County, MD Department of Environmental Resources, Watershed Protection Branch, MD Department of Environmental Protection, Landover, MD.

Pandey, G., Lovejoy, S., & Schertzer, D. (1998). Multifractal analysis of daily river flows including extremes for basins of five to two million square kilometres, one day to 75 years. *Journal of Hydrology*, *208*(1-2), 62-81.

Pathirana, A., & Herath, S. (2002). Multifractal modelling and simulation of rain fields exhibiting spatial heterogeneity. *Hydrology and Earth System Sciences*, *6*(4), 695–708.

Pathirana, Assela, Herath, S., & Yamada, T. (2003). Estimating rainfall distributions at high temporal resolutions using a multifractal model. *Hydrology and Earth System Sciences*, *7*(5), 668–679.

Parent-du-Châtelet, J. (2003). Aramis, le réseau français de radars pour la surveillance des précipitations. *La Météorologie*.

Praskievicz, S., & Chang, H. (2009). A review of hydrological modelling of basin-scale climate change and urban development impacts. *Progress in Physical Geography, 33*(5), 650-671.

Pechlivanidis, I. G., Jackson, B. M., Mcintyre, N. R., & Wheater, H. S. (2011). Catchment scale hydrological modelling: a review of model types, calibration approaches and uncertainty analysis methods in the context of recent developments in technology and applications. *Global NEST journal, 13*(3), 193-214.

Pyke, C., Warren, M.P., Johnson, T., LaGro, J., Scharfenberg, J., Groth, P., Freed, R., Schroeer, W., & Main, E. (2011). Assessment of low impact development for managing stormwater with changing precipitation due to climate change. *Landscape and Urban Planning*, *103*(2), 166-173.

PITEL,W. (2011). Une expérience historique pour une résilience renforcée. l'exemple des villes du nord de la france (mi xvie-mi xixe siècle).

Park, D., Sandoval, N., Lin, W., Kim, H., & Cho, Y. (2014). A case study : Evaluation of water storage capacity in permeable block pavement. *Journal of Civil Engineering*, 18(2), 514–

520.

Palla, A., & Gnecco, I. (2015). Hydrologic modeling of Low Impact Development systems at the urban catchment scale. *Journal of Hydrology*, *528*, 361–368.

Praticò, F.G., Amodeo, L., Lamari, D., Lanciano, C., Placido, V., Praticò, M., & Scattareggia, T. (2015). Pavement life cycle cost analysis for city logistics. *WIT Transactions on The Built Environment*, *146*, 337-348.

Paz, I. (2018). Quantifying the rain heterogeneity by X-band radar measurements for improving flood forecasting. Ph.D Thesis, Ecole des Ponts ParisTech, Université Paris-Est, Champs-sur-Marne, France, 308 pp.

Paz, I., Willinger, B., Gires, A., Ichiba, A., Monier, L., Zobrist, C., … Schertzer, D. (2018). Multifractal comparison of reflectivity and polarimetric rainfall data from C- and X-band radars and respective hydrological responses of a complex catchment model. *Water (Switzerland)*, *10*(3).

Paz, I., Willinger, B., Gires, A., de Souza, B. A., Monier, L., Cardinal, H., … Schertzer, D. (2019). Small scale rainfall variability impacts analyzed by fully-distributed model using C-band and X-band radar data. *Water (Switzerland)*, *11*(6).

Paz, I., Tchiguirinskaia, I., & Schertzer, D. (2020). Rain gauge networks' limitations and the implications to hydrological modelling highlighted with a X-band radar. *Journal of Hydrology*, *583* (October 2019), 124615.

Qin, H. peng, Li, Z. xi, & Fu, G. (2013). The effects of low impact development on urban flooding under different rainfall characteristics. *Journal of Environmental Management*, *129*, 577–585.

Royer, J. F., Biaou, A., Chauvin, F., Schertzer, D., & Lovejoy, S. (2008). Multifractal analysis of the evolution of simulated precipitation over France in a climate scenario. *Comptes Rendus - Geoscience*, *340*(7), 431–440.

Rossman, L. A. (2010). *Storm water management model user's manual, version 5.0* (p. 276). Cincinnati: National Risk Management Research Laboratory, Office of Research and Development, US Environmental Protection Agency.

Rozos, E., Makropoulos, C., & Maksimović, Č. (2013). Rethinking urban areas: An example of an integrated blue-green approach. *Water Science and Technology: Water Supply*, *13*(6), 1534–1542.

Richard, J., Giangola-Murzyn, A., Tchiguirinskaia, I. & Schertzer, D. (2013) MH ASSIMTOOL: An assimilation tool dedicated to a fully distributed model. *Poster presented at International Conference on Flood Resilience*. 5-7. United Kingdom.

Razzaghmanesh, M., & Beecham, S. (2014). The hydrological behaviour of extensive and intensive green roofs in a dry climate. *Science of the total environment*, *499*, 284-296.

Raymond, C. M., Frantzeskaki, N., Kabisch, N., Berry, P., Breil, M., Razvan, M., … Calfapietra, C. (2017). A framework for assessing and implementing the co-benefits of nature-based solutions in urban areas. *Environmental Science and Policy*, *77*(July), 15–24.

Rivas-Tabares, D., de Miguel, Á., Willaarts, B., & Tarquis, A. M. (2020). Self-organizing map of soil properties in the context of hydrological modeling. *Applied Mathematical Modelling*, *88*, 175–189.

Rodríguez-Sinobas, L., Zubelzu, S., Martín-Sotoca, J. J., & Tarquis, A. M. (2021). Multiscaling analysis of Soil Water Content during irrigation events. Comparison between surface and subsurface drip irrigation. *Geoderma*, *382*(October 2020), 114777.

Schertzer, D. & Lovejoy, S. (1984). On the dimension of atmospheric motions. *Turbulence and Chaotic phenomena in Fluids*, 505-512.

Schertzer, D., & Lovejoy, S. (1985). The dimension and intermittency of atmospheric dynamics. In *Turbulent Shear Flows 4* (pp. 7-33). Springer, Berlin, Heidelberg.

Schertzer, D., & Lovejoy, S. (1987). Physical modeling and analysis of rain and clouds by anisotropic scaling mutiplicative processes. *Journal of Geophysical Research*, *92*(D8), 9693–9714.

Schertzer, D., & Lovejoy, S. (1989). Generalised scale invariance and multiplicative processes in the atmosphere. *Pure and Applied Geophysics PAGEOPH*, *130*(1), 57–81.

Schertzer, D., & Lovejoy, S. (1989). Nonlinear variability in geophysics: Multifractal simulations and analysis. *Fractals' Physical Origin and Properties*, 49-79.

Schertzer, D., & Lovejoy, S. (1992). Hard and soft multifractal processes. *Physica A: Statistical Mechanics and Its Applications*, *185*(1–4), 187–194.

Schertzer, D., & Lovejoy, S. (1993). Multifractal generation of self-organized criticality. *Fractals in the natural and applied sciences*, 325-339.

Schertzer, D., Lovejoy, S., & Lavallée, D. (1993). Generic multifractal phase transitions and self-organized criticality. *Cellular Automata: prospects in astronomy and astrophysics*, 216-227.

Schertzer, D., & Lovejoy, S. (1993). EGS Richardson AGU Chapman NVAG3 Conference: Nonlinear variability in geophysics3: scaling and multifractal processes. Lecture Notes, 67-69.

Schmitt, F., Schertzer, D., Lovejoy, S., & Brunet, Y. (1994). Empirical study of multifractal phase transitions in atmospheric turbulence. *Nonlinear Processes in Geophysics*, *1*(2–3), 95–104.

Schertzer, D., & Lovejoy, S. (1997). Universal multifractals do exist!: Comments on “a statistical analysis of mesoscale rainfall as a random Cascade.” *Journal of Applied Meteorology*, *36*(9), 1296–1303.

Schertzer, Daniel, & Lovejoy, S. (2004). Uncertainty and predictability in geophysics: Chaos and multifractal insights. *Geophysical Monograph Series*, *150*, 317–334.

Scholz, M., & Grabowiecki, P. (2007). Review of permeable pavement systems. *Building and environment, 42*(11), 3830-3836.

Sailor, D. J. (2008). A green roof model for building energy simulation programs. *Energy and Buildings*, *40*(8), 1466–1478.

Schertzer, D., Tchiguirinskaia, I., Lovejoy, S., & Hubert, P. (2010). Ni monstres, ni miracles: L’hydrologie n’est pas un horsain des sciences non-linéaires! *Hydrological Sciences Journal*, *55*(6), 965–979.

Spatari, S., Yu, Z., & Montalto, F.A. (2011). Life cycle implications of urban green infrastructure. *Environmental Pollution*, *159*(8-9), 2174-2179.

Schertzer, D., & Lovejoy, S. (2011). Multifractals, generalized scale invariance and complexity in geophysics. *International Journal of Bifurcation and Chaos*, *21*(12), 3417-3456.

Stovin, V., Vesuviano, G., & Kasmin, H. (2012). The hydrological performance of a green roof test bed under UK climatic conditions. *Journal of Hydrology*, *414–415*, 148–161.

Sun, Y., Li, Q., Liu, L., Xu, C., & Liu, Z. (2014). Hydrological simulation approaches for BMPs and LID practices in highly urbanized area and development of hydrological performance indicator system. *Water Science and Engineering*, *7*(2), 143-154.

Selex. (2015). Selex METEOR manual

Schertzer, D., & Tchiguirinskaia, I. (2015). Multifractal vector fields and stochastic Clifford algebra. *Chaos: An Interdisciplinary Journal of Nonlinear Science*, *25*(12), 123127.

Salvadore, E., Bronders, J., & Batelaan, O. (2015). Hydrological modelling of urbanized catchments: A review and future directions. *Journal of Hydrology*, *529*(P1), 62–81.

Stanić, F., Cui, Y.J., Delage, P., De Laure, E., Versini, P.A., Schertzer, D., & Tchiguirinskaia, I. (2019). A device for the simultaneous determination of the water retention properties and the hydraulic conductivity function of an unsaturated coarse material; application to a green-roof volcanic substrate. *Geotechnical Testing Journal*, *43*(3).

Song, Y., Kirkwood, N., Maksimović, Č., Zhen, X., O’Connor, D., Jin, Y., & Hou, D. (2019). Nature based solutions for contaminated land remediation and brownfield redevelopment in cities: A review. *Science of the Total Environment*, *663*, 568–579.

Singh, K. K. (2019). Rain Garden—A Solution to Urban Flooding: A Review. Sustainable Engineering, *30*, 27-35.

Stanić, F., Delage, P., Tchiguirinskaia, I., Versini, P. A., Cui, Y. J., & Schertzer, D. (2020). A New Fractal Approach to Account for Capillary and Adsorption Phenomena in the Water Retention and Transfer Properties of Unsaturated Soils. *Water Resources Research*, *56*(12), 1–15.

Tholin, A. L., & Keifer, C. J. (1960). Hydrology of urban runoff. *Transactions of the American Society of Civil Engineers*, *125*(1), 1308-1355.

Tessier, Y., Lovejoy, S., Hubert, P., Schertzer, D., & Pecknold, S. (1996). Multifractal analysis and modeling of rainfall and river flows and scaling, causal transfer functions. *Journal of Geophysical Research Atmospheres*, *101*(21), 26427–26440.

Tchiguirinskaia, I., Lu, S., Molz, F. J., Williams, T. M., & Lavallée, D. (2000). Multifractal versus monofractal analysis of wetland topography. *Stochastic Environmental Research and Risk Assessment*, *14*(1), 8–32.

Tchiguirinskaia, I., Schertzer, D., Hubert, P., Bendjoudi, H., & Lovejoy, S. (2004). Multiscaling geophysics and sustainable development. *IAHS Publications-Series of Proceedings and Reports*, *287*, 113–136.

Takebayashi, H., & Moriyama, M. (2007). Surface heat budget on green roof and high reflection roof for mitigation of urban heat island. *Building and Environment*, *42*(8), 2971–2979.

Todini, E. (2007). Hydrological catchment modelling: Past, present and future. *Hydrology and Earth System Sciences*, *11*(1), 468–482.

Tarquis, A. M., Mèndez, V., Grau, J. B., Antòn, J. M., & Andina, D. (2007). Fractals as pre-processing tool for computational intelligence application. In *Computational Intelligence* (pp. 193-212). Springer, Boston, MA.

Tarquis, A. M., Heck, R. J., Grau, J. B., Fabregat, J., Sanchez, M. E., & Antón, J. M. (2008). Influence of thresholding in mass and entropy dimension of 3-D soil images. *Nonlinear Processes in Geophysics*, *15*(6), 881–891.

Tarquis, A. M., De Lima, J. L. M. P., Krajewski, W. F., Cheng, Q., & Gaonac'H, H. (2011). Preface "nonlinear and scaling processes in Hydrology and Soil Science." *Nonlinear Processes in Geophysics*, *18*(6), 899–902.

Tabary, P., Boumahmoud, A. A., Andrieu, H., Thompson, R. J., Illingworth, A. J., Le Bouar, E., & Testud, J. (2011). Evaluation of two " integrated" polarimetric Quantitative Precipitation Estimation (QPE) algorithms at C-band. *Journal of Hydrology*, *405*(3-4), 248-260.

Tchiguirinskaia, I., Schertzer, D., Hoang, C. T., & Lovejoy, S. (2011, April). Multifractal study of three storms with different dynamics over the Paris region. *12th International Conference on Urban Drainage*, Porto Alegre, Brazil.

Tchiguirinskaia, I., Schertzer, D., Hoang, C. T., & Lovejoy, S. (2012). Multirracial study of three storms with different dynamics over the paris region. *IAHS-AISH Publication*, *351*(April 2011), 421–426.

Turconi, Faccini, Marchese, Paliaga, Casazza, Vojinovic, & Luino. (2020). Implementation of Nature-Based Solutions for Hydro-Meteorological Risk Reduction in Small Mediterranean Catchments: The Case of Portofino Natural Regional Park, Italy. *Sustainability*, *12*(3), 1240.

USEPA. (2000). Low impact development (LID): A literature review.

UNDP/BCPR (2004), A Global Report Reducing Disaster Risk-A Challenge for Development, United Nations Development Programme, Bureau for crisis Prevention and Recovery. Pokhrel, L. N. (2002), Water Induced Disasters in Nepal and Its Management, in Disaster Review 2002, (July 2003) DWIDP.

UNESCO-IHE. (2013). FVI. http://www.unesco-ihe.org/. United nations NY. 1982. Proceedings of the Seminars on Flood Vulnerability Analysis and on the Principles of Floodplain Management for Flood Loss Prevention. Bangkok.

Viessman, W., Lewis, G. L., Knapp, J. W., & Harbaugh, T. E. (1989). Introduction to hydrology.

Viessman Jr, W. (1996). Integrated water management. Journal of Contemporary Water Research and Education, 106(1), 2.

VanWoert, N. D., Rowe, D. B., Andresen, J. A., Rugh, C. L., Fernandez, R. T., & Xiao, L. (2005). Green roof stormwater retention: effects of roof surface, slope, and media depth. J*ournal of environmental quality, 34*(3), 1036-1044.

Velleux, M. L., England Jr, J. F., & Julien, P. Y. (2008). TREX: Spatially distributed model to assess watershed contaminant transport and fate. *Science of the Total Environment*, *404*(1), 113-128.

Van der Knijff, J.M., Younis, J., & de Roo, A.P.J. (2010). LISFLOOD: A GIS-based distributed model for river basin scale water balance and flood simulation. *International Journal of Geographical Information Science*, *24*(2), 189-212.

Versini, P. A., Ramier, D., Berthier, E., & de Gouvello, B. (2015). Assessment of the hydrological impacts of green roof: From building scale to basin scale. *Journal of Hydrology*, *524*, 562–575.

Versini, Pierre Antoine, Gires, A., Tchinguirinskaia, I., & Schertzer, D. (2016). Toward an operational tool to simulate green roof hydrological impact at the basin scale: A new version of the distributed rainfall-runoff model Multi-Hydro. *Water Science and Technology*, *74*(8), 1845–1854.

Van den Bosch, M., & Ode Sang. (2017). Urban natural environments as nature-based solutions for improved public health – A systematic review of reviews. *Environmental research, 158, 373-384.*

Versini, P. A., Kotelnikova, N., Poulhes, A., Tchiguirinskaia, I., Schertzer, D., & Leurent, F. (2018). A distributed modelling approach to assess the use of Blue and Green Infrastructures to fulfil stormwater management requirements. *Landscape and Urban Planning*, *173*, 60–63.

Vicari, R., Tchiguirinskaia, I., Tisserand, B., & Schertzer, D. (2019). Climate risks , digital media , and big data : following communication trails to investigate urban communities ' resilience. *Natural Hazards and Earth System Science*, *19*, 1485–1498.

Versini, P. A., Gires, A., Tchiguirinskaia, I., & Schertzer, D. (2020). Fractal analysis of green roof spatial implementation in European cities. *Urban Forestry & Urban Greening*, *49*, 126629.

Wisconsin, D. N. R. (2004). Bioretention for infiltration, Conservation Practice Standard. *Madison, WI: Wisconsin DNR*.

WI DNR. (2006). Bioretention for infiltration. Conservation Practice Standard (1004). Wisconsin Department of Natural Resources.

Wong, T. H. (2006). An overview of water sensitive urban design practices in Australia. *Water Practice and Technology*, *1*(1).

Wheater, H. S., Ballard, C., Bulygina, N., McIntyre, N., & Jackson, B. M. (2012). Modelling environmental change: quantification of impacts of land use and land management change on UK flood risk. In *System Identification, Environmental Modelling, and Control System Design* (pp. 449-481). Springer, London.

Wang, L. P., Ochoa-Rodríguez, S., Simões, N. E., Onof, C., & Maksimović, Č. (2013). Radar-raingauge data combination techniques: A revision and analysis of their suitability for urban hydrology. *Water Science and Technology*, *68*(4), 737–747.

Winston, R. J., Dorsey, J. D., & Hunt, W. F. (2016). Quantifying volume reduction and peak flow mitigation for three bioretention cells in clay soils in northeast Ohio. *Science of the Total Environment*, *553*, 83-95.

Wu, J., Xu, M., & Zhang, P. (2018). The impacts of governmental performance assessment policy and citizen participation on improving environmental performance across Chinese provinces. *Journal of Cleaner Production*, *184*, 227–238.

Wang, M., Zhang, D. Q., Su, J., Dong, J. W., & Tan, S. K. (2018). Assessing hydrological effects and performance of low impact development practices based on future scenarios modeling. *Journal of Cleaner Production*, *179*, 12–23.

Winston, R. J., Arend, K., Dorsey, J. D., Johnson, J. P., & Hunt, W. F. (2020). Hydrologic performance of a permeable pavement and stormwater harvesting treatment train stormwater control measure. J*ournal of Sustainable Water in the Built Environment, 6*(1), 04019011.

Xing, W., Li, P., Cao, S. bing, Gan, L. li, Liu, F. lin, Zuo, J. e. (2016). Layout effects and optimization of runoff storage and filtration facilities based on SWMM simulation in a demonstration area. Water Sci. Eng. 9, 115–124.

Yang, W.Y., Li, D., Sun, T., & Ni, G.H. (2015). Saturation-excess and infiltration-excess runoff on green roofs. *Ecological Engineering*, *74*, 327-336.

Yao, L., Chen, L., & Wei, W. (2016). Assessing the effectiveness of imperviousness on stormwater runoff in micro urban catchments by model simulation. *Hydrological Processes*, *30*(12), 1836-1848.

Yao, L., Wei, W., & Chen, L. (2016). How does imperviousness impact the urban rainfall-runoff process under various storm cases?. *Ecological Indicators*, *60*, 893-905.

Yuan, J., Dunnett, N., & Stovin, V. (2017). The influence of vegetation on rain garden hydrological performance. *Urban Water Journal*, *9006*, 1–7.

Zachary Bean, E., Frederick Hunt, W., & Alan Bidelspach, D. (2007). Evaluation of four permeable pavement sites in eastern North Carolina for runoff reduction and water quality impacts. *Journal of Irrigation and Drainage Engineering, 133*(6), 583-592.

Zahmatkesh, Z., Burian, S., Karamouz, M., Tavakol-Davani, H., & Goharian, E. (2015). Low-Impact Development practices to mitigate climate change effects on urban stormwater runoff: case study of New York City. *Journal of Irrigation and Drainage Engineering*, *141*(1), 04014043.

Zölch, T., Henze, L., Keilholz, P., & Pauleit, S. (2017). Regulating urban surface runoff through nature-based solutions – An assessment at the micro-scale. *Environmental research*, *157*, 135-144.

Zhang, Z., Szota, C., Fletcher, T.D., Williams, N.S.G., & Farrell, C. (2019). Green roof storage capacity can be more important than evapotranspiration for retention performance. *Journal of environmental management*, *232*, 404-412.

Zhu, Z., Chen, Z., Chen, X., & Yu, G. (2019). An assessment of the hydrologic effectiveness of low impact development (LID) practices for managing runoff with different objectives, *Journal of environmental management, 231, 504-514*.